UNIVERSITÀ DEGLI STUDI DI MILANO

Dottorato di Ricerca in Scienze della Terra

Ciclo XXXIV

The role of melt/olivine ratio in dissolution and reactive crystallization: an experimental and microstructural study (Electron Back-Scattered Diffraction - EBSD) at 0.5 GPa

Tesi di Dottorato / Ph.D. Thesis

SSD GEO/07

Michela Grammatica

I.D nr. R12367

Tutor	***Academic Year***	***Coordinator***
Prof.ssa Patrizia Fumagalli	*2020-2021*	*Prof. Fernando Camara Artigas*
Co-tutors		
Dr. Giulio Borghini		
Prof. Giancarlo Capitani		

A mio nonno Nanè,

“Bisogna fare ciò che è necessario”.

INDEX

ABSTRACT

Microstructural and geochemical studies have emphasized that melt-rock reactions play a paramount role in the origin of gabbroic rocks in the lower oceanic crust. It is widely accepted that olivine-rich troctolites might form through dunite infiltrated followed by reactive crystallization of interstitial melts. Furthermore, experiments on the origin of olivine-rich troctolites have suggested that melt/olivine ratio is a fundamental factor in basalt-dunite interactions (Borghini et al., 2018). However, the effect of melt/rock ratio on the chemistry and the development of microstructures induced by reactive dissolution and crystallization processes have not been well defined yet. This work aims to experimentally evaluate and quantify the effect of melt/olivine ratio on mineral chemistry, melt evolution and microstructural development of olivine-rich troctolites formed by reactive processes. Electron Back-Scattered Diffraction (EBSD) analysis gives the opportunity to parametrize microstructures as a function of different melt/olivine ratio.

Ten experiments were performed in piston cylinder apparatus at 0.5 GPa using San Carlos olivine (Fo_{90}) and a MORB-type glass (AH6) as starting materials, mixed together in different proportions (*i.e.*, the Initial Melt Amount, IMA, was equal to 10, 25 or 50wt%). Out of ten experiments, seven were isothermal runs at 1200, 1250 and1300°C, lasted 24 hours, and three were step-cooled runs carried out by lowering the temperature, with a fix rate of 1°C/min, from an isothermal dwell (at 1300°C) down to 1100°C.

Run products of isothermal experiments at 1200°C consist of olivine, plagioclase, clinopyroxene and traces of glass, whereas at 1300°C consist only of olivine and glass. Texturally we distinguish two types of olivine: i) large subhedral crystals (up to100 μm) with both straight and lobate rims and ii) smaller (5-20 μm) rounded grains. Olivine grain size increases with the IMA; on contrary, the amount of smaller rounded grains is inversely correlated. At 1300°C, high IMA enhances the melt-olivine reaction, promoting olivine dissolution and crystal growth that leads to an increase in the olivine grain boundaries tortuosity. At 1200°C, mineral chemistry of olivine suggests that X_{Mg} values are not correlated with different IMA. At 1300°C, X_{Mg} in olivine increases from 0.89 ± 0.01 to 0.91 ± 0.01 with the increase of the IMA. The NiO content in olivine is strongly temperature dependent. At 1300°C, the NiO content in olivine decreases with the IMA. Clinopyroxene presents $X_{Mg} = 0.89 \pm 0.00_{IMA10wt\%.}$, $0.89 \pm 0.02_{IMA25wt\%}$ and $0.84 \pm 0.02_{IMA50wt\%}$. Plagioclase has $X_{An} = 0.68 \pm 0.03_{IMA10wt\%}$, $0.61 \pm 0.06_{IMA25wt\%.}$ and $0.66 \pm 0.02_{IMA50wt\%.}$ Reacted glasses at 1200°C have higher SiO_2 and lower X_{Mg} than glasses at 1300°C, thus suggesting a strong control of olivine and interstitial phases on the residual glass composition. EBSD analysis suggests that the interaction between olivine matrix and basalt at $50wt\%_{IMA}$

and 1300°C strongly affects the pre-existing dunite matrix recovering its plastic deformation (*i.e.*, deformed olivines grains underwent an annealing re-crystallization), thus generating an "undeformed" olivine-rich matrix. The average intragranular deformation parameter defined by the Grain Orientation Spread (GOS), indicates that no differences occur between the two different olivine morphologies. The smaller and rounded olivine has GOS = ~ 0.49 and the larger one with straight and lobate rims has GOS value = ~ 0.41. Hence, in terms of deformation grade, the assessment of a pre-existing olivine grain (**Olivine$_1$**) and a new crystallized olivine (**Olivine$_2$**) is not straightforward.

Step-cooled experiments result in dunite (10wt%$_{IMA}$), olivine-rich troctolite (25wt%$_{IMA}$) and olivine-gabbro (50wt%$_{IMA}$). The olivine texture is formed by elongated crystals with high tortuosity of grain boundaries independently of the grain size and IMA. In contrast to a normal fractional crystallization path, the reactive crystallization of melt within an olivine matrix leads to early clinopyroxene crystallization rather than plagioclase. This is likely related to a combined effect of: i) the MgO enrichment of reacted melt due to the high extent of olivine dissolution and ii) small amount of H_2O in reacted melts that can suppress the plagioclase crystallization. EBSD analysis suggests that the reactive dissolution and crystallization processes efficiently promote the "recovery" of olivine plastic deformation independently of the grain size (and shape) and the different IMA.

Experimental results of this work show several textural and chemical analogies with observations made on natural olivine-rich troctolite from oceanic and ophiolitic massifs. The results achieved in this thesis provide new and useful insights into melt-rock reactions between a dunite and an impregnating MORB-type melt.

Chapter 1
STATE OF THE ART AND AIMS

1.1 –Introduction

The main goal of this brief introduction is to give an overall idea of the importance of the experiments presented in thus thesis and how they fit in the current (fall 2021) state of the art. Several studies of natural olivine-rich troctolites have suggested that the melt/rock ratio plays a paramount role in the interaction between an olivine matrix and an impregnating MORB-type melt, affecting the textural features and the geochemical composition of these rocks in the lower oceanic crust and the evolution of MORBs (*e.g.*, Renna & Tribuzio, 2011; Sanfilippo & Tribuzio, 2011, 2013; Sanfilippo et al., 2014, 2015; Rampone et al., 2016; Renna et al., 2016; Borghini et al., 2018). However, the reaction couple experimental strategies used in the experiments performed by previous authors did not allow to better quantify the total amount of residual melt that interacts with the olivine matrix, hence, as a matter of fact, a rigorous quantitative evaluation of the effects induced by different melt/olivine ratios has never been addressed.

Moreover, in the natural rocks as well as in the experimental synthesis, it seems to be possible to distinguish two sets of morphologically different olivines i) larger deformed and subhedral grains with both straight and lobate rims (up to100 μm) (also defined as $Olivine_1$) and ii) smaller undeformed and rounded grains (~20 μm) (also defined as $Olivine_2$) (*e.g.*, Drouin et al., 2010; Basch et al., 2018, 2019 and 2021; Ferrando et al., 2018) (details in **Section 1.2**). However, no extended EBSD analysis has ever been conducted on assemblages resulting by experimental synthesis. Also, chemically, a non-negligible variability of the major elements in recovered mid-ocean ridge basalts (MORB) has been observed. The latter, is not simply related to a fractional crystallization process, but it may result from a reactive crystallization (*e.g.*, Lissenberg & Dick, 2008; Collier & Kelemen, 2010). Hence, different models have been proposed in order to evaluate how the melt-rock reactions affect the chemical evolution of the reacting melt and, as a consequence, the lithology resulted during the crystallization process. Overall, it has been observed that the reaction processes lead to a more enriched chemical composition of the impregnating melt. In particular, it has been proposed that the reactive crystallization Liquid Lines of Descent (LLDs) are characterized by a nearly constant MgO content coupled with a strong decrease in Ca# and higher SiO_2 and Na_2O contents than ones predicted in fractional crystallization (Collier & Kelemen, 2010). Isothermal experiments are used to study how the reaction processes between an olivine matrix and a reacting MORB-type melt can influence the texture and

chemistry as well as the amount of dissolved olivine and how the reacted melt evolves through the reaction. On the other hand, the step-cooled experiments allow to study the crystallization process of the reacted melt by analyzing the resulted lithology from the crystallization of the reacted melt.

In this study, for the first time, the experimental procedure coupled with the chemical analysis allowed to quantify how different melt/olivine ratios affect the olivine dissolution process as well as the total amount of dissolved olivine and the residual reacted melt. The experiments aim to provide new detailed insights on melt-rock reaction processes by relating the chemical data obtained from Electron Microprobe Analysis (EMPA) (details in **Chapter 3, 4** and **5**) with a detailed textural study on olivine grains using Electron Back-Scattered Diffraction (EBSD) analysis which, at the best of our knowledge, has never been performed before. At this purpose, this innovative technique will be employed in order to better define and rigorously quantify the textural features and intragranular deformation grade of olivine grains resulted from dunite-basalt interactions (details in **Chapter 3, 4** and **5**).

1.2 – Origin of olivine-rich troctolite by melt-rock reactions

Recent studies have highlighted how the melt-rock reaction processes play an important role in the origin of gabbroic rocks in the lower oceanic crust (*e.g.*, Lissenberg & Dick, 2008; Collier & Kelemen, 2010; Sanfilippo et al., 2016; Basch et al., 2018, 2019). Olivine is the major mineral of the mantle peridotites and dunites and it is known to be the first phase to crystallize from a primitive MORB (*i.e.*, Mid-Ocean Ridge Basalt, Grove et al., 1992). Several works based on field-based studies and experiments have suggested that the chemistry and microstructures of olivine in dunites and peridotites could be powerful tools to unravel how melt-rock reaction processes affect the primitive olivine-rich lower oceanic crust (*e.g.*, Suhr et al., 2009; Drouin et al., 2009, 2010; Sanfilippo & Tribuzio, 2013; Basch et al., 2018, 2019; Ferrando et al., 2018). Moreover, the interaction between an olivine matrix and an impregnating melt plays an important role in affecting the chemical evolution of MORB (*e.g.*, Collier & Kelemen, 2010; Yang et al., 2013; Paquet et al., 2016) at the mantle-crust transition (Drouin et al., 2009; Lissenberg et al., 2013). Although in literature troctolites have commonly been interpreted as olivine and plagioclase cumulates crystallized from primitive MORB, it has been proposed that the olivine-rich troctolite end-members (olivine >70 vol%) might form by reaction between an olivine-rich matrix and migrating MORB-type melts saturated in clinopyroxene and plagioclase (*e.g.*, Suhr et al., 2008; Drouin et al., 2010, Dick et al., 2010; Renna and Tribuzio, 2011). However, two dominant petrogenic hypothesis have been formulated on the origin of the olivine-rich troctolite. In the first, as a response to cooling of primitive basalts emplaced within the lower crust and/or at mantle-crust transition, the olivine-rich matrix could derived by a magmatic segregation. In this regard, Renna et al., (2016) studied olivine-rich troctolite and harrisites included in the mid-ocean ridge (MOR)-type gabbroic sequences from the Internal Ligurian ophiolites exposed along the Alpine-Appennine belt. They proposed an "intra-crustal" origin for the Ligurian olivine-rich troctolite – harrisite association, suggesting that they may formed by an open-system magmatic crystallization as a consequence of primitive melt injections into the growing lower crust (Renna et al., 2016, 2021). According to the second hypothesis, the pristine rocks of the olivine-rich troctolite are supposed to be "replacive" dunites formed at lithospheric mantle conditions as a consequence of reactive percolation of olivine-saturated melts. In the last decades, this interpretation has been invoked for several troctolites from oceanic (*e.g.*, Suhr et al., 2008; Drouin et al., 2009, 2010; Sanfilippo et al., 2013, 2016) and ophiolitic environments (*e.g.*, Renna & Tribuzio, 2011; Sanfilippo & Tribuzio, 2011, 2013; Sanfilippo et al., 2014, 2015; Rampone et al., 2016).

Recently, Basch et al., (2018, 2019) have demonstrated the hybrid and reactive nature of some olivine-rich troctolites from Mt. Maggiore peridotitic massif (Alpine Corsica, France) and Erro-Tobbio

ultramafic body (Western Alps, Italy) combining the results of microstructural and geochemical studies. Basch et al. (2019) observed the presence of two main generations of olivine: i) large subhedral crystals with both straight and lobate rims and ii) smaller rounded undeformed grains (***Fig. 1-1b-c***). Clinopyroxene and plagioclase do not show any evidence of deformation and occur as interstitial phases between boundaries of adjacent olivine grains (***Fig. 1-1c***). This textural evidence suggests a disequilibrium: the originally subhedral olivines have been partially corroded and the clinopyroxene and plagioclase crystallized simultaneously from the reacted melt as suggested by several authors (*e.g.*, Borghini et al. 2007; Drouin et al., 2009; Sanfilippo & Tribuzio, 2013; Sanfilippo et al., 2016; Basch et al., 2019).

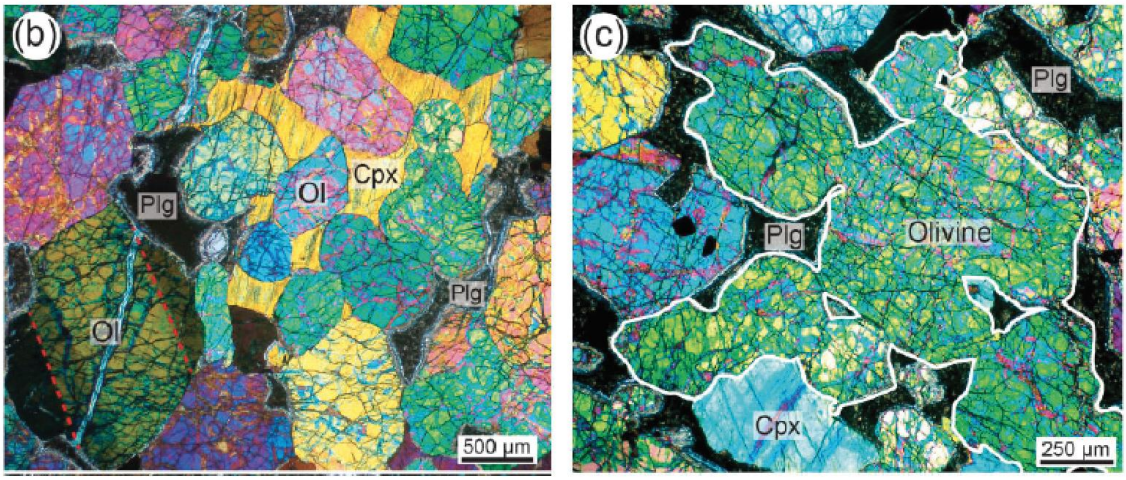

Figure 1-1 *(b) Olivine smaller rounded undeformed grains and (c) large subhedral crystals with both straight and lobate rims with plagioclase and clinopyroxene interstitial showing any evidence of deformation, from Basch et al., 2019.*

From a chemical point of view, high X_{Mg} value (X_{Mg} = molar Mg/ (Mg + Fe^{tot})) and NiO content in olivine have been theorized to support the hypothesis of a mantle origin of some troctolites (Drouin et al., 2009; Sanfilippo et al., 2014; Rampone et al., 2016). Rampone et al., (2016) documented a decoupling between olivine texture (**Olivine$_1$** and **Olivine$_2$**) and its trace element composition, with an **Olivine$_1$** more enriched in trace element thus being a potential relict of a pre-existing mantle dunite matrix. In this regard, Basch et al., (2021) recently provided new constrains on reactive origin of olivine-rich troctolites (Erro-Tobbio ophiolitic mantle) performing a detailed chemical and microstructural (Electron Back Scattered Diffraction-EBSD and Transmission Electron Microscopy -TEM) study on the two olivine morphologies, in order to explain their trace elements enrichments. The microstructural investigation of the deformed olivine grains highlighted the presence of numerous parallel polyphase inclusions constituted by pargasitic amphibole, clinopyroxene and chromite (10 to 50 µm long). Overall, the inclusions are characterized by a preferred orientation parallel to subgrain boundaries of the host

olivine. Moreover, they show straight, planar shapes and occur at subgrain boundaries or parallel to olivine kink band and subgrain boundaries. EBSD analysis suggested that the inclusions are parallel to crystal dislocations of the host olivine, providing different evidences that do not support an exsolution origin of these inclusions:

1- The association between amphibole, clinopyroxene and chromite in olivine crystals have never been documented as exsolutions.
2- The contact between the host olivine and inclusion walls or between the phases that form the inclusions is irregular.
3- The crystallographic orientations of the phases in the inclusions do not show any relationship with the orientation of the host olivine.
4- Minerals show different orientations and all portions of a specific phase have a single orientation, suggesting that the latter belong to a single interstitial crystal.

The presence of these polyphase inclusions has been interpreted as an important evidence of intracrystalline melt migration that led to the melt evolution and becoming residual after the reactive crystallization of the olivine-rich troctolites percolated within the most deformed olivine grains along subgrain boundaries and iso-oriented crystal dislocations (Basch et al., 2021) Hence, the presence of intracrystalline melt enhanced diffusive re-equilibration between the evolved melt and the percolated **Olivine$_1$,** which acquired the enriched trace elements composition expected in neo-formed olivine crystals **Olivine$_2$**

The interstitial phases like clinopyroxene and plagioclase have been generally used to define the chemistry of the reacted melt and the possible influence of pressure in the crystallization process. In particular, a high-Mg# clinopyroxene *(i.e.,* 90-89) is inconsistent with an origin by a low-pressure crystallization of MORB-type melt. In particular, melts that fractionated at low-pressure and follow a liquid line of descent ruled by olivine $\rightarrow$ olivine + plagioclase $\rightarrow$ olivine + plagioclase + clinopyroxene, will be chemically different from those differentiated at higher pressures. The pressure increase promotes the extent of clinopyroxene stability field at the expense of plagioclase and olivine (*e.g.*, Groove et al., 1992; Lissenberg & Dick, 2008), enhancing the early saturation of melt in clinopyroxene. Hence, further observations on troctolites (*e.g.*, Lissenberg & Dick et al., 2008; Sanfilippo & Tribuzio, 2013; Basch et al., 2019) suggested that high-Mg# in clinopyroxene reflects an origin through MORB-like melt fractionation at moderate-high pressure (P = 0.5-0.7 GPa). High-Mg# clinopyroxene occurs as oikocrysts crystals (*i.e.,* enclose) suggesting that they crystallized as interstitial phases between olivine and plagioclase, following the normal low pressures fractionation trend for MORB. Hence, the origin of

high-Mg# could not be related to crystallization at high pressure. Moreover, the coexisting plagioclase has low anorthite (An) content (range from 83 to 65) contrary to plagioclase typically crystallized at high-*P*. In this case, the early clinopyroxene crystallization results in lower Mg# value in melt by the time it saturates in plagioclase, leading to low-Mg# clinopyroxene at a given plagioclase An content. In this regard, the more likely hypothesis is that high-Mg# clinopyroxene forms when a relatively evolved, clinopyroxene-saturated melt reacts with primitive cumulates (*e.g*., Lissenberg and Dick, 2008; Lissenberg and MacLeod 2016; Sanfilippo et al., 2015; Basch et al., 2018; Borghini et al., 2018). High TiO_2 and Cr_2O_3 contents in clinopyroxene oikocrysts differ from those expected for fractional crystallization of a MORB-type melt as documented in Internal Ligurian and Pineto ophiolitic sequences (*e.g.*, Renna & Tribuzio, 2011, Sanfilippo & Tribuzio, 2013).

Furthermore, trace elements compositions show that clinopyroxene is characterized by small Eu-negative anomalies and that plagioclase displays a strong positive Eu anomaly. Plagioclase also displays positive anomalies in U, Sr and Ti relative to their neighboring elements and strong negative anomalies in Nb and Zr (*e.g*., Drouin et al., 2009; Ferrando et al., 2018). The clinopyroxene trace element pattern is depleted in Light Rare Earth Elements (LREE) (La_N-Sm_N = 0.08 – 016) with an almost flat Medium REE (MREE) to Heavy REE (HREE). Moreover, clinopyroxene is generally characterized by moderate negative anomalies in Ti and slight depletion in Zr and Hf and a strong fractionation in Sr, Ba and Pb (*e.g*., Drouin et al., 2009; Rampone et al., 2016; Basch et al., 2018; Ferrando et al., 2018). These chemical evidences indicate that clinopyroxene precipitated from melts that have slightly fractionated through the plagioclase crystallization. In particular, the plagioclase and clinopyroxene chemistry suggest that they could have precipitated from a chemically buffered reservoir similar to a magmatic chamber (Drouin et al, 2009). In summary, according to a multistage melt-mantle reaction process, different models of olivine-rich troctolites origin (***Fig. 1-2***) were proposed:

1) formation of dunite through the interaction between basaltic melts and mantle peridotite resulting in pyroxenes dissolution and olivine precipitation. At this stage, the progressive dissolution of pyroxenes results in the increasing of Si and Cr contents of the percolating MORB (Arai et al., 1997). Texturally, the dunitization contributes to disrupt the pre-existing olivine fabric and to weaken the olivine CPO from axial – [100] in peridotite to axial - [001] in dunite, increasing the melt fraction (≥30%) (Drouin et al., 2009; Basch et al., 2018, Ferrando et al., 2018). In this way, the reacted melt becomes silica-saturated;

2) formation of olivine-rich troctolite through the melt impregnation of dunite leading to olivine-melt reaction and crystallization of plagioclase and clinopyroxene at decreasing temperature. At this

stage, the dunitic matrix and the reacted melt are in disequilibrium resulting in partial dissolution of mantle olivine. The high extent of olivine assimilation contributes in the MgO enrichment of reacted melt resulting in the early crystallization of high-Mg# clinopyroxene compared to plagioclase (*e.g.*, Borghini and Rampone, 2007; Lissenberg and Dick, 2008; Sanfilippo et al., 2015; Borghini et al., 2018; Yang et al., 2019);

3) the late-stage of crystallization results in clinopyroxene rims and interstitial plagioclase enrichment in lithophile elements (*e.g.*, Drouin et al., 2009; Basch et al., 2018; Ferrando et al., 2018).

Collier & Kelemen (2010) performed thermodynamic models based on the assimilation of mantle peridotite into a primitive melt that migrates through the shallow mantle to evaluate the chemical effects of melt-rock reaction in abyssal peridotites sampled from mid-ocean-ridges. They supposed that most MORB liquids do not exclusively crystallize by fractional crystallization, but also experienced an increment of crystallization that is influenced by chemical exchange with the host mantle rock. They theorized that at the grain-scale, the melt migration via porous flow at the transition from melting to crystallization beneath the ocean ridges, promote a reactive crystallization. The occurrence of melt transport through the thermal boundary layer in larger conduits (*i.e.*, dikes) leads to a fractional crystallization. They found that the reactive crystallization Liquid Line of Descends (LLDs) are characterized by a nearly constant MgO content coupled with a strong decrease in Ca#. Moreover, SiO_2 and Na_2O contents are characterized by higher values than ones predicted in fractional crystallization. On the contrary, the fractional crystallization LLDs are characterized by the decrease of Ca# and Mg#. Hence, they inferred that a process of only pure fractional crystallization could not explain the peculiar major elements compositional trend mentioned above in mid-ocean ridges basalts (MORBs), but a contribute of reactive crystallization was required. In this regard, they suggested that it is possible to link the degree of reactive crystallization obtained by the local MORB major element observations variability to the thickness of igneous crust and to the proportion of gabbroic impregnation, veins and plutons emplaced into the underlying mantle.

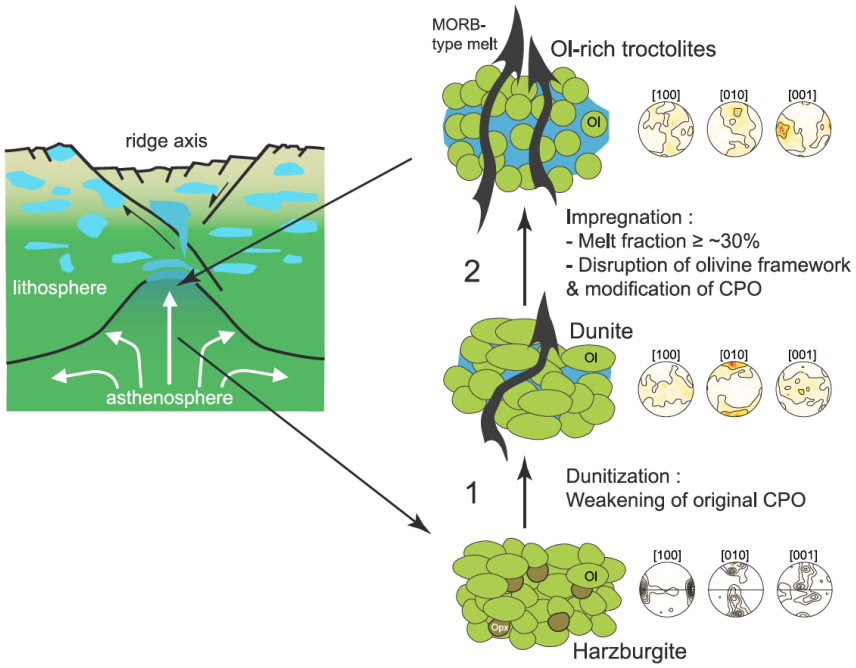

Figure 1-2 *Schematic illustration of olivine-rich troctolite origin proposed by Drouin et al., 2010.*

1.3 – Experimental investigations of melt-rock reactions processes

A remarkable progress in the understanding of melt-rock reaction processes has been made studying the role of melt-peridotite interaction during melt migration in the upper mantle-crust transition zone through dissolution experiments. Daines & Kohlstedt (1994) performed reaction couple experiments at 1250°C and 300 MPa, in which a olivine-saturated melt infiltrated a synthetic peridotite. Their experimental study suggested that the reaction between peridotite and melt results in total pyroxenes dissolution and concomitant increase of melt amount and olivine grain size. In particular, the instability of the reaction front leads to the formation of finger-like structures or channels with higher melt content that could facilitate the transition from a porous to channelized flow in the mantle. The transition from porous flow along triple junctions and grain boundaries to channelized flow in the mantle is enhanced by solid compaction, which forms impermeable regions between channels. Morgan & Liang (2003, 2005) performed reactive dissolution experiments of harzburgite and lherzolite in basaltic liquid (P = 0.6-1 GPa and T = 1250-1300°C) highlighting how melt fraction (the volume of melt involved in the percolation processes) and the preferred pyroxenes dissolution affect the melt evolution in the development of dunite channels in the mantle. Their experimental results suggested that the formation of large dunite channels in the mantle is favored by a higher melt/rock ratio (*e.g.*, focusing factor Ω_D =

18, from Asimow, 1999). They also inferred that melt fraction variation and the mineral grain size are crucial in the development of channelized of diffusive porous flow in the mantle.

Lambart et al., (2008) performed experiments of decompression melting, focused magma and transport into highly permeable channels to investigate and better constrain the amount of melt required to the dunite formation by melt-rock reaction processes. Their experimental procedure had some experimental limitations due to i) the assumption that after the focusing event at 1.25 GPa, the system is closed and the only decompression melting proceeds to 0.5 GPa and ii) a single focusing event is not in agreement with natural evidences, in which the focusing is supposed to be a continuous process or a succession of discrete events. Despite some experimental limitations, their experiments reproduced the reaction between a liquid and peridotite. They confirmed that a relatively low melt/rock ratio (a focusing factor of ≈ 4, that is a melt/rock ratio equal to ≈ 0.26) is required to generate the dunites by the dissolution of all pyroxenes of a lherzolite. They supported the assumption that magma transport through a focused flow can explain the genesis of dunite channels and the generation of primitive MORBs (*e.g.* Kelemen et al., 1995; Asimov & Stolper, 1999). A few years later, Van den Bleeken (2010, 2011) conducted a series of melt-peridotite reaction experiments overlaying a layer of primitive basaltic powder with a peridotite one and a layer of vitreous carbon spheres in order to enhance the melt flow into the peridotite. These studies concluded that melt-rock interactions in the lithospheric mantle lead to chemical modification of mineral phases and melts during their infiltration into a peridotite, depending on a series of factors such as temperature, diffusion and/or dissolution-reprecipitation, or only dissolution processes.

Tursack & Liang (2012) and Saper & Liang (2014) performed reactive dissolution (T =1330 or 1320°C, P = 1 GPa) and crystallization experiments, through a step cooling procedure, between a spinel-lherzolite and basalt (T = 1300 to 1100°C, P = 1-0.7 GPa). They suggested that the role of melt-rock reaction processes, driven by a pyroxene-undersaturated melts percolation into a depleted peridotite, plays a fundamental role in building the dunite-harzbugite and dunite-harzburgite-lherzolite sequences (Tursack & Liang, 2012) and hybrid plagioclase-bearing peridotite and plagioclase-bearing wehrlite (Saper & Liang, 2014), documented in ultramafic massifs. They reproduced experimentally compositional variations in olivine and clinopyroxene that are comparable to field observations. They depend on different factors: temperature, pressure, reactive melt composition, mineralogy and chemical composition of the host peridotite, and grain-scale processes that occur during the melt-rock interaction stages. However, they did not experimentally investigate the reactive crystallization within an olivine matrix (dunite).

Although few experimental studies have been carried out to better understand the interactions between basalt and host peridotite and the formation of dunite, very little attention has been paid to the formation of olivine-rich troctolite in the lower oceanic crust, especially in experimental studies. Borghini et al., (2018) performed reactive dissolution and crystallization experiments in order to constrain the origin of olivine-rich troctolites. They juxtaposed a melt-bearing dunite against a layer of MORB-type glasses and vitreous carbon spheres at 1300°C and then cooling to 1150°C at constant pressure of 0.5 and 0.7 GPa (***Fig.1-3***). The high-porosity melt trap made of a thin layer of vitreous carbon spheres has been placed at the top of the capsule in order to promote the reactive melt percolation. Although, the total amount of melt migrated into the carbon spheres has not been defined, this study provides important evidence that support the idea that olivine-rich troctolite are generated at the mantle-crust transition through melt-dunite reaction processes. In particular, the chemical evidences related to the reaction interface between dunite and MORB-type melt, suggested that the initial melt/rock ratio strongly influences the extent of melt-rock interaction and, thus, the final chemistry (*e.g.,* NiO content in reacted olivine) and phases abundance.

More recently, Yang et al., (2019) focused their experimental study in the reaction between a molten MORB and troctolite at 0.5 GPa in order to investigate the role of melt-rock reaction in affecting the mechanisms of dissolution-reprecipitation and chemical consequences of mineral phases and reacted melts. Their experimental results support the evidence that melt-mush reactions proceed through diffusion-assisted dissolution and reprecipitation, thus modifying the final mineral chemistry (*e.g.* MgO and Al_2O_3 enrichment of reacted melt and high-Mg# clinopyroxene) and phase abundance. Reacted residual melts became more enriched in MgO and Al_2O_3 and depleted in TiO_2 and Na_2O contents, crystallizing more primitive olivine and plagioclase. Olivines in troctolites are characterized by different Fo-Ni correlations for different starting melt compositions as a result of varied Ni partition coefficients with different MgO contents of the melt. Clinopyroxenes precipitated in troctolites have high-Mg# (>83) and enriched in Na_2O and TiO_2 contents, suggesting that they cannot simply indicate a high-pressure crystallization but they can result from melt-mush reaction (*e.g.,* Lissenberg and Dick, 2008; Sanfilippo et al., 2015; Lissenberg and MacLeod 2016; Basch et al., 2018; Borghini et al., 2018). Yang et al., (2019) highlighted that the Fo-Ni correlation in reacted olivine and Mg# *vs*. TiO_2 and Na_2O correlations of clinopyroxenes in olivine-rich troctolite, are useful to study how melt-mush reactions affect the chemical variations of primitive olivine-rich lower oceanic crust. ***Table 7.1*** (in Appendix) shows a brief summary of all the aforementioned experimental studies reported in literature.

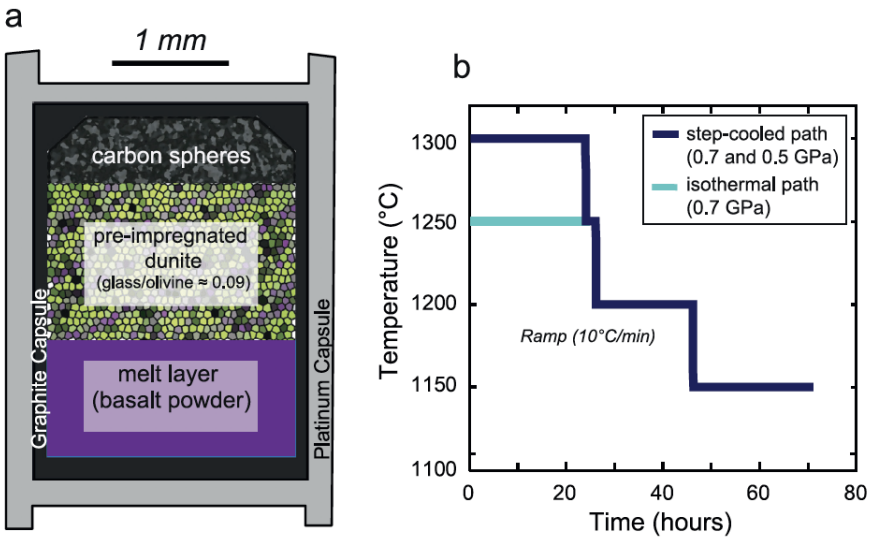

Figure 1-3 *(a) Schematic illustration of experimental setup adopted in Borghini et al., (2018): three-layer experimental setup of the graphite lined platinum capsule and (b) temperature vs. time path of the dissolution-crystallization experiments (Borghini et al., 2018).*

1.3.1 – Olivine dissolution process

Crystal dissolution in silicate melts is an essential process in igneous petrology. When major elements in a partial melt and its host crystalline matrix are out of chemical equilibrium and at constant pressure and temperature, dissolution or reprecipitation can occur. At this purpose, numerous experimental and theoretical studies on crystal dissolution process have been carried out highlighting that dissolution and reprecipitation processes play an important role in crystal-melt interaction under upper mantle and lower crust conditions (*e.g.*, Daines & Kohlstedt, 1994; Kelemen et al., 1995a, 1995b; Spiegelman et al., 2001; Liang et al., 2010). Liang, Y., (1999, 2000 & 2003), suggested that is possible to distinguish two regimes of crystal-melt re-equilibration in a two-phase aggregate:

i) Regime I: dissolution refers to diffusion-in- melt-limited dissolution,

ii) Regime II: dissolution refers to diffusion-in-solid-limited reprecipitation.

The Regime I occurs if the dissolution rate is much faster than the diffusive exchange rate in the solid and the dissolved crystal will retain its interior or far-field composition that has not been affected by diffusion. The Regime I occurs when the diffusion rate in the liquid is more than four to six orders of magnitude faster than the diffusion rate in the solid. In this case, the dissolution rate is proportional to the diffusion rate in the liquid, independently of the crystallographic orientations of the dissolved crystal. If the dissolution rate is much slower than the rate of diffusion in the solid, the dissolved crystal will maintain its solidus composition at the crystal-melt interface (Regime II dissolution). This regime is

important when the dissolving crystal and melt are in near chemical equilibrium. In this case, the dissolution rate is proportional to the diffusion rate in the solid and depends on the crystallographic orientation of the dissolved crystal if the degree of under-saturation is extremely small (Liang, Y., 1999, 2000 & 2003).

Donaldson, C. H., (1985), performed experiments demonstrating that the olivine dissolution rate is not time-dependent and it is defined by a combination of diffusion and convection of components to and from the crystal-liquid interface (*e.g.*, at 1210°, 12° above the liquidus temperature of the basalt, magnesian olivine dissolves with a rate of about 9-14μm/h) (Donaldson C. H., 1985). More recently, Zhang et al., (1989) and Chen & Zhang (2008), suggested that olivine dissolution in molten silicates is a rather fast process. In particular, because the interface melt compositions are not dependent on the experimental duration (at given *PT* conditions) and according to the olivine-saturated melt compositions, they inferred that the interface melt reaches in no more than 2 minutes the near-saturation for olivine dissolution in basaltic melt. Lasaga et al., (2003) studied the olivine dissolution mechanisms performing a theoretical model suggesting that the dissolution theory is based on the movement of dissolution step-waves stemming from surface defects. They inferred that as the equilibrium between the fluid and the rock is approached, the dissolution rate law for solid-fluid interactions decreases. They validated their model through Monte Carlo simulations of crystal dissolution showing the generation of dissolution step-waves and the non-linear dependence of the overall rate on the saturation state. Their results were in agreement with the far-from-equilibrium experimental works and other studies that approached equilibrium.

Hence, numerous theoretical and experimental studies have highlighted that the extent of olivine dissolution and the reacted melt composition depend on different parameters such as *PT* conditions, time, melt composition, viscosity and olivine grain size. However, a detailed chemical and microstructural (EBSD) experimental study on the role of different melt/rock ratio is still missing and it is currently not fully understood how this affects the dissolution processes during the melt-rock interaction processes, at the upper-mantle and lower-crust conditions.

1.3.2 – Olivine grain growth mechanisms

The study of the crystal-growth mechanisms from the melt and the effects of the various factors that influence crystal growth could provide important information on textural and chemical features and crystallization histories of igneous rocks. **Crystallization** or **freezing** (liquid solidification by crystallization) process occurs when a liquid becomes supersaturated with a dissolved chemical component producing a new crystalline phase (Vernon, 2004, 2018). Nucleation and growth mechanisms will be discussed below.

Nucleation: local thermal, compositional or deformational fluctuations facilitate the generation of small aggregation of atoms, called "nuclei" which probably consist of 10 to 1000 atoms (Lasaga, 1998). The atoms at the surface of the crystal have higher energy due to the disordered bonds with the lattice, hence, the relatively abrupt change of atomic structure at the liquid-solid interface produces a definite boundary with a specific interfacial energy (γ) per unit area. When the total free energy of the system (*Gt*) decreases, crystallization of liquid can occur. The formation of a nucleus is associated to the formation of an area of interface, which increases the interfacial free energy (γ). The free energy change (ΔGt) involved in nucleation is defined by equation (1):

$$\Delta Gt = -(4/3)\pi r^3 \Delta G_V + 4\ \pi r^2\ \gamma \qquad (1)$$

where ΔGv is the difference in free energy between the solid and liquid and *r* is the radius of the embryonic nucleus (assumed to be spherical). If ΔGt is negative, spontaneous nucleation occurs. The dissolution of a nucleus (unstable) can occur when its radius is smaller than r* (defined as critical radius). In this scenario the external area is too large with respect to its volume. A nucleus is defined as "stable" when its radius is larger than r*. It is worth to underline the presence of an energy barrier (***Fig. 1-4***), which means that a certain grade of temperature decreases below the equilibrium freezing temperature (by means of an undercooling or supercooling processes) must occur before crystallization begins (Cabane et al., 2005; Vernon, 2004, 2018).

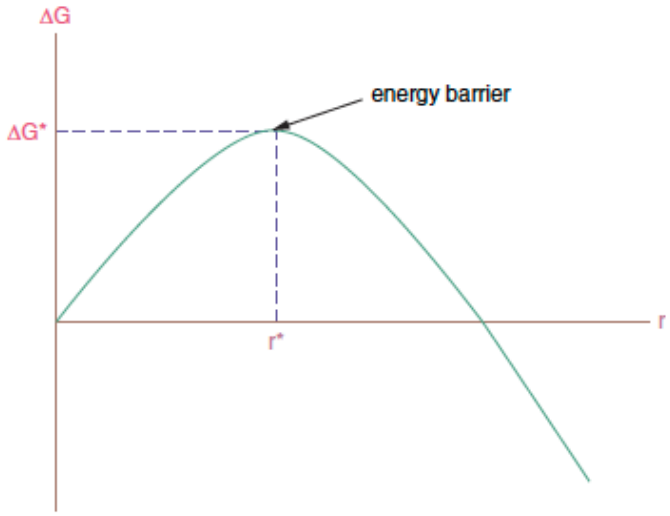

Figure 1-4 *Free energy of nucleation (ΔG) of an embryonic nucleus vs. radius (r) (Vernon. R. H., 2004 & 2018).*

There are two different types of nucleation: a) ***homogeneous***, when random thermal fluctuations occur. This process is not very common and it occurs usually because of strong supercooling, and b) ***heterogeneous***, when seeds, phase boundaries or solid surfaces decreases the effective surface energy; this diminishes the free energy barrier and facilitates the nucleation, requiring only a few degrees of undercooling. Different factors affect the nucleation rates, such as temperature, oxygen activity, degree of undercooling and the viscosity of the magma. In particular, theoretical and experimental studies suggested that olivine tends to nucleate more rapidly than feldspar and pyroxene (Kirkpatrick, 1975). Toramaru (1991) inferred that the most important factor that can affect the nucleation is the diffusivity. This parameter is dependent on the chemical composition and temperature of the magma, suggesting that at higher temperature, hot magma with high diffusivity tend to promote the nucleation of crystals of a specific mineral more easily than a cooler magma with low diffusivity. Once the radius of the nuclei of a given phase grow above **r* (**critical radius), "Ostwald ripening" process can occur. The "Ostwald ripening" process implies that large grains can grow with time at the expense of the small ones. The driving force of this process is the reduction of the excess energy associated with solid-liquid interface. This leads to an increase of the mean grain size and to a decrease of the number of grains per unit volume, even though the total volume of each phase remains constant during the process (Cabane et al., 2005). However, Boistelle & Astier (1988), suggested that the Ostwald ripening process is very fast for particles of radius less than 1 µm, fast for particles with **r** ~ 1 µm and very slow for particles with radius around 100 µm.

Grain growth: the advancement of the interface into the liquid results in the crystal growth and the final shape of the crystal will depend on a number of factors such as:

a) the flow of latent heat of crystallization away from the growing crystal surface,
b) the rate at which nutrient chemical components diffuse through the liquid to the advancing interface,
c) the rate at which unwanted chemical components can diffuse or be convected, away from the advancing interface,
d) reactions at the crystal-melt interface and
e) atomic structure of the specific mineral (Vernon, 2004, 2018).

Generally, it is possible to distinguish two different conditions ***(Fig. 1-5***):

- The attachment of atoms at the crystal-melt interface controls the growth rate (*G*) when diffusion in melt is much faster than the uptake and rejection of components at the interface. At this point, the liquid composition at the interface is similar to its composition. This situation typically occurs at small amount of undercooling (*ΔT*), where *G* is relatively small and the rate of diffusion (*D*) is large, due to the relatively high temperature.
- Diffusion in the melt (*D*) controls the growth rate (*G*) when the rate of absorption or rejection of components is much faster than diffusion in the melt. This situation typically occurs with large undercoolings (*ΔT*), where *G* is larger and *D* is smaller, due to the relatively lower temperature.

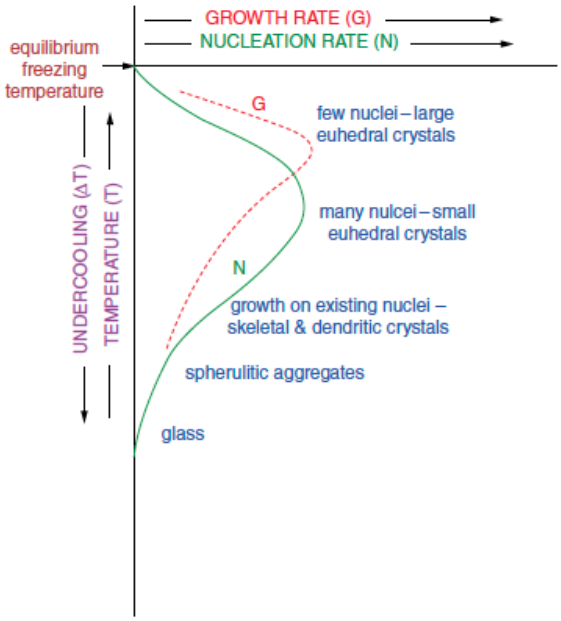

Figure 1-5 *Schematic representation of the variation of nucleation rate (N) and growth rate (G) with increasing undercooling* (ΔT). *It also reports the typical grains size and shapes generated at different stage.*

1.3.3– Olivine grain shape and size

The ratio between diffusion and grain growth (*D/G*) controls the resulted grain shape. When *G* is small and *D* is large at small to moderate degrees of supersaturation, ***euhedral*** crystals can grow. On the other hand, when *G* is large and *D* is small at higher degrees of supersaturation, ***skeletal*** and ***dendritic*** crystals can grow (Donaldson, C. H., 1974 & 1976; O'Driscoll et al., 2007). Skeletal crystals are characterized by accentuated edge growth and/or incomplete facial growth, in contrast, dendritic crystals have accentuated corner growth and/or growth of spikes, or fibers, of rational or irrational crystallographic orientation. Overall, it is possible to distinguish 10 categories of morphologies related to the increase of effective undercooling in a progression sequence (Donaldson, C. H., 1976; O'Driscoll et al., 2007) (***Fig. 1-6***):

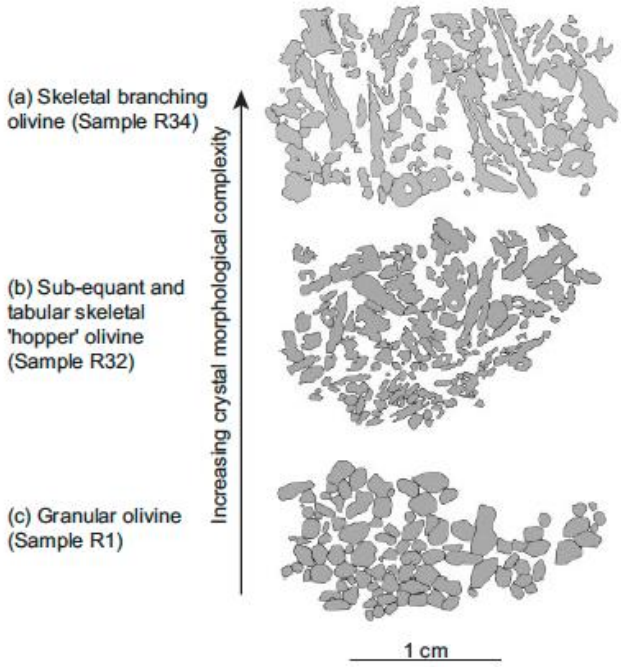

Figure 1-6 *From O'Driscoll et al., (2007), schematic illustration of olivine morphologies evolution and complexity in a progression from granular olivine to skeletal branching olivine.*

During the growth of euhedral crystals, faces with higher energy tend to growth faster than ones with lower energy resulting in crystals with both slower-growing and faces with lower energy. By contrast, faces with higher energy are "stepped" because they have more sites in which atoms can attach. Franck (1949) suggested that a ***screw dislocation*** emerging at the surface of a growing crystal could provide a permanent step. "Spiral ramps" were generated when screw dislocations intersect the crystal surface.

The grade of undercooling affects not only the shape of crystals, but also their grain size. The undercooling is defined as the difference between the temperature at which the specific mineral crystallizes from the melt at equilibrium conditions (*T liquidus*, T_L) and the actual temperature ($\Delta T=T_L - T$). ***Fig. 1-5***, reports a schematic illustration of the variation of nucleation rate (*N*) and grain growth rate (*G*) with increasing undercooling (*ΔT*), reporting the specific grain size and shape at different stage. With the increasing degrees of undercooling, nucleation rate (*N*) and the growth rate (*G*) reach the maximum value, although *G* increases at a smaller *ΔT* than *N*. On the contrary, at lower temperatures that reduce the rates of diffusion of chemical components in the increasingly viscous melt, both *N* and *G* decline with further undercooling, resulting in the reduction of the atoms aggregation rates unable to form new nuclei and inhibiting addition of atoms to the growing crystals (Vernon, 2004, 2018).

Numerical theoretical and experimental studies provided important information on grain growth mechanisms and how they could affect the shape and size of a grain through a lot of factors such as, grade of undercooling, *PT* conditions, kinetics (run duration of a process), melt composition and deformation. However, how melt/rock ratio affects the texture of olivine in terms of shape and grain size is actually well not defined.

1.4 – Aims

Microstructural and chemical observations have emphasized that melt-rock reactions processes play an important role in the origin of troctolites in the lower oceanic crust. Several authors have investigated the role of different factors, such as temperature, pressure, melt composition and kinetic of the melt-rock reaction in the formation of these rocks. However, the role of different melt/rock ratio in the reactive dissolution crystallization processes has not been definite yet. A detailed textural study through Electron back-scattered diffraction (EBSD) analysis on the microstructures features and intra-granular deformation of olivine grains resulted from reaction and crystallization experiments, are still lacking. In this study, reaction experiments were performed using a mixture of olivine and melt in different proportion to investigate the effects of different melt/olivine ratio. Isothermal experiments were carried out at different temperature and with different initial melt/olivine ratio in order to define and quantify their effect on:

I. texture and chemistry of the reacted olivine,
II. chemistry of reacted melt,
III. amount of the dissolved olivine

In addition, step-cooled experiments were conducted in order to define how different initial melt/olivine ratio affects the resulted lithology and the final mineral chemistry after cooling and interstitial melt crystallization. The experimental approach combined with a detailed study of the crystallographic orientation of olivine grains through EBSD analysis, were used to better constrain the origin of olivine-rich troctolite through melt-rock reaction processes and to enlarge our understanding on mechanism of chemical and microstructural modification of olivine. This work aims to evaluate and quantify the role of melt/olivine ratio and the effect of temperature on mineral chemistry and textures resulted from reactive dissolution and crystallization processes.

Chapter 2
MATERIALS AND METHODS

Melt-dunite reaction and crystallization processes were studied by performing experiments with the End-Loaded (EL) piston cylinder at the Laboratory of Experimental Petrology, Department of Earth Science "Ardito Desio" (University of Milan). It is generally considered that "replacive" dunites are formed by reactive dissolution triggered by percolation of olivine-normative basalts through a harzburgite or lherzolite matrix (Dygert et al., 2016 and references therein). Hence, the experiments aim to study the role of different melt/olivine ratio in melt-olivine interactions, which is still poorly constrained. Differently to layered reaction couples used by Francomme, J. E. (20016-2017), and Borghini et al., (2018), the experiments performed in this study are characterized by homogeneous mixtures of olivine and melt in order investigate the effect of different melt/olivine ratio and how this parameter influences the results of melt-dunite interaction and crystallization in terms of textures and mineral chemistry. This experimental thesis performed experiments with starting melt-olivine mixtures with 10, 25 and 50wt% of starting melt added to olivine powder. As a way to reproduce the *P-T* environment at which the melt-dunite reaction and crystallization processes occur, the experiments were carried out at *P-T* conditions that are typically encountered at mantle-crust transition zone underneath oceanic spreading centers. Therefore, for each of the three mixtures, eleven isothermal experiments were performed at a fixed pressure of 0.5 GPa (which correspond to about 15 km of depth), temperature from 1200 to 1300°C and run for 24 hours. Then, in order to allow the reactive crystallization of the interstitial melt, five step-cooled experiments were performed decreasing temperature with a rate of 1°C/min from 1300°C down to 1100°C for 72 hours (***Fig. 2-1***). On this chapter a detailed explanation of the starting materials, experimental procedures, analytical techniques and EBSD analysis will be addressed.

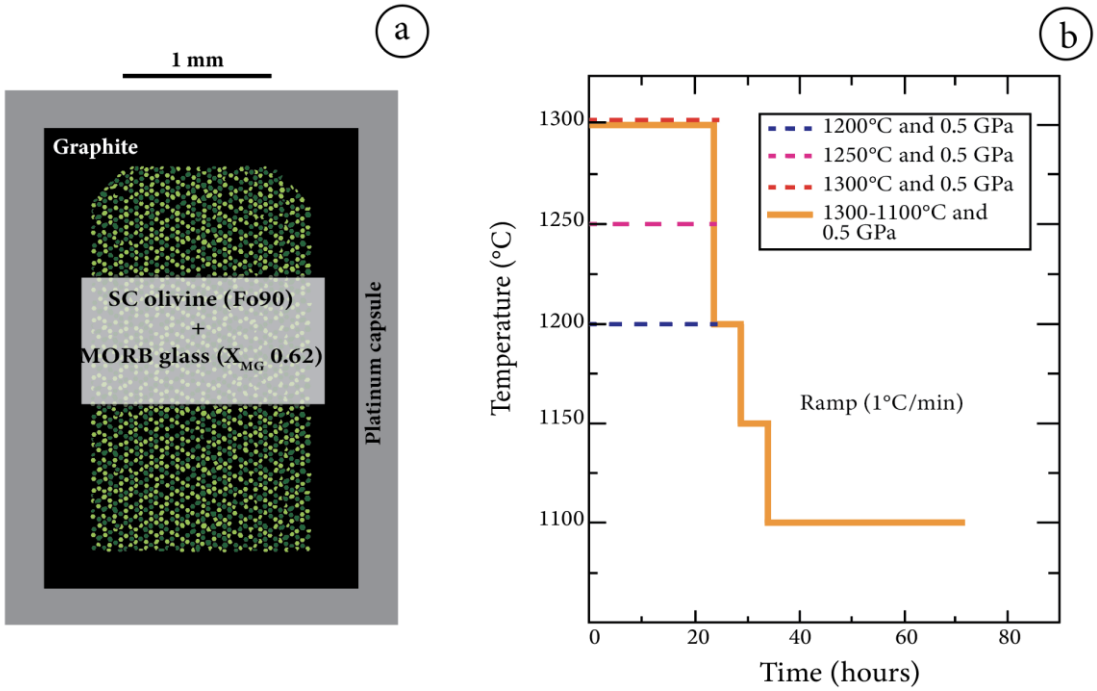

Figure 2-1 *(a) Schematic illustration of experimental setup used in this study: the melt/olivine mixture (black and green spheres respectively) is put in a double Pt-C capsule and (b) temperature vs. time path of the dissolution-crystallization experiments.*

2.1 – Starting material

The **dunite matrix** has been simulated using a powder of San Carlos olivine (Dohmen et al., 2007). The San Carlos olivine (Fo_{90}) is extracted from the mantle xenoliths from the San Carlos Volcanic Field, Arizona, USA and is characterized by a very homogeneous chemical composition and gem-quality crystals found within the lherzolite xenolith nodules (Dohmen et al., 2007). Because of that, San Carlos olivine is used extensively for high-temperature physical property measurements as part of investigations of the behaviour of the earth's upper mantle (Kohlstedt & Mackwell 1987). Olivine crystals were selected optically under a binocular microscope in order to avoid the grains containing inclusions, which would inevitably affect the chemical composition of the starting material. Subsequently, the crystals were grinded for 30 minutes with ethanol in an agate mortar, dried and sieved through a 36-64μm mesh. The final olivine powder was dried at 250°C for 1h in a horizontal oven in air and kept at 110°C under vacuum in order to eliminate any H_2O molecules. ***Table 2-1*** reports the San Carlos olivine average composition, chemically characterized by EMPA using JEOL 8200 Super Probe at the Department of Earth Science “Ardito Desio”, University of Milan.

	San Carlos olivine (n =18)[b]	AH6[a]
SiO_2	40.68 (32)	47.70
TiO_2	0.00 (0)	0.89
Al_2O_3	0.01 (1)	16.76
Cr_2O_3	0.03 (3)	0.09
FeO	8.90 (26)	9.51
MgO	49.14 (20)	8.62
MnO	0.12 (4)	0.19
NiO	0.37 (4)	0.00
CaO	0.07 (2)	13.80
Na_2O	0.01 (1)	2.28
K_2O	0.00 (0)	0.10
P_2O_5		0.05
Total	99.34 (67)	99.94
X_{Mg}[c]	0.908 (5)	0.618
X_{Ca}[d]		0.770

Table 2-1 *Composition in major elements of starting materials (in wt%). [a] Composition of MORB-type basalt from Husen et al. (2016). [b]n: number of microprobe analysis. The standard deviation associated to each analysis is between round brackets. [c]X_{Mg} =Mg/(Mg+Fe). [d]X_{Ca} =Ca/(Ca+Na).*

The starting **reacting melt** is a synthetic analogue glass of naturally quenched basaltic glass recovered during IODP Expedition 324 at Shatsky Rise, provided by the Laboratory of Hannover (the e.s.d. is negligible). This synthetic glass, AH6, emulates a tholeiitic composition and it has an X_{Mg}= 0.62 (X_{Mg}=Mg/(Mg+Fe^{tot})) and an X_{Ca}= 0.77 (X_{Ca}= Ca/(Ca+Na)) (***Fig. 2-2***). Its phase relations and liquid lines of descent were experimentally investigated by Husen et al. (2016). The MgO-rich and Ni-free AH6 glass (8.6wt% MgO) represents the average composition of 15 Ol-hosted melt inclusions from moderately altered Ol-phyric basalts, cored at the Ori Massif (Almeev et al., 2011; Husen et al., 2016). Since AH6 is not in equilibrium with mantle olivine, this melt is expected to be reactive with mantle-like San Carlos olivine. ***Tab. 2-1*** lists the synthetic glass composition used in the reaction experiments. Melt impregnation has been simulated by mixing olivine and basalt in different ratio [9:1], [3:1] and [1:1]. Furthermore, although Francomme, J. E. (2016-2017) and Borghini et al., (2018) previously performed reaction and crystallization experiments by juxtaposing a melt-bearing dunite to a layer of powdered MORB glass (***Fig. 1-3***), they also used the glass AH6 to simulate a MORB-type melt. Hence, this provided a direct comparison between the two different experimental strategies.

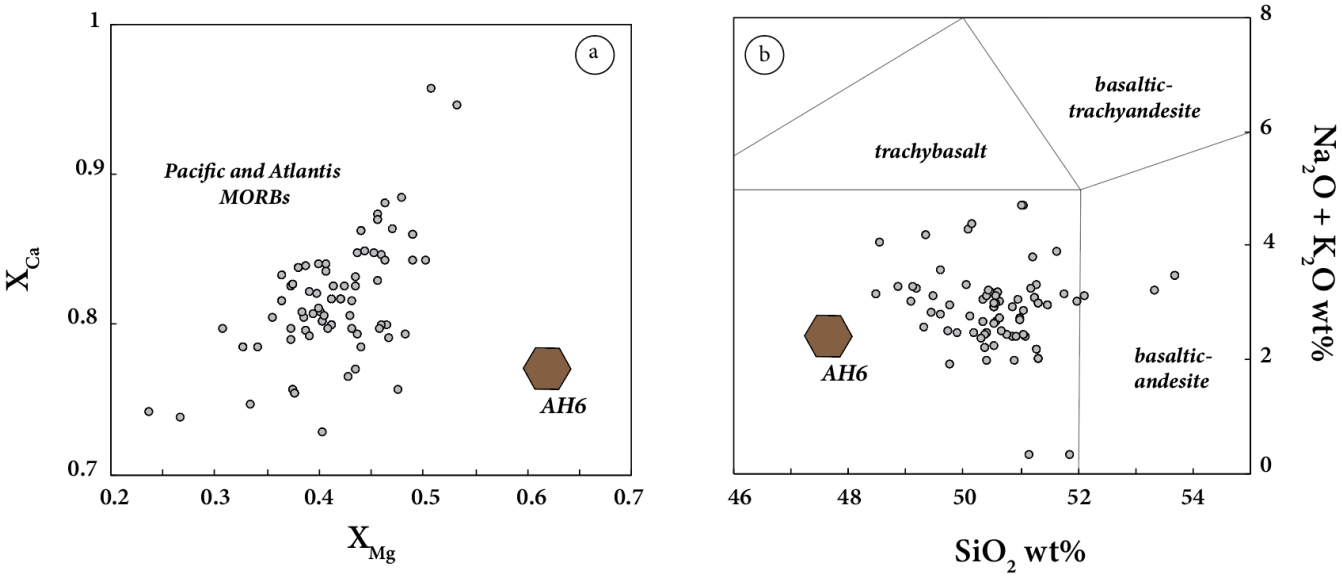

Figure 2-2 *(a) X_{Mg} = Mg/(Mg+Fe) vs. X_{Ca} = Ca/(Ca+Na) and (b) TAS (Total Alkali versus Silica) of starting synthetic glass AH6 (Husen et al., 2016) compared to the compositions of Pacific and Atlantic MORBs (PetDB, http://www.earthchem.org/petdb)*

2.2 – Experimental procedure

Melt-dunite reaction processes were studied in a series of experiments in which a double container made of a graphite crucible was fitted into a platinum capsule, in order to avoid Fe loss towards the noble metal (Ulmer & Luth, 1991) (***Fig. 2-1***). The graphite container, about 6 mm long and 1.8 mm of inner diameter (ID) and 2 mm of outer diameter (OD) was loaded with ~ 20-20.8 mg of starting powder, covered with a graphite lid and then put into a platinum capsule (8 mm long, 3 mm OD and 2.8 mm ID). From the outside to the inside, the piston-cylinder assemblage consists of a talc cell wrapped in a mylar foil, an inner Pyrex cylinder, a graphite furnace and two cylinders of crushable MgO spacers. The thermocouple tip is separated from the platinum capsule by a 0.5 mm thick hard alumina disc. The furnace assembly was held in oven at 110°C for 24h and then loaded into the piston-cylinder apparatus in order to minimise the amount of absorbed water (***Fig. 2-3b-c***).

Temperature was measured using a Pt-PtRh thermocouple (S-type) and monitored using a Eurotherm controller with an estimated accuracy of ± 5°C. At initial pressure of 0.25 GPa the sample was heated to 400°C for 10 minutes in order to soften the Pyrex; then, pressure was raised to the experimental value before reaching the desired temperature. Runs were terminated by turning off the power. After quenching the experiment, the charge was unloaded and the platinum capsule was extracted and embedded in Epoxy resin. After the solidification of the resin, the capsules were hand-polished using several silicon carbide grinding papers (from P600 to P4000) and then with a 1 µm diamond paste. The

samples so prepared were impregnated with a drop of Epoxy resin and placed under vacuum for few seconds in order to induce the impregnation of the resin. Then, the samples were polished and carbon-coated, a standard treatment in order to prepare them for the electron microprobe and scanning electron microscope analyses (a fully detailed description of which can be found in **Sections 2.3.1 and 2.4.3**).

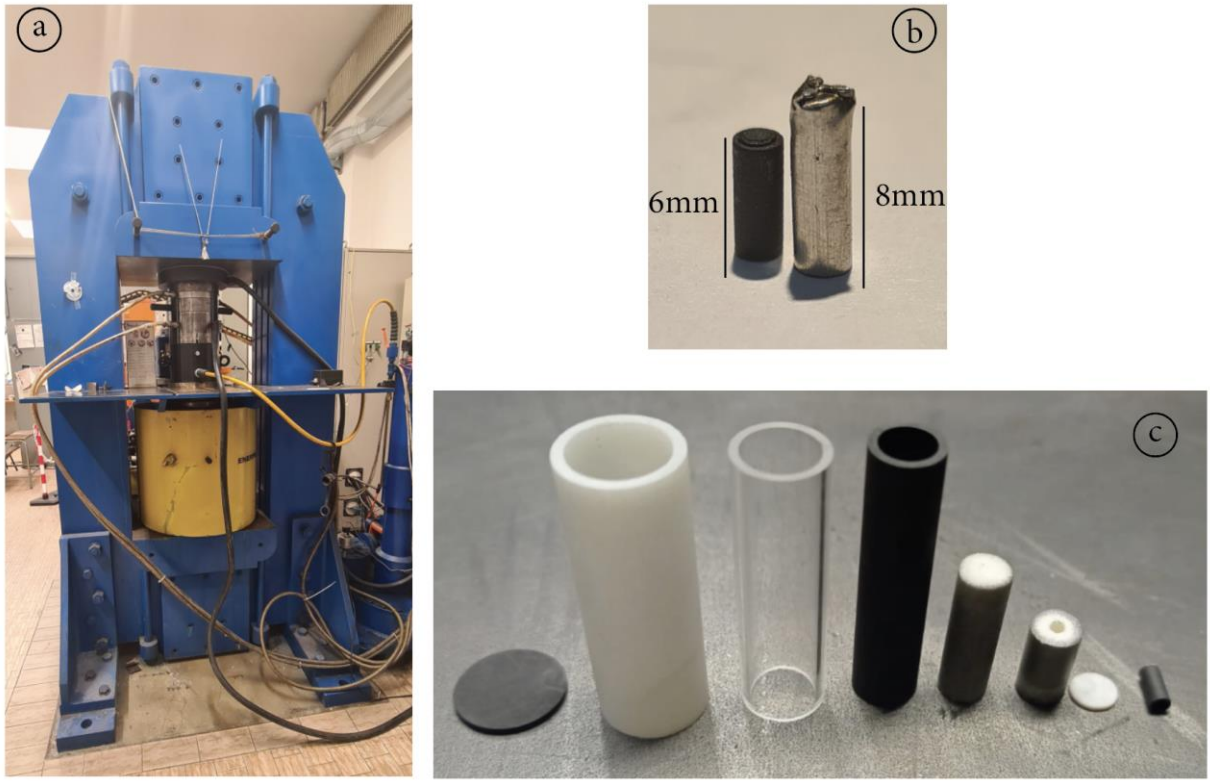

Figure 2-3 *(a) End- Loaded piston cylinder apparatus the Laboratory of Experimental Petrology, Department of Earth Science "Ardito Desio", University of Milano (Italy); (b) double contains of graphite crucible fitted into a platinum capsule and (c) the furnace assembly.*

2.2.1 – END-Loaded piston cylinder apparatus

Reaction and crystallization experiments were performed in an End-Loaded piston cylinder apparatus similar to the original Boyd & England (1960) type design. Pressure can range from 0.5 – 4.0 GPa and temperature can reach 1700°C. An important goal of much of experimental igneous, metamorphic, and mantle petrology is to be able to assign pressure and temperature to earth environments and to predict the physical and chemical properties of rocks and melts within those environments (Burnley et al., 2012). In particular, the End-Loaded piston cylinder apparatus is equipped with two hydraulic rams: the second hydraulic one is used to apply an additional vertical pressure compared to a Single Stage Piston cylinder apparatus (Boyd & England, 1960) (***Fig. 2-4***).

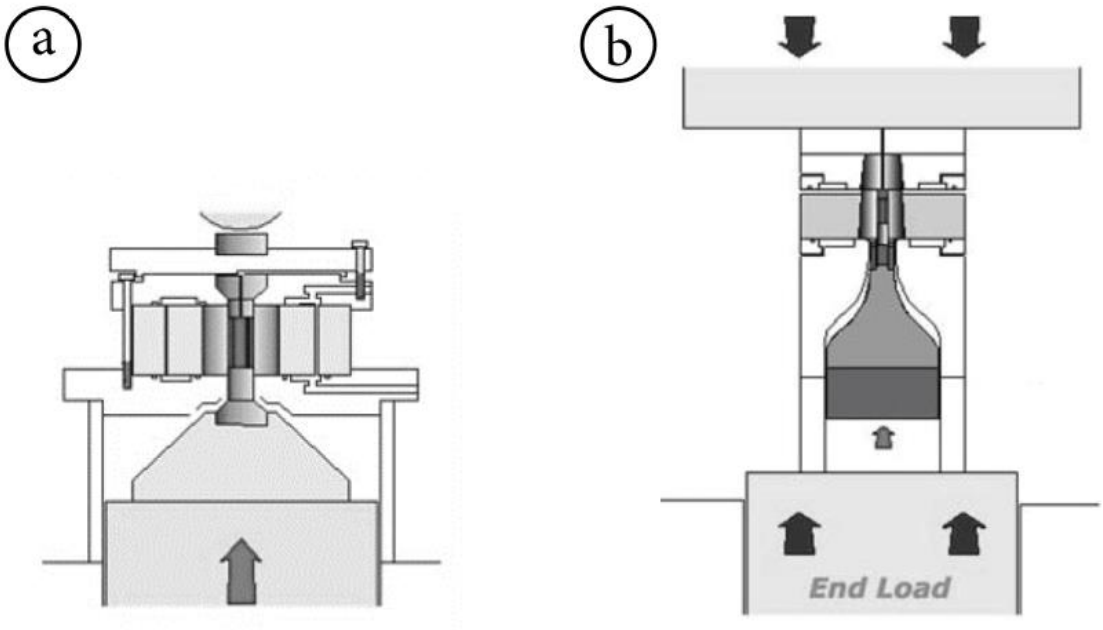

Figure 2-4 *(a) Schematic illustration of Single Stage Piston cylinder and (b) End-Loaded Piston cylinder apparatus.*

2.2.2 – Isothermal experiments – experimental strategy

Eleven olivine reactive dissolution and reprecipitation experiments were performed using a piston cylinder apparatus at fixed pressure of 0.5 GPa and run duration of 24h between 1200 and 1300°C with variable mixtures of San Carlos olivine and moderately evolved tholeiitic glass ***(Tab. 2-1)***. However, because of technical failures, not all of them were entirely successful and therefore not all the experiments will be considered in the discussion. In two experiments in particular, most probably due to the insufficient packing of the graphite container with the starting materials, the powder spread out from the inner graphite capsule. Additionally, three experiments quenched before reaching the target temperature due to unexpected voltage drops. However, three experiments performed at 1200°C, with different initial melt amount expressed in weight percentage (10, 25 and 50wt% and named MG10, MG12 and MG14, respectively) were successful. One reaction experiment was performed at 1250°C with 50wt% of initial melt (MG11) and three more experiments were carried out at 1300°C with different initial melt amount from 10 to 50wt% (MG18, MG1 and MG5, respectively). ***Tab. 2-2*** lists the experimental run conditions and phase assemblages of the all reaction-experiments. The experimental results will be discussed in detail in **Chapter 3.**

2.2.3 – Step-cooled experiments – experimental strategy

Five olivine reactive dissolution and crystallization experiments were carried out using piston cylinder apparatus at 0.5 GPa for 72h. In particular, from the isothermal dwell at 1300°C, these experiments were cooled down to 1200°C with a fixed rate of 1°C/min. After 4 hours the temperature was decreased again, at the same rate, to 1150°C and, after another 4 hours, finally to 1100°C. Two step-cooled experiments (MG2 and MG3) will not be considered in the discussion for the same problems cited in **Section 2.2.2.**

Three reactive crystallization experiments were performed using three variable proportions of San Carlos olivine and the moderately evolved tholeiitic glass 10, 25 and 50wt% (MG15, MG4 and MG16, respectively). ***Tab. 2-2*** lists the experimental run conditions and products. The experimental results will be discussed in detail in **Chapter 4.**

	Run	P (GPa)	T (°C)	t (h)	Initial melt amount (wt%)	Run products (wt%)
Starting materials SCO[a] +AH6						
Isothermal	MG10	0.5	1200	24	10	Ol[b]-Pl[c]-Cpx[d]
	MG6	0.5	1300	24	10	-[f]
	MG18	0.5	1300	24	10	Ol-Gl[e]
	MG12	0.5	1200	24	25	Ol-Pl-Cpx-Gl
	MG1	0.5	1300	24	25	Ol-Gl
	MG13	0.5	1200	24	50	-[f]
	MG14	0.5	1200	24	50	Ol-Pl-Cpx-Gl
	MG11	0.5	1250	24	50	Ol-Gl
	MG5	0.5	1300	24	50	Ol-Gl
	MG7	0.5	1300	24	50	-[f]
	MG8	0.5	1300	24	50	-[f]
	MG9	0.5	1300	24	50	-[f]
Step-cooled	MG15	0.5	$1300_{(i)}$-$1100_{(f)}$	72	10	Ol-Gl
	MG2	0.5	$1300_{(i)}$-$1100_{(f)}$	72	25	-[f]
	MG3	0.5	$1300_{(i)}$-$1100_{(f)}$	72	25	-[f]
	MG4	0.5	$1300_{(i)}$-$1100_{(f)}$	72	25	Ol-Cpx-Gl
	MG16	0.5	$1300_{(i)}$-$1100_{(f)}$	72	50	Ol-Pl-Cpx-Gl

Table 2-2 *A summary of run information: pressure, temperature, duration t, initial melt amount, phase assemblages and modes. [a] San Carlos olivine. [b] Olivine. [c] Plagioclase. [d] Clinopyroxene. [e] Glass. [f] Failed experiment (see text for explanation).*

2.3 – Analytical techniques

2.3.1 – Sample preparation and Electron Microprobe analysis (EMPA)

Run products have been texturally and chemically characterized by EMPA (BSE/SE images, X-ray chemical maps and WDS/EDS chemical analysis) using JEOL 8200 Super Probe at the Department of Earth Science "Ardito Desio", University of Milan. The analytical conditions were an accelerating voltage of 15 kV and a beam of 5 nA and 1µm size. Because of the occurrences of glass as interstitial phase, a large beam size could not be used. Counting time was 30 s for peak and 10 s for background (***Fig. 2-5***). The following standards were used for the calibration: Cr_2O_3 (Cr) grossular (Si, Ca and Al), olivine (Mg), omphacite (Na), ilmenite (Ti), fayalite (Fe), rhodonite (Mn), niccolite (Ni) and K-feldspar (K).

Figure 2-5 *JEOL 8200 Super Probe at the Department of Earth Science "Ardito Desio", University of Milan.*

The electron microprobe analysis (EMPA or "electron probe analysis-EPMA") is a technique for quantitative and qualitative chemical analysis of small selected volume of solid samples (μm^3) in which X-rays are excited by a focused electron beam. On the one hand, qualitative analysis is obtained by identifying the characteristic lines of the elements present from their wavelength or photon energies (Energy Dispersive Spectroscopy- EDS). On the other hand, a quantitative analysis is obtained by comparing their intensities with those emitted from standard samples (Wavelength Dispersive Spectroscopy- WDS). Under normal conditions, spatial resolution is limited to about 1 µm by the spreading of the beam within the sample. A line of profiles or two-dimensional "maps" can be recorded in order to analyze the spatial distributions of specific elements. The two-dimensional maps are commonly displayed using a "false" color scale to represent element concentrations (Electron Backscattered images – BSE) (Reed, S. J. B., 2005).

2.3.2 – Electron Back-Scattered Diffraction (EBSD) analysis

The microstructure of the samples was investigated by EBSD, which provides information about the crystallographic orientation of the crystalline grains in the samples. The system used was a Bruker Quantax e-Flash HD system equipped with Argus diodes for FSE/BSE (forwardly and backscattered electron) imaging and attached to a Field Emission Gun (FEG) Scanning Electron Microscope (SEM) Zeiss Gemini 500 installed at the Platform of Microscopy of the University of Milano-Bicocca (***Fig. 2-6***).

Figure 2-6 *FEG-SEM Zeiss Gemini 500 at the Platform of Microscopy of the University of Milano-Bicocca.*

2.4 – Development of EBSD in Earth Sciences

2.4.1 – Introduction

In the Earth Sciences, the word "texture" is most commonly used to refer to the microstructure of a rock. In particular, "lattice preferred orientations" (LPO) or "crystallographic preferred orientation" (CPO) are the terms most commonly used by geologist to refer the same term "texture" used by metallurgists (Prior et al., 2009; Mainprice, D., 2012). The combination of SEM and EBSD was called "Orientation imaging" by Adams et al., (1993) and presented the advantage of measuring orientation pixels within grains in a statistical way. In particular, it is possible to distinguish two different types of orientation images:

- EBSD (Electron Back-Scattered Diffraction) maps: this type of image provides quantitative information on the crystallographic orientation of the crystalline grains in the samples;
- FSE (Forward Scattered Electron (FSE) images: this type of images greatly enhances the diffraction contrast that depends on the grain orientation rather than its chemical composition. This type of image provides qualitative information on crystallographic orientation.

For the first time, it was possible to get information about misorientation within grains, between grains and some grain boundary parameters that can be represented in different ways, *i.e.*, pole figures, inverse pole figures and ODFs. Furthermore, thanks to the ability of SEM to zoom the magnification from the cm to nm scales, the exploration of the microstructure could begin in statistical and digital way over seven orders of magnitude from 10^{-2} to 10^{-9} m. The first observation of a diffraction pattern in backscattering mode was reported in 1928 by Nishikawa and Kikuchi followed by a series of papers until the 1990s (*e.g.*, Wright and Adams, 1992; Adams et al., 1993; Kunze et al., 1993). In particular, Finch & Wilman in 1937, wrote a series of papers in which they showed high-quality diffraction patterns that contained Kikuchi lines and a few diffraction spots indicating that the diffraction geometry with a very low angle of incidence was close to thin film limit where Bragg diffraction spots appear. Subsequently, in 1965 the Cambridge Scientific Instrument Company provided a new Commercial Scientific Electron Microscope (SEM) named the "StereoScan". In 1967, the rocking of the electron beam about a point on the specimen surface using the modified scanning coils, provided a new diffraction technique called electron-channelling patterns (ECPs). The EBSD technique known nowadays started in 1990s with Adams and co-authors papers that introduced a system featuring an SEM controlled by mini-supercomputer, low light level sensitive camera, video acquisition card for on-line diffraction pattern acquisition and in-house software for automatic indexing. This system was essentially

proposed for the characterization of the microstructure and CPO in the metallurgical tradition. Michael & Goehner (1993, 1994) provided new high quality EBSD pattern with chemical information from X-ray spectrometers, both semi-quantitative energy dispersive (EDS) and quantitative wavelength dispersive (WDS).

2.4.2 – SEM settings for EBSD analysis

EBSD is characterized by the recording of diffraction pattern formed by the interaction of the stationary collimated electron beam with 20° angle of incidence with sample surface and a sample tilted at 70° from the horizontal. Hence, EBSD patterns are generated on a phosphor screen by backscatter diffraction of a stationary beam of high-energy electrons from a volume of crystal material of ~ 20 nm deep in specimen, times the projected area of the incident beam. The typical analytical conditions used for EBSD analysis are an accelerating voltage between 10-30 kV and a beam of about 6-8nA. A high accelerating voltage (30kV) is generally used when the carbon coat is thicker than 5nm, contrary to a lower accelerating voltage that is usually used in case the sample is strongly deformed. On the other hand, a high incident beam current (10-100nA) is usually used in order to map very quickly.

The EBSD patterns generated on a phosphor screen are called “Kikuchi bands”. In particular, the characteristic feature of a backscatter Kikuchi pattern is the regular arrangement of parallel bright bands on a steep continuous background. The intersection of Kikuchi bands forms the prominent and distinct zone axes (Prior et al., 2009; Schwartz et al., 2009; Mainprice, D., 2012; Britton et al., 2016). The geometry of a Kikuchi pattern can be interpreted as a gnomonic projection of the crystal lattice on the flat phosphor screen. In particular, in order to define the olivine phase, the average number of bands needed is between 6 and 8 (***Fig. 2-7***).

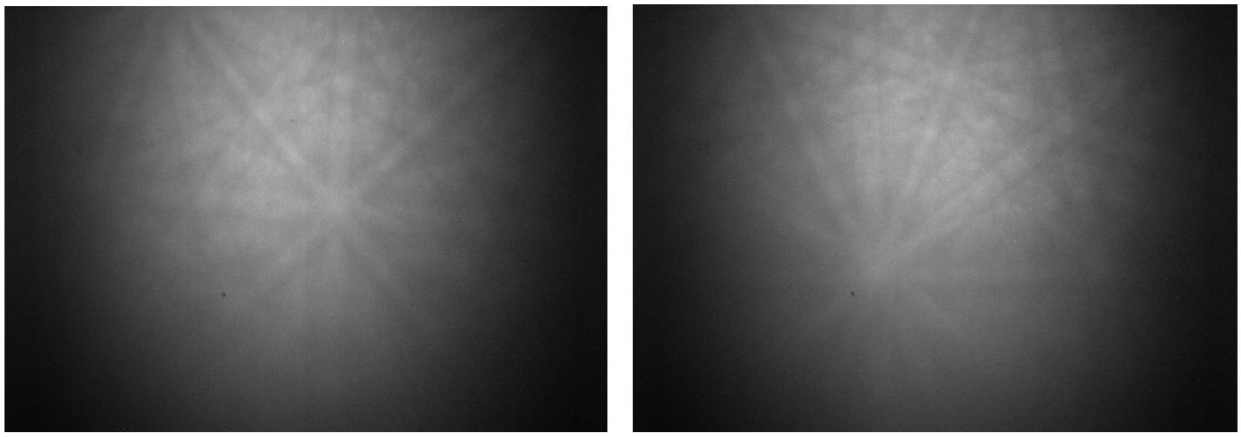

Figure 2-7 *Patterns (Kikuchi bands) from the olivine grain in reacted experiments (this study).*

2.4.3 – Sample preparation

As mentioned before, the diffraction patterns derived from the back-scattered electrons that are diffracted in the near sub-surface of the crystalline materials. For this reason, the sample preparation is a crucial step in order to obtain high quality diffraction measurements. In particular, the specimens should be conductive and not decompose in vacuum or under the electron beam. The surface should be flat and free from foreign layers. In this regard, after the experimental run, the capsules were embedded in epoxy resin in cylindrical moulds 1-inch in diameter. The samples were then cut and carefully polished to produce ideally flat and defect free surfaces. The following rotational polishing steps were observed (***Fig. 2-8a***):

- 9 μm ϕ diamond paste for 5 hours;
- 6 μm ϕ diamond paste for 3 hours;
- 3 μm ϕ diamond paste for 2 hours;
- 1 μm ϕ diamond paste for 30 minutes;
- 0.3 μm ϕ alumina paste for 2 hours.

After the rotational polishing procedure, in order to obtain ideally defect-free surfaces, the final polishing step was achieved by chemical-mechanical polishing (CMP) using a colloidal silica suspension (0.02-0.06 μm) for 5 hours and a vibrational polishing apparatus (***Fig. 2-8b***). Finally, the samples were carbon coated with a thin layer of 4 nm. A correct carbon coating is particularly important in EBSD analysis: if the coating is too thick, the signal to noise ratio will decrease significantly resulting in a poor data-quality while if the coating is too thin, the surface will not be sufficiently conductive and therefore enable to dissipate the electrostatic charge formed during the observations.

Figure 2-8 *(a) Struers LaboPol-35 used for polishing samples with different diamond grain size paste and (b) Saphir Vibro used for chemical-mechanical polishing (CMP).*

2.4.4 – Data collection methodology and data processing

The EBSD data were collected as an XY controlled systematic grid of points. More than one single map was collected for samples MG1 and MG5. The automated collected data will inevitably contain:

- Non-indexed points: points with no orientation solution generated at grain boundaries, cracks and surface contaminants and defects.
- Mis-indexed points: points assigned to an orientation that is different from the actual solution by an angle significantly greater than the angular error affecting the EBSD indexing procedure.
- Wild-spikes: single data pixels that are surrounded by 8 pixels of a different orientation.

Consequently, for a sample that contains several phases or multiple grains, a 100% indexing cannot be achieved due to the grain boundaries. Hence, the maps were carefully processed decreasing/removing any non-indexed points and mis-indexed points in order to avoid artefacts (incorrect interpretations). A high-quality data processing is an essential tool in order to eliminate errors and artefacts. In this regard, once the raw data were collected, the ESPRIT software allowed absorbing wild-spikes or zero-solutions counting 40-50 neighbouring pixels and filling the non-indexed pixels with 5 identical neighbours that have similar orientation. Moreover, the data processing allowed removing the small grains, in terms of pixel counting (10 pixels), that were not well indexed and not more representative of a specific sample. The identification of the grains was done applying 10° threshold angle between neighbouring pixels.

2.4.5 – MTEX toolbox

The EBSD post-processed quantitative texture analyses were elaborated and illustrated using MTEX (Mainprice et al., 2011 and 2012). MTEX provides a unique way to represent, analyse and interpret crystallographic preferred orientation such as, texture base on integral (pole figure) or individual orientation (EBSD) measurements. In this regard, for the quantitative texture analysis of large multi-file projects as the MatLab® Software uses a scripted language and a complex analysis can be developed in a m-file, which can evolve with changing requirements of the project. This software is a free open-source available MatLab® toolbox that covers a wide range of problems in quantitative texture analysis, as EBSD data analysis, grain modelling and anisotropic physical properties description (Hielscher & Schaeben 2008; Bachmann et al., 2010; Bachmann et al., 2011; Mainprice et al., 2011,

2014). MTEX allowed an extensive investigation of textures and the definition of the following quantitative textural parameters for each sample:

1- Equivalent Diameter: is defined as the longest distance between any two vertices of the grain boundary. This parameter is calculated by defining the area of a grain and then assuming the grain is a circle. At this point, the diameter is equal to $2\sqrt{A/\pi}$.
2- The Grain Area: is the area of a grain in μm^2. This parameter is calculated by summing up the number of points in a grain multiplied by the product of the square of the step size and a factor depending on the type of scanning grid. For square grids, the factor is 1 and for hexagonal grids is $(1/2)\sqrt{3}$.
3- The PARIS Factor (Percentile Average Relative Indented Surface): defines the grain boundary lobateness and it is settled by the comparison between the perimeter of the grain and its smallest envelope.
4- The Shape Factor: it defines the roundness of a grain and is calculated by the ratio between the perimeter of a grain and its equivalent perimeter (perimeter of a circle that has the same area as the considered grain).
5- The Aspect Ratio: it defines the elongation of a grain and corresponds to the ratio between the length (long axis) and the width (short axis).

Furthermore, in order to study the intra-granular deformation, three intra-granular misorientation parameters were elaborated. In this regard, it is important to specify that there are two types of local misorientation analyses: *grain based* and *kernel based*. The first ones are useful to recognize grains with varying local misorientation or the local orientation variations within a grain. On the other hand, the Kernel-based functions are based on a given area, the size of which will be defined by the user.

1- Grain Orientation Spread (GOS): this parameter is grain-based and it defines an average intragranular deformation of a grain. At first, the average orientation for a grain is calculated. Subsequently, the misorientation between this average orientation and the orientation of each individual measurement point within the grain is determined. The spread is then the average deviation between the orientation of each point in the grain and the average orientation for the grain. At this point, the distribution of the orientation spread for all the grains in the microstructure is the GOS (Britton et al., 2016).
2- Kernel Average Misorientation (KAM): this parameter is Kernel-based parameters and it allows identifying the sub-grains determining local values of intragranular lattice rotation (phase boundaries with misorientation angle $\leq 10°$, “low-angles grain boundaries”). It is a measure of

the average misorientation of a point (pixel) with respect to a selected number of its nearest neighbours.

3- Misorientation to Mean (Mis2Mean): it is Kernel-based and it allows identifying the kink bands (generated when slip on a single slip plane is inadequate to maintain homogeneous deformation).

MTEX is also useful to study the orientation distribution function (ODF) of a crystal orientations which is defined by the volume fraction of crystals that have the orientation with an infinitesimal orientation volume **dg**. In particular, the orientation of a crystal is historically defined in texture by the letter **g**, which is typically characterized by a Euler angle triplet. In this regard, in order to understand if the reaction results in the orientated olivine grains along a preferred orientation, the Inverse Pole Figure were elaborated. The Inverse Pole Figure (IPF): is the angular distribution function of a chosen specimen direction x, **y, z** in crystal coordinates, hence, the IPF uses crystal directions as the reference axes. The IPF can be conveniently used as a colour key for Crystal Orientation Map (COMs) because the figure has three corners and individual orientation measurements relate to a single point plotted in an Inverse Pole Figure. By assigning colours such as red, blue and green to each of the corners of the figure, any specific measurement can be related to a distinct colour in the COM.

Chapter 3
OLIVINE REACTIVE DISSOLUTION AND RE-PRECIPITATION PROCESS - ISOTHERMAL EXPERIMENTS

In this section the chemical and textural observations of the isothermal experiments will be presented into detail. The chapter is organized into 3 sections: a brief introduction followed by two longer sections which describe the textural and chemical features. ***Tab. 3-1*** lists the experimental run conditions and phase assemblages of the reaction experiments. Another sample named **OM23,** will be taken in consideration and will be compare to the **MG18** experiment in order to understand how two different experimental setups can affect the chemistry and microstructure of the run products. This reaction experiment was conducted in the PhD thesis of Justine Francomme (2016-2017), at similar experimental *PT* conditions, and with 9wt% of initial melt amount (hereafter referred to as IMA).

Run	P (GPa)	T (°C)	t (h)	Initial melt amount (wt%)	Phase assemblages and mode (wt%) [a]			
Starting materials SCO [b] +AH6					Ol[d]	Pl[e]	Cpx[f]	Gl[g]
MG10	0.5	1200	24	10	92 (2)	5.3 (5)	3 (1)	Absent
MG18	0.5	1300	24	10	90 (2)	Absent	Absent	10 (1)
OM23[c]	0.5	1300	0.5	9	89	Absent	Absent	11
MG12	0.5	1200	24	25	76 (2)	7 (3)	8 (1)	9 (5)
MG1	0.5	1300	24	25	73 (2)	Absent	Absent	27 (2)
MG14	0.5	1200	24	50	58 (2)	24 (1)	14 (5)	4 (16)
MG11	0.5	1250	24	50	47 (2)	Absent	Absent	53 (1)
MG5	0.5	1300	24	50	45 (2)	Absent	Absent	55 (2)

Table 3-1 *A summary of the experimental conditions and run products. [a] Modes are calculated using mass balance calculations: e.g., 92 (2) and 5.3 (5) represent 92.26 ± 1.54 and 5.34 ± 0.47, respectively. [b] San Carlos olivine. [c] Reaction experiment from PhD thesis of Francomme, J. E. (2016-2017). [d] Olivine. [e] Plagioclase. [f] Clinopyroxene. [g] Glass.*

3.1 – Results

3.1.1 – Phase assemblages and texture

All experiments show homogeneous phases distribution within the charges suggesting that no melt segregation occurred after melt-olivine reaction (***Fig. 3-1a-b***). The reaction experiments performed at 1200°C, named **MG10**, **MG12** and **MG14** (with 10, 25 and 50wt%$_{IMA}$, respectively), results in olivine, plagioclase, clinopyroxene and small amount of interstitial basaltic glass. Phase abundances are reported in ***Tab. 3-1*** and will be discussed in details in **Chapter 5**. Olivine is the dominant phase but the grain boundaries are difficult to define by BSE images, especially in the experiments with 10 and 25wt% of initial melt (***Fig. 3-2a-b-c-d***). Increasing the initial melt amount (50wt%), olivine morphology is pseudo-tabular and grain boundaries become better defined due to the presence of interstitial phase (*e.g.*, plagioclase and clinopyroxene) and small amount of interstitial glass (***Fig. 3-2e-f***). Interstitial phases, *i.e.*, plagioclase and clinopyroxene in the experiment with 10wt% of melt, occur along olivine grain boundaries in which show sharp and straight contacts. On the other hand, in reaction experiments with 25 and 50wt%$_{IMA}$, they occur with a typical *myrmekite* microstructure, a common example of "symplectitic intergrowths" (***Fig. 3-2c-d-e-f***). Although the olivine-plagioclase-clinopyroxene intergrowths are less common than ones of quartz-sodic plagioclase, they were recovered in some gabbros (*e.g.*, de Haas et al, 2002) and this could suggest the co-precipitation of these two phases from small amounts of the reacted melt. In order to better recognize the mineral phase in "graphic intergrowths", a detailed compositional map - EDS (*Energy Dispersive Spectroscopy*) maps (***Fig. 3-3)*** were recovered in MG14 (50wt%$_{IMA}$). The EDS maps show the chemical distribution of Na in plagioclase (***Fig. 3-3c***), Ca in clinopyroxene (***Fig. 3-3d***), and Mg-Fe in a fine-grained olivine aggregate (~2-5μm) (***Fig. 3-3a-b***).

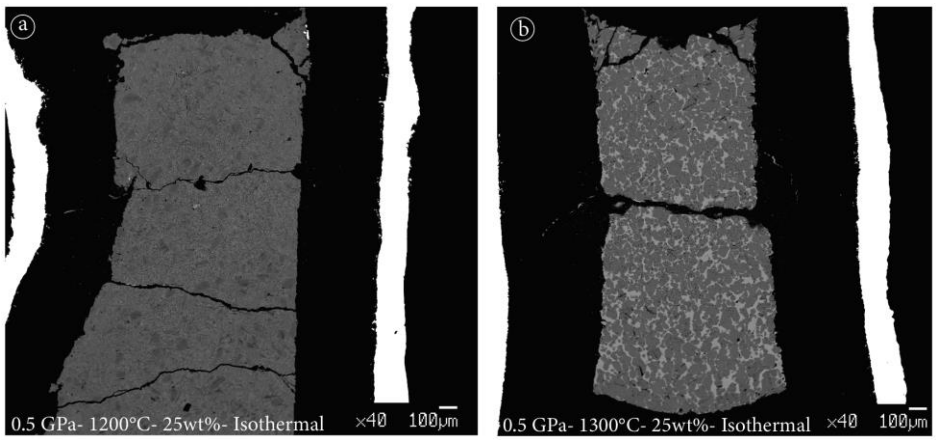

Figure 3-1 *Back- Scattered-Electron (BSE) images showing a panoramic view of the capsule after the reaction. a) The isothermal run MG12 (0.5 GPa, 1200°C, 25wt%, 24h) and b) the isothermal run MG1 (0.5 GPa, 1300°C, 25wt%, 24h).*

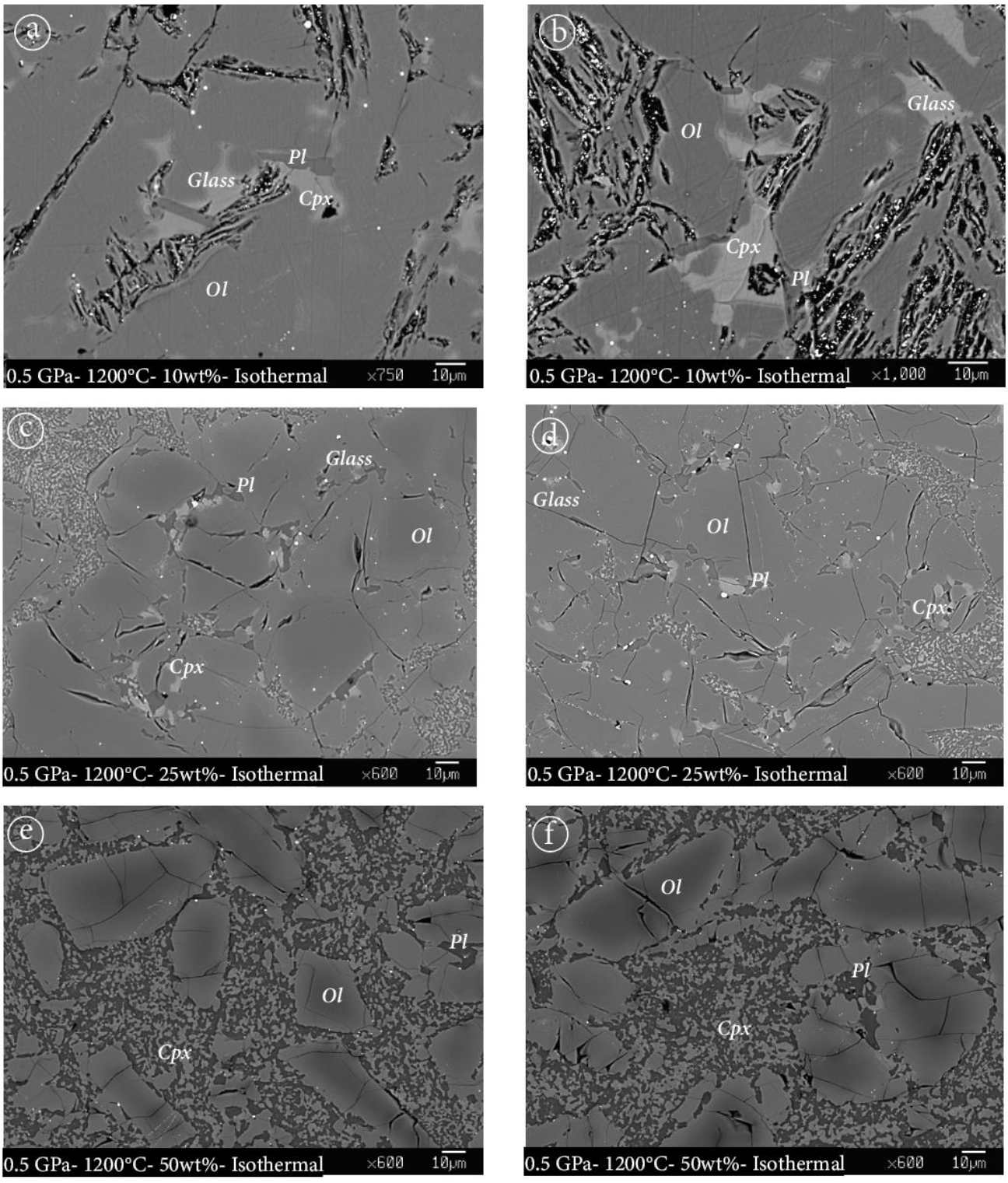

Figure 3-2 *Representative BSE images showing texture in isothermal experiment with 10wt% of melt (a-b), 25wt% of melt (c-d) and 50wt% of melt (e-f) performed at 0.5 GPa and 1200°C for 24h.*

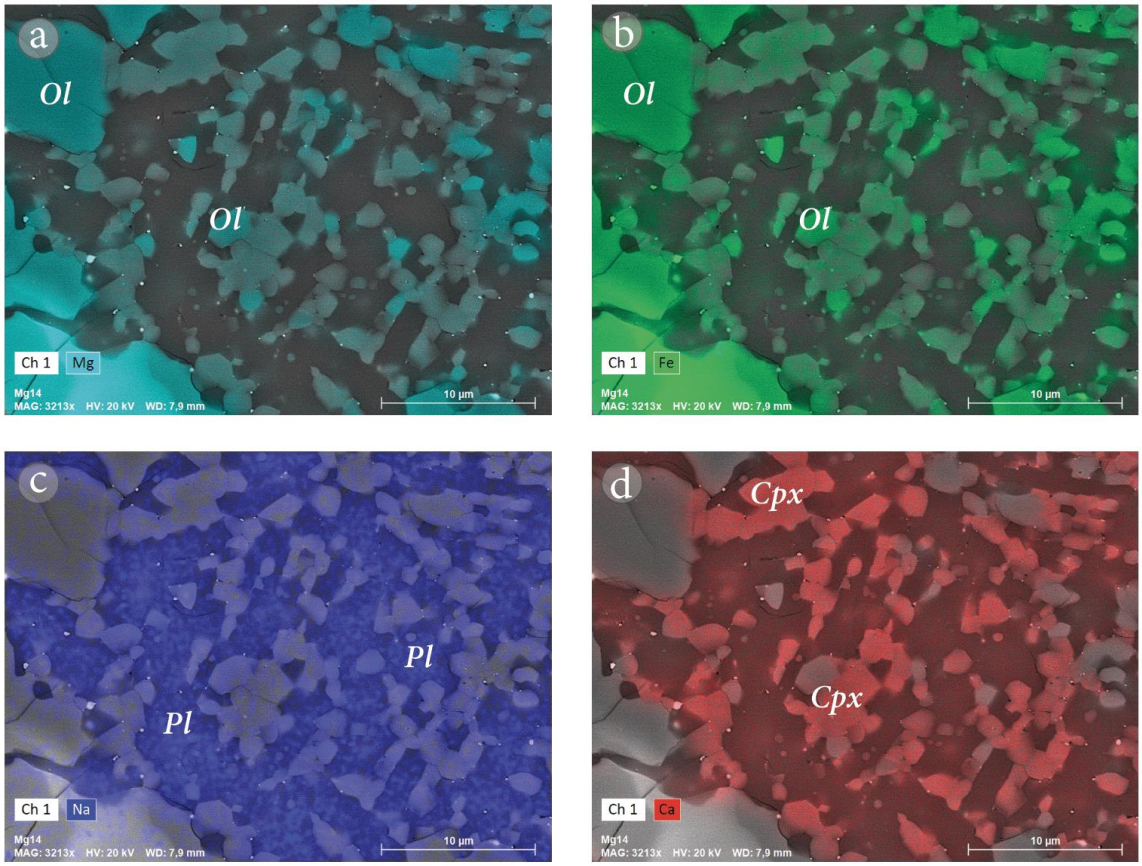

Figure 3-3 *EDS maps performed at Department of Environment and Earth, University of Milano-Bicocca show the (a-b) Mg- Fe distribution (light blue and green, respectively) in small crystals of olivine (~2-5µm), (c) Na content (blue) in plagioclase and (d) Ca content (red) in clinopyroxene*

The isothermal experiment **MG11** performed at 0.5 GPa and 1250°C with 50wt% of initial melt consists of olivine and basaltic glass (***Fig. 3-4a***). Olivine occurs either as fine-grained euhedral crystals (10-15μm) or as coarse-grained subhedral crystals (~100μm) (***Fig. 3-4b***).

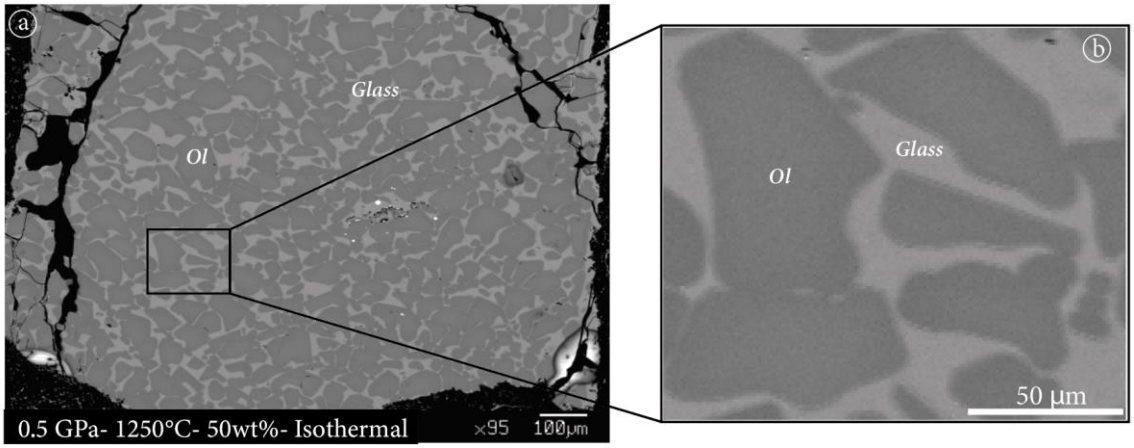

Figure 3-4 *Representative BSE images showing texture in isothermal experiment with 50wt% of melt (a-b), performed at 0.5 GPa and 1250°C for 24h.*

Run products of isothermal experiment **OM23**, **MG18**, **MG1** and **MG5** performed at 0.5 GPa and 1300°C with different initial melt amount (9, 10, 25 and 50wt%, respectively) consist of olivine crystals and basaltic glass. Phase abundances are reported in ***Tab. 3-1***, and will be discussed in details **Chapter 5**. A preliminary study of the texture through BSE images allows to distinguish two sets of olivine crystals morphologically different: i) large subhedral crystals (up to 100 μm) with both straight and lobate rims and ii) small rounded grains with a more regular habit (5-20 μm). In the reaction experiment **OM23** and **MG18**, with 9 and 10wt%$_{IMA}$ respectively, an overall smaller crystal grain size (~20 μm) is observed. Moreover, the number of olivine grains with regular morphology, as rounded and euhedral habit is higher than those larger with irregular habit (***Fig. 3-5a-b-c-d***). In run **MG1** and **MG5** at 1300°C with 25 and 50wt% of initial melt, the overall gran size and high diffusion of large irregular olivine with straight and lobate rims (up to 180 μm) increase (***Fig. 3-5e-f-g-h***). In particular, with the increasing of initial melt amount from 10 to 50wt%, olivine grain size increases and the amount of smaller rounded grain decreases.

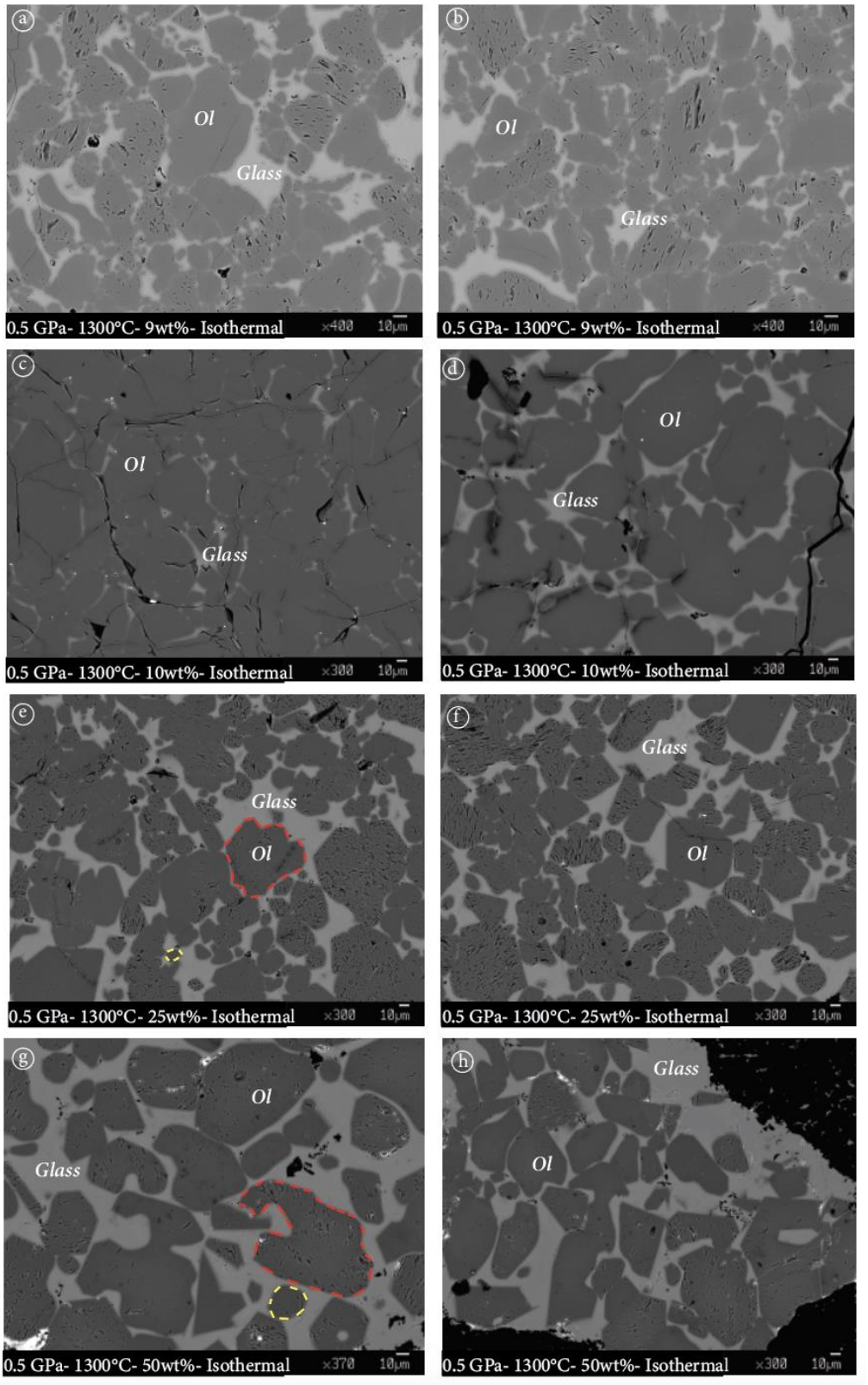

Figure 3-5 *Representative BSE images showing texture in isothermal experiment with 9 wt% of melt (a-b) from Francomme PhD Thesis, 10wt% of melt (c-d), 25wt% of melt (e-f) and 50wt% of melt (g-h) performed at 0.5 GPa and 1300°C. e-g) large subhedral olivine crystals (~100 µm) with both straight and lobate rims (red dashed line) and smaller rounded grains (5-20 µm) (yellow dashed line).*

3.1.2 – Mineral and glass chemistry

The major element compositions of the mineral phases (olivine, plagioclase, clinopyroxene and glass) in the reaction experiments are reported in ***Table 3-2a-b-c-d.*** In order to evaluate the role of temperature, the results will be discussed comparing the experiments run at 1200°C with those performed at 1250 and 1300°C. On the other hand, the effect of melt/olivine ratio will be evaluated comparing the experiments with different initial melt amount, from 10 to 50wt%. The complete dataset is given in ***Tab. 7-2, 7-4, 7-6, 7-8*** **(in Appendix)**.

Sample	**MG10**	σ[e]	**MG12**	σ	**MG14**	σ	**MG11**	σ	**OM23**	σ	**MG18**	σ	**MG1**	σ	**MG5**	σ
IMA[a] (wt%)	10		25		50		50		9		10		25		50	
T[b]	1200		1200		1200		1250		1300		1300		1300		1300	
n[c]	29		54		15		73		25		17		120		47	
SiO_2	40.75	0.30	40.51	0.27	40.47	0.60	40.86	0.26	40.79	0.19	40.61	0.26	40.69	0.62	40.99	0.29
TiO_2	0.02	0.02	0.02	0.02	0.03	0.03	0.02	0.02	0.01	0.02	0.01	0.01	0.02	0.02	0.02	0.02
Al_2O_3	0.04	0.03	0.02	0.02	0.04	0.02	0.05	0.03	0.04	0.03	0.05	0.01	0.07	0.05	0.07	0.03
Cr_2O_3	0.03	0.03	0.02	0.03	0.03	0.03	0.04	0.03	0.02	0.03	0.04	0.03	0.03	0.03	0.04	0.03
FeO	10.96	0.16	9.94	0.70	13.98	2.16	9.94	0.80	9.72	0.47	10.31	0.46	9.17	0.24	8.26	0.49
MgO	48.96	0.63	49.11	0.58	46.19	1.58	50.12	0.65	48.82	0.47	49.62	0.70	50.11	0.67	50.99	0.59
MnO	0.16	0.04	0.15	0.03	0.21	0.05	0.16	0.03	0.14	0.02	0.13	0.03	0.14	0.03	0.13	0.03
NiO	0.17	0.08	0.27	0.10	0.19	0.13	0.10	0.08	0.34	0.08	0.16	0.08	0.04	0.08	0.02	0.02
CaO	0.24	0.08	0.14	0.07	0.28	0.15	0.32	0.10	0.21	0.12	0.27	0.02	0.33	0.06	0.35	0.04
Na_2O	0.01	0.01	0.01	0.02	0.01	0.01	0.02	0.02	0.01	0.02	0.01	0.01	0.02	0.02	0.01	0.02
K_2O	0.00	0.01	0.00	0.01	0.00	0.00	0.00	0.01	0.00	0.01	0.00	0.01	0.01	0.01	0.01	0.01
Sum	101.33	0.62	100.19	0.34	101.43	0.58	101.64	0.35	100.11	0.26	101.22	0.48	100.62	0.97	100.89	0.53
Si	0.99	0.01	0.99	0.01	1.00	0.01	0.98	0.01	1.00	0.00	0.98	0.01	0.99	0.01	0.99	0.01
Ti	0.00	0.00	0.00	0.00	0.00	0.00	0.00	0.00	0.00	0.00	0.00	0.00	0.00	0.00	0.00	0.00
Al	0.00	0.00	0.00	0.00	0.00	0.00	0.00	0.00	0.00	0.00	0.00	0.00	0.00	0.00	0.00	0.00
Cr	0.00	0.00	0.00	0.00	0.00	0.00	0.00	0.00	0.00	0.00	0.00	0.00	0.00	0.00	0.00	0.00
Fe	0.22	0.00	0.20	0.01	0.29	0.05	0.20	0.02	0.20	0.01	0.21	0.01	0.19	0.00	0.17	0.01
Mg	1.77	0.01	1.79	0.02	1.70	0.04	1.80	0.02	1.78	0.01	1.79	0.02	1.81	0.01	1.83	0.01
Mn	0.00	0.00	0.00	0.00	0.00	0.00	0.00	0.00	0.00	0.00	0.00	0.00	0.00	0.00	0.00	0.00
Ni	0.00	0.00	0.01	0.00	0.00	0.00	0.00	0.00	0.01	0.00	0.00	0.00	0.00	0.00	0.00	0.00
Ca	0.01	0.00	0.00	0.00	0.01	0.00	0.01	0.00	0.01	0.00	0.01	0.00	0.01	0.00	0.01	0.00
Na	0.00	0.00	0.00	0.00	0.00	0.00	0.00	0.00	0.00	0.00	0.00	0.00	0.00	0.00	0.00	0.00
K	0.00	0.00	0.00	0.00	0.00	0.00	0.00	0.00	0.00	0.00	0.00	0.00	0.00	0.00	0.00	0.00
Sum	3.00	0.03	3.00	0.04	3.00	0.11	3.00	0.05	3.00	0.04	3.00	0.04	3.00	0.04	3.00	0.03
X_{Mg}[d]	0.88	0.00	0.89	0.01	0.85	0.02	0.89	0.01	0.89	0.01	0.89	0.01	0.90	0.00	0.91	0.01

Table 3-2a *Representative major element compositions of olivine from isothermal experiments.* [a] *Initial melt mount.* [b] *Temperature.* [c] *n = number of analysis.* [d] X_{Mg} *= Mg/(Mg+Fe).* [e] σ *= standard deviation.*

Sample	**MG10**	σ[e]	**MG12**	σ	**MG14**	σ
IMA[a] (wt%)	10		25		50	
T[b]	1200		1200		1200	
n[c]	12		9		9	
SiO_2	51.35	0.61	51.58	1.33	51.88	0.40
TiO_2	0.09	0.06	0.18	0.11	0.11	0.05
Al_2O_3	29.30	1.18	28.21	1.29	28.20	0.95
Cr_2O_3	0.01	0.01	0.01	0.02	0.02	0.02
FeO	0.32	0.30	0.07	0.20	0.28	0.23
MgO	0.78	0.71	1.72	1.23	0.40	0.23
MnO	0.01	0.02	0.00	0.01	0.03	0.02
NiO	0.07	0.08	0.05	0.03	0.03	0.03
CaO	13.53	0.79	11.80	1.05	13.39	0.41
Na_2O	3.43	0.33	4.06	0.62	3.74	0.21
K_2O	0.10	0.04	0.18	0.07	0.09	0.02
Sum	99.48	0.80	98.65	0.72	98.52	0.96
Si	2.35	0.03	2.37	0.05	2.40	0.01
Ti	0.00	0.00	0.01	0.00	0.00	0.00
Al	1.58	0.06	1.53	0.08	1.54	0.04
Cr	0.00	0.00	0.00	0.00	0.00	0.00
Fe	0.01	0.01	0.00	0.01	0.01	0.01
Mg	0.05	0.05	0.12	0.08	0.03	0.02
Mn	0.00	0.00	0.00	0.00	0.00	0.00
Ni	0.00	0.00	0.00	0.00	0.00	0.00
Ca	0.66	0.04	0.58	0.06	0.66	0.02
Na	0.30	0.03	0.36	0.05	0.34	0.02
K	0.01	0.00	0.01	0.00	0.01	0.00
Na+Ca	0.97	0.07	0.94	0.11	1.00	0.04
X_{An}[d]	0.68	0.03	0.61	0.06	0.66	0.02

Table 3-2b *Representative major element compositions of plagioclase from isothermal experiments.* [a] *Initial melt mount.* [b] *Temperature.* [c] *n = number of analysis.* [d] $X_{An} = Ca/(Ca+Na)$. [e] σ *= standard deviation.*

Sample	**MG10**	σ[e]	**MG12**	σ	**MG14**	σ
IMA[a] (wt%)	10		25		50	
T[b]	1200		1200		1200	
n[c]	10		12		10	
SiO_2	51.27	0.54	50.10	1.62	51.30	0.72
TiO_2	1.58	0.40	2.11	1.08	1.48	0.34
Al_2O_3	5.22	0.63	5.09	1.88	5.13	0.67
Cr_2O_3	0.16	0.04	0.19	0.09	0.19	0.03
FeO	3.76	0.14	3.53	0.35	5.22	0.56
MgO	17.30	0.80	16.42	1.54	15.84	1.34
MnO	0.10	0.03	0.09	0.04	0.14	0.04
NiO	0.05	0.03	0.05	0.04	0.05	0.05
CaO	20.39	0.60	20.49	0.65	21.01	0.78
Na_2O	0.40	0.05	0.47	0.22	0.43	0.07
K_2O	0.01	0.01	0.01	0.01	0.01	0.01
Sum	100.24	0.58	98.57	0.69	100.81	0.63
Si	1.86	0.02	1.85	0.06	1.86	0.02
Ti	0.04	0.01	0.06	0.03	0.04	0.01
Al	0.22	0.03	0.22	0.08	0.22	0.03
Cr	0.00	0.00	0.01	0.00	0.01	0.00
Fe	0.11	0.00	0.11	0.01	0.16	0.02
Mg	0.93	0.04	0.90	0.09	0.86	0.07
Mn	0.00	0.00	0.00	0.00	0.00	0.00
Ni	0.00	0.00	0.00	0.00	0.00	0.00
Ca	0.79	0.02	0.81	0.03	0.82	0.03
Na	0.03	0.00	0.03	0.02	0.03	0.00
K	0.00	0.00	0.00	0.00	0.00	0.00
Sum	4.00	0.14	4.00	0.31	4.00	0.19
X_{Mg}[d]	0.89	0.00	0.89	0.02	0.84	0.02

Table 3-2c *Representative major element compositions of clinopyroxene from isothermal experiments.* [a] *Initial melt mount.* [b] *Temperature.* [c] *n = number of analysis.* [d] $X_{Mg} = Mg/(Mg+Fe)$. [e] σ *= standard deviation.*

Sample	MG10	σ[f]	MG12	σ	MG14	σ	MG11	σ	OM23	σ	MG18	σ	MG1	σ	MG5	σ
IMA[a] (wt%)	10		25		50		50		9		10		25		50	
T[b]	1200		1200		1200		1250		1300		1300		1300		1300	
n[c]	5		3		2		32		8		16		45		24	
SiO_2	51.69	0.28	49.62	0.56	49.28	0.34	48.73	0.32	49.36	0.56	49.53	0.50	48.06	0.90	48.44	0.50
TiO_2	1.26	0.10	2.89	0.12	2.14	0.29	0.80	0.05	1.09	0.22	0.81	0.07	0.81	0.06	0.82	0.06
Al_2O_3	16.70	0.42	17.46	0.50	16.86	1.15	15.47	0.46	17.10	1.15	14.37	1.02	15.52	0.83	15.62	0.76
Cr_2O_3	0.01	0.02	0.03	0.02	0.01	0.01	0.06	0.03	0.05	0.04	0.04	0.05	0.04	0.03	0.05	0.03
FeO	6.66	0.21	5.18	0.09	7.79	0.34	7.41	0.37	7.99	0.38	10.10	0.32	9.11	0.35	7.57	0.27
MgO	7.21	0.91	5.61	1.22	5.17	1.63	11.62	1.23	7.61	2.33	8.59	2.34	11.05	1.66	12.20	1.71
MnO	0.13	0.03	0.14	0.03	0.18	0.03	0.15	0.03	0.15	0.04	0.21	0.02	0.19	0.03	0.16	0.03
NiO	0.07	0.04	0.02	0.02	0.03	0.04	0.01	0.02	0.01	0.02	0.01	0.01	0.02	0.03	0.01	0.02
CaO	11.96	0.34	8.02	0.20	12.39	0.28	12.97	0.48	13.94	1.13	11.97	0.68	12.47	0.52	12.86	0.66
Na_2O	2.84	0.18	5.24	0.12	3.38	0.08	2.10	0.13	2.59	0.23	1.97	0.33	2.07	0.15	2.05	0.16
K_2O	0.36	0.02	1.73	0.07	0.39	0.06	0.13	0.02	0.13	0.04	0.09	0.02	0.15	0.02	0.11	0.02
Sum	98.90	0.29	95.93	0.07	97.61	0.15	99.44	0.33	100.00	0.00	97.70	0.48	99.48	0.86	99.88	0.57
X_{Mg}[d]	0.66	0.03	0.65	0.06	0.54	0.07	0.73	0.03	0.62	0.06	0.59	0.07	0.68	0.03	0.74	0.03
X_{Ca}[e]	0.81	0.01	0.73	0.11	0.68	0.10	0.73	0.12	0.83	0.04	0.86	0.00	0.86	0.01	0.86	0.01

Table 3-2d *Representative major element compositions of glass from isothermal experiments.* [a] *Initial melt amount.* [b] *Temperature.* [c] *n = number of analysis.* [d] $X_{Mg} = Mg/(Mg+Fe)$. [e] $X_{Ca} = Ca/(Ca+Na)$. [f] σ *= standard deviation.*

3.1.2.1 – Olivine chemistry

Fig. 3-6 shows the X_{Mg} value [X_{Mg} is defined as $Mg/(Mg+Fe_{tot})$] versus NiO content (wt%) measured in the cores and rims of olivine in each experiment. Reacted olivine at 1200, 1250 and 1300°C are characterized by negligible core-to-rim compositional variations, except for the reaction experiment MG14 performed at 1200°C with 50wt%$_{IMA}$ in which the olivine has rims with lower NiO (0.08wt% ± 0.10) and higher CaO (0.30wt% ± 0.10) than the cores (NiO = 0.09wt% ± 0.11 and CaO = 0.28wt% ± 0.09). However, the olivine grains are generally characterized by a slightly decrease of NiO content towards the profiles from rim to core. ***Figs. 3-7c and 3-8h*** show an example of NiO profiles from rim to core of some olivine grains in MG5 experiment.

Due to the negligible difference between core and rim, the total analysis of olivine, which include core and rim, will be considered. ***Fig. 3-9*** shows the X_{Mg} versus NiO and CaO content (wt%) of olivine in reaction experiments at 1200 and 1300°C (and 0.5 GPa) with initial melt amount of 10, 25 and 50wt%, respectively. Overall, the reacted olivine (*i.e.*, new olivine) resulted from the reaction with the melt, is chemically different compared to its initial composition (San Carlos olivine), in particular:

- At **1200°C**, X_{Mg} values of the reacted olivine always plot below the composition of San Carlos olivine (X_{Mg} = 0.90) and they are also lower than the X_{Mg} values of higher temperature reaction experiments (1250 and 1300°C). Interestingly, it has not been observed any correlation between the X_{Mg} values in reacted olivine and initial different melt amount. In particular, the MG12 experiment with 25wt%$_{IMA}$ has a higher X_{Mg} value (X_{Mg} = 0.89 ± 0.01) with respect to the ones with 10 and 50wt%$_{IMA}$ (X_{Mg} = 0.88 ± 0.00 and X_{Mg} = 0.85 ± 0.02,

respectively). The NiO content is higher than those observed in olivine from runs at 1300°C. No correlation between the NiO content and the initial melt amount was observed. The olivine in run MG12 performed with 25wt%$_{IMA}$ has a NiO content higher (NiO = 0.27wt% ± 0.10) than olivine from the experiments performed with 10 and 50wt%$_{IMA}$ (NiO = 0.17wt% ± 0.08 and NiO = 0.19wt% ± 0.13, respectively). The CaO content in reacted olivine is not correlated to the different initial melt amount, however, the isothermal experiment MG14 with 50wt%$_{IMA}$ has a higher CaO content (CaO = 0.28wt% ± 0.15) with respect to the experiments with 10 and 25wt%$_{IMA}$ (CaO = 0.24wt% ± 0.08 and CaO = 0.14wt% ± 0.07, respectively) (***Fig. 3-9b***).

- At **1250** and **1300°C**, the reacted olivine is characterized by overall higher X_{Mg} values in olivine than the initial composition of San Carlos olivine and increase by increasing the initial melt amount (***Fig. 3-9***). In particular, the isothermal experiment MG5 (50wt%$_{IMA}$) has a X_{Mg} higher (X_{Mg} = 0.91 ± 0.01) than the ones with 10 and 25wt%$_{IMA}$ (X_{Mg} = 0.89 ± 0.00 and X_{Mg} = 0.90 ± 0.01, respectively). No correlation is observed between the olivine morphologies (textural details in **Section 3.1.1**) and their X_{Mg} values. The NiO content decrease with the increase of the starting melt amount. In particular, the MG5 reaction experiment (1300°C, 50wt%$_{IMA}$) is characterized by lower NiO content (NiO = 0.02wt% ± 0.02) than the experiments with 10 and 25wt%$_{IMA}$ (NiO = 0.16wt% ± 0.08 and NiO = 0.04wt% ± 0.08, respectively). It is observed a negative correlation between the covariation of X_{Mg} value and the NiO content. In particular, at higher X_{Mg} value corresponds lower NiO content with the increase of initial melt amount (*e.g.*, the experiment with 50wt%$_{IMA}$) (***Fig. 3-9a***). The CaO content increases with the increase of initial melt amount. In particular, the reaction experiment MG5 with 50wt%$_{IMA}$ has a higher CaO content (CaO = 0.35wt% ± 0.04) than the experiments performed with 10 and 25wt%$_{IMA}$ (CaO = 0.27wt% ± 0.02 and CaO = 0.33wt% ± 0.06, respectively) (***Fig. 3-9b***).

Hence, these chemical evidences suggest that:

1- At constant high initial melt amount (50wt%$_{IMA}$), *T* strongly influences the NiO content in reacted olivine (***Fig. 3-9a***). In particular, it decreases with the increase of temperature from 1200 to 1300°C.

2- The melt-olivine reaction results in a systematic increase of CaO content in olivine with respect to San Carlos Olivine (CaO = 0.07 ± 0.02). At constant high initial melt amount (50wt%$_{IMA}$), *T* influences the CaO content in reacted olivine. In particular, it increases with the increase of *T* from 1200 to 1300°C (***Fig. 3-9b***).

3- At fixed *T* of 1300°C, the NiO content strongly dependent on the initial melt amount. It decreases with the increase of IMA (***Fig. 3-9a***).

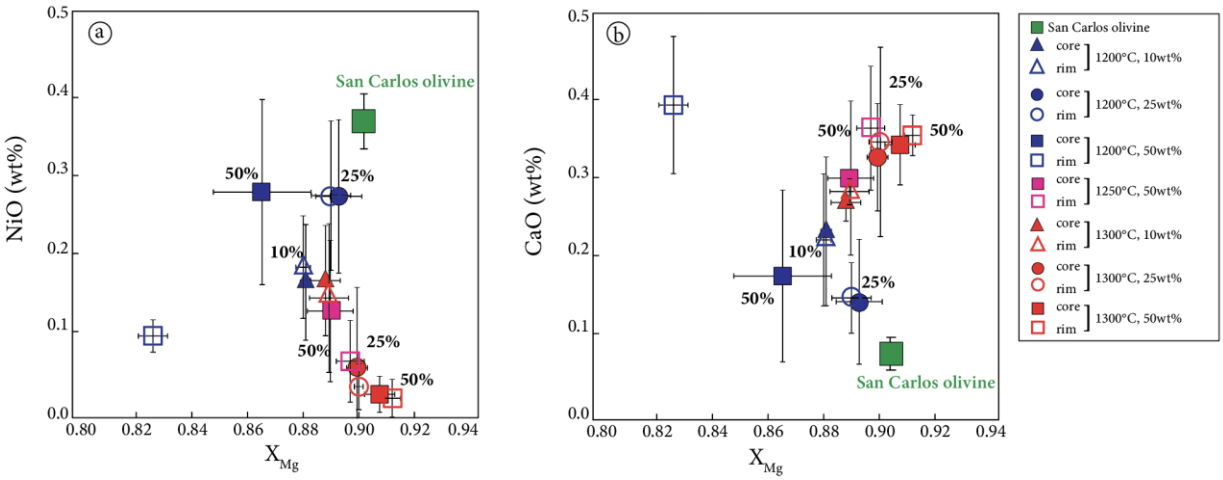

Figure 3-6 *(a) X_{Mg} vs. NiO content (wt%) and (b) X_{Mg} vs. CaO content (wt%) in olivine from reaction experiments performed at 0.5 GPa and temperature from 1200 to 1300°C with different initial melt amount (10, 25 and 50wt%). Full and empty symbols represent cores and rims, respectively.*

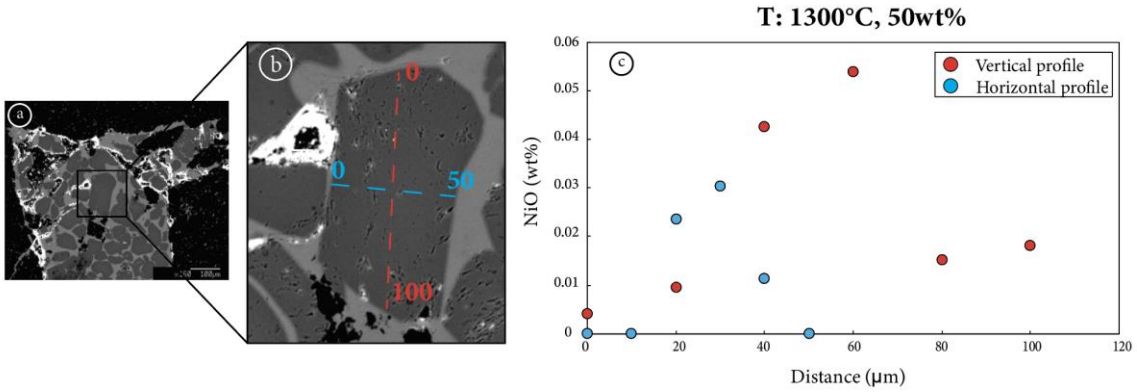

Figure 3-7 *Representative BSE images showing texture in isothermal experiment with 50wt% of initial melt amount (MG5), performed at 0.5 GPa and 1300°C (a-b) and corresponding NiO profiles (c) for selected large subhedral crystal with both straight and lobate rims (b) recovered at the top of the capsule. Total length of the horizontal profile (blue dashed line) is 50 µm. Step size is 10 µm. Total length of the vertical profile (red dashed line) is 100 µm. Step size is 20 µm.*

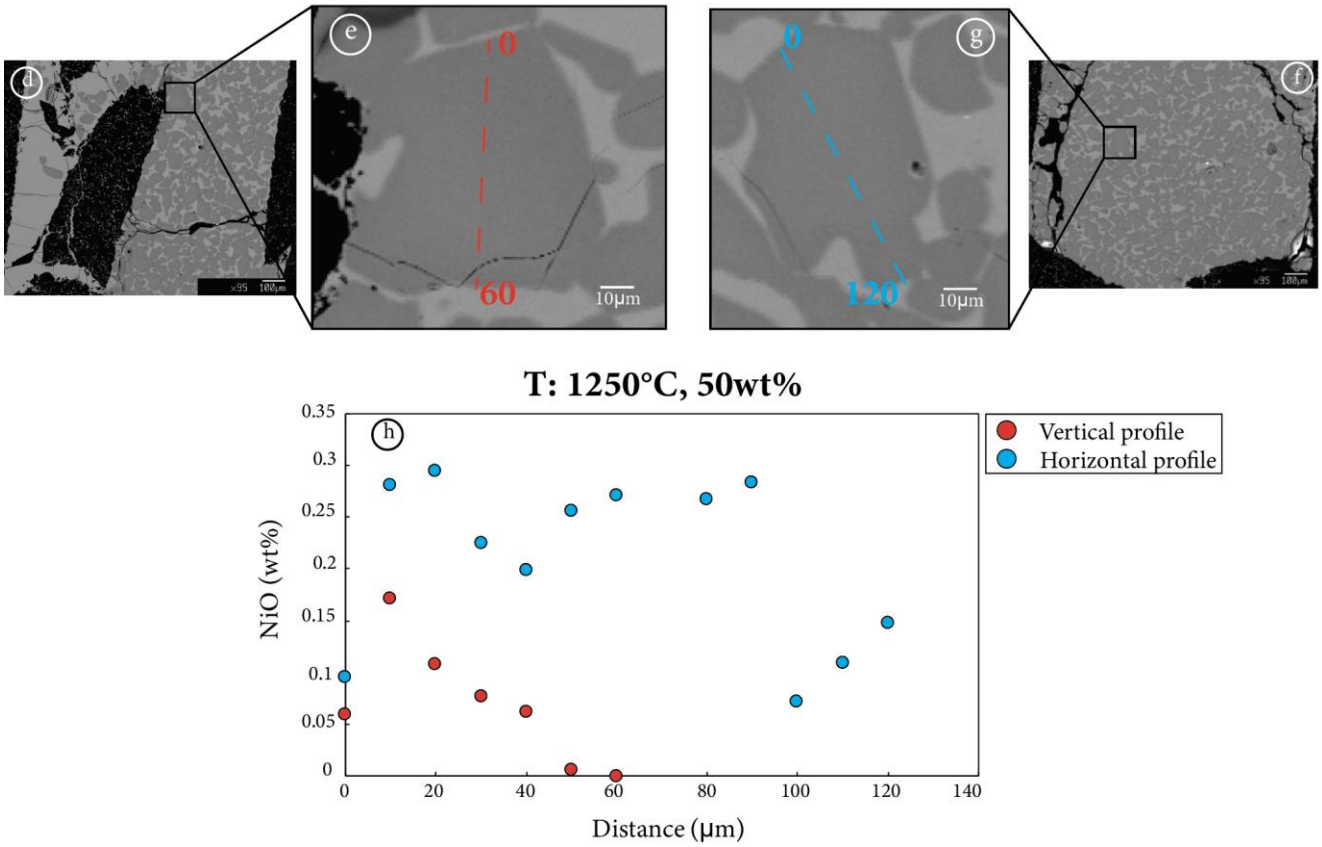

Figure 3-8 *Representative BSE images showing texture in isothermal experiment with 50wt% of initial melt amount (MG11), performed at 0.5 GPa and 1250°C (d-c-f-g) and corresponding NiO profiles (h) for selected large subhedral crystal with both straight and lobate rims (e-g) recovered at the center and the bottom of the capsule. Total length of the vertical profile (red dashed line) is 60 µm. Step size is 10 µm (e). Total length of the vertical profile (blue dashed line) is 120 µm. Step size is 10 µm (g).*

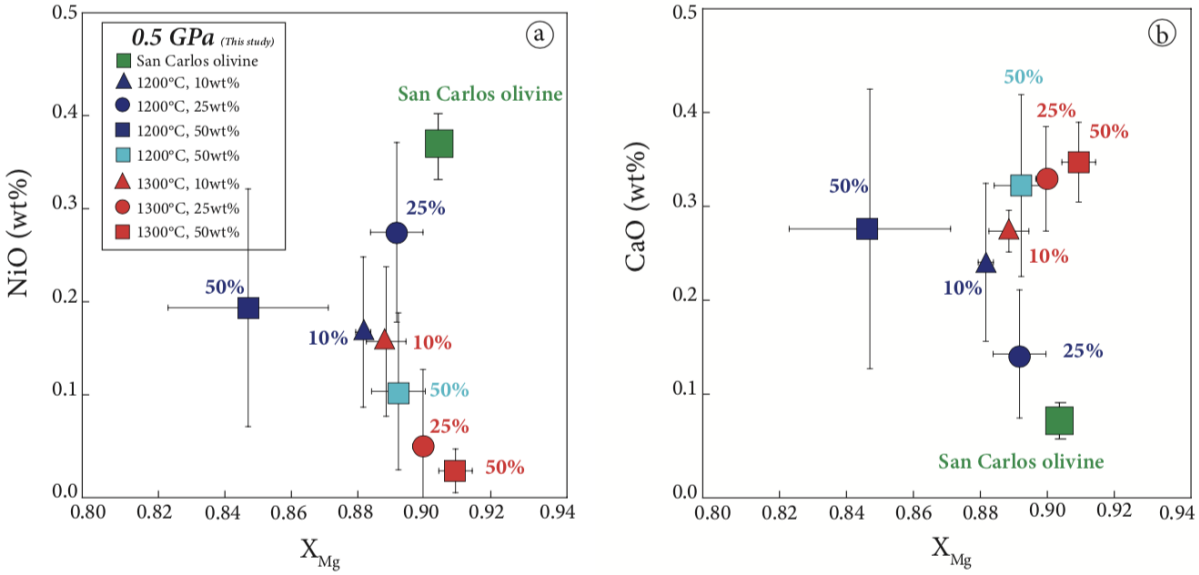

Figure 3-9 *X_{Mg} vs. NiO content (wt%) and (b) X_{Mg} vs. CaO content (wt%) in olivine from reaction experiments performed at 0.5 GPa and temperature from 1200 to 1300°C with different initial melt amount (10, 25 and 50wt%). The chemical data include core and rim.*

3.1.2.2 – Plagioclase chemistry

Plagioclase occurs only in the run performed at 0.5 GPa and 1200°C (***Tab. 3-1***). ***Fig. 3-10*** shows the covariation of the X_{Mg} of olivine and clinopyroxene with X_{An} [X_{An} = Ca/(Ca+Na)] of plagioclase. No significant differences in plagioclase composition are observed as a function of different initial melt amount from 10 to 50wt%. In particular, plagioclase in run MG10 with 10wt%$_{IMA}$ has higher anorthite content (X_{An} = 0.68 ± 0.03) than that in runs with 25 and 50wt% (X_{An} = 0.61 ± 0.06 and X_{An} = 0.66 ± 0.02, respectively). It is observed a positive correlation between the X_{An} of plagioclase and X_{Ca} of the reacted melt (***Fig. 3-10c***). In particular, the highest X_{An} value of plagioclase in run with 10wt%$_{IMA}$ is correlated to the highest X_{Ca} value in the reacted melt (0.81 ± 0.01). On the contrary, the lowest X_{An} value of plagioclase in run with 50wt%$_{IMA}$ corresponds to the lowest X_{Ca} value in the reacted melt (0.68 ± 0.10).

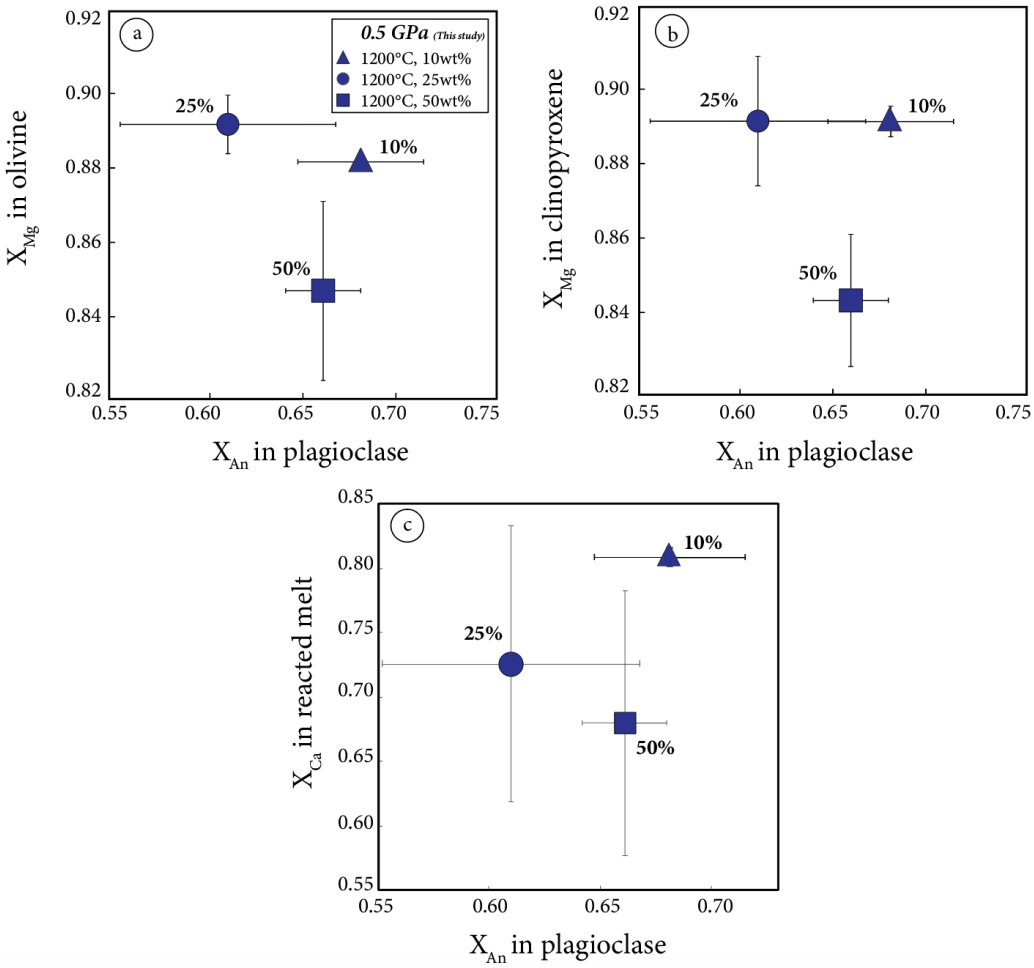

Figure 3-10 *reports: (a) X_{Mg} in olivine vs. X_{An} in plagioclase; (b) X_{Mg} in clinopyroxene vs. X_{An} in and (c) X_{An} in plagioclase vs. X_{Ca} in the reacted melt of reaction experiments at 0.5 GPa and 1200°C with different initial melt amount (10, 25 and 50wt%).*

3.1.2.3 – Clinopyroxene chemistry

Fig. 3-11 shows the clinopyroxene composition in reaction experiments performed at 0.5 GPa and 1200°C with different initial melt amount from 10 to 50wt%. No significant differences in X_{Mg} value are observed between the experiments with 10 and 25wt% of initial melt (X_{Mg} = 0.89 ± 0.01 and X_{Mg} = 0.89 ± 0.02, respectively), except for the clinopyroxene in run with 50wt%$_{IMA}$, showing X_{Mg} value slightly lower (X_{Mg} = 0.84 ± 0.02). No significant differences in clinopyroxene composition are observed as a function of initial melt amount in terms of Cr_2O_3 and Al_2O_3 contents (***Fig. 3-11a-b***). The run with 25wt%$_{IMA}$ has a slightly higher Na_2O content (Na_2O = 0.47wt% ± 0.22) than ones with 10 and 50wt%$_{IMA}$ (Na_2O = 0.40wt% ± 0.05 and Na_2O = 0.43wt% ± 0.07, respectively) (***Fig. 3-11c***). In particular, TiO_2 content from isothermal experiment with 25wt%$_{IMA}$ is significantly higher than ones with 10 and 50wt%$_{IMA}$ (***Fig. 3-11d***).

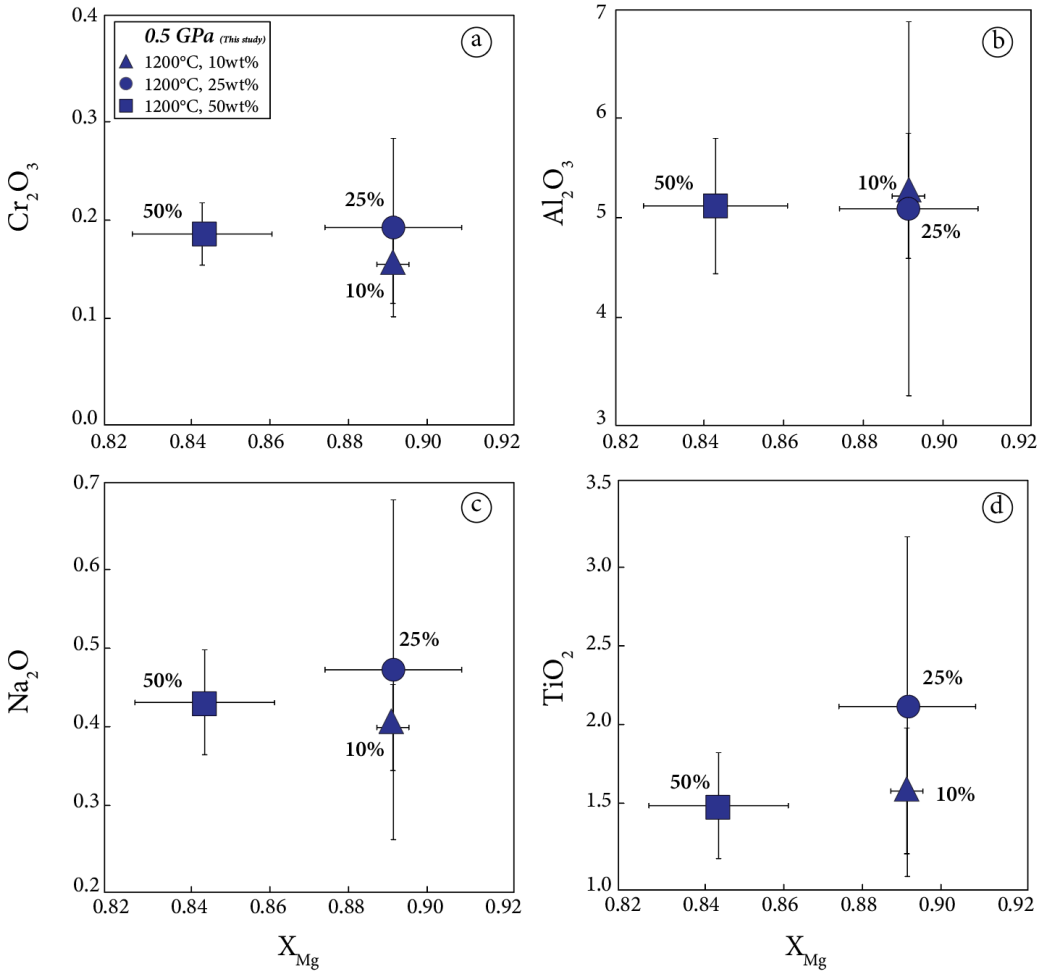

Figure 3-11 *X_{Mg} vs. Cr_2O_3 (a), Al_2O_3 (b), Na_2O (c) and TiO_2 (d) contents (wt%) in clinopyroxene from isothermal experiments performed at 0.5 GPa and 1200°C with different initial melt amount from 10 to 50wt%,*

3.1.2.4 – Glass chemistry

Fig. 3-12 shows the reacted melt compositions in isothermal experiments performed at 0.5 GPa and 1200-1300°C with 10, 25 and 50wt%$_{IMA}$. Overall, the chemistry of the resulted reacted melts is significantly different compared to their initial composition (AH6), as a consequence of reaction with olivine (*e.g.,* olivine dissolution and reprecipitation). In particular:

- At **1200°C**, the reacted melt has low MgO content, compared to the initial melt composition (AH6, MgO = 8.62wt%, X_{Mg} = 0.61). In particular, its value decreases with the increasing of initial melt amount (MgO = 7.21wt% ± 0.91 and MgO = 5.17wt% ± 1.63) for runs with 10 to 50wt% of starting glass, respectively). The glasses have higher SiO_2, Al_2O_3 and Na_2O but lower CaO contents with respect to the initial melt composition. In particular, the experiment with 10wt%$_{IMA}$ has higher SiO_2 content (SiO_2 = 51.69wt% ± 0.28) than ones with 25 and 50wt%$_{IMA}$ (SiO_2 = 48.6wt% ± 0.56 and SiO_2 = 49.28wt% ± 0.34, respectively). The reacted melt in isothermal experiment with 25wt% of initial melt is characterized by higher Al_2O_3 and Na_2O content (Al_2O_3 = 17.46wt% ± 0.50 and Na_2O = 5.24wt% ± 0.12) with respect both the 10wt%$_{IMA}$ (Al_2O_3 = 16.70wt% ± 0.42 and Na_2O = 2.84wt% ± 0.18) and 50wt%$_{IMA}$ (Al_2O_3 = 16.86wt% ± 1.15 and Na_2O = 3.38wt% ± 0.08). On the contrary, the run with 25wt%$_{IMA}$ has lower CaO content (CaO = 8.02wt% ± 0.20) than experiments with 10wt%$_{IMA}$ (CaO = 11.96wt% ± 0.34) and 50wt%$_{IMA}$ (CaO = 12.39wt% ± 0.28) (***Fig. 3-12***). The NiO content in reacted melts at 1200°C increases compared to the initial melt composition (AH6, NiO = 0.00wt%) but its variation is not correlated to the different initial melt amount from 10 to 50wt% (see ***Tab. 3-2d*** and ***Fig. 3-13***).
- At **1250°C**, the isothermal experiment performed with 50wt%$_{IMA}$ has glass MgO content (MgO = 11.62wt% ± 1.23) comparable with that observed in run at 1300°C with 50wt%$_{IMA}$. Compared to the initial composition, the reacted melt at 1250°C results in higher SiO_2 content (48.73wt% ± 0.32) but lower Al_2O_3 (15.47wt% ± 0.46), Na_2O (2.10wt% ± 0.13) and CaO contents (12.97wt% ± 0.48) (***Fig. 3-12***). The NiO content in reacted melt is 0.01wt% ± 0.02 (see ***Tab. 3-2d*** and ***Fig. 3-13***).
- At **1300°C**, the reaction between olivine and melt increased the MgO content of the final glass that varies from 8.59wt% to 12.20wt%. This MgO increase is also correlated to the increasing of initial melt amount from 10 to 50wt% (MgO = 8.59wt% ± 2.34 and 12.20wt% ± 1.71, respectively). Compared to the initial melt composition, the reacted melt in run with 10wt%$_{IMA}$ has higher SiO_2 content (49.53wt% ± 0.50) but lower Al_2O_3 (14.37wt% ± 1.02), Na_2O (1.97wt%

± 0.33) and CaO contents (12.86wt% ± 0.66). Comparing the two different set of experiments performed at 1200 and 1300°C, the latter results enriched in MgO and CaO contents but depleted in SiO_2, Al_2O_3 and Na_2O (***Fig. 3-12***). The reaction between olivine and melt also results in higher NiO content than the initial melt composition. In particular, the NiO content increases proportionally to the initial melt amount (NiO = 0.01wt% ± 0.01 and NiO = 0.01wt% ± 0.02 for 10 and 50wt% of initial glass, respectively). At 1300°C, the reacted melts have higher NiO content than experiments carried out at 1200°C (see ***Tab. 3-2d*** and ***Fig. 3-13***).

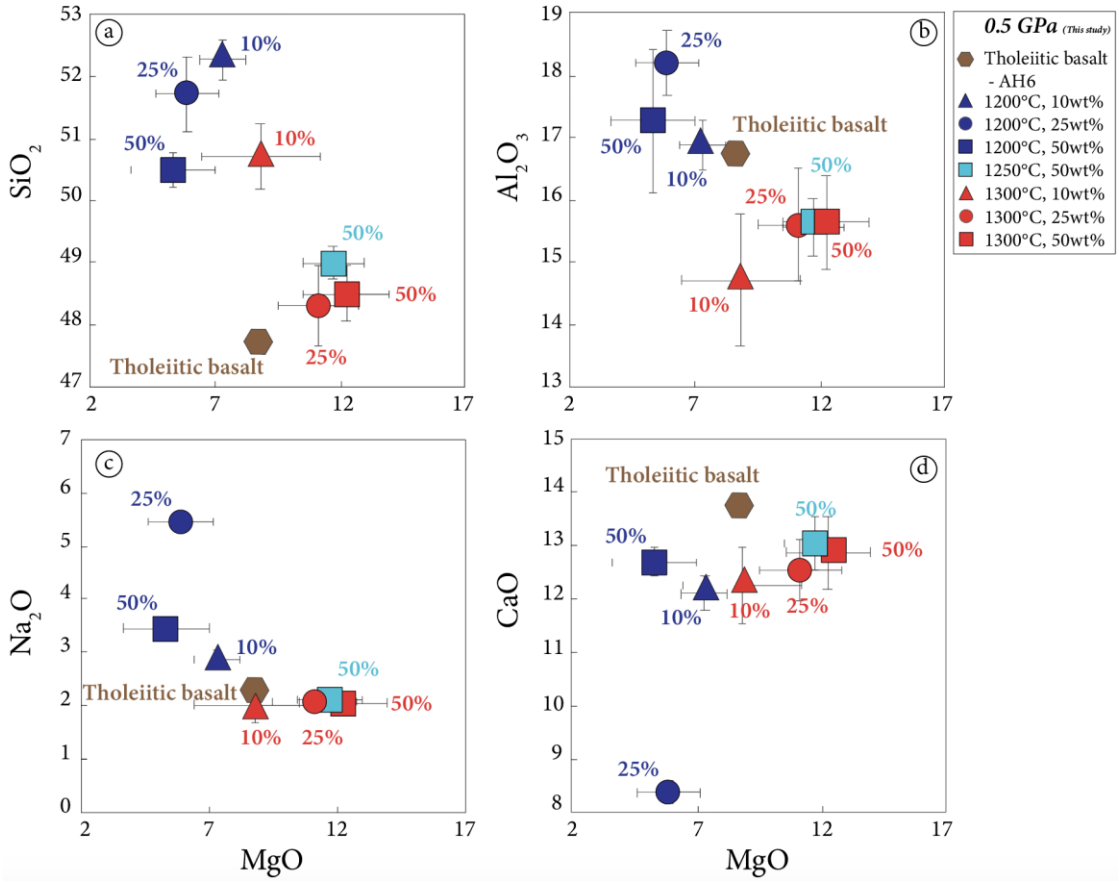

Figure 3-12 *MgO vs. SiO_2 (a), Al_2O_3 (b), Na_2O (c) and CaO (d) content in reacted melts from isothermal experiments performed at 0.5 GPa and1200,1250 and 1300°C with different initial melt amount from 10 o 50wt%. In the diagrams, the chemical compositions of reacted melts were normalized to 100%.*

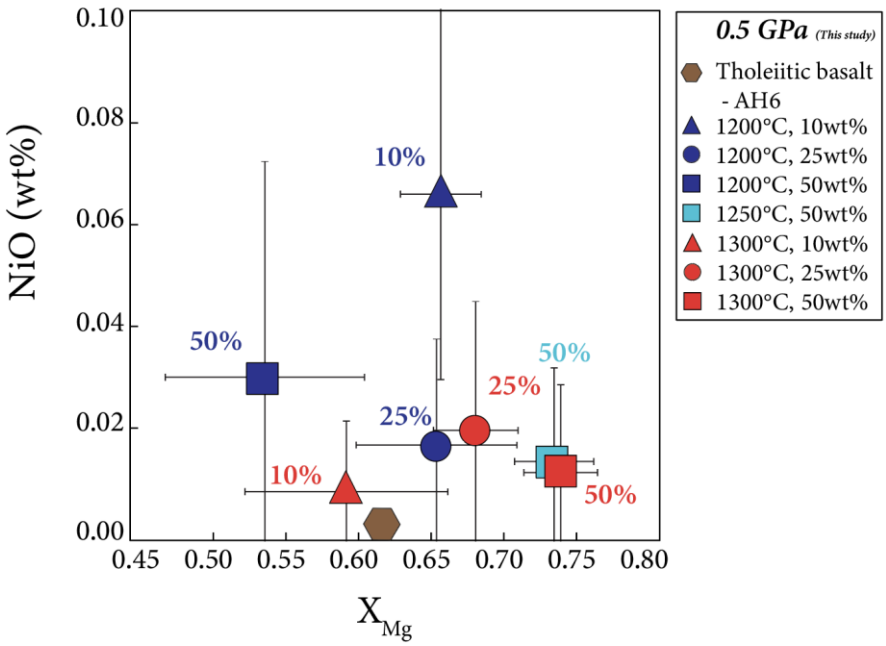

Figure 3-13 *X_{Mg} vs. NiO content (wt%) in reacted melts from reaction experiments performed at 0.5 GPa and T from 1200 to 1300°C with different initial melt amount from 10 to 50wt%.*

3.1.3 – Textural analysis of olivine grains – EBSD analysis

In order to understand how the olivine texture has been affected by *T* and different initial melt amount during the reaction, a detailed study of textures through EBSD analysis has been performed at the Platform of Microscopy of the University of Milano-Bicocca. ***Figs. 3-14, 3-15*** and ***3-16*** show the Phase maps and the Inverse Pole Figures (IPF) for each reaction experiments (except for MG18, details are discussed below): the different colors in IPF maps suggest that the reacted olivine grains are not preferred oriented. In particular, the MTEX toolbox was also useful to define quantitatively geometrical factors (*e.g.*, Equivalent diameter, Grain Area, Aspect Ratio, Shape Factor and PARIS Factor) and deformation parameters (*e.g.*, GOS, Mis2Mean and KAM) (details in **Chapter 2** and ***Tab. 3-3***). Because of the *T* oscillation during the experimental procedure, the MG18 will not be considered for the textural and deformation evaluation. For this reason, the OM23 will be considered (Francomme, J. E., 2016-2017), due to its reliability in terms of EBSD analysis. ***Tab. 3-4*** reports the summary of geometrical factors as average values for each experiment performed at *T* from 1200 to 1300°C with different IMA considering all classes of grain size. They will be discussed in details in **Sections 3.1.3.1** and **3.1.3.2**.

PARAMETERS	DESCRIPTION
Equivalent diameter (µm)	It is the longest distance between any two vertices of the boundary.
Grain Area (μm^2)	It is the area of a grain.
Aspect Ratio	Defines the elongation of a grain and corresponds to the ratio between the length (long axis) and the width (short axis).
Shape Factor	Defines the roundness of a grain and is calculated by the ratio between the perimeter of a grain and its equivalent perimeter.
PARIS Factor	Defines the grain boundary labateness and it is defined by the comparison between the perimeter of the grain and its smallest envelope.
GOS	Defines an average intragranular deformation of a grain and the spread is the average deviation between the orientation of each point in the grain and the average orientation for the grain.
KAM	It is a measure of the average misorientation of a point (pixel) with respect to a selected number of its nearest neighbours.
Mis2Mean	A single point is a function of the misorientation between each pixel orientation to the grain mean orientation

Table 3-3 *Summary of geometrical factors (e.g., Equivalent diameter, Grain Area, Aspect ratio, Shape Factor and PARIS Factor,) and intra-granular deformation parameters (e.g., GOS, Mis2Mean and KAM).*

Run		Initial melt amount (wt%)	Grain area (micron^2)	σ[b]	Equivalent diameter (micron)	σ	Aspect Ratio	σ	Shape Factor	σ	PARIS Factor (%)	σ
Isothermal at 1200°C	MG10	10	1819.64	1541.28	43.02	22.31	1.47	0.12	1.31	0.11	26.29	16.03
	MG12	25	1065.77	882.82	33.18	16.72	1.74	0.13	1.30	0.07	17.69	6.92
	MG14	50	1208.76	1153.87	34.70	19.16	1.64	0.22	1.35	0.13	28.78	27.15
Isothermal at 1250°C	MG11	50	2748.64	2239.69	53.44	26.13	1.63	0.20	1.25	0.11	14.42	9.93
Isothermal at 1300°C	OM23[a]	9	2728.43	2801.75	51.16	30.15	1.55	0.13	1.40	0.16	37.80	20.08
	MG1	25	2709.37	2155.76	53.37	25.24	1.42	0.05	1.19	0.05	7.75	4.56
	MG5	50	2896.60	2481.49	54.53	27.58	1.50	0.12	1.34	0.10	30.30	13.49

Table 3-4 *Summary of geometrical factors of the reaction experiments performed at 0.5 GPa and temperature from 1200 to 1300°C with different initial melt amount (10, 25 and 50wt%) considering all grain size classes.* [a] *Reaction experiment from PhD Thesis of Francomme, J. E. (2016-2017).* [b] *σ = standard deviation.*

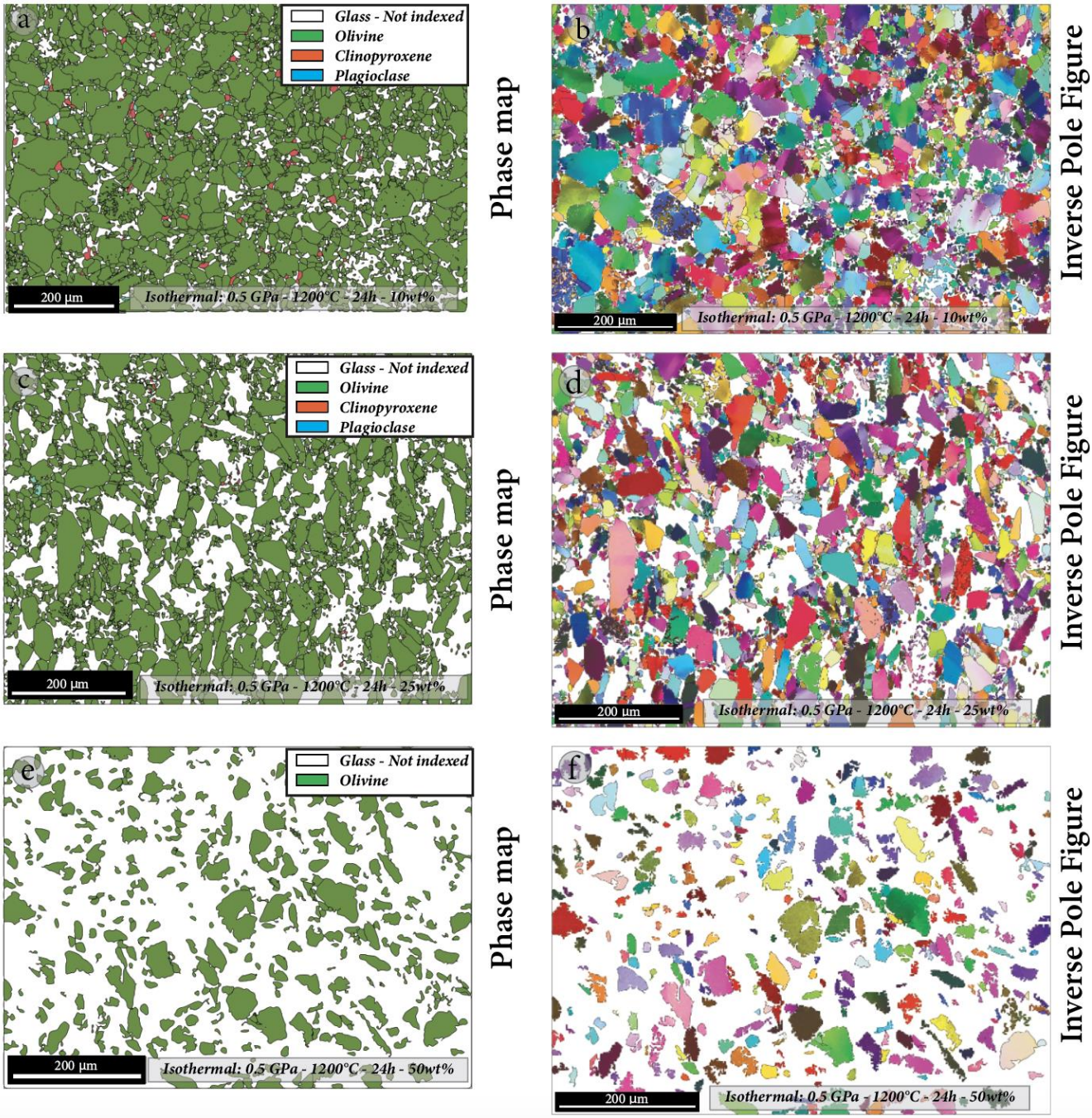

Figure 3-14 *Phase maps and IPF maps for each isothermal experiment performed at 1200°C with 10wt% (a-b), 25wt% (c-d) and 50wt% of initial melt (e-f).*

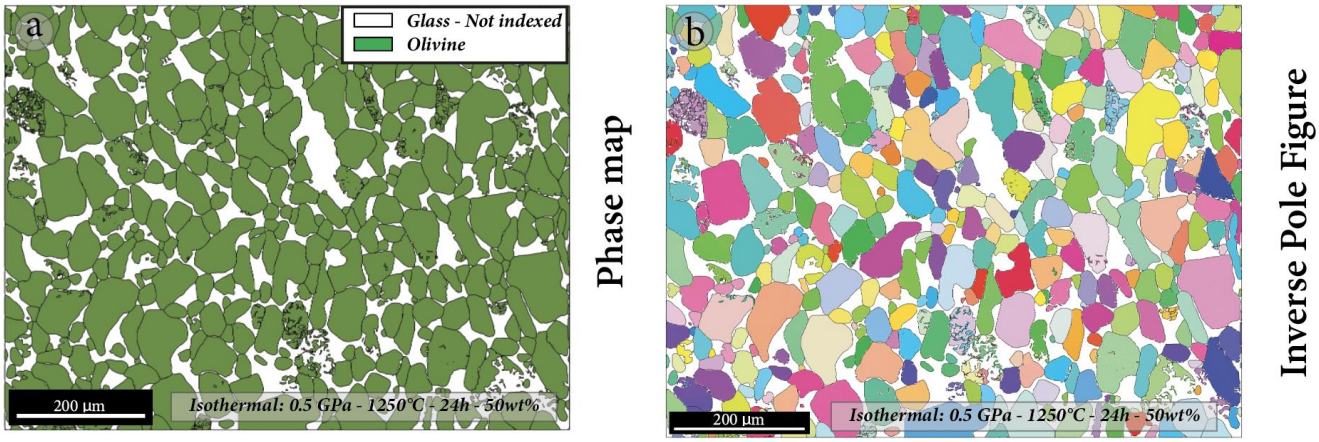

Figure 3-15 *Phase maps and IPF maps for each isothermal experiment performed at 1250°C with 50wt% of initial melt (a-b).*

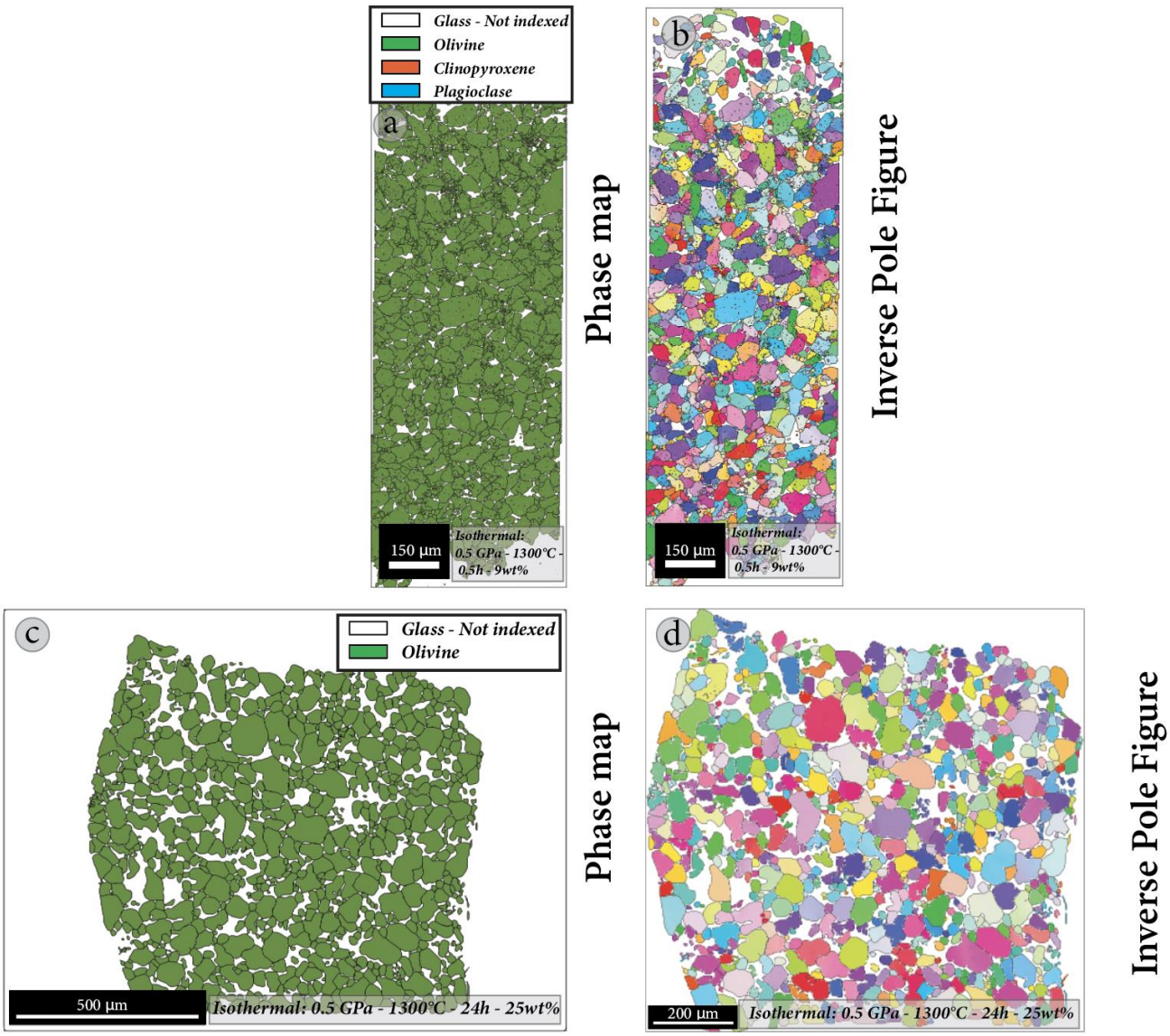

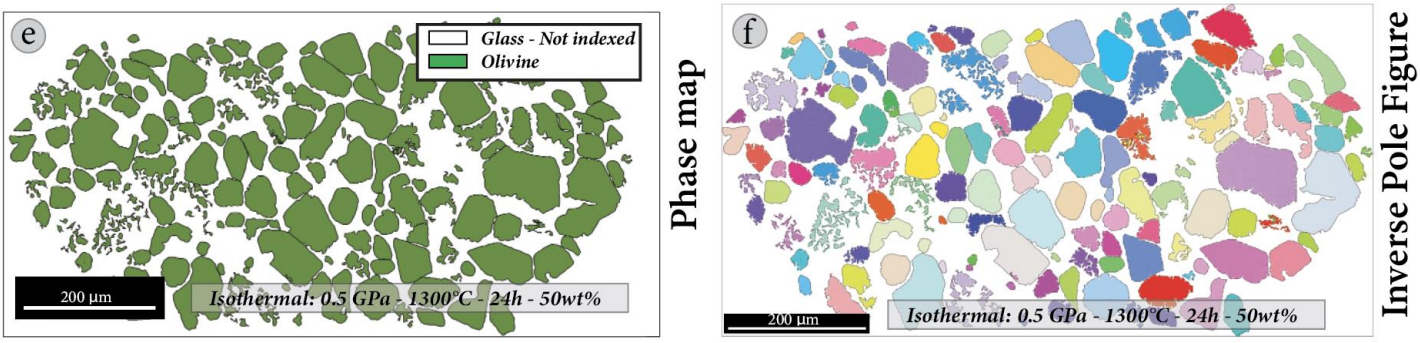

Figure 3-16 *Phase maps and IPF maps for each isothermal experiment performed at 1300°C with 9wt%(a-b) (from Francomme PhD thesis, 2016-2017), 25wt% (c-d) and 50wt% of initial melt (e-f).*

3.1.3.1 – Olivine geometrical parameters and temperature

The aim of this section is to evaluate the role of temperature in the development of olivine textures in terms of geometrical factors, comparing experiments performed at 1200, 1250 and 1300°C. The grain size will not be discussed in this section but in details in **Section 3.1.3.2.** All of geometrical parameters are firstly represented as an EBSD map and then defined quantitatively in diagrams, while the PARIS Factor is represented only through a diagram. The EBSD maps shown in the present thesis are mainly characterized by olivine grains: white colour indicates non-indexed portion (*e.g.*, glass or other not considered mineral phases) and some olivine grain non-indexed because of poor local surface quality caused by defects not eliminated during the polishing procedure.

The two geometrical parameters that describe the grain dimension are the **Equivalent diameter (µm)** and the **Grain Area (µm^2)** (defined in **Chapter 2** and ***Tab. 3-3***). In the color-codes map, blue represents the smallest grains whereas yellow the largest. At first, these parameters are related with the **Aspect Ratio**, which defines the elongation of a grain and corresponds to the ratio between the length (long axis) and the width (short axis). In this case, the color-codes varies from blue to yellow (1 to 5, respectively), in order to represent the least elongated grain and the most elongated grain (***Figs. 3-17, 3-18 and 3-19***). Considering the investigated temperature range, the reaction at lower temperature (1200°C) results in more elongated grains than those at higher temperature (1250-1300°C) (***Fig. 3-20a-b***). On the other hand, at 1250 and 1300°C, no differences were observed between larger and smaller grains in terms of elongation.

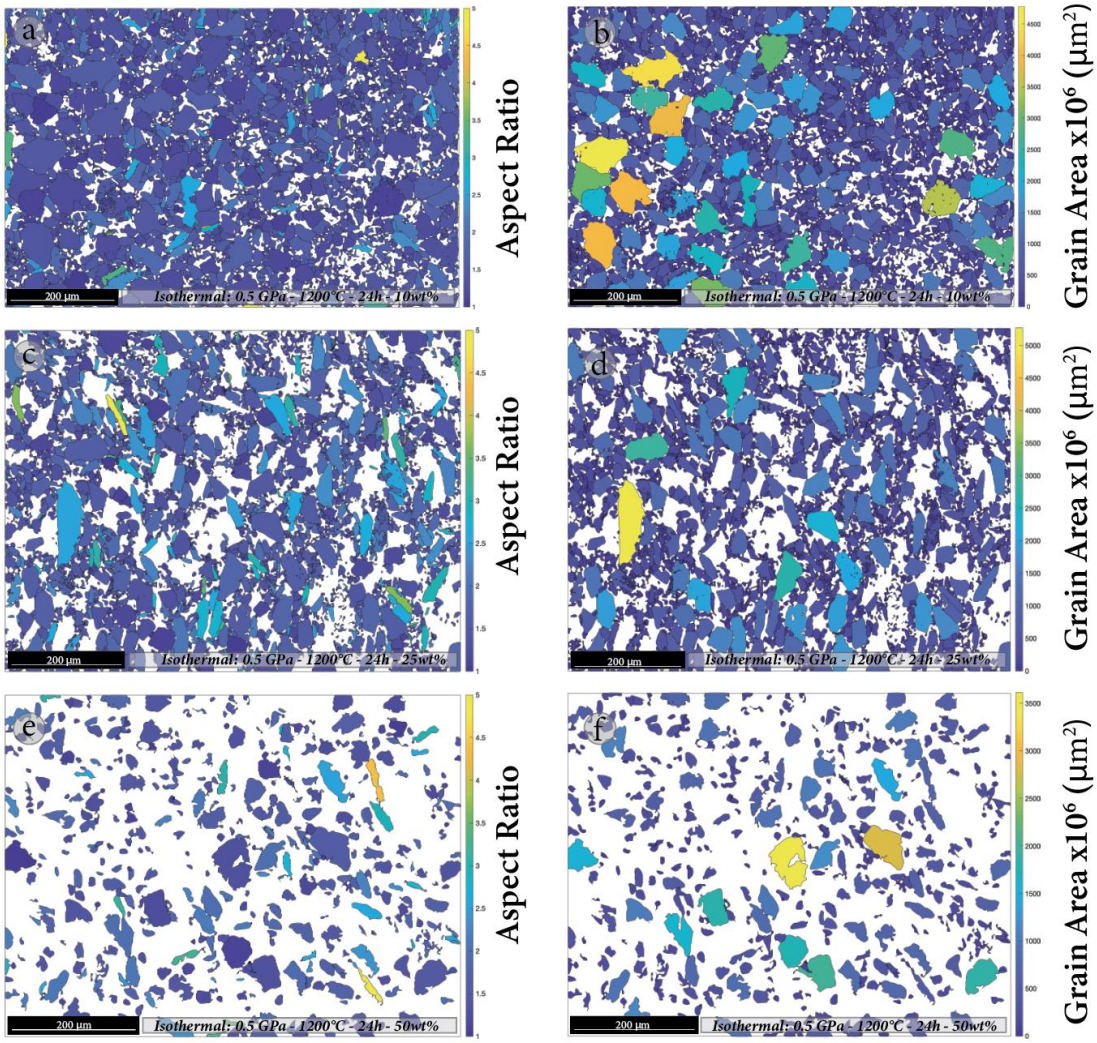

Figure 3-17 *EBSD maps representative of Aspect Ratio and Grain Area for each isothermal experiment performed at 1200°C with 10wt% (a-b), 25wt% (c-d) and 50wt% of initial melt (e-f).*

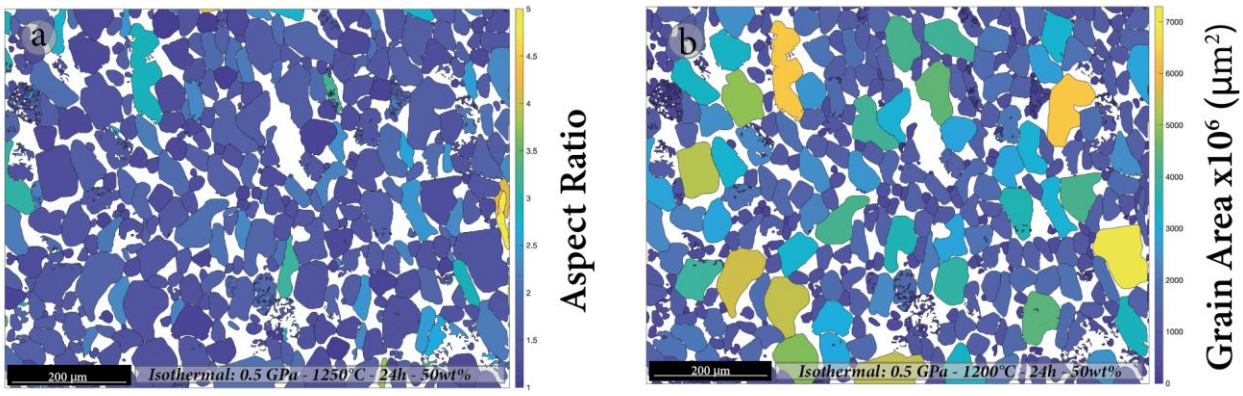

Figure 3-18 *EBSD maps representative of Aspect Ratio (a) and Grain Area (b) for the isothermal experiment performed at 1250°C with 50wt% of initial melt.*

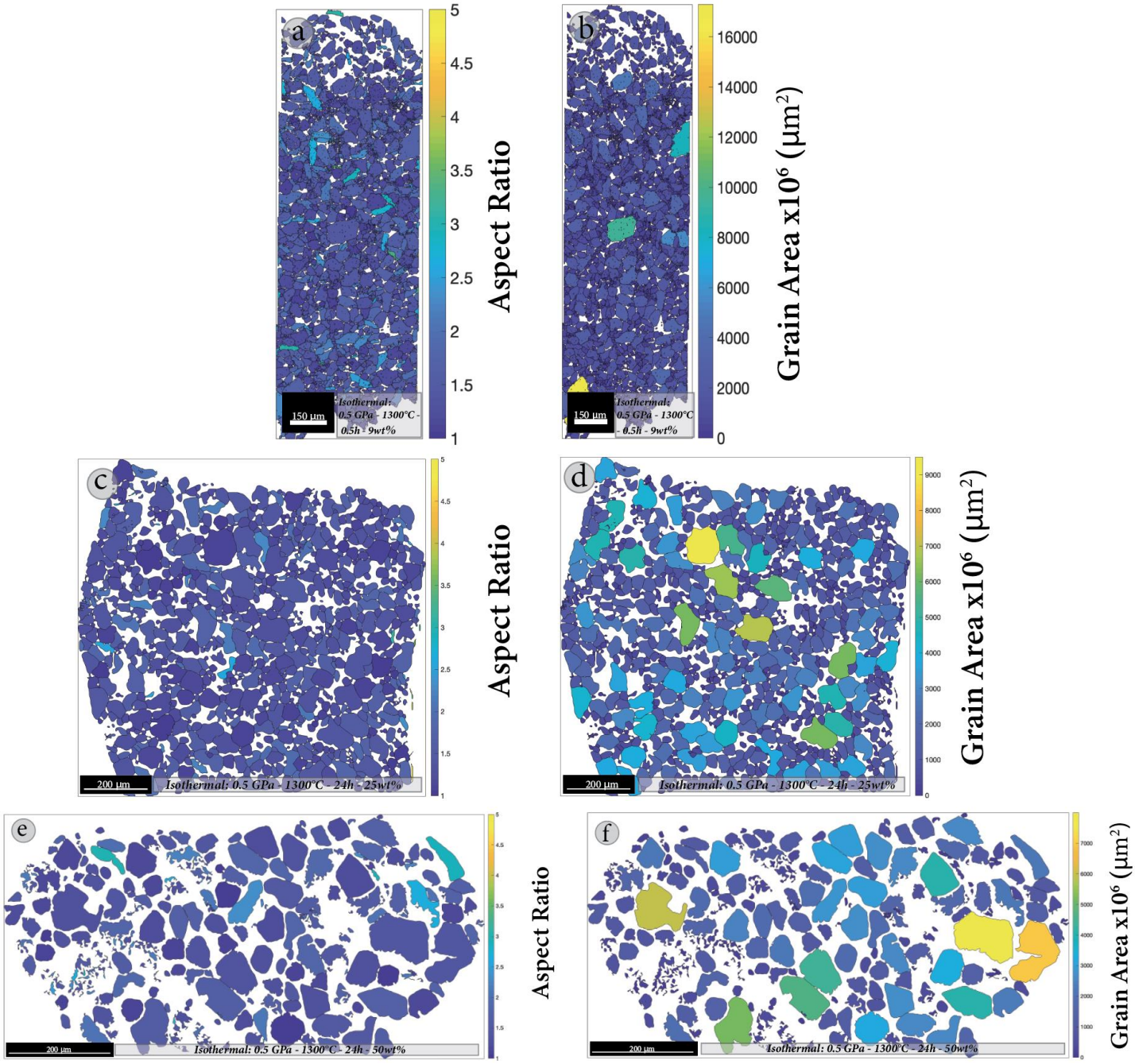

Figure 3-19 *EBSD maps representative of Aspect Ratio and Grain Area for each isothermal experiment performed at 1300°C with 9wt%(a-b) (from Francomme PhD thesis, 2016-2017), 25wt% (c-d) and 50wt% of initial melt (e-f).*

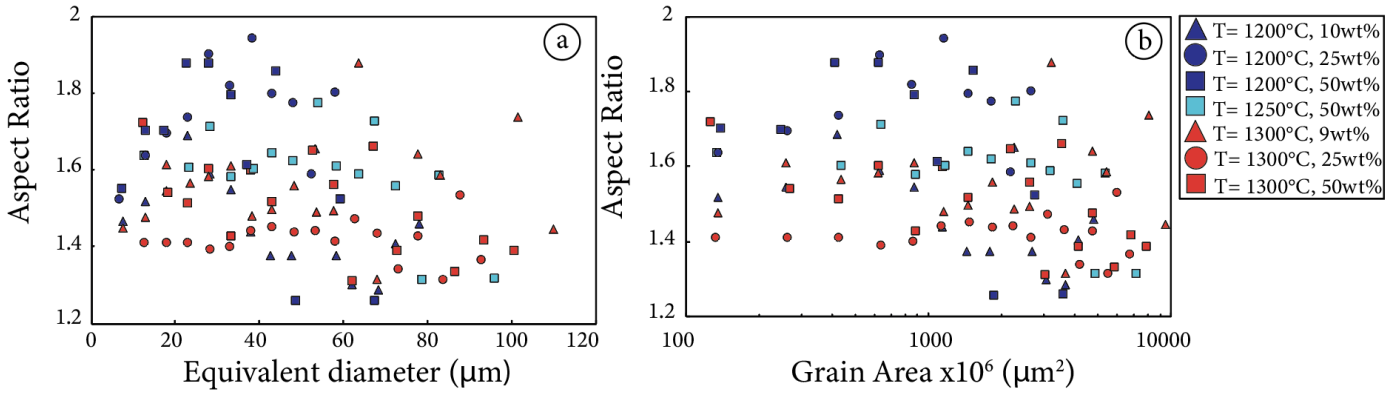

Figure 3-20 *(a) Aspect Ratio vs. Equivalent diameter (µm) and (b) Aspect Ratio vs. Grain Area (µm²) of reaction experiments performed at 0.5 GPa and 1200 to 1300°C with different initial melt amount.*

The Shape Factor and the PARIS Factor also describe the geometrical morphology of olivine**.** The sample maps are shown in ***Figs. 3-21, 3-22*** and ***3-23***. Blue and yellow indicate respectively low and high Shape Factor values that are numerically reported in diagram comparing them to the Equivalent diameter and the Grain Area (***Fig. 3-24a-b***). By contrast, the PARIS Factor defines the grain boundary lobateness (*i.e.*, the tortuosity of grain boundaries) and it is quantitatively defined and reported in a graphic *versus* the Equivalent diameter and the Grain Area (***Fig. 3-24c-d***). Independently to the grains size, the experiments at higher temperature (1250-1300°C) result in slightly more tortuous and less rounded grains than those at lower temperature (1200°C) (***Fig. 3-24***).

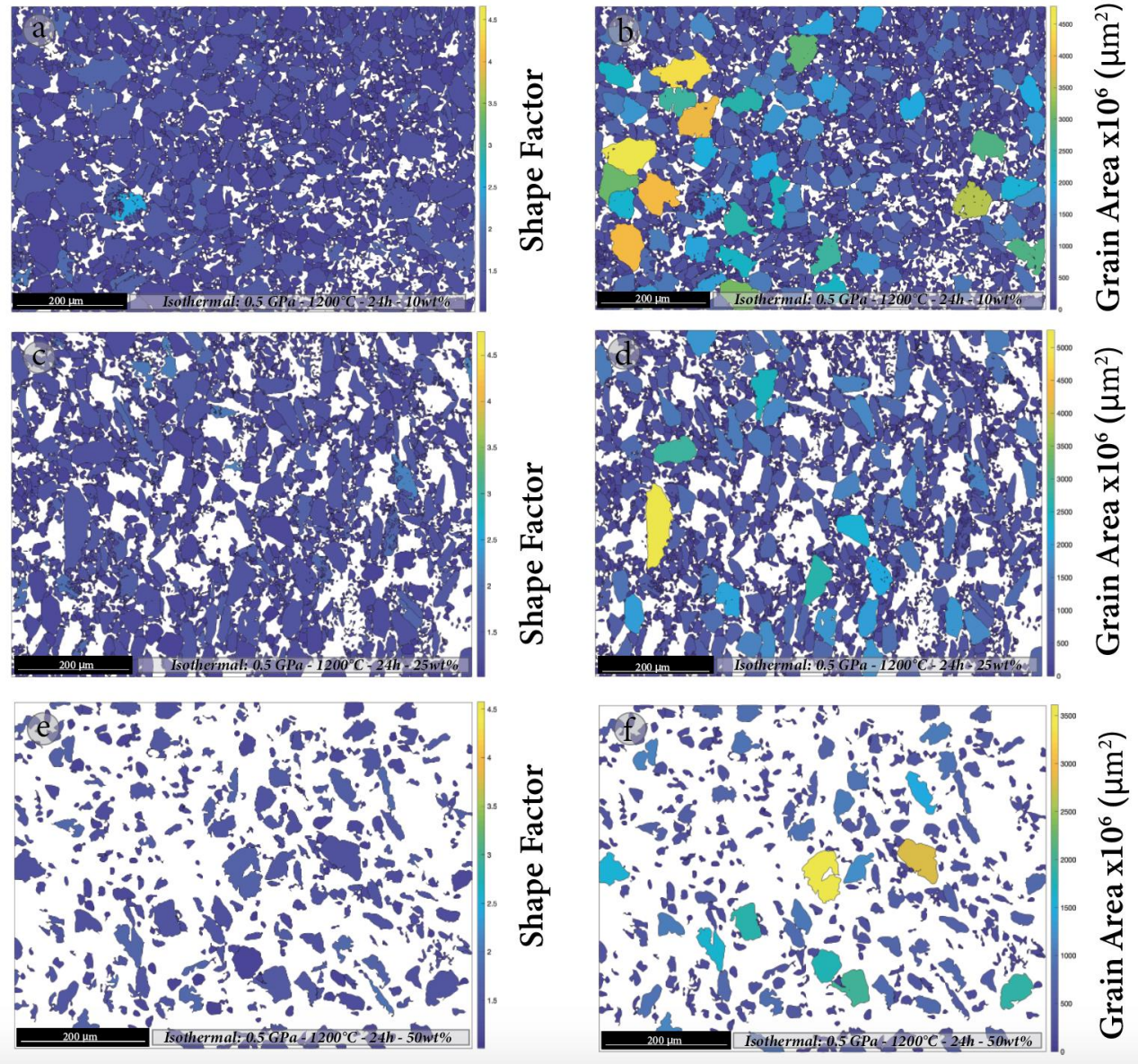

Figure 3-21 *EBSD maps representative of Shape Factor and Grain Area for each isothermal experiment performed at 1200°C with 10wt% (a-b), 25wt% (c-d) and 50wt% of initial melt (e-f).*

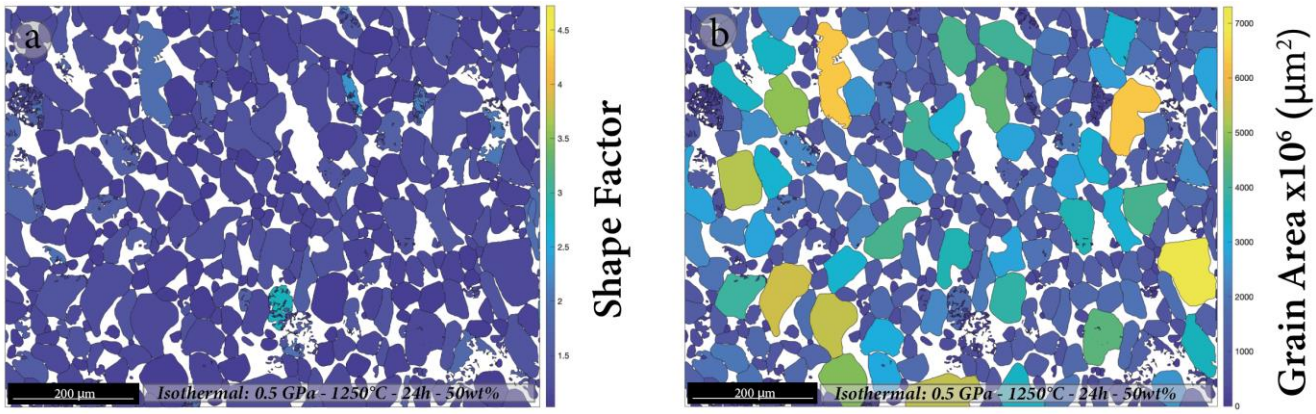

Figure 3-22 *EBSD maps representative of Shape Factor (a) and Grain Area (b) for the isothermal experiment performed at 1250°C with 50wt% of initial melt.*

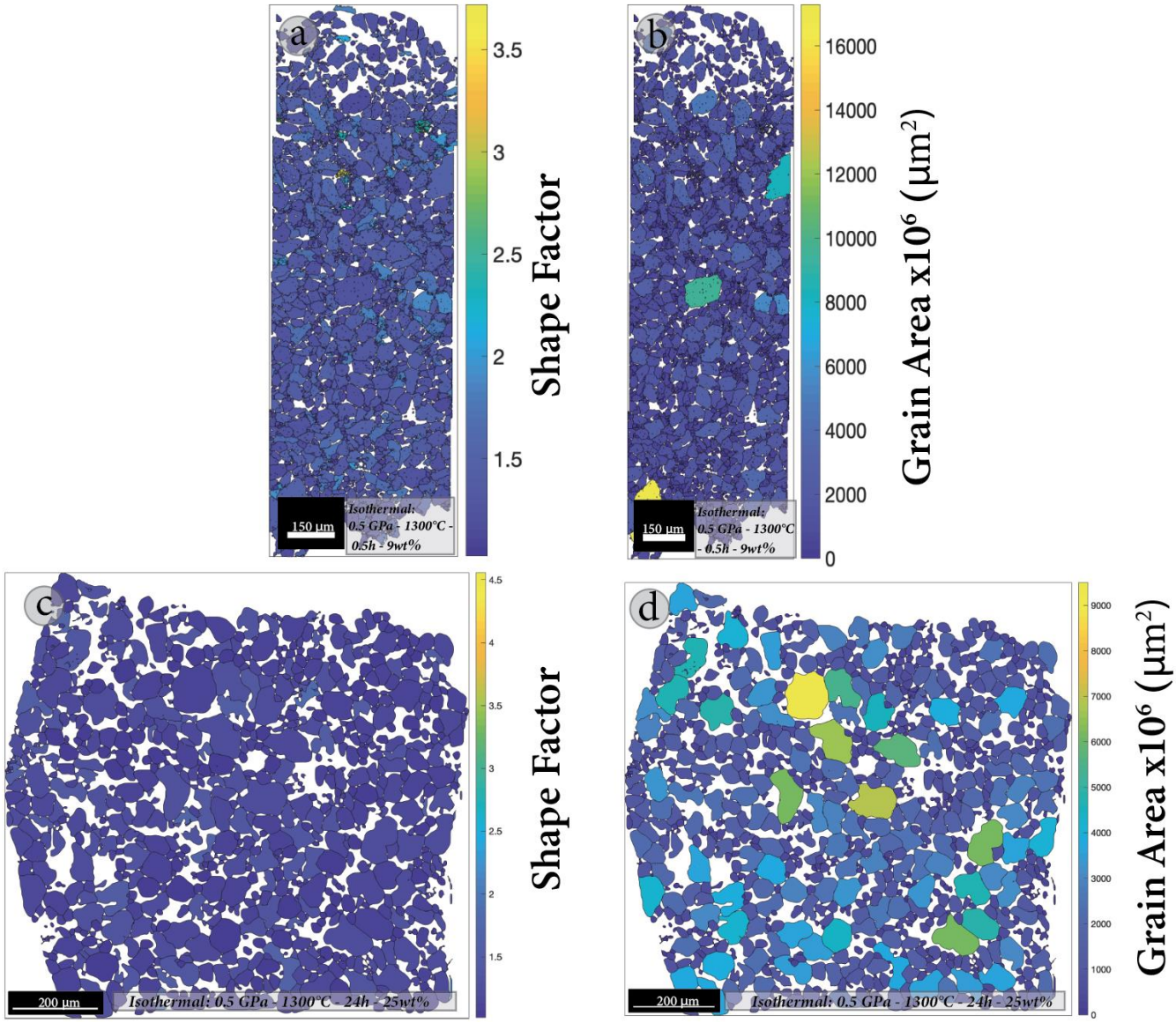

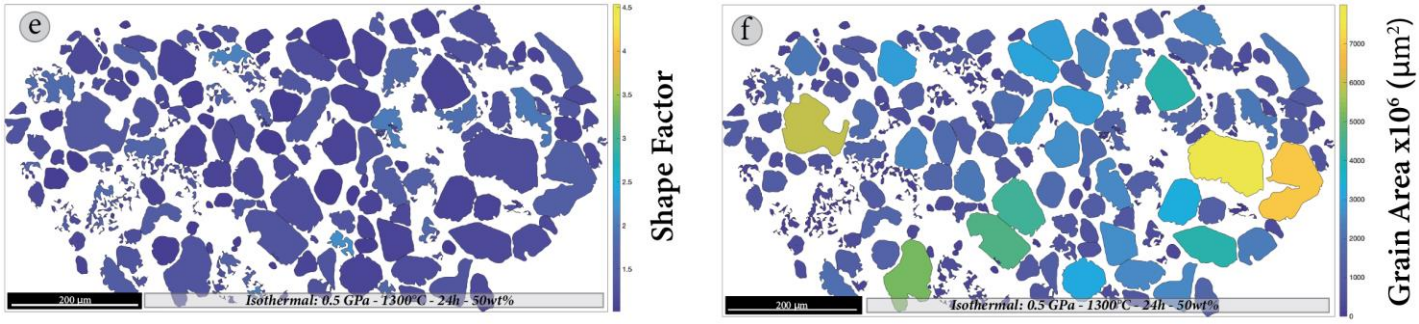

Figure 3-23 *EBSD maps representative of Shape Factor and Grain Area for each isothermal experiment performed at 1300°C with 9wt% (a-b) (from Francomme PhD thesis, 2016-2017), 25wt% (c-d) and 50wt% of initial melt (e-f).*

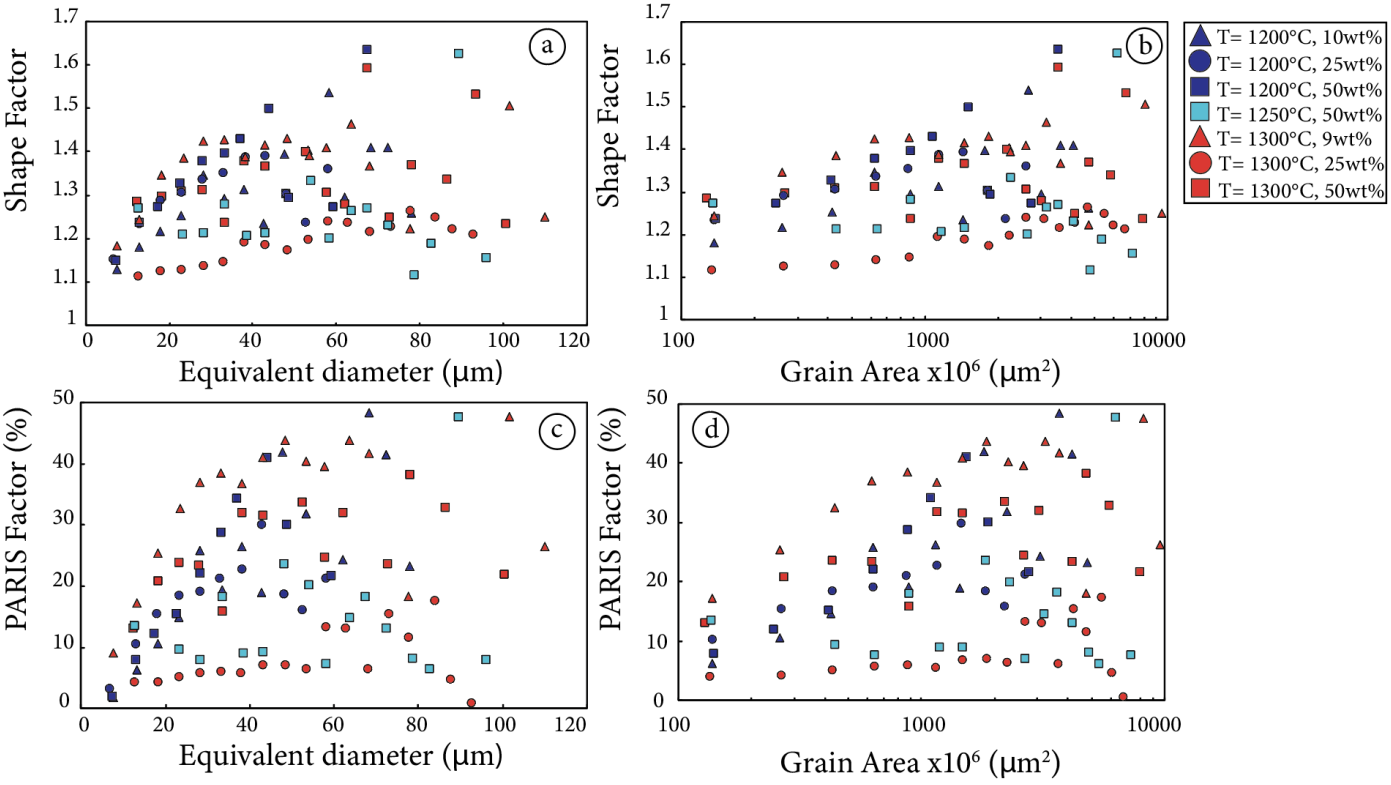

Figure 3-24 *Shape Factor and PARIS Factor vs. Equivalent diameter (µm) (a-c) and vs. Grain Area (µm²) (b-d) of reaction experiments performed at 0.5 GPa and temperature from 1200 to 1300°C with different initial melt amount.*

3.1.3.2 – Olivine geometrical parameters and initial melt amount (IMA)

The aim of this section is to show how different initial melt amounts (10, 25 and 50wt%) affect the olivine texture in terms of grain size (*e.g.*, Equivalent diameter and Grain Area) and geometrical factors such as, Aspect Ratio, Shape Factor and PARIS Factor, obtained through the EBSD analysis. The olivine textural development will be discussed selecting experiments at 1200°C and 1300°C, in order to exclude the effect of *T*. At this purpose, each experiment was studied by defining a series of grain size (in terms of Equivalent diameter) classes from 5-10 µm to 105-110 µm. The complete textural dataset of textural data for each classes of the reaction experiments, is given in ***Tab. 7-10, 7-11, 7-12, 7-13, 7-14, 7-15-, 7-16*** **(in Appendix)**.

At 1200°C, the average value of **Aspect Ratio** (elongation of a grain) increases from 1.47 ± 0.12 to 1.64 ± 0.22 with the increasing of initial melt amount from 10 to 50wt%, although it is as high as 1.74 ± 0.13 in the run with 25wt%$_{IMA}$. The olivine grains in the reaction experiments performed with high initial melt (25 and 50wt%), generally tend to display grains larger and more elongated with respect to those observed in the experiment with 10wt%$_{IMA}$ (***Fig. 3-25a-b***).

At 1300°C, the Aspect Ratio values is almost constant varying from 1.55 ± 0.13 to 1.50 ± 0.12 with the increase of initial melt amount from 10 to 50wt%. In this case, at 1300°C the reaction does not result in relevant differences in terms of elongation between smaller and larger grains as a function of different initial melt amounts (***Fig. 3-25c-d***).

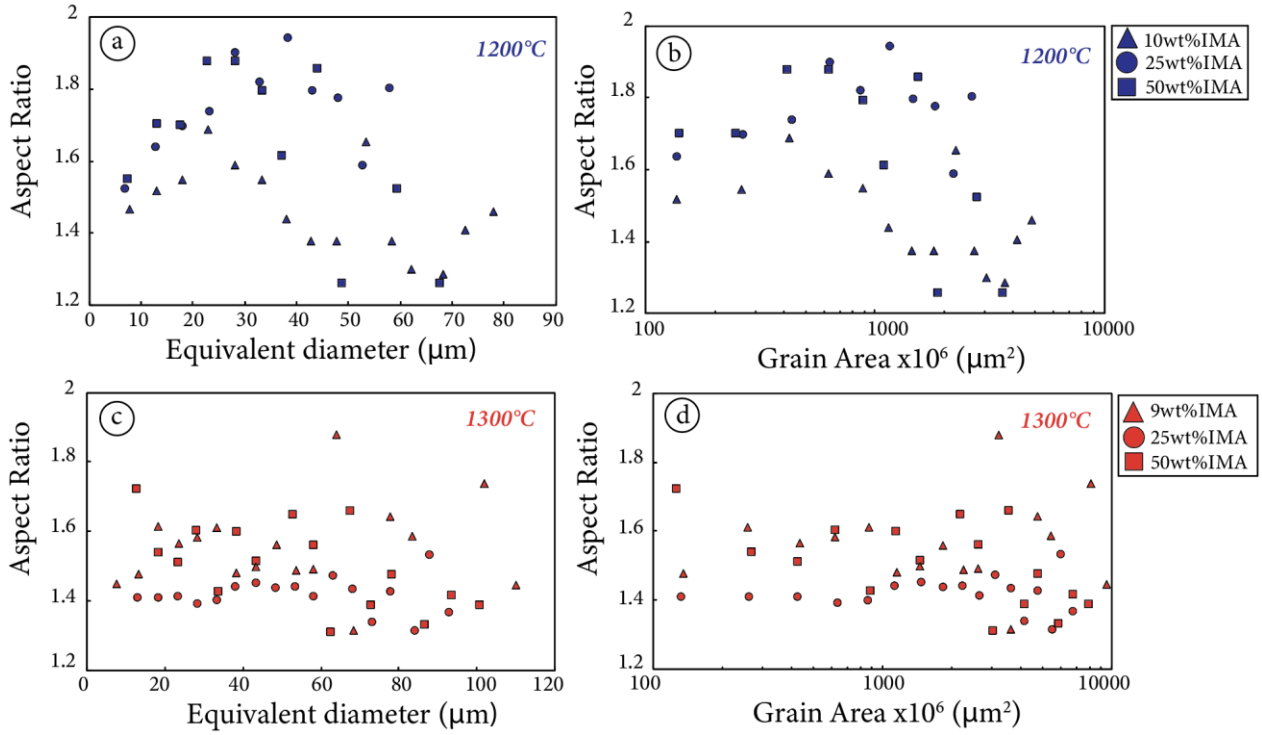

Figure 3-25 *Aspect Ratio vs. Equivalent diameter (µm) and vs. Grain Area (µm²) of reaction experiments performed at 0.5 GPa and temperature of 1200 °C (a-b) and 1300°C (c-d) with different initial melt amount.*

As mentioned above, **Shape Factor** and **PARIS Factor are** two important geometrical parameters that describe the roundness and the tortuosity of grains, respectively. BSE images allows to distinguish, especially at 1300°C, two different olivine morphologies: i) large subhedral crystals (up to 100 µm) with both straight and lobate rims (***Fig. 3-26b***) and ii) smaller and rounded grains (5-20 µm) (***Fig. 3-26c***).

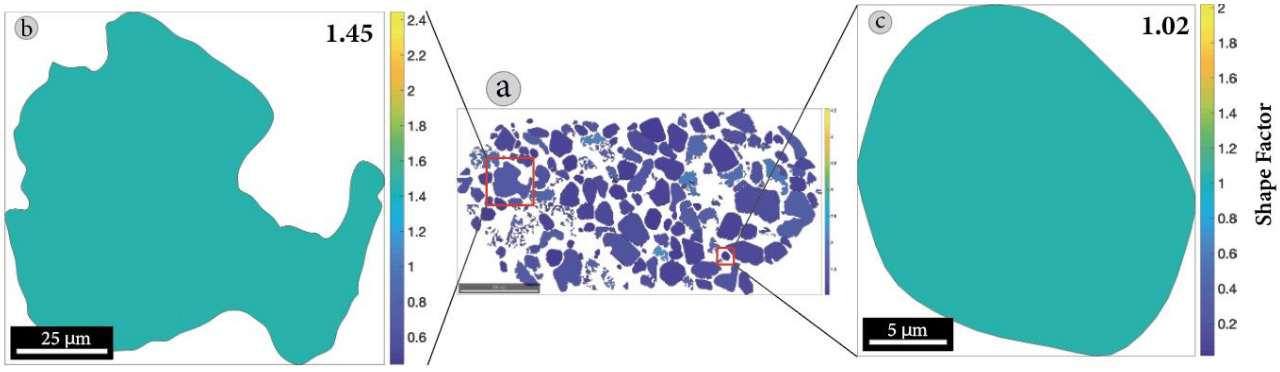

Figure 3-26 *(a) Shape Factor map with details of (b) large subhedral crystals (~87 µm) with both straight and lobate rims and (c) smaller and rounded grains (21 µm) in reaction experiment performed at 0.5 GPa and 1300°C with 50wt% of initial melt amount.*

At 1200°C, the products obtained in the experiment with 50%$_{IMA}$ have a slightly higher Shape Factor values (1.35 ± 0.13 *vs* 1.31 ± 0.11 of the experiment with an initial melt amount of 10wt%). This is also paired with an increase of the PARIS Factor value (26.29 ± 16.03$_{10wt\%IMA}$ to 28.78 ± 27.15$_{50wt\%IMA}$). Both parameters are slightly lower in the experiment performed with 25wt%$_{IMA}$ (Shape Factor = 1.30 ± 0.07 and PARIS Factor = 17.69 ± 6.92). Therefore, the larger grains result in higher values of Shape Factor and PARIS Factor independently of the initial melt amount (***Fig. 3-27a-b-c-d***).

At 1300°C, the Shape Factor value varies from 1.40 ± 0.16 (in the sample with 10wt%$_{IMA}$) to 1.34 ± 0.10 (50wt%$_{IMA}$), and the PARIS Factor ranges from 37.80 ± 20.08 (in the sample with 10wt%$_{IMA}$) to 30.30 ± 13.49 (50wt%$_{IMA}$). Also in this case, the larger grains are characterized by higher value of Shape Factor (*i.e.*, lower grade of roundness) and PARIS Factor (*i.e.*, higher tortuosity), independently of the different melt amount (***Fig. 3-28a-b-c-d***).

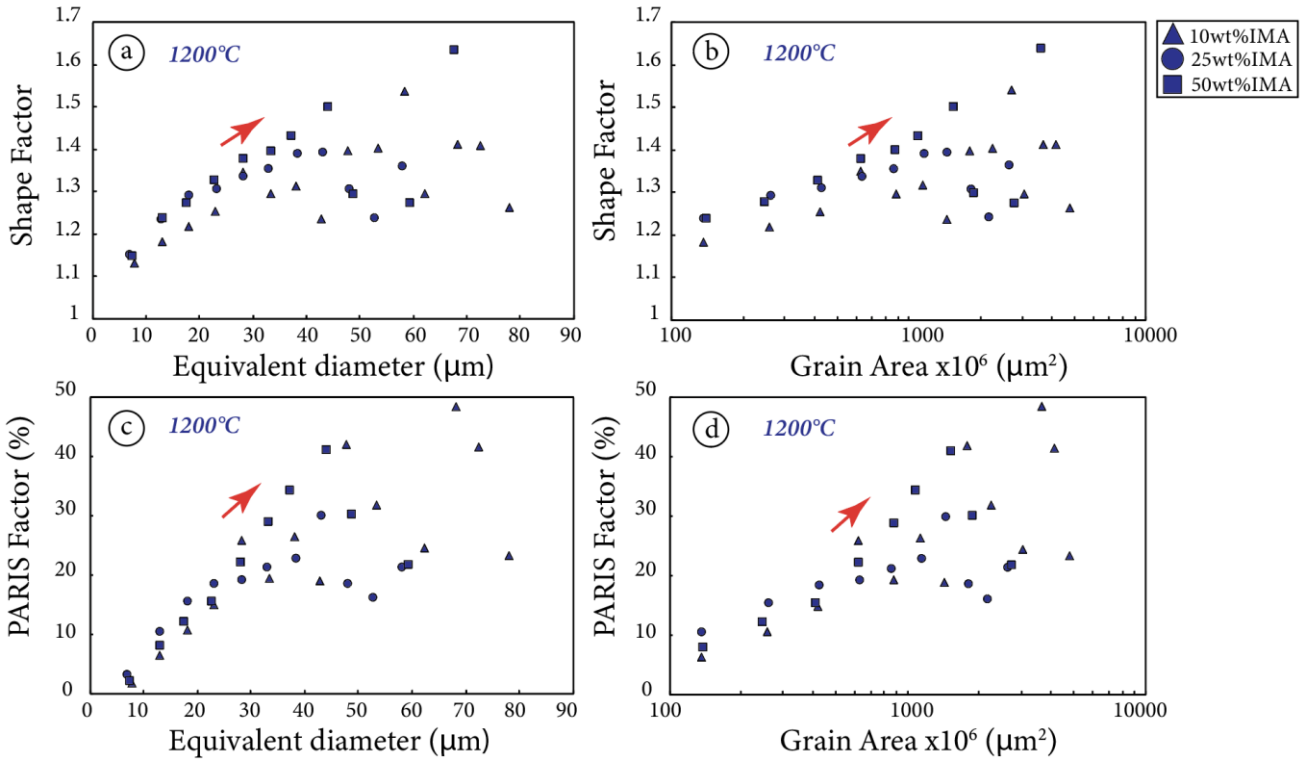

Figure 3-27 *Shape Factor and PARIS Factor vs. Equivalent diameter (µm) (a-c) and Grain Area (µm²) (b-d) of reaction experiments performed at 0.5 GPa and temperature of 1200 °C with different initial melt amount. The red arrows indicate the increasing trend of Shape Factor and PARIS Factor with the increase of the grain size.*

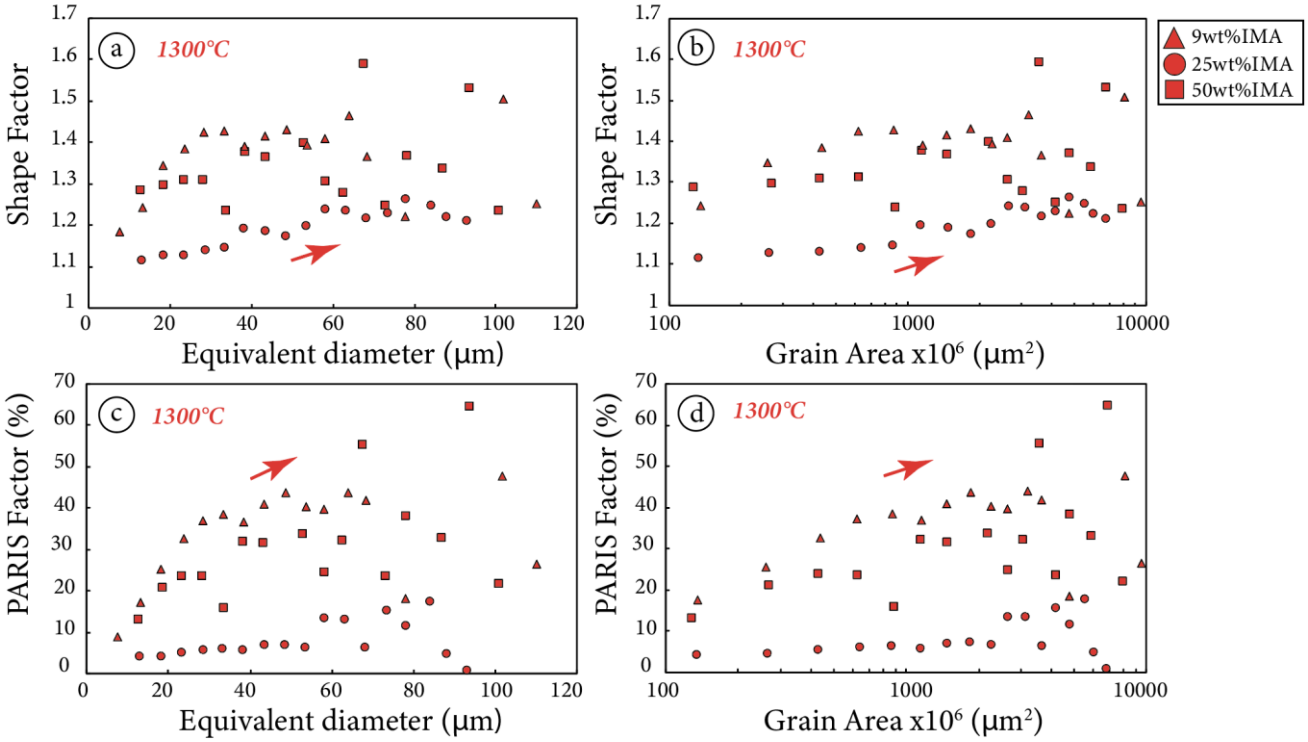

Figure 3-28 *Shape Factor and PARIS Factor vs. Equivalent diameter (µm) (a-b) and Grain Area (µm²) (c-d) of reaction experiments performed at 0.5 GPa and temperature of 1300 °C with different initial melt amount. The red arrows indicate the increasing trend of Shape Factor and PARIS Factor with the increase of the grain size.*

Preliminary investigation through BSE images also suggested that with increasing from 10 to 50wt%$_{IMA}$ causing the decrease of total modal olivine (vol%), olivine grain size increases and the amount of smaller rounded grain decreases (***Fig. 3-29***). This trend is more evident in the experiments performed at 1300°C. EBSD data processing through MTEX toolbox provided a quantification of the number of smaller grains (5-20 µm) for each experiment (***Tab. 3-5***). The elaborated data allowed to confirm and quantify the preliminary investigations through BSE images (***Tab. 3-5***).

	Run	Initial melt amount (wt%)	N° small grains (5-20 µm)	Tot grains	%	Modal olivine (vol%)
Isothermal at 1200°C	MG10	10	1447	1702	85	92
	MG12	25	1512	1708	89	76
	MG14	50	341	417	82	58
Isothermal at 1250°C	MG11	50	119	399	30	47
Isothermal at 1300°C	OM23[a]	10	1081	1597	68	89
	MG1	25	546	1380	40	73
	MG5	50	103	349	30	45

Table 3-5 *Number of small grains (5-20 µm) of olivine for each reaction experiment performed at 1200 to 1300°C (P = 0.5 GPa) with different initial melt amount. [a] Reaction experiment from the PhD Thesis of Francomme, J. E., (2016-2017).*

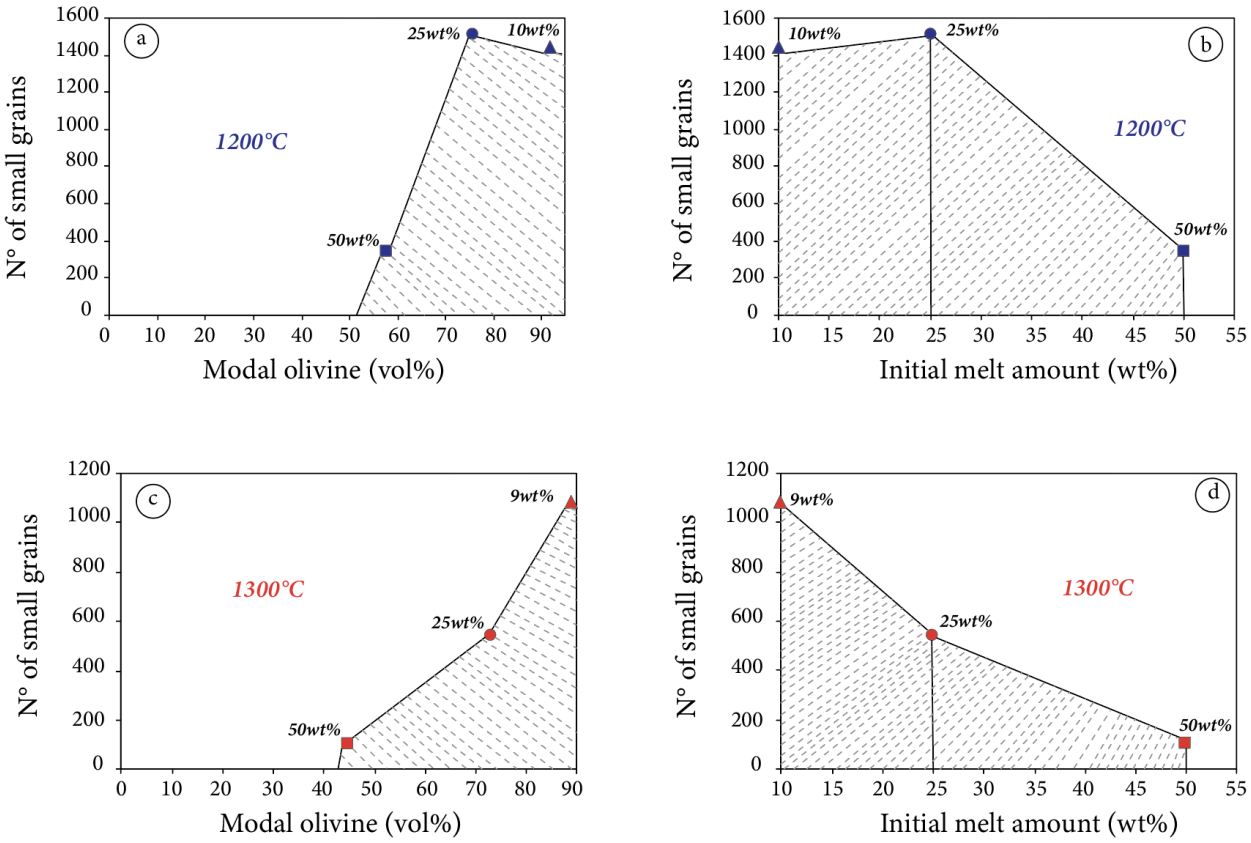

Figure 3-29 *Number of small grains (5-20 µm) vs. modal olivine (vol%) and initial melt amount (wt%) for reaction experiments performed at 0.5 GPa, at 1200°C (a-b) and 1300°C (c-d) and different initial melt amount.*

3.1.4 – The study of deformation grade of olivine grains by EBSD analysis

Although a preliminary BSE images study was useful to understand the size and morphology of olivine in the experiments, they did not provide any detailed information on the intra-granular deformation of each grain. In this section, the intra-granular deformation parameters (*e.g.*, GOS, KAM and Mis2Mean) provided by EBSD analysis and subsequently elaborated through MTEX toolbox of MatLab Software, will be discussed in relation to the *T* and IMA. The resulted data are presented from ***Figs. 3-31 to 3-38.***

Tab. 3-6 reports the summary of intra-granular deformation as average values for each experiment considering all the different grain size classes, which will be discussed in the following sections.

Run		Initial melt amount (wt%)	Grain area (micron^2)	σ^b	Equivalent diameter (micron)	σ	GOS (°)	σ
Isothermal at 1200°C	MG10	10	1819.64	1541.28	43.02	22.31	2.36	0.76
	MG12	25	1065.77	882.82	33.18	16.72	1.45	0.29
	MG14	50	1208.76	1153.87	34.70	19.16	1.14	0.79
Isothermal at 1250°C	MG11	50	2748.64	2239.69	53.44	26.13	0.41	0.04
Isothermal at 1300°C	OM23[a]	9	2728.43	2801.75	51.16	30.15	2.41	0.98
	MG1	25	2709.37	2155.76	53.37	25.24	0.87	0.23
	MG5	50	2896.60	2481.49	54.53	27.58	0.41	0.04

Table 3-6 *Summary of intra-granular deformation value of the reaction experiments performed at 0.5 GPa and temperature from 1200 to 1300°C with different initial melt amount (10, 25 and 50wt%) considering all grain size classes.* [a] *Reaction experiment from PhD Thesis of Francomme, J. E., (2016-2017).* [b] *σ = standard deviation.*

3.1.4.1 –Olivine intra-granular deformation parameters and temperature

The evaluation of the temperature influence on olivine intra-granular deformation grade in the reaction experiments has been estimated by analysing the deformation parameters provided by EBSD analysis, and comparing the experiments performed at fixed temperature.

Before discussing the olivine intra-granular deformation, it is important to establish that the San Carlos olivine, used as starting material in reaction experiments, is not naturally deformed as demonstrated by the **Grain Orientation Spread (GOS)** map elaborated (***Fig.3-30a-b***) through EBSD analysis by Francomme, J. E., (2016-2017) (see definition in **Chapter 2** and ***Tab. 3-3***). In details, the GOS color-codes in the map vary from blue to yellow (0 to 10°, respectively), indicating grains with low or zero grade of deformation *(i.e.*, undeformed) and grains with higher grade of deformation. Francomme, J. E., also heated the starting olivine at 1200°C (*P* = 0.7 GPa) for 120 hours in order to study how the sintering process affects the olivine texture independently of the reaction with the melt. Hence, the GOS map of sintered olivine ***Fig. 3-30d*** evidenced that the resulted olivine is strongly deformed (GOS value up to 10°).

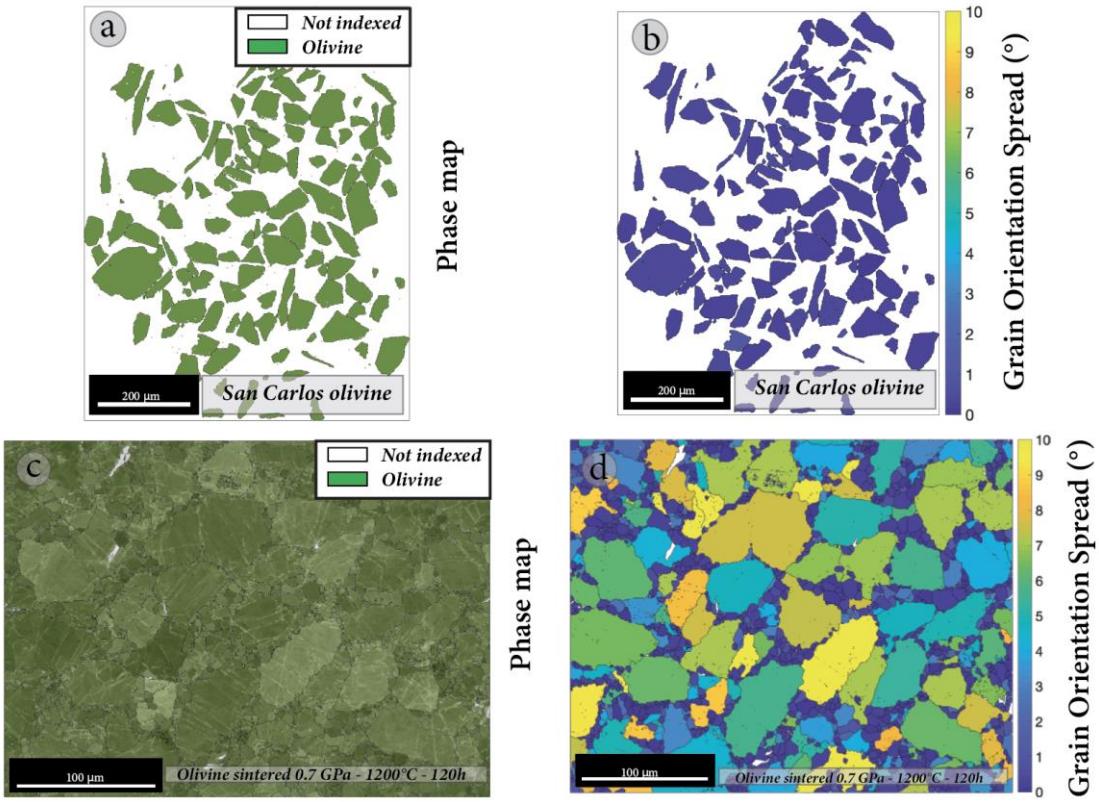

Figure 3-30 *Phase map of selected San Carlos olivine crystals, grinded, dried and sieved through a 36-64µm mesh (a) and its GOS map (b). Phase map of sintered San Carlos olivine at 0.7 GPa and 1200°C for 120h (PhD Thesis of Francomme, J. E., 2016-2017).*

Figs. 3-31 and ***3-32*** show the Grain Orientation Spread (GOS) maps of each reaction experiments performed at 1200 to 1300°C (and 0.5 GPa) with variable initial melt amount. At 1200°C, the grade of olivine deformation decreases progressively from $2.36_{IMA10} \pm 0.76$ to $1.14_{IMA50} \pm 0.79$ ***(Fig. 3-33a-b***). At 1250°C, in MG11 experiment (***Fig. 3-31d***) performed with the highest initial melt amount (50wt%), the GOS value is 0.41. The reaction at 1300°C results in the decrease of GOS values from 2.41 ± 0.98 to 0.41 ± 0.04 with the increase of melt from 10 to 50wt%, respectively.

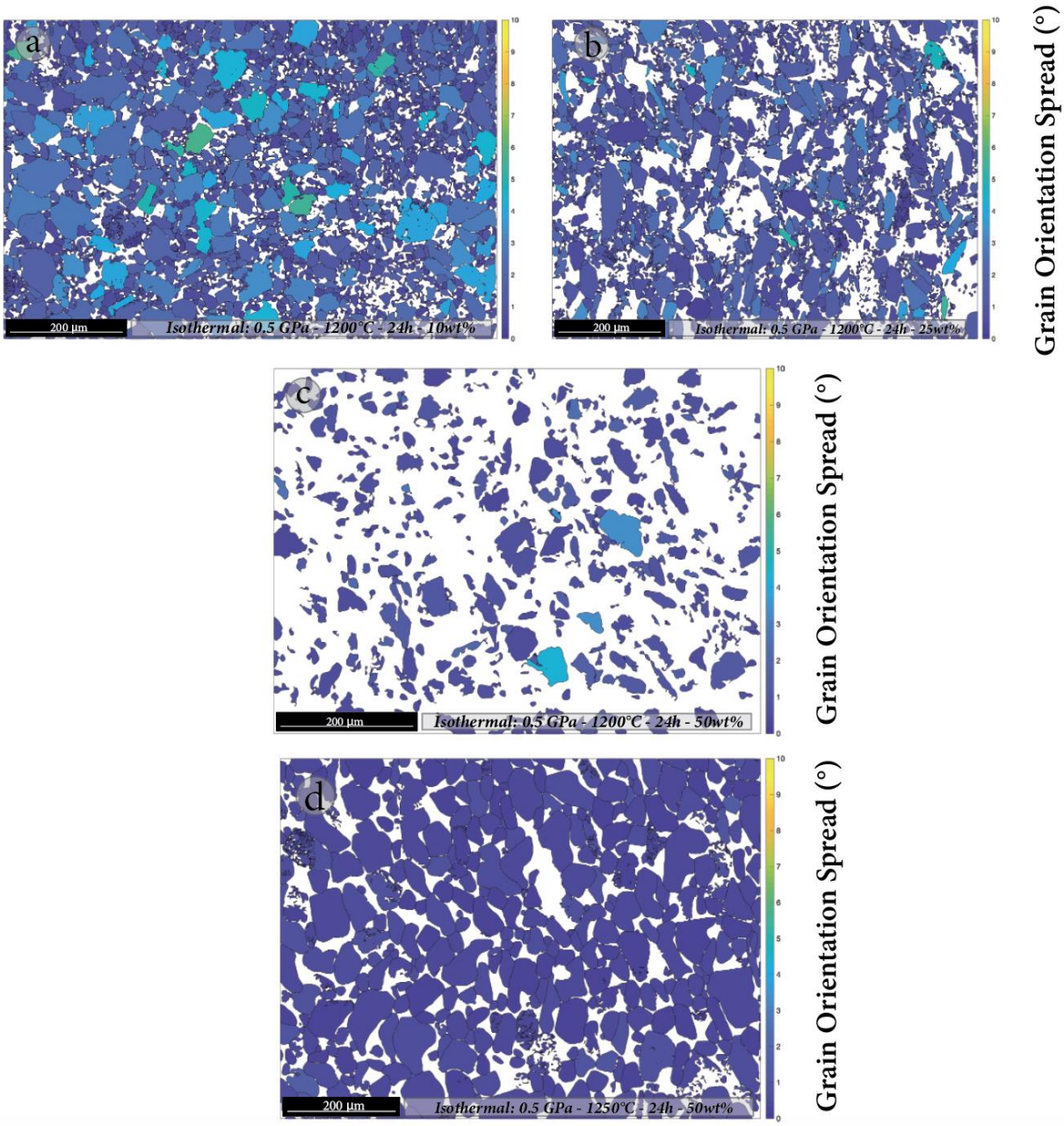

Figure 3-31 *EBSD maps representative of Grain Orientation Spread (GOS) in the isothermal experiments performed at 1200°C with 10wt% (a), 25wt% (b) and 50wt% of initial melt (c) and isothermal experiment run t 1250°C with 50wt% of initial melt (d).*

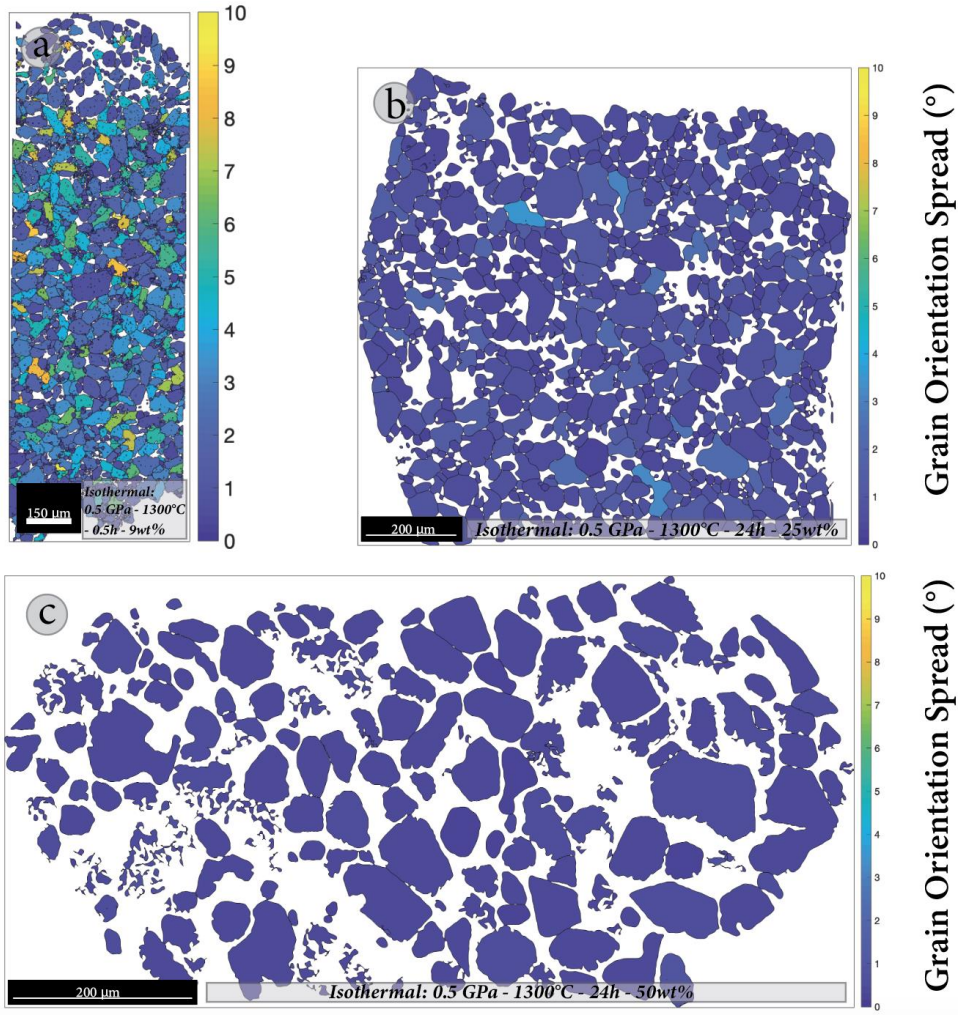

Figure 3-32 *EBSD maps representative of Grain Orientation Spread (GOS) for each isothermal experiment performed at 1300°C with 10wt% (a), 25wt% (b) and 50wt% of initial melt (c).*

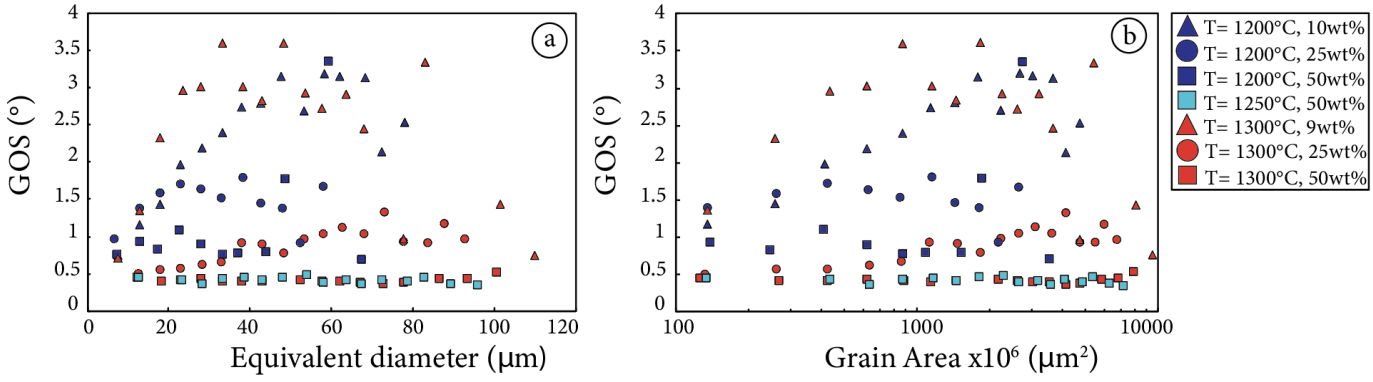

Figure 3-33 *(a) Grain Orientation Spread (GOS) vs. Equivalent diameter (µm) and (b) Aspect Ratio vs. Grain Area (µm²) of reaction experiments performed at 1200 to 1300°C and 0.5 GPa with different initial melt amount.*

The decreasing of the Grain Orientation Spread value at increasing temperature and initial melt amount, is correlated with other two important intra-granular deformation parameters:

I- **Misorientation to Mean (Mis2Mean)**: is useful to identify the *kink bands* (generated when a slip on a single slip plane is inadequate to maintain homogeneous deformation). A single point is a function of the degree of its rotation with respect to the average orientation of a grain.

II- **Kernel Average Misorientation (KAM):** it allows to identify the *sub-grains* (phase boundaries with misorientation angle ≤ 10°, "low-angles grain boundaries") and is a measure of the average misorientation of a point (pixel) with respect to a selected number of its nearest neighbours.

Figs. 3-34, 3-35 and ***3-36*** shows the Mis2Mean and KAM maps where the color-codes vary from blue to yellow (0 to 10° and from 0 to 5°, respectively), indicating the grain boundaries with low and high deformation grade. At 1200°C, the reaction with low initial melt amount (10wt%) resulted in a large number of olivine grains displaying the occurrence of kink bands and sub-grains. In particular, some of the kink bands in olivine grains correspond to sub-grains boundaries (details will be discussed in **Section 3.1.4.2**). At 1250 and 1300°C, with the reaction between olivine and melt, the kink bands and sub-grains in olivine are almost entirely recovered.

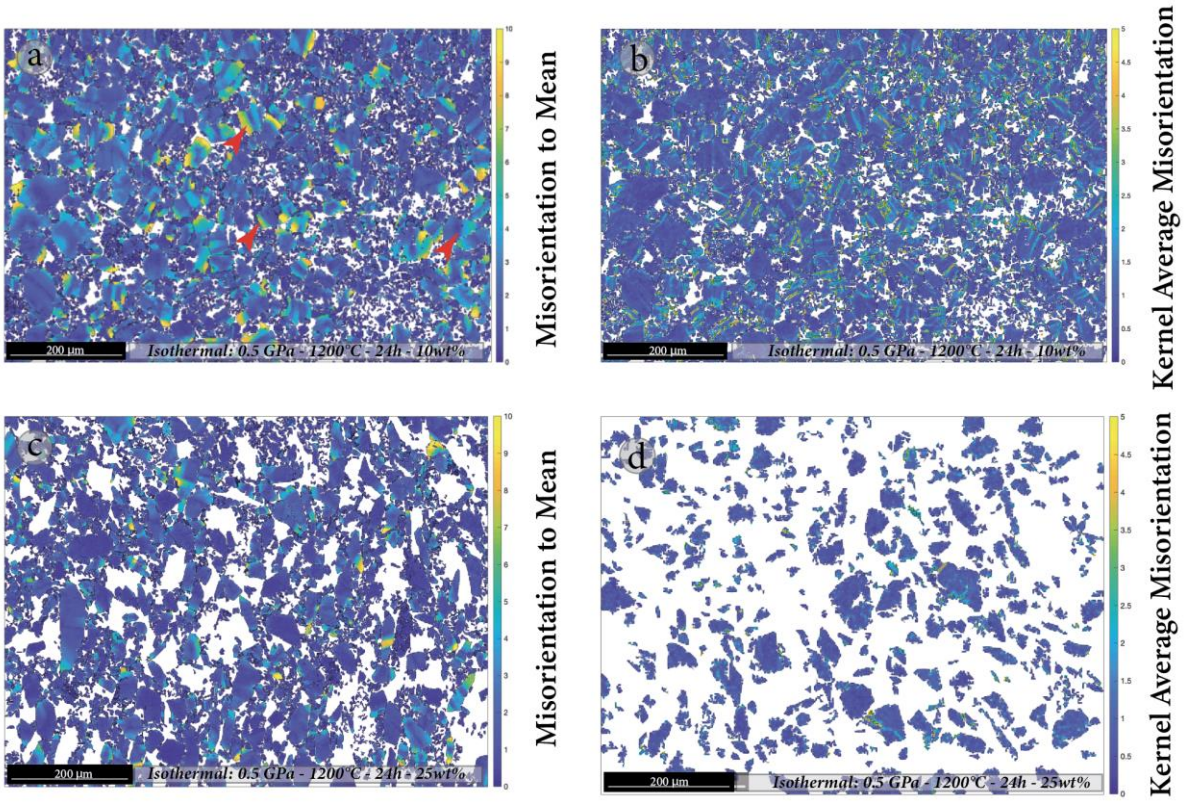

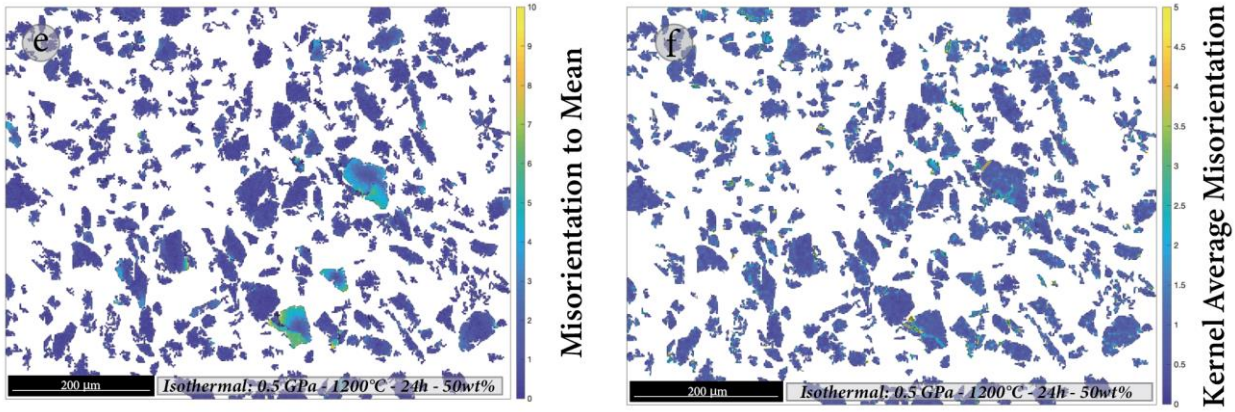

Figure 3-34 *EBSD maps representative of Misorientation to Mean and Kernel Average Misorientation for each isothermal experiment performed at 1200°C with 10wt% (a-b), 25wt% (c-d) and 50wt% of initial melt (e-f). Red arrows in (a) show the occurrence of kink bands (details in Fig.* ***3-38****).*

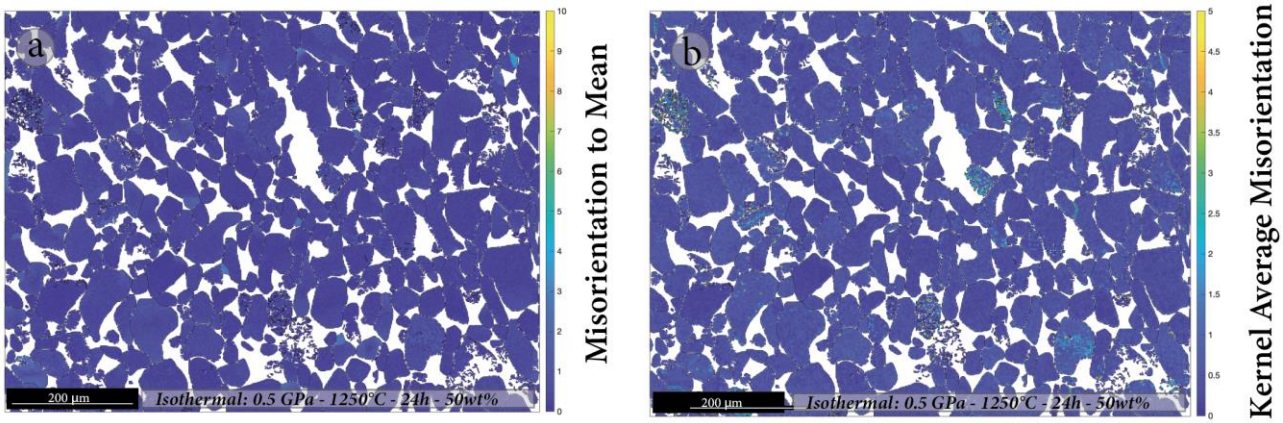

Figure 3-35 *EBSD maps representative of Misorientation to Mean and Kernel Average Misorientation for isothermal experiment performed at 1250°C with 50wt% of initial melt (a-b).*

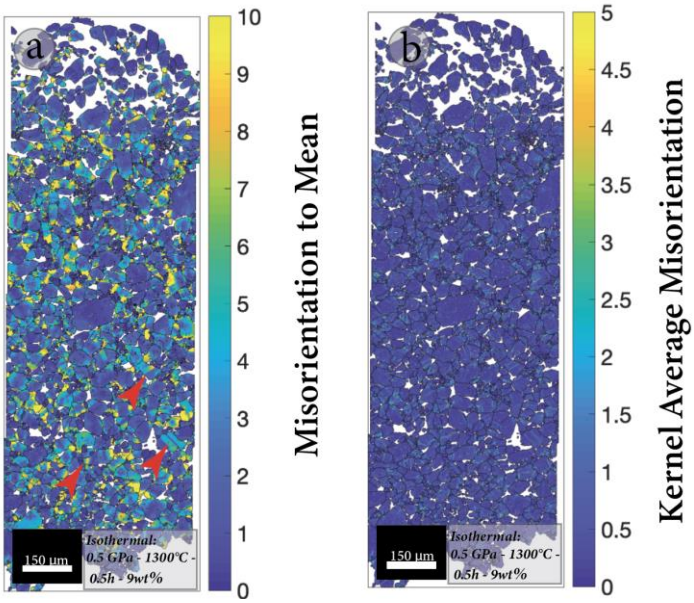

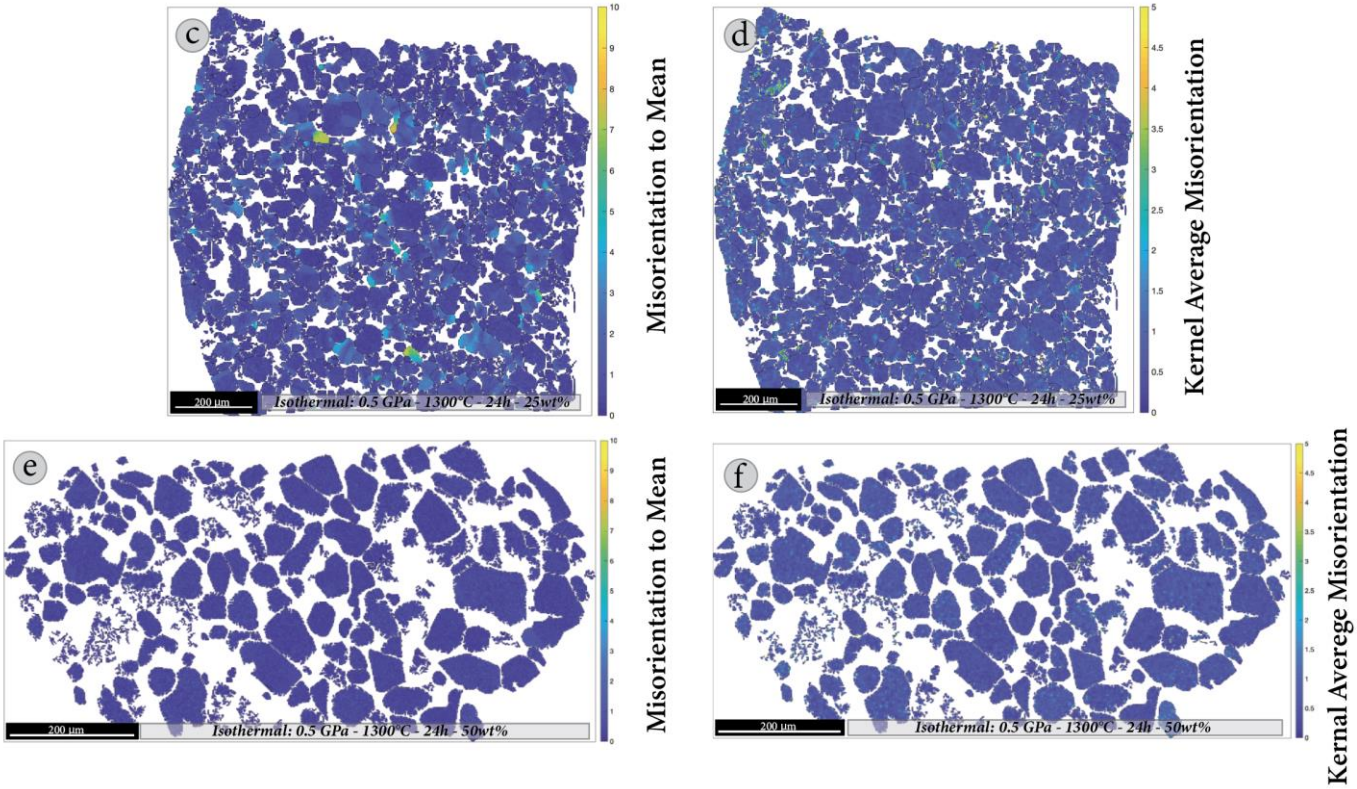

Figure 3-36 *EBSD maps representative of Misorientation to Mean and Kernel Average Misorientation for each isothermal experiment performed at 1300°C with 10wt% (a-b), 25wt% (c-d) and 50wt% of initial melt (e-f). Red arrows in (i) show the occurrence of kink bands (details in* ***Fig. 3-38****).*

3.1.4.2 –Olivine intra-granular deformation parameters and initial melt amount (IMA)

The purpose of this section is to evaluate how different initial melt amounts affect the olivine grains deformation. This has been done calculating grain size (*e.g.*, Equivalent diameter and Grain Area) and intra-granular deformation parameters such as, Grain Orientation Spread (GOS), Misorientation to Mean (Mis2Mean) and Kernel Average Misorientation (KAM). The EBSD maps are reported in **Section 3.1.4.1**.

At 1200°C, the value of **Grain Orientation Spread** (*i.e.*, an average intra-granular deformation) decreases from 2.36 ± 0.76 (with 10%$_{IMA}$) to 1.14 ± 0.79 (with 50wt%$_{IMA}$). In particular, ***Fig. 3-37a-b*** shows that the large olivine grains in reaction experiment with 10wt%$_{IMA}$ are characterized by a higher grade of intra-granular deformation than smaller grains. This trend decreases progressively the increase of the initial melt amount from 10 to 50wt%. In this case, all olivine grains independently of the grain size, reach the minimum grade of deformation of 0.75.

At 1300°C, the GOS value also decreases from 2.41 ± 0.98 to 0.41 ± 0.04 with increasing initial melt amount from 10 to 50wt%. As for the experiments carried out at 1200°C, the reaction at higher temperature with 10wt% of melt is characterized by large olivine grains with a higher grade of intra-granular deformation than small ones (***Fig. 3-37c-d***). In particular, also in this case, the grade of deformation reaches the minimum value (GOS = 0.35) at 50wt%$_{IMA}$.

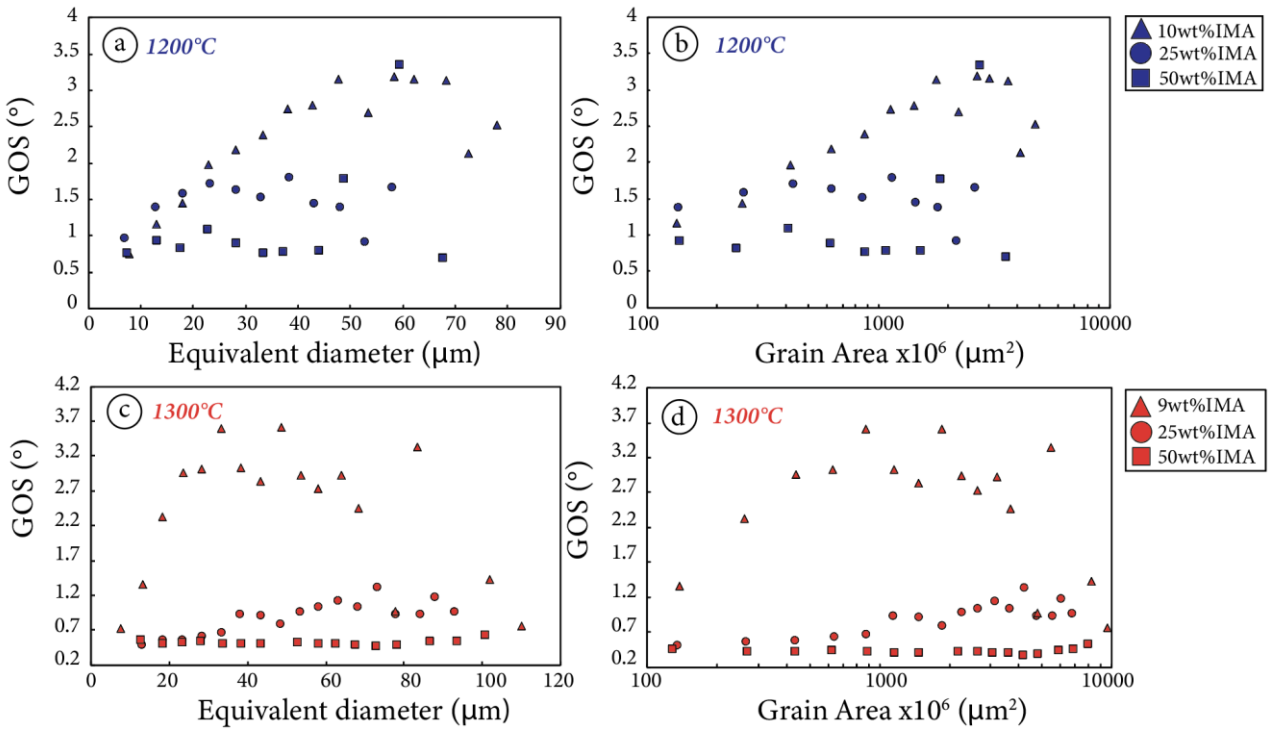

Figure 3-37 *GOS vs. Equivalent diameter (µm) and vs. Grain Area (µm²) of reaction experiments performed at 0.5 GPa and temperature of 1200 °C (a-b) and 1300°C (c-d) with different initial melt amount.*

The melt/olivine ratio affects not only the GOS value, but also the occurrence of kink bands and sub-grains both at 1200 and 1300°C, structural evidences that usually tend to characterize medium and larger grains. As mentioned before, some of the kink bands (***Fig. 3-38b***) in olivine grains correspond to the boundary of sub-grains (***Fig. 3-38b***).

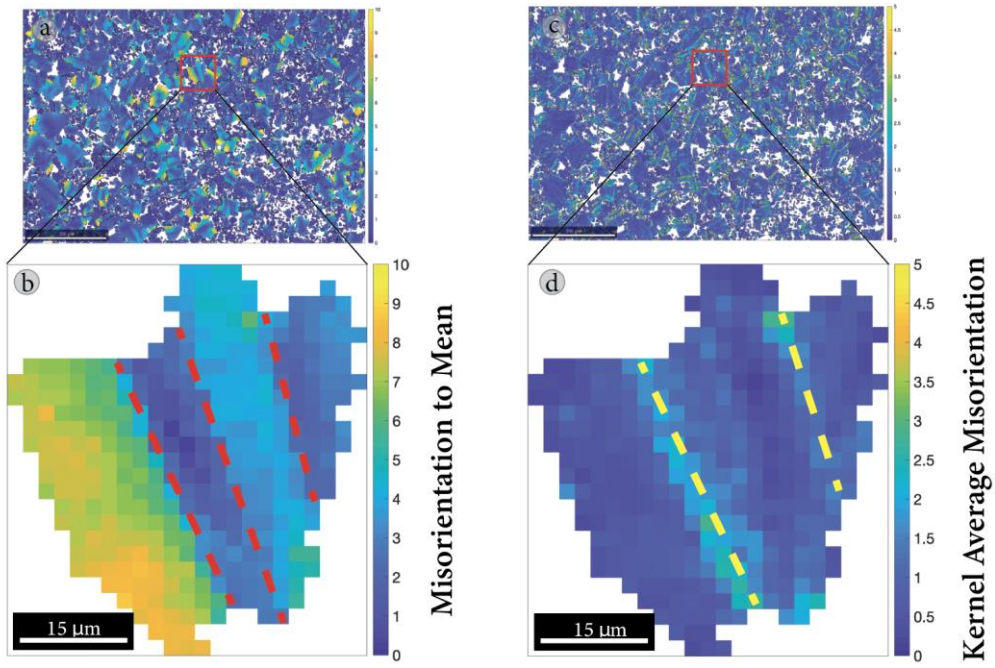

Figure 3-38 *(a) Mis2Mean map with details (b) that displays the occurrence of kink bands (red dashed lines) and (c) KAM maps with details (d) that displays the boundary of sub-grains (yellow dashed lines) in a large subhedral deformed and corroded crystals (~48 µm) with both straight and lobate rims in the reaction experiment performed at 0.5 GPa and 1200°C with 10wt% of initial melt.*

Chapter 4
OLIVINE REACTIVE CRYSTALLIZATION – STEP-COOLED EXPERIMENTS

4.1 – Introduction

The aim of this chapter is to study how the Initial Melt Amount - IMA (*i.e.*, 10, 25 and 50wt%) affects the mineralogical association and the final mineral chemistry of olivine-rich troctolites originated by dissolution/re-precipitation and reactive crystallization processes. Three step-cooled experiments (**MG15**, **MG4** and **MG16**) were carried out in an END-Loaded piston cylinder at fixed pressure (P = 0.5 GPa) on three different homogeneous mixes of San Carlos olivine and tholeiitic glass AH6 (X_{Mg} = 0.62) (***Tab. 2-1***). The experiments were run at 1300°C for 24h and then cooled down to 1100°C by 1°C/min (further details in **Chapter 2** and ***Fig. 4-1***). ***Tab. 4-1*** reports the experimental run conditions and phase assemblages of the step-cooled experiments.

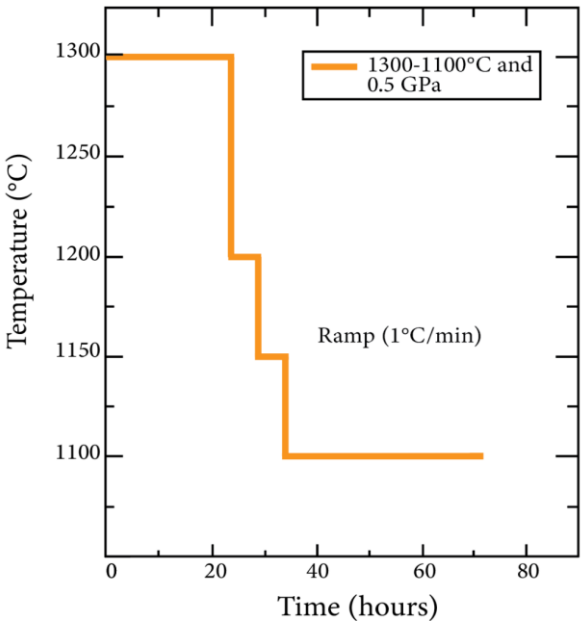

Fig. 4-1 *Schematic illustration of temperature vs. path of step-cooled experiments performed at 0.5 GPa and temperature from 1300 down to 1100°C with different initial melt amount.*

Run	P (GPa)	T (°C)	t (h)	Initial melt amount (wt%)	Phase assemblages and mode (wt%) [a]			
Starting materials SCO [b] +AH6					Ol [c]	Pl [d]	Cpx [e]	Gl [f]
MG15	0.5	$1300_{(i)}$-$1100_{(f)}$	72	10	89 (2)	Absent	Absent	10.3 (2)
MG4	0.5	$1300_{(i)}$-$1100_{(f)}$	72	25	75 (1)	Absent	3 (1)	22 (1)
MG16	0.5	$1300_{(i)}$-$1100_{(f)}$	72	50	55 (2)	26 (3)	11 (1)	8 (1)

Table 4-1 *A summary of the main features of the experiments. [a] Modes are calculated using mass balance: e.g., 89 (2) and 10.3 (2) represent 89 ± 2 and 10.27 ± 0.2. [b] San Carlos olivine. [c] Olivine. [d] Plagioclase. [e] Clinopyroxene. [f] Glass.*

4.2 – Results

4.2.1 – Phase assemblages and texture

Step-cooled runs resulted in homogeneous phases distribution suggesting that no melt segregation occurred during the melt-olivine reaction (***Fig. 4-2a-b***).

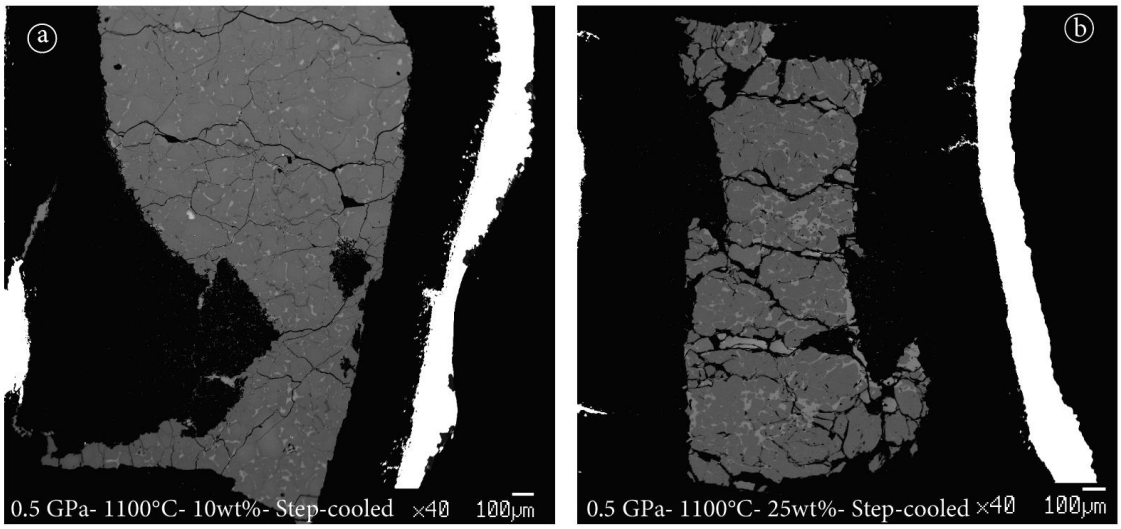

Figure 4-2 *Back-Scattered-Electron (BSE) images showing a panoramic view of the capsule after the reaction between olivine and melt and the crystallization of interstitial phase, i.e., plagioclase and clinopyroxene in step-cooled experiments carried out at 0.5 GPa and final temperature of 1100°C with 10wt% (a) and 25wt% of initial melt (b).*

The experiment performed with 10wt%$_{IMA}$ consists of olivine crystals and interstitial basaltic glass. Although, in some cases is difficult to define the olivine grain boundaries by BSE images, it is possible to distinguish two different olivine morphologies:

i) large subhedral crystals (up to 100 µm) with both straight and lobate rims;
ii) smaller and rounded grains (5-20 µm) (***Fig. 4-3a-b***).

The run products of step-cooled experiment with 25wt%$_{IMA}$ consist of olivine, glass and interstitial clinopyroxene. Olivine occurs both as smaller rounded grains embedded in poikilitic clinopyroxene and as large subhedral crystals (***Fig. 4-3c-d***). Experiments with 50wt%$_{IMA}$ resulted in olivine, interstitial phases (*i.e.,* plagioclase and clinopyroxene) and smaller amount of glass than run with 25wt%$_{IMA}$ (***Fig. 4-3e-f***). In particular, plagioclase and clinopyroxene occur interstitial to olivine grain boundaries in which show sharp and straight contacts (***Fig. 4-4b-d***). The olivine grain size generally decreases with the increase of IMA from 10 to 50wt% (~135 µm and ~105 µm, respectively).

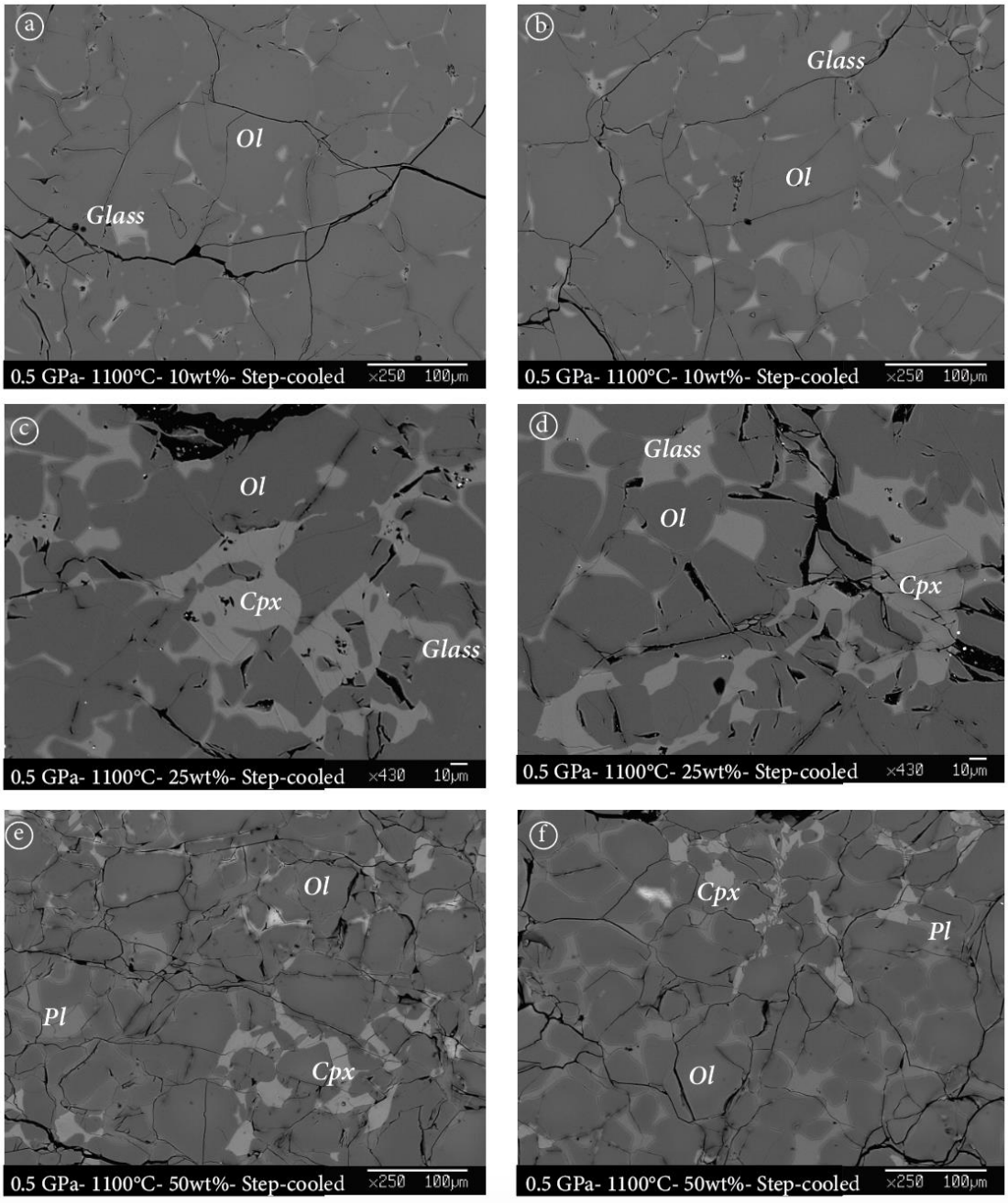

Figure 4-3 *BSE images showing texture in reactive crystallization experiment with 10wt% of melt (a-b), 25wt% of melt (c-d) and 50wt% of melt (e-f) performed at 0.5 GPa and final temperature of 1100°C. Experiments lasted 72h.*

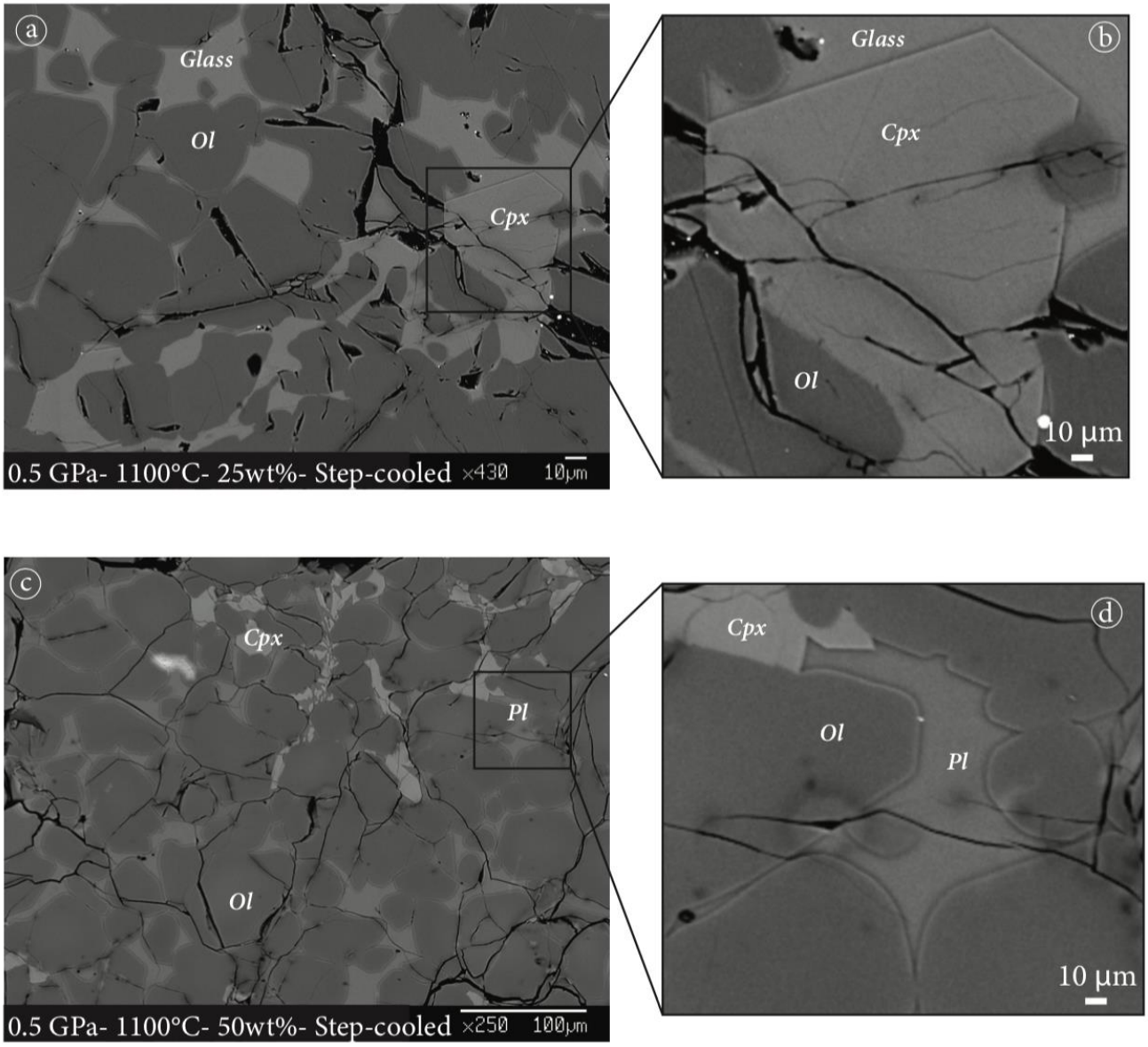

Figure 4-4 *Detailed BSE images showing clinopyroxene texture in reactive crystallization experiment with 25wt% of melt (a-b) and plagioclase texture in run with 50wt% of melt (c-d) performed at 0.5 GPa and final temperature of 1100°C.*

4.2.2 – Mineral and glass chemistry

Tab. 4-2 reports the average major element compositions, in terms of oxides percentage, of the olivine, plagioclase, clinopyroxene and glass. Single analyses are reported in ***Tab. 7-3, 7-5, 7-7, 7-9*** **(in Appendix).**

Sample	**MG15**	σ^e	**MG4**	σ	**MG16**	σ
IMA[a](wt%)	10		25		50	
T[b]	$1300_{(i)}$-$1100_{(f)}$		$1300_{(i)}$-$1100_{(f)}$		$1300_{(i)}$-$1100_{(f)}$	
n[c]	72		93		56	
SiO_2	41.32	0.62	40.56	0.34	41.11	0.27
TiO_2	0.01	0.02	0.02	0.02	0.02	0.02
Al_2O_3	0.05	0.03	0.07	0.09	0.03	0.02
Cr_2O_3	0.03	0.03	0.03	0.03	0.04	0.03
FeO	8.10	1.45	8.91	0.31	7.11	0.90
MgO	51.21	1.29	49.71	0.50	51.25	0.66
MnO	0.14	0.03	0.14	0.03	0.14	0.03
NiO	0.06	0.07	0.03	0.03	0.09	0.07
CaO	0.23	0.02	0.33	0.08	0.34	0.23
Na_2O	0.01	0.02	0.01	0.02	0.01	0.01
K_2O	0.00	0.01	0.00	0.01	0.00	0.01
Sum	101.18	0.50	99.82	0.50	100.13	0.49
Si	0.99	0.01	0.99	0.01	0.99	0.01
Ti	0.00	0.00	0.00	0.00	0.00	0.00
Al	0.00	0.00	0.00	0.00	0.00	0.00
Cr	0.00	0.00	0.00	0.00	0.00	0.00
Fe	0.16	0.03	0.18	0.01	0.14	0.02
Mg	1.83	0.03	1.81	0.01	1.85	0.02
Mn	0.00	0.00	0.00	0.00	0.00	0.00
Ni	0.00	0.00	0.00	0.00	0.00	0.00
Ca	0.01	0.00	0.01	0.00	0.01	0.01
Na	0.00	0.00	0.00	0.00	0.00	0.00
K	0.00	0.00	0.00	0.00	0.00	0.00
Sum	3.00	0.08	3.00	0.04	3.00	0.05
X_{Mg}[d]	0.91	0.02	0.90	0.00	0.92	0.01

Table 4-2a *Average major element compositions of olivine from step-cooled experiments. [a] Initial melt amount. [b] Temperature. [c] n = number of analysis. [d] X_{Mg} = Mg/(Mg+Fe). [e] σ = standard deviation.*

Sample	**MG16**	σ
IMA[a](wt%)	50	
T[b]	$1300_{(i)}$-$1100_{(f)}$	
n[c]	3	
SiO_2	50.92	0.69
TiO_2	0.05	0.04
Al_2O_3	30.53	0.30
Cr_2O_3	0.01	0.01
FeO	0.15	0.14
MgO	0.30	0.03
MnO	0.01	0.02
NiO	0.02	0.02
CaO	14.52	0.49
Na_2O	3.30	0.24
K_2O	0.05	0.02
Sum	100.12	0.21
Si	2.32	0.03
Ti	0.00	0.00
Al	1.64	0.02
Cr	0.00	0.00
Fe	0.01	0.01
Mg	0.02	0.00
Mn	0.00	0.00
Ni	0.00	0.00
Ca	0.71	0.03
Na	0.29	0.02
K	0.00	0.00
Na+Ca	1.00	0.05
X_{An}[d]	0.71	0.02

Table 4-3b *Average major element compositions of plagioclase from step-cooled experiments.* [a] *Initial melt amount.* [b] *Temperature.* [c] *n = number of analysis.* [d] $X_{An} = Ca/(Ca+Na)$. [e] σ *= standard deviation.*

Sample	**MG4**	σ	**MG16**	σ
IMA[a](wt%)	25		50	
T[b]	$1300_{(i)}$-$1100_{(f)}$		$1300_{(i)}$-$1100_{(f)}$	
n[c]	93		56	
SiO_2	50.42	1.22	51.13	0.69
TiO_2	0.69	0.15	0.95	0.28
Al_2O_3	7.50	1.38	6.61	1.67
Cr_2O_3	0.21	0.06	0.21	0.11
FeO	2.90	0.19	2.32	0.40
MgO	16.92	0.88	16.78	0.93
MnO	0.09	0.02	0.09	0.03
NiO	0.02	0.03	0.03	0.03
CaO	20.62	0.71	22.06	0.58
Na_2O	0.29	0.04	0.29	0.05
K_2O	0.00	0.01	0.00	0.01
Sum	99.67	0.47	100.47	0.40
Si	1.83	0.04	1.84	0.03
Ti	0.02	0.00	0.03	0.01
Al	0.32	0.06	0.28	0.07
Cr	0.01	0.00	0.01	0.00
Fe	0.09	0.01	0.07	0.01
Mg	0.91	0.05	0.90	0.05
Mn	0.00	0.00	0.00	0.00
Ni	0.00	0.00	0.00	0.00
Ca	0.80	0.03	0.85	0.02
Na	0.02	0.00	0.02	0.00
K	0.00	0.00	0.00	0.00
Sum	4.00	0.19	4.00	0.20
X_{Mg}[d]	0.91	0.00	0.93	0.01

Table 4-2c *Average major element compositions of clinopyroxene from step-cooled experiments.* [a] *Initial melt amount.* [b] *Temperature.* [c] *n = number of analysis.* [d] X_{Mg} *= Mg/(Mg+Fe).* [e] σ *= standard deviation.*

Sample	**MG15**	σ[f]	**MG4**	σ	**MG16**	σ
IMA[a](wt%)	10		25		50	
T[b]	$1300_{(i)}$-$1100_{(f)}$		$1300_{(i)}$-$1100_{(f)}$		$1300_{(i)}$-$1100_{(f)}$	
n[c]	72		93		56	
SiO_2	53.82	1.34	50.06	0.66	32.58	1.62
TiO_2	0.71	0.11	0.92	0.05	0.69	0.27
Al_2O_3	12.65	1.26	19.76	0.48	12.19	4.35
Cr_2O_3	0.04	0.03	0.02	0.02	0.03	0.04
FeO	6.70	1.33	5.09	0.20	5.92	0.05
MgO	9.78	5.02	7.29	0.48	7.35	0.57
MnO	0.16	0.03	0.11	0.03	0.15	0.02
NiO	0.02	0.02	0.02	0.02	0.04	0.02
CaO	11.48	1.78	12.38	0.27	29.18	6.39
Na_2O	1.78	0.17	2.74	0.07	1.03	0.73
K_2O	0.10	0.02	0.19	0.02	0.17	0.16
Sum	97.23	1.32	98.59	0.55	89.32	0.22
X_{Mg}[d]	0.70	0.09	0.72	0.01	0.69	0.02
X_{Ca}[e]	0.78	0.03	0.71	0.01	0.93	0.06

Table 4-2d *Average major element compositions of glass from step-cooled experiments.* [a] *Initial melt amount.* [b] *Temperature.* [c] *n = number of analysis.* [d] X_{Mg} *= Mg/(Mg+Fe).* [e] X_{Ca} *= Ca/(Ca+Na).* [f] σ *= standard deviation.*

4.2.2.1 – Olivine chemistry

Fig. 4-5 shows the composition of olivine cores and rims in terms of X_{Mg}, NiO and CaO contents. Reacted olivines at 1100°C are characterized by negligible core and rim compositional variations between cores and rims (NiO_{CORE} = 0.05wt% ± 0.05 and CaO_{CORE} = 0.28wt% ± 0.06, NiO_{RIM} = 0.05wt% ± 0.06 and CaO_{RIM} = 0.29wt% ± 0.11). Due to the negligible difference between core and rim, the total analysis of olivine, which include core and rim, will be considered. ***Fig. 4-6*** shows the X_{Mg} versus NiO and CaO content (wt%) of olivine. X_{Mg} values generally plot above the one of San Carlos olivine (X_{Mg} = 0.90). The X_{Mg} value in olivine in run with 50wt%$_{IMA}$ is higher (X_{Mg} = 0.92 ± 0.01) than runs performed with 10 and 25wt%$_{IMA}$ (X_{Mg} = 0.91± 0.02 and X_{Mg} = 0.90 ± 0.00, respectively). No correlation can be drawn between olivine X_{Mg} and its habit (subhedral-irregular *vs*. euhedral-regular habit, see **Section 4.2.1**).

The NiO contents in olivine from step-cooled runs are systematically lower than the NiO content of San Carlos and they are not correlated with the IMA. In particular, the reactive crystallization experiment MG16 (50wt%$_{IMA}$) is characterized by olivine with NiO content (0.09wt% ± 0.07) higher than the olivine in experiments performed with 10 and 25wt%$_{IMA}$ (NiO = 0.06wt% ± 0.07 and NiO = 0.03wt% ± 0.03, respectively). No correlation can be drawn between different olivine morphologies and the NiO content.

Olivines resulting from experiments have CaO contents higher than San Carlos olivine (CaO = 0.07wt%). In particular, olivines in experiments with 25 and 50wt%$_{IMA}$ have CaO contents (CaO = 0.33wt% ± 0.08 and 0.34wt% ± 0.23, respectively) higher than those in run with 10wt%$_{IMA}$ (CaO = 0.23wt% ± 0.02).

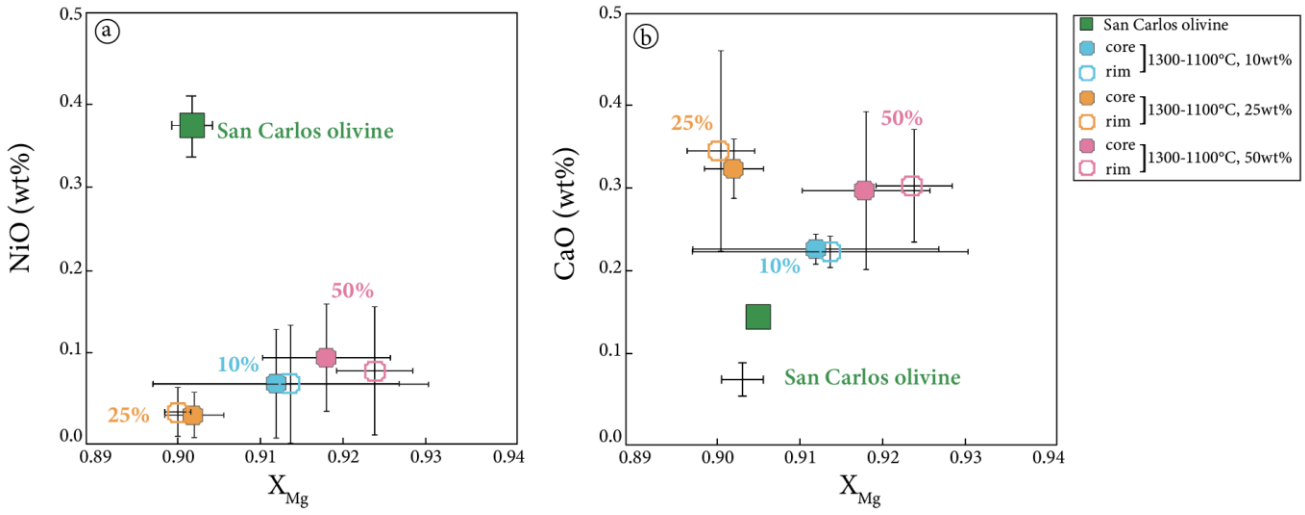

Figure 4-5 *(a) X_{Mg} vs. NiO content (wt%) and (b) X_{Mg} vs. CaO content (wt%) in olivine from reactive crystallization experiments performed at 0.5 GPa and final temperature of 1100°C with different initial melt amount. Full and empty symbols represent cores and rims, respectively.*

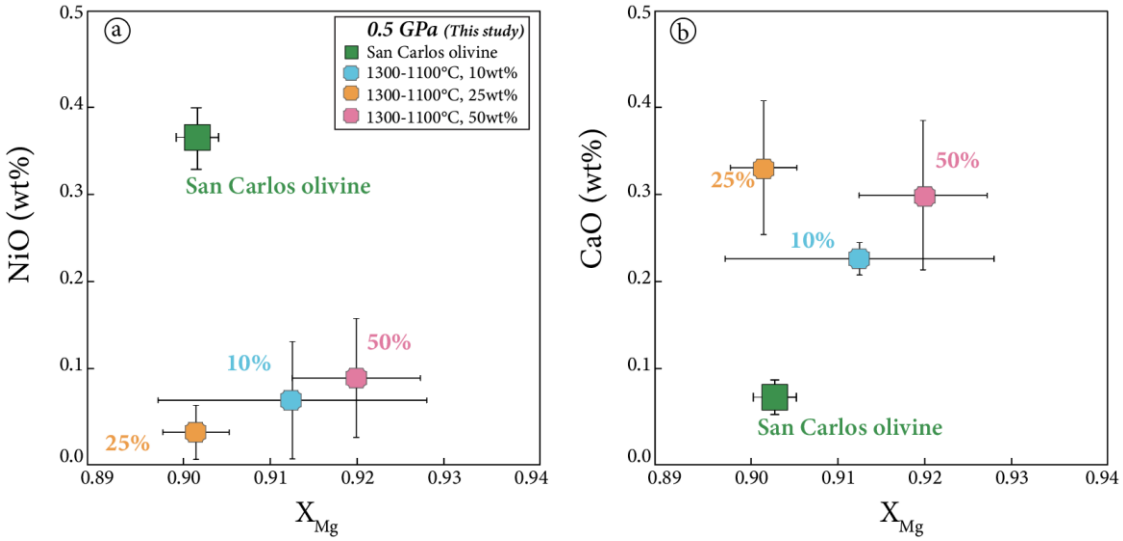

Figure 4-6 *X_{Mg} vs. NiO content (wt%) and (b) X_{Mg} vs. CaO content (wt%) in olivine from reactive crystallization experiments performed at 0.5 GPa and temperature of 1100°C with different initial melt amount (10, 25 and 50wt%).*

4.2.2.2 – Plagioclase and clinopyroxene compositions

Plagioclase is recovered only in step-cooled experiment with 50wt%$_{IMA}$ (***Tab. 4-1***). ***Fig. 4-7*** shows the covariation of X_{Mg} in olivine and clinopyroxene with X_{An} [X_{An} = Ca/(Ca+Na)] in coexisting plagioclase compared to experiments carried out at 0.5 and 0.7 GPa (Borghini et al., 2018). In particular, plagioclase in run MG16 with 50wt%$_{IMA}$ is characterized by an anorthite content of 0.71 ± 0.02. This experimental result will be compared to data from Borghini et al., (2018) in **Chapter 5**, **Section 5.3.2**.

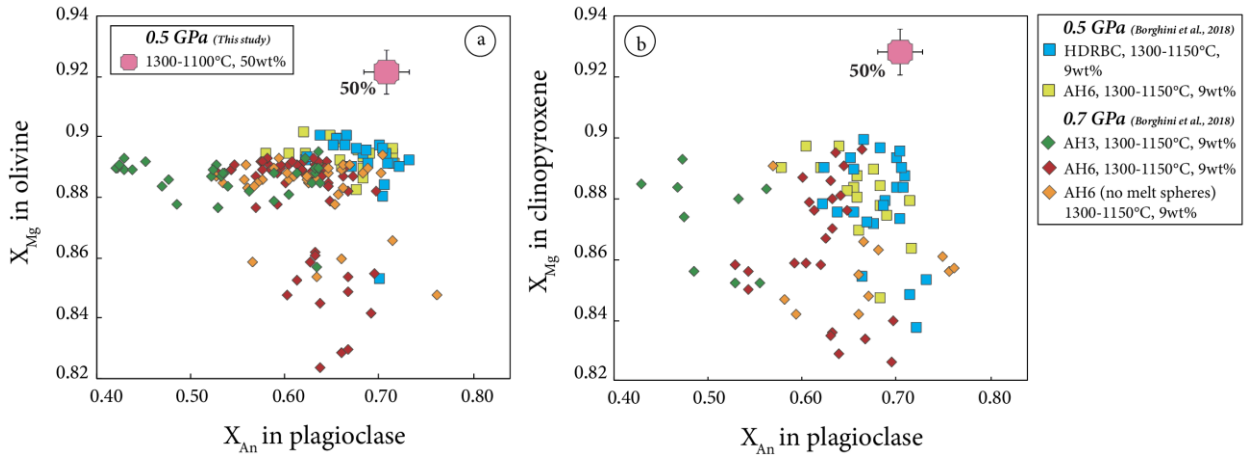

Figure 4-7 *(a) X_{Mg} in olivine vs. X_{An} in plagioclase and (b) X_{Mg} in clinopyroxene vs. X_{An} in plagioclase of step-cooled experiment at 0.5 GPa and 1100°C compared to experimental data performed at 0.5 and 0.7 GPa from Borghini et al., 2018.*

Clinopyroxene in the run MG16 (50%$_{IMA}$) has average X_{Mg} value of 0.93 ± 0.01 that is higher than clinopyroxene X_{Mg} in experiment with 25wt%$_{IMA}$ (X_{Mg} = 0.91 ± 0.01). No significant differences in clinopyroxene composition are observed as a function of different initial melt amount (25 to 50wt%) in terms of Cr_2O_3 and Na_2O contents. However, clinopyroxene in experiment with 25wt%$_{IMA}$ is characterized by a higher Al_2O_3 content (7.50wt% ± 1.38) but lower TiO_2 content (0.69 ± 0.15) than the one in run with 50wt%$_{IMA}$ (Al_2O_3 = 6.61wt% ± 1.67 and TiO_2 = 0.95 ± 0.28).

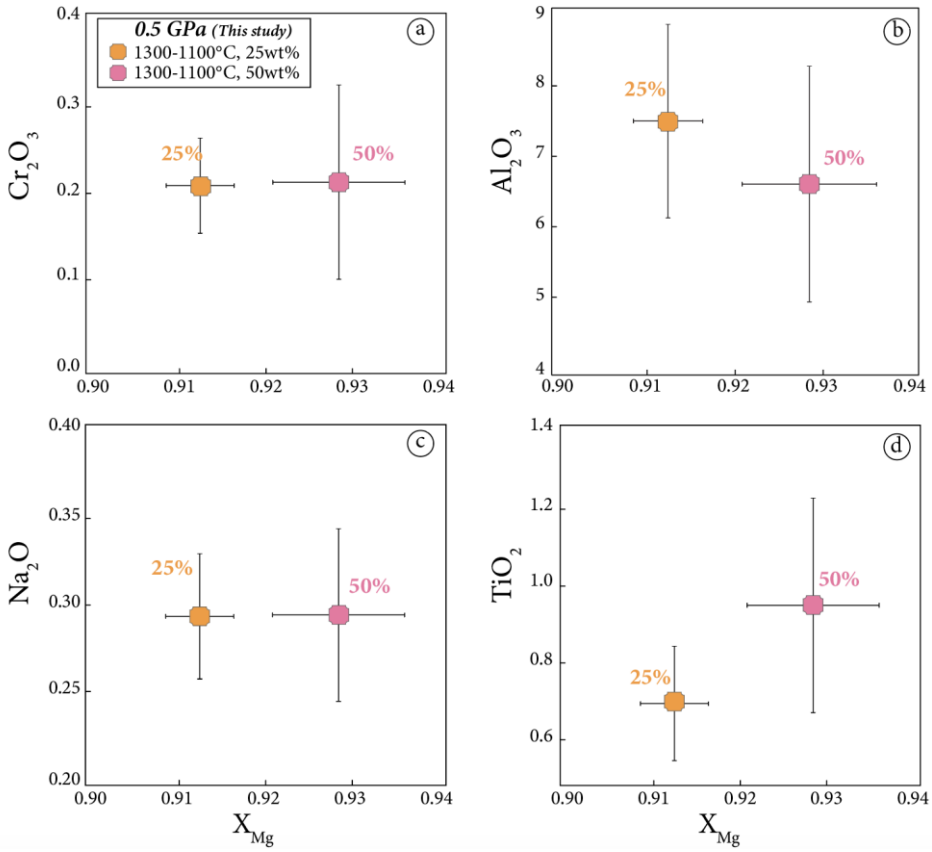

Figure 4-8 *X_{Mg} vs. Cr_2O_3 (a), Al_2O_3 (b), Na_2O (c) and TiO_2 (d) contents (wt%) in clinopyroxene from step-cooled experiments performed at 0.5 GPa and final temperature of 1100°C with different initial melt amount from 10 to 50wt%,*

4.2.2.3 – Glass composition

Fig. 4-9 shows the chemical composition of glasses in step-cooled experiments compared to the initial tholeiitic basalt AH6 (MgO = 8.62wt%, X_{Mg} = 0.61). No correlation is observed between the initial melt amount and final glasses compositions. In particular, after the reaction with olivine and the crystallization of interstitial phases (*i.e.*, plagioclase and clinopyroxene), the residual melt in the experiment with 10wt%$_{IMA}$ acquired higher MgO content (9.78wt% ± 5.02) than the glasses analysed in runs with 25 and 50wt%$_{IMA}$ (MgO = 7.29wt% ± 0.48 and MgO = 7.35wt% ± 0.57, respectively). The glasses in runs with 10 and 25wt%$_{IMA}$ have higher SiO_2 (53.82wt% ± 1.34 and 50.06wt% ± 0.66, respectively) and lower CaO contents (11.48wt% ± 1.78 and 12.38wt% ± 0.27, respectively) than the glasses in experiments with 50wt%$_{IMA}$ (SiO_2 = 32.58wt% ± 1.62 and CaO = 29.18wt% ± 6.39) and their initial composition (***Fig. 4-9a-d***). Furthermore, the glasses in step-cooled experiment with 25wt%$_{IMA}$ have higher Al_2O_3 and Na_2O contents (19.76wt% ± 0.48 and 2.74wt% ± 0.07, respectively) than those in runs with 10wt%$_{IMA}$ (Al_2O_3 = 12.65wt% ± 1.26 and Na_2O = 1.78wt% ± 0.17) and 50wt%$_{IMA}$ (Al_2O_3 = 12.19wt% ± 4.35 and Na_2O = 1.03wt% ± 0.73) and even higher with respect to the initial glass (***Fig. 4-9b-c***).

Fig. 4-10 displays the NiO content versus X_{Mg} in experimental glasses compared to the initial melt composition AH6 (NiO = 0.00wt%, X_{Mg} = 0.62). No correlation with initial melt amount can be drawn (see ***Tab. 4-2***). In particular, glasses in experiment with 50wt%$_{IMA}$ have higher NiO content (0.04wt% ± 0.02) than glasses in runs with 10 and 25wt%$_{IMA}$ (NiO = 0.02wt% ± 0.02 and NiO = 0.02wt% ± 0.02).

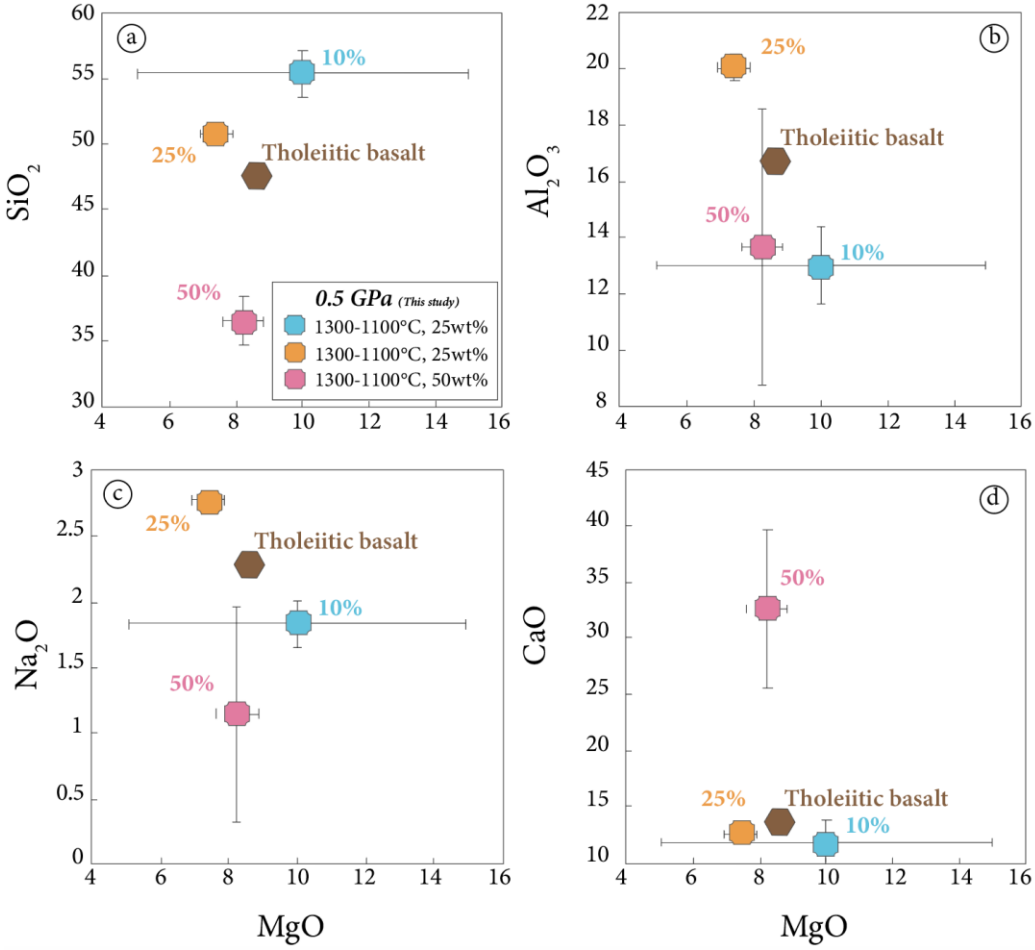

Figure 4-9 *MgO vs. SiO_2 (a), Al_2O_3 (b), Na_2O (c) and CaO (d) content in reacted residual melts from step-cooled experiments performed at 0.5 GPa final temperature of 1100°C with different initial melt amount (10, 25 and 50wt%). In the diagrams, the chemical compositions of reacted melts were normalized to 100%.*

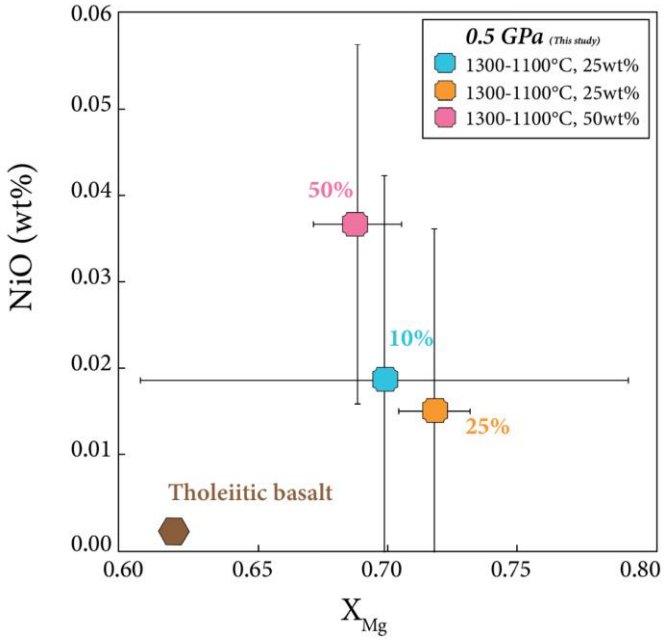

Figure 4-10 *X_{Mg} vs. NiO content (wt%) in reacted residual melts from step-cooled experiments performed at 0.5 GPa and final T of 1100°C with different initial melt amount from 10 to 50wt%.*

4.2.3 – Textural analysis of olivine grains – EBSD analysis

In order to investigate the effect of initial melt amount (*i.e.*, 10, 25 and 50wt%) on the olivine texture after melt-olivine reaction and reactive crystallization, EBSD analysis was performed on the step-cooled experiments. This study used the FEG-SEM at the Platform of Microscopy of the University of Milano-Bicocca. ***Fig. 4-11*** shows the Phase maps and the Inverse Pole Figures (IPF) for each reaction experiments. Different colors suggest that the reacted olivine grains are not preferred oriented along a specific axis, but they all are randomly oriented along different axis. The MTEX toolbox was used to quantitatively define the geometrical factors (*e.g.*, Aspect Ratio, Shape Factor, PARIS Factor and Grain Area) and deformation parameters (*e.g.*, GOS, Mis2Mean and KAM) already described in **Chapter 2** and reported in ***Tab. 3-3***. ***Tab. 4-3*** reports the summary of geometrical factor as average values for each step-cooled experiment by considering the grain size classes from 10-15 µm to 130-135 µm. They will be discussed in details in **Sections 4.2.3.1.**

Run		Initial melt amount	Grain area (micron^2)	σ[a]	Equivalent diameter (micron)	σ	Aspect Ratio	σ	Shape Factor	σ	PARIS Factor (%)	σ
Step-cooled at $1300_{(i)}$ -$1100_{(f)}$°C	MG15	10	3526.32	3402.28	60.49	29.68	1.49	0.20	1.24	0.11	15.85	11.50
	MG4	25	2759.41	2917.73	52.14	29.16	1.44	0.12	1.25	0.09	19.13	13.12
	MG16	50	2606.56	2547.78	50.66	28.53	1.57	0.25	1.31	0.14	24.42	19.25

Table 4-3 *Summary of geometrical factors of the reactive crystallization experiments performed at 0.5 GPa and final temperature of 1100°C with different melt/olivine ratio (10, 25 and 50wt%) considering all grain size classes. [a] σ = standard deviation.*

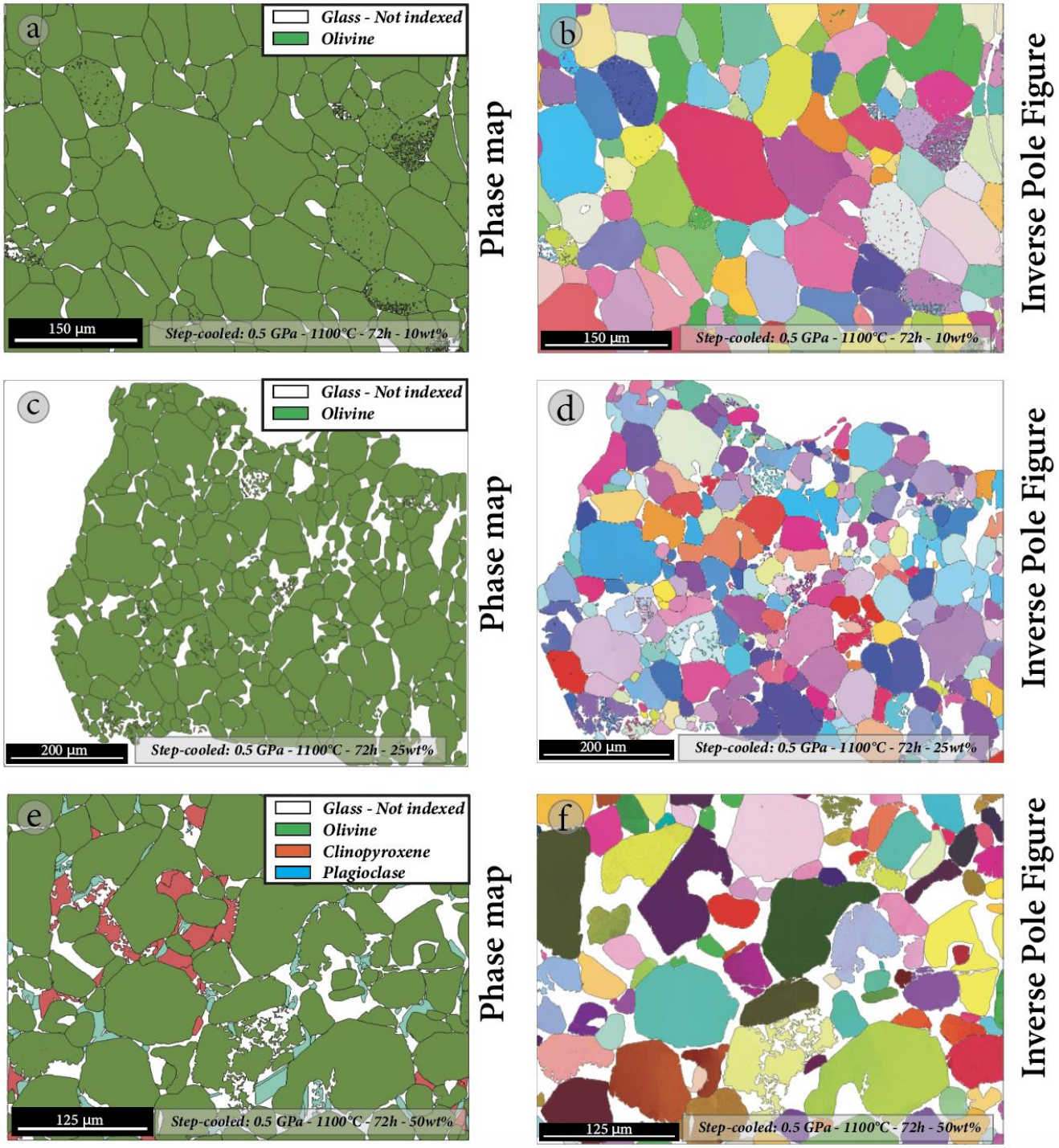

Figure 4-11 *Phase maps and IPF maps for each step-cooled experiment performed at final temperature of 1100°C with 10wt% (a-b), 25wt% (c-d) and 50wt% of initial melt (e-f).*

4.2.3.1 – Olivine geometrical parameters and initial melt amount (IMA)

This section aims to evaluate the effect of the initial melt amount on the olivine texture after the reaction with melt and reactive crystallization of the interstitial reacted melt. Olivine textural development was estimated by determining through EBSD analysis the geometrical factors such as Grain Area, Equivalent diameter, Aspect Ratio, Shape Factor and PARIS Factor (details in **Chapter 2** and ***Tab. 3-4***). The following EBSD maps are mainly characterized by olivine grains: white colour indicates non-indexed portion (*e.g.*, glass or other not considered mineral phases such as plagioclase and clinopyroxene) and some olivine grain non-indexed because of poor local surface quality caused by defects not eliminated during the polishing procedure.

Olivine grain size is described by the **Equivalent diameter (µm)** and the **Grain Area (µm^2)** parameters (already described in **Chapter 2)**. In the Grain Area map, dark blue represents the smallest grains whereas yellow the largest. The aforementioned parameters are firstly compared to the elongation of grain defined by the **Aspect Ratio**. In these maps, the color-codes vary from blue to yellow (from 1 to 5, respectively), in order to represent the least and the most elongated grain respectively (***Fig. 4-12***). The value of Aspect Ratio in the experiments with 10 and 50wt%$_{IMA}$ is higher (1.49 ± 0.20 to 1.57 ± 0.25, respectively) than one in the run MG4 with 25wt%$_{IMA}$, whose value is slightly lower (1.44 ± 0.12). Overall, no differences are observed between small and large crystals in terms of elongation values, independently of the different initial melt amount (***Fig. 4-12, 4-13***).

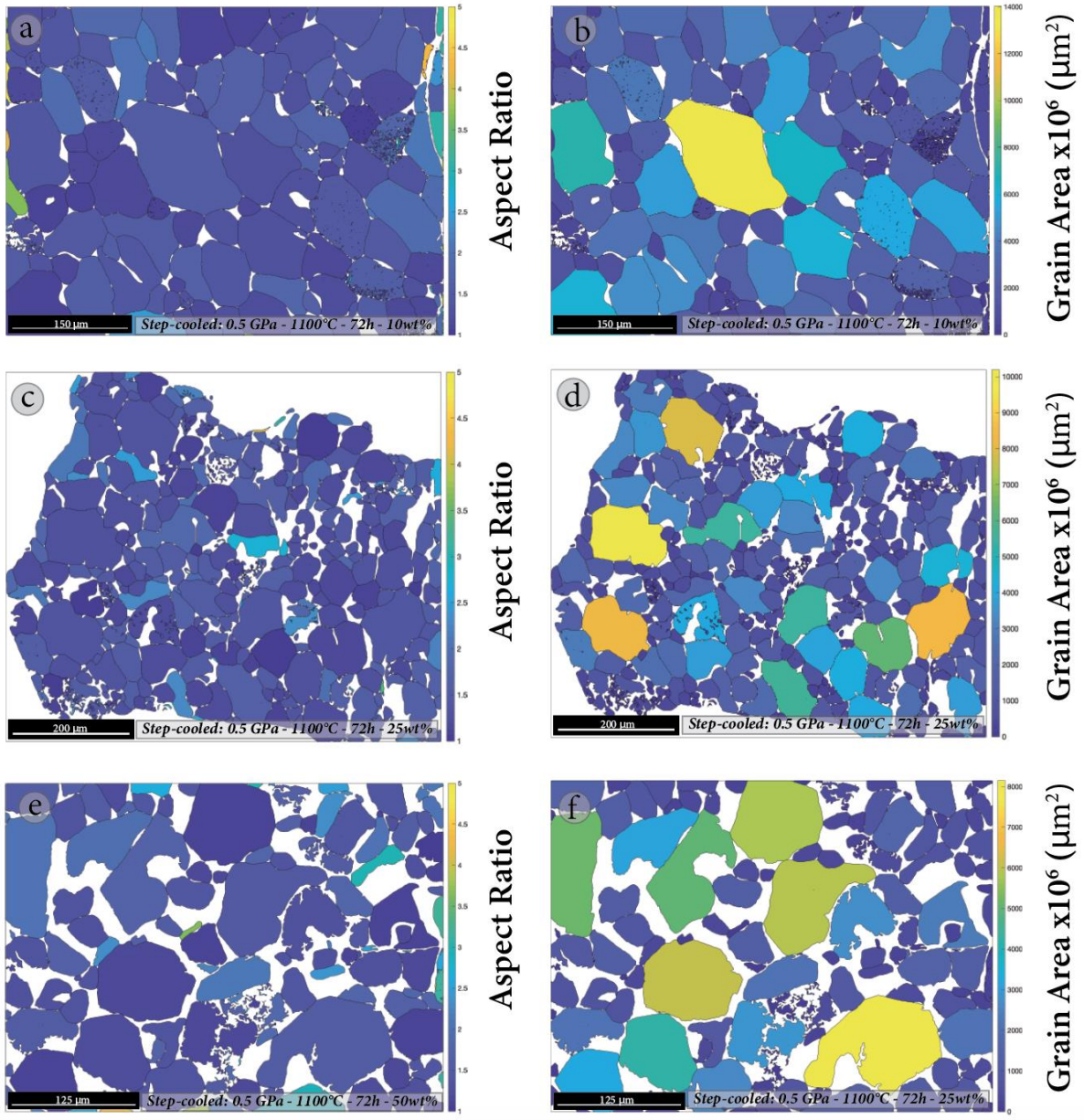

Figure 4-12 *EBSD Aspect Ratio (a, c, e) and Grain Area (b, d, f) maps for each step-cooled experiment with 10wt% (a-b), 25wt% (c-d) and 50wt% (e-f) of initial melt amount.*

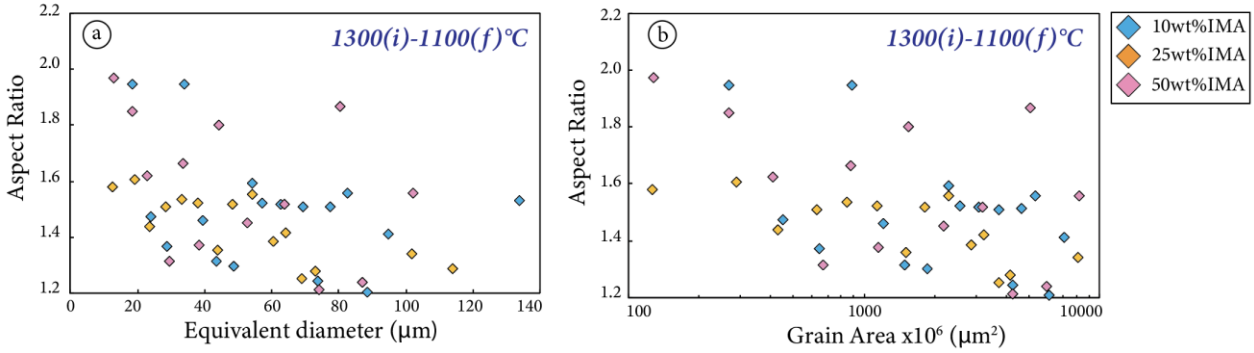

Figure 4-13 *(a) Aspect Ratio vs. Equivalent diameter (µm) and (b) Aspect Ratio vs. Grain Area (µm²) of reactive crystallization experiments performed at 1100°C with different initial melt amount.*

In the sample maps shown in *Fig.* ***4-14*** blue indicates low Shape Factor values and yellow high Shape Factor of olivine crystals. Shape Factor values are also numerically reported in diagram and compared to the Equivalent Diameter and the Grain Area (***Fig. 4-16a-b***). The PARIS Factor is only quantitatively defined and correlated to the Equivalent diameter and the Grain Area in ***Fig. 4-16c-d***. Overall, both the Shape and PARIS Factor values increase with the initial melt amount IMA (from 1.24 ± 0.11 to 1.31 ± 0.14 and from 15.85 ± 11.50 to 24.42 ± 19.25, respectively). BSE images and EBSD data (*i.e.*, GOS) have highlighted two main olivine morphologies: i) large subhedral crystals (up to 100 µm) with both straight and lobate rims (***Fig. 4-15b***) and ii) smaller and rounded grains (5-20 µm) (***Fig. 4-15c***). Hence, there are no differences, in terms of tortuosity grade, between smaller and larger olivine grains.

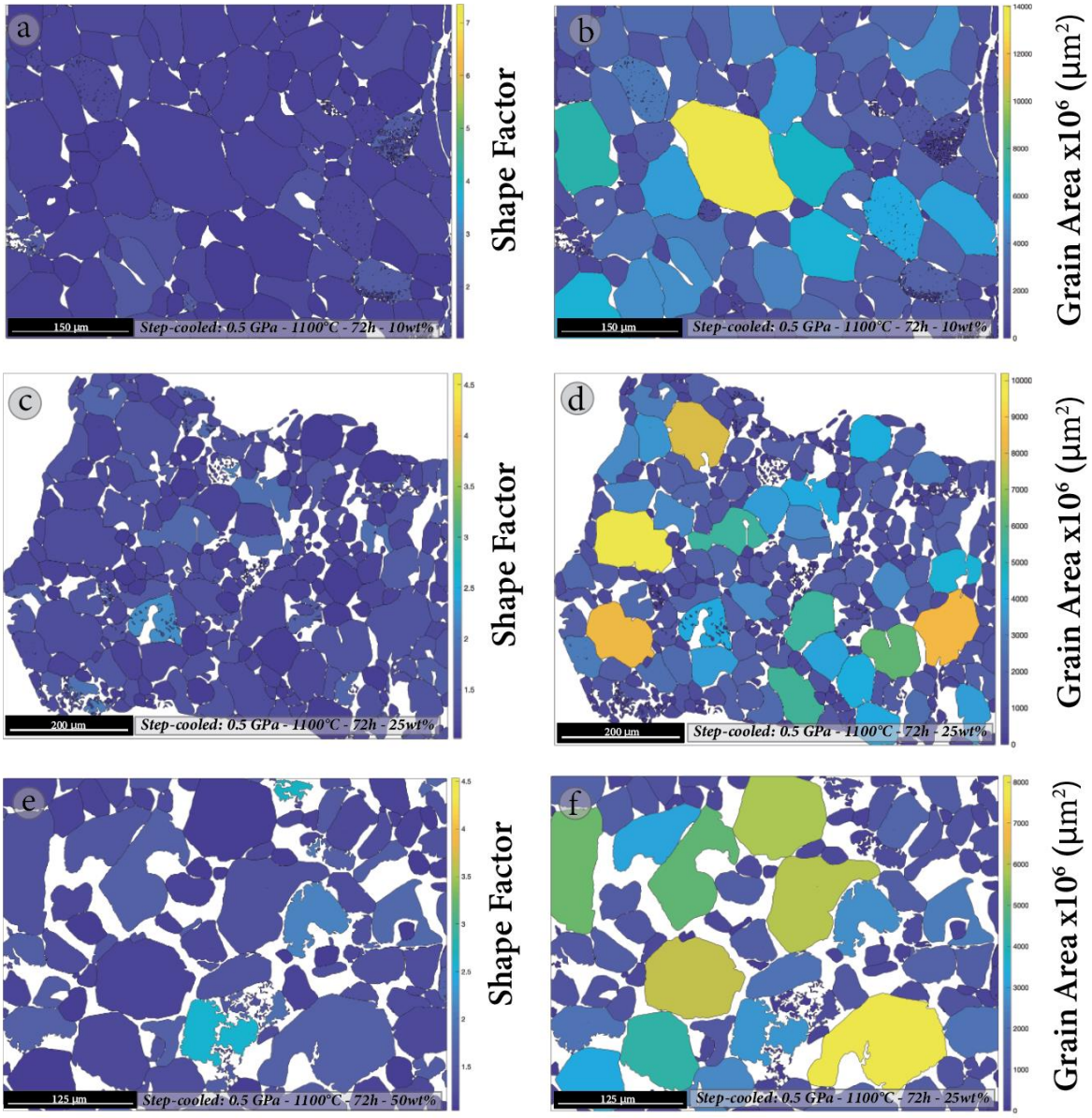

Figure 4-14 *EBSD maps showing the Shape Factor and Grain Area for each step-cooled experiment with 10wt% (a-b), 25wt% (c-d) and 50wt% of initial melt amount (e-f).*

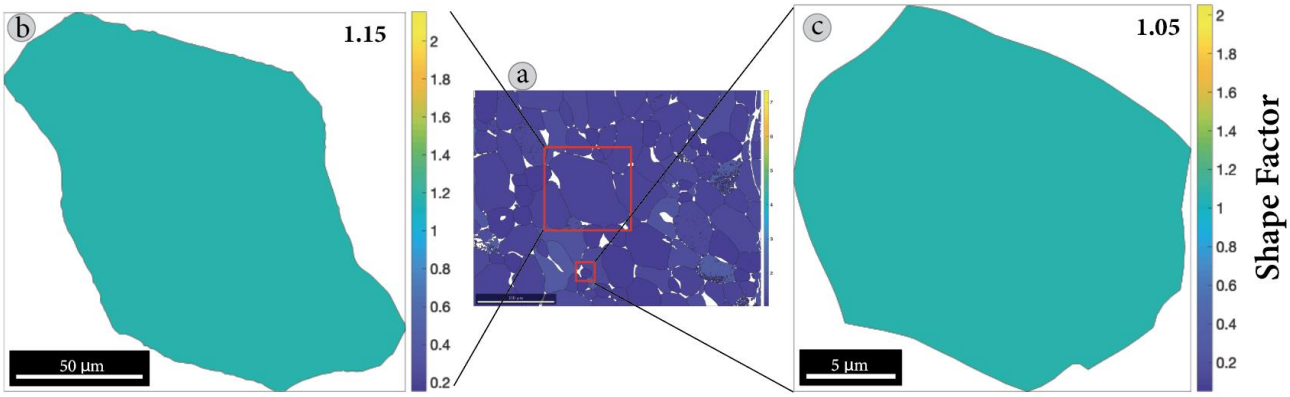

Figure 4-15 *(a) Shape Factor map with details of (b) large subhedral crystals (~134 µm) with both straight and lobate rims and (c) smaller rounded grains (21 µm) in reactive crystallization experiment performed at 0.5 GPa and 1100°C with 10wt% of initial melt amount.*

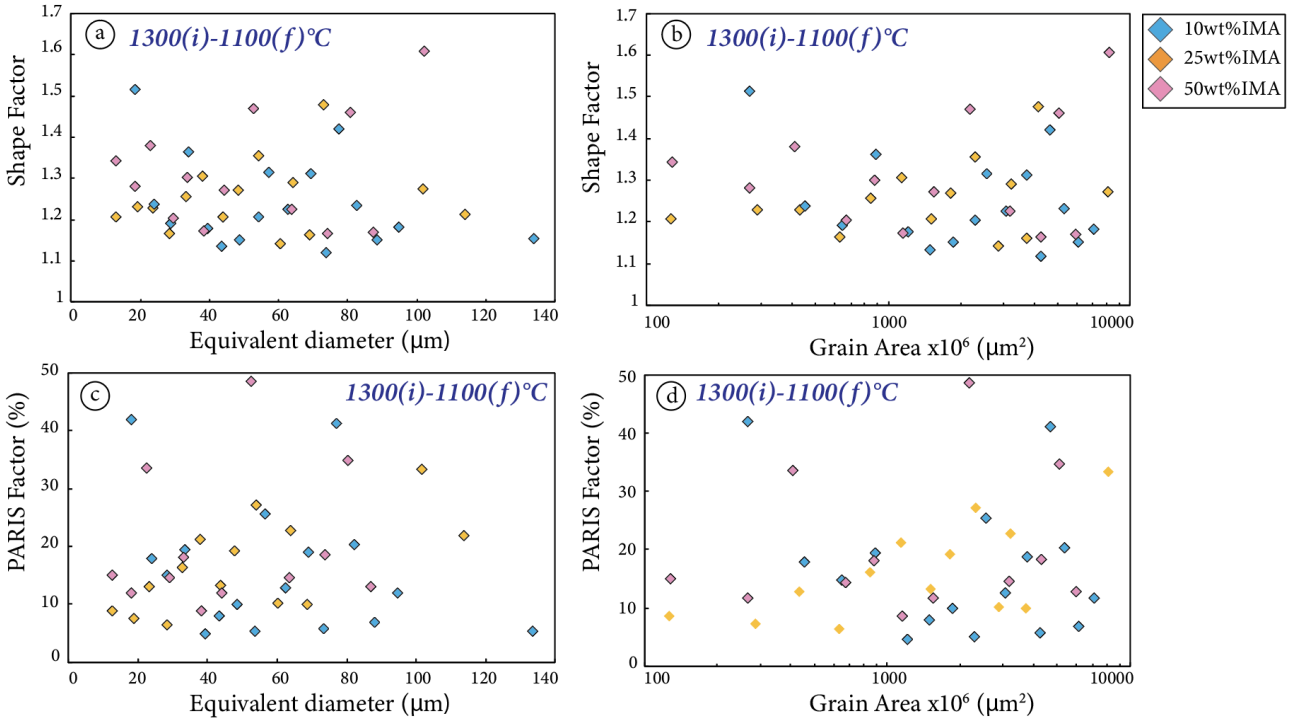

Figure 4-16 *Shape Factor and PARIS Factor vs. Equivalent diameter (µm) (a-c) and vs. Grain Area (µm²) (b-d) of reactive crystallization experiments performed at 0.5 GPa and temperature of 1100°C with different initial melt amount.*

The elaboration of EBSD data through the MTEX toolbox quantified the amount of small grains (15-20 µm) for each step-cooled experiment (***Tab. 4-4***). Contrarily to isothermal experiments (***Fig. 3-21***), in which the number of small grains (5-20 µm) decreases with the increase of initial melt amount and the decrease of modal olivine (vol%), the EBSD data of step-cooled runs do not show any correlation with IMA (***Fig. 4-17***).

	Run	Initial melt amount (wt%)	N° small grains (5-20 µm)	Tot grains	%	Modal olivine (vol%)
Step-cooled at $1300_{(i)}$ -$1100_{(f)}$°C	MG15	10	19	120	16	89
	MG4	25	108	183	60	75
	MG16	50	46	108	43	55

Table 4-4 *Number of smaller grains (5-20 µm) of olivine for each reactive crystallization experiment performed at 1100°C (P= 0.5 GPa) with different initial melt amount.*

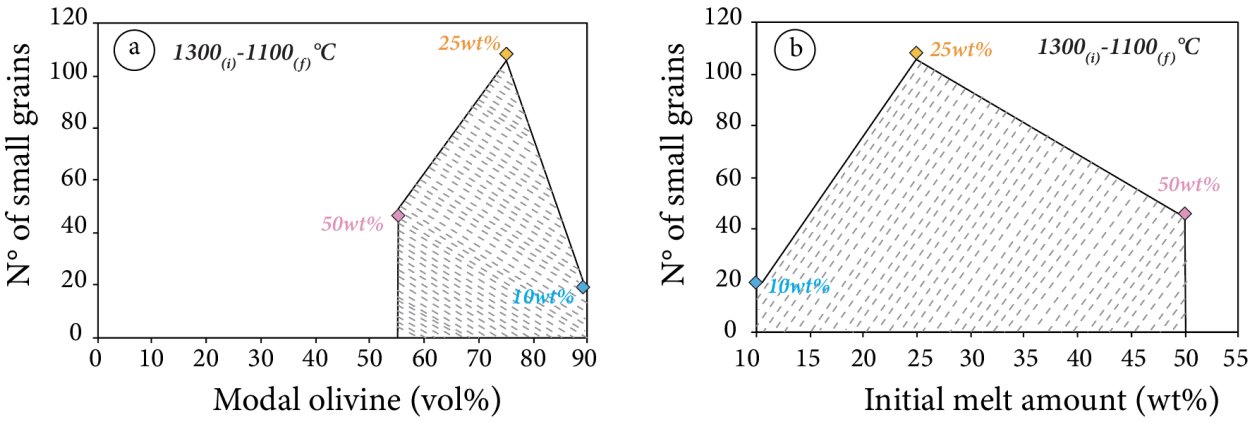

Figure 4-17 *Number of small grains (5-20 µm) vs. (a) modal olivine (vol%) and (b) initial melt amount (wt%) for reactive crystallization experiments performed at 0.5 GPa, at 1100°C.*

4.2.4 – The study of deformation grade of olivine grains – EBSD analysis

EBSD data elaboration through the MTEX toolbox implemented in MatLab provided interesting information on the intra-granular deformation of grains resulted from reactive crystallization process starting from different melt/olivine ratio (IMA). In this section, deformation parameters (details in **Chapter 2** and ***Tab. 3-4*)** such as Grain Orientation Spread (GOS), Misorientation to Mean (Mis2Mean) and Kernel Average Misorientation (KAM) will be discussed. Data are presented in ***Figs. 4-18, 4-19, 4-20, 4-21, 4-22.***

Tab. 4-5 reports the summary of the intra-granular deformation as average values for each step-cooled experiment by considering the selected grain size classes (10-15 µm to 130-135 µm). A more detailed discussion will be addressed in **Sections 4.2.4.1**.

Run		Initial melt amount	Grain area (micron^2)	σ^a	Equivalent diameter (micron)	σ	GOS (°)	σ
Step-cooled at	MG15	10	3526.32	3402.28	60.49	29.68	0.54	0.13
$1300_{(i)}$ -$1100_{(f)}$°C	MG4	25	2759.41	2917.73	52.14	29.16	0.54	0.10
	MG16	50	2606.56	2547.78	50.66	28.53	0.52	0.08

Table 4-5 *Summary of intra-granular deformation value of the reactive crystallization experiments performed at 0.5 GPa and 1100°C (final T) with different initial melt amount (10, 25 and 50wt%). All grain size classes are considered. [a] σ = standard deviation.*

4.2.4.1 –Olivine intra-granular deformation parameters and initial melt amount

The aim of this section is to evaluate how the initial melt amount (10, 25 and 50wt%) affects the olivine intra-granular deformation grade in step-cooled experiments. The microstructural information is provided by EBSD analysis by comparing the grains size in terms of Equivalent diameter and Grain Area with deformation parameters such as, Grain Orientation Spread (GOS), Misorientation to Mean (Mis2Mean) and Kernel Average Misorientation (KAM). Experiments were studied defining a series of grain size classes from 5-10 µm to 130-135 µm. The complete textural dataset is reported in ***Tab. 7-17, 7.18, 7-19*** **(in Appendix)**.

It is important to remind that, as mentioned in **Section 3.1.4.1**, the San Carlos olivine is not naturally deformed but a process of sintering leads to a high grade of deformation (details in ***Fig. 3-30***, *from Francomme, J. E., PhD Thesis 2016-2017*). ***Fig. 4-18*** shows the Grain Orientation Spread (GOS) maps indicating that no significant difference in GOS values is observed between the experiments with 10 and 25wt%$_{IMA}$ (GOS = 0.54 ± 0.13 and GOS = 0.54 ± 0.10, respectively), whereas the GOS value of the experiment with 50wt%$_{IMA}$ is slightly lower (0.52 ± 0.08) (***Fig. 4-18, 4-19***). Overall, the reaction

and crystallization processes simulated by the step-cooled experiments result in a very low-grade deformation independently to the initial melt amount and the different grain size (***Fig. 4-19, 4-20)***.

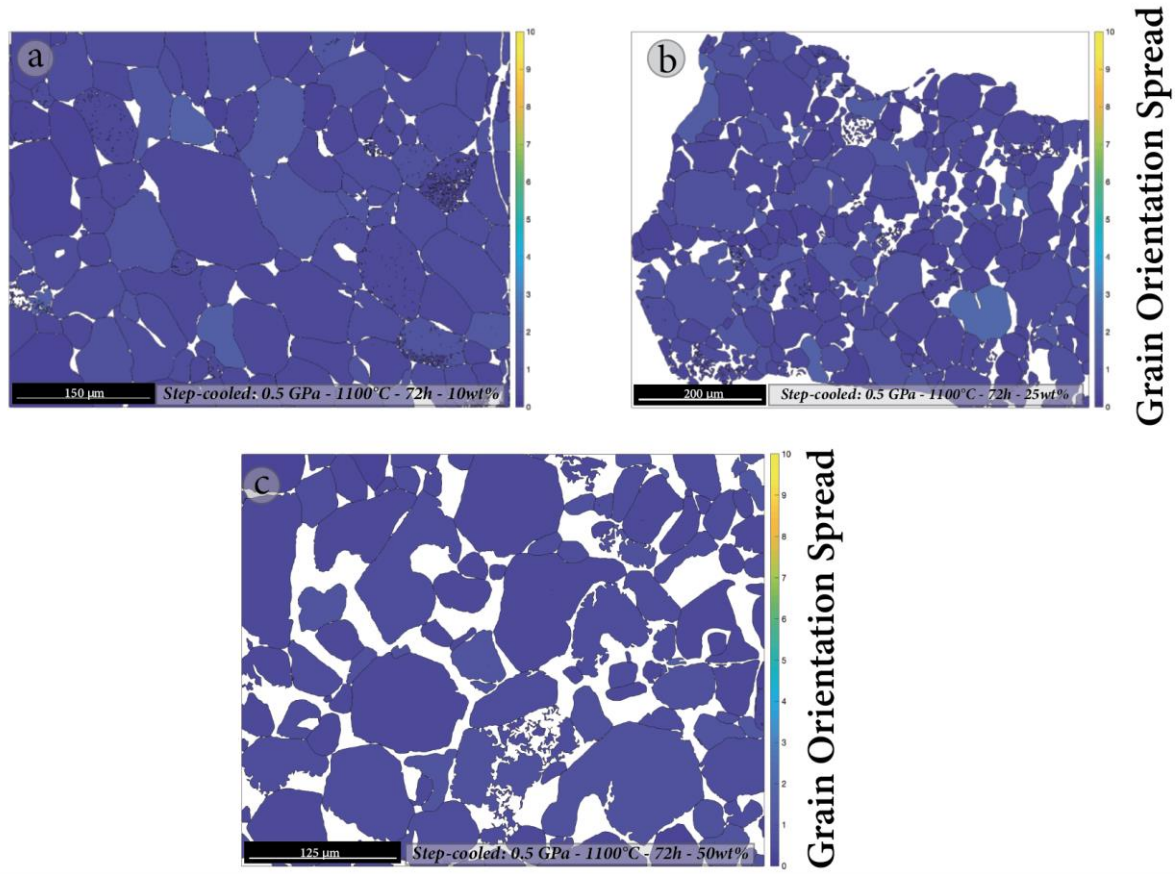

Figure 4-18 *EBSD maps representative of Grain Orientation Spread (GOS) in the step-cooled experiments performed at 1100°C with 10wt% (a), 25wt% (b) and 50wt% of initial melt amount (c).*

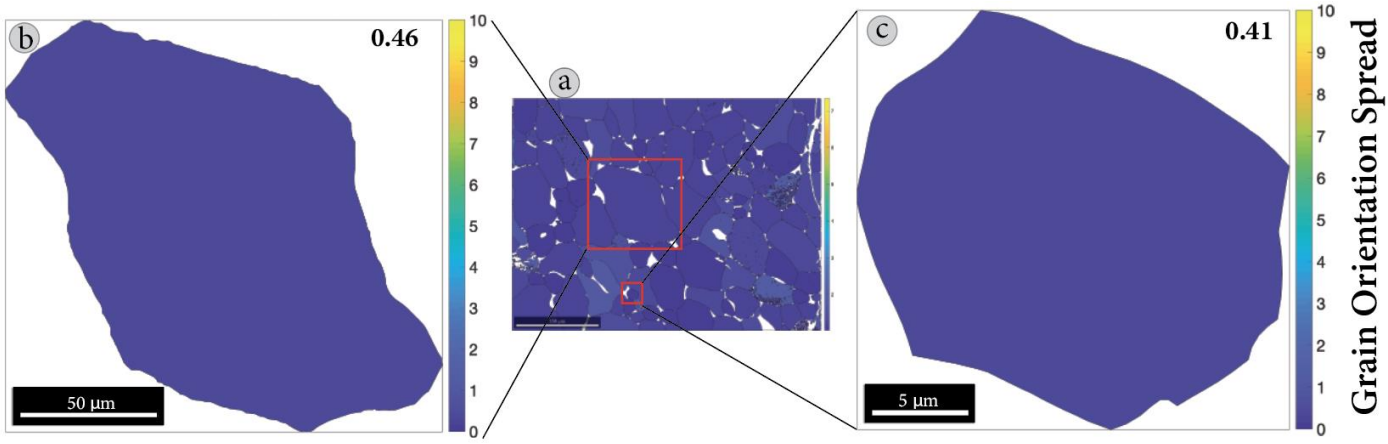

Figure 4-19 *(a) Grain Orientation Spread (GOS) map with details of (b) large subhedral deformed and corroded crystals (~134 µm) with both straight and lobate rims and (c) smaller undeformed rounded grains (21 µm) in reactive crystallization experiment performed at 0.5 GPa and 1100°C with 10wt%$_{IMA}$.*

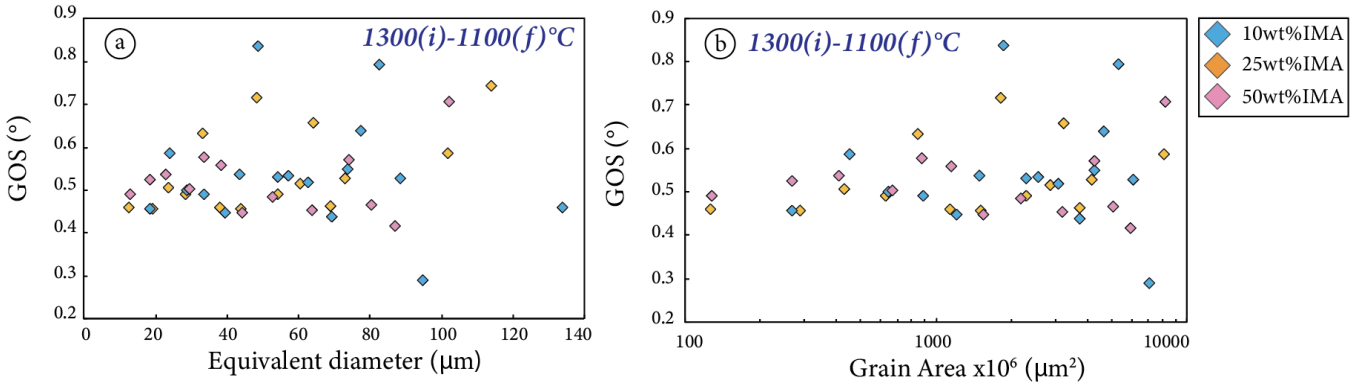

Figure 4-20 *(a) Grain Orientation Spread (GOS) vs. Equivalent diameter (µm) and (b) Aspect Ratio vs. Grain Area (µm²) of reactive crystallization experiments performed at 1100°C and 0.5 GPa with different initial melt amount.*

The decreasing of the average intra-granular deformation of olivine crystals, indicated by the Grain Orientation Spread (GOS) parameter, is correlated to the **Misorientation to Mean** (Mis2Mean) and **Kernel Average Misorientation** (KAM) parameters (details in ***Tab. 3-3*** and **Chapter 2**). ***Fig. 4-21*** shows the Mis2Mean and KAM maps of step-cooled experiments, reporting the occurrence of kink bands in some olivine grains in run with 10wt%$_{IMA}$ (***Fig. 4-21a-b***). In particular, some of the kink bands in olivine grains correspond to the boundary of sub-grains (***Fig. 4-22a-b***). On the contrary, in the run with 50wt%$_{IMA}$ no evidences of kink bands and sub-grains were observed (***Fig. 4-21e-f***).

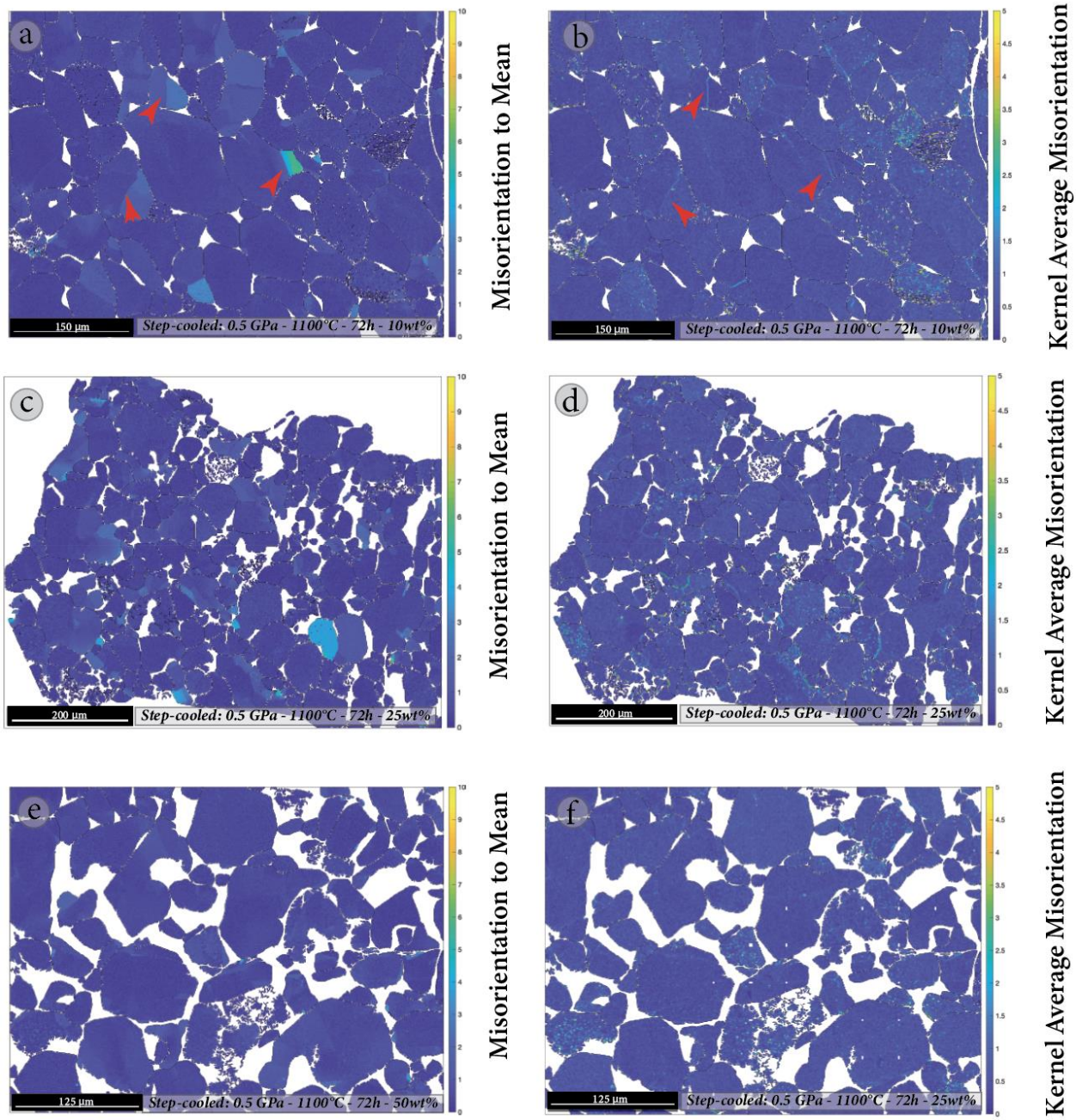

Figure 4-21 *EBSD maps representative of Misorientation to Mean and Kernel Average Misorientation for each step-cooled experiment performed at 1100°C with 10wt%$_{IMA}$ (a-b), 25wt%$_{IMA}$ (c-d) and 50wt%$_{IMA}$ (e-f). Red arrows in (a-b) show the occurrence of kink bands and sub-grains (details in Fig.* ***4-22a-b****, respectively).*

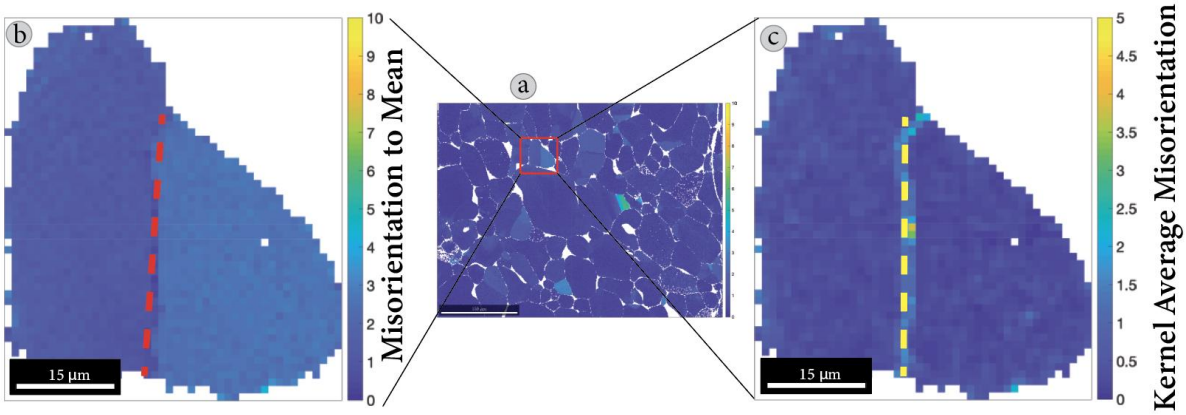

Figure 4-22 *(a) Mis2Mean map with details (b) displaying the occurrence of kink bands (red dashed lines). In the KAM maps (c) is shown the boundary of sub-grains (yellow dashed lines) in a large subhedral deformed and corroded crystals (~51 µm) with both straight and lobate rims (reactive crystallization experiment with 10wt%$_{IMA}$)*

Chapter 5
DISCUSSION

The aim of this study was to investigate how the initial melt amount affects the origin of olivine-rich troctolite through melt-rock reaction processes at mantle-crust transition and to provide new insights on chemical and microstructural modification. The experiments performed in this study differ from the layered coupled reaction experiments performed by Francomme, J. E., (2016-2017) and Borghini et al., (2018). Experiments on mixtures made by variable proportions of San Carlos olivine (Fo_{90}) and a relatively evolved MORB-type melt (X_{Mg}= 0.62 and X_{Ca}= 0.77) allowed to quantify the residual reacted melt resulted from the reaction with the olivine matrix. In this chapter, the experimental results will be discussed in terms of:

1- Phases abundances in order to understand how IMA (*i.e.*, 10, 25 and 50wt%) affects the resulted lithology, the amount of dissolved olivine and of the residual reacted melt at different temperature.
2- The role of *T* and IMA in modifying the texture of olivine during the reaction with melts comparing the experimental data to natural troctolites from the mid-ocean ridge environment (*e.g.*, Suhr et al., 2008; Drouin et al., 2009), the ophiolitic analogues (*e.g.*, Rampone et al., 2004, 2005; Borghini & Rampone, 2007; Borghini et al., 2007; Rampone & Borghini, 2008; Renna & Tribuzio, 2011; Sanfilippo & Tribuzio, 2013; Sanfilippo et al., 2014; Basch et al., 2019) and experiments performed at 0.5 and 0.7 GPa (Francomme, J. E., 2016-2017; Borghini et al., 2018).
3- The role of *T* and IMA in affecting the chemistry of the reacted olivine, interstitial phases (*i.e.*, plagioclase and clinopyroxene) and reacted melt. Chemical data will be compared to natural olivine-rich troctolite and experimental data as mentioned above.
4- The "recovery" of plastic deformation in reacted olivine from reaction and crystallization experiments. A detailed textural and microstructural study provided by the EBSD analysis evaluating intra-granular deformation (*i.e.*, GOS, Mis2Mean and KAM) that will be compared to natural occurrences (*i.e.*, Basch et al., 2018, 2019 and 2021; Ferrando et al., 2019) and experimental data (Francomme, J. E., 2016-2017).

5.1 – Phases abundance

Figs. 5-1, 5-2, 5-3 and ***5-4*** report the phases abundance obtained by mass-balance calculations based on the least squares (LS) method performed using Mathematica Software. In order to take into account the error propagation of uncertainties in the analytical determination of the phases chemical composition, a Monte Carlo approach was considered. Different sets of data have therefore been obtained by collecting 10.000 randomly distributed values around the averages of chemical components. The chemical components considered in the mass-balance-calculations were: SiO_2, Al_2O_3, Cr_2O_3 FeO_{tot}, MgO, CaO, Na_2O, NiO, TiO_2. Three different bulk compositions were used as to simulate different initial melt amount (*i.e.*, 10, 25 and 50wt%) and the average composition of San Carlos olivine (Fo_{90}) was assumed among the reactants. For the reacting MORB-type melt, the composition of the synthetic tholeiitic glass – AH6 (X_{Mg}= 0.62 and X_{Ca} = 0.77) was used. For the products of the reaction we used the observed mineral composition.

Unfortunately, due to the negligible chemical differences between smaller - rounded olivine grains and larger ones with irregular habit, the amount of neo-formed olivine cannot be defined by mass-balance calculations (see ***Tab. 3-1***). Hence, the experiments will be described in terms of total amount of olivine and the proportions of interstitial phases, *i.e.*, plagioclase, clinopyroxene and glass.

The histograms in ***Figs. 5-1, 5-2 and 5-3,*** show the initial phase proportion (grey column) compared to the final phase abundance after the reaction at 1200, 1250 and 1300°C (brown, orange and green columns). ***Tabs. 5-1, 5-2 and 5-3*** report the results of mass-balance calculations in terms of initial and modeled bulk compositions and the sum of the squares of residuals (R^2).

At **1200°C**, phases abundance in isothermal experiments shows an increase of modal olivine (+8wt%) in the MG14 experiment (IMA=50wt%). In this set of experiments (1200°C) the higher initial melt amount resulted in higher percentages of interstitial phases, *i.e.*, plagioclase and clinopyroxene (from 5.3wt%$_{IMA10}$ to 24wt%$_{IMA50}$ and from 3wt%$_{IMA10}$ to 14wt%$_{IMA50}$, respectively) (***Fig. 5-1***). High sums of squares of residuals (R^2) in ***Tab. 5-1*** suggest that experiments performed with 10wt%$_{IMA}$ (MG10) and 25wt%$_{IMA}$ (MG12) are affected by slightly Ni- and Fe-loss (0.03 and 0.62, respectively), due to the formation of some Ni-Fe oxides. Due to the high rate or crystallization in run with 10wt%$_{IMA}$, the small amount of chemical analysis on residual glass not reflect its real composition but is probably influenced by a quenching effect. Hence, the glass composition of run with 10wt%$_{IMA}$ was not considered in the mass balance calculations.

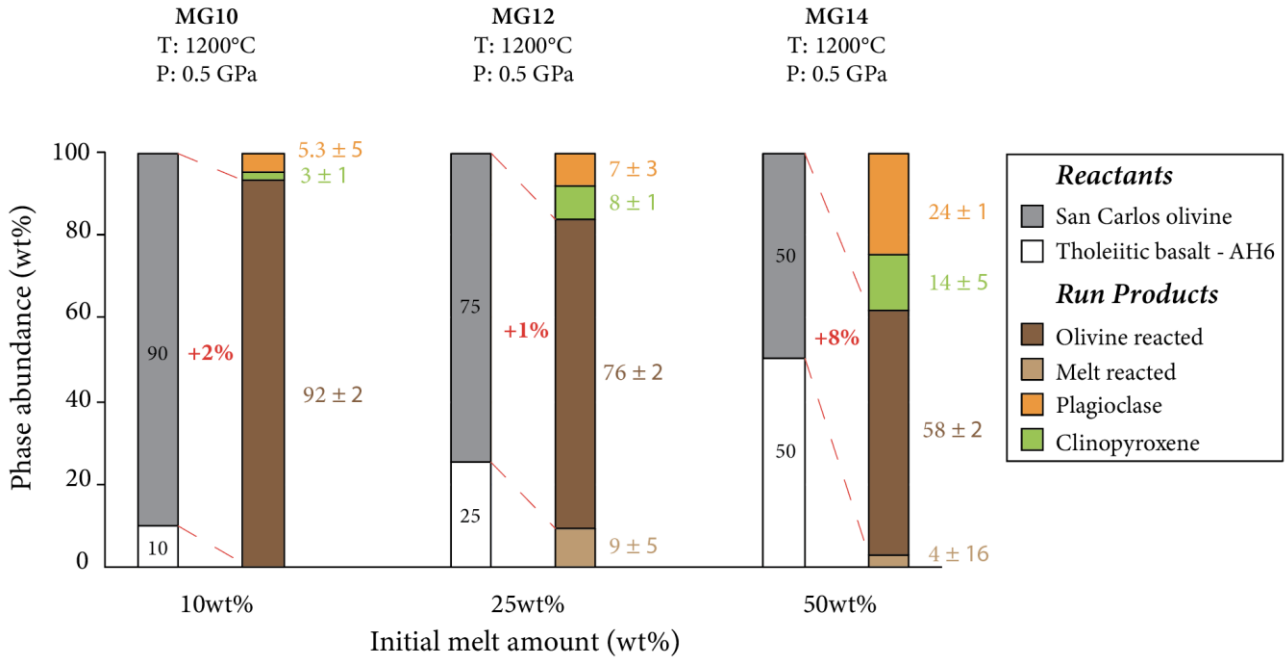

Figure 5-1 *Phases abundance in isothermal experiments performed at 0.5 GPa and 1200°C derived by mass balance calculations. The histogram shows the initial phase proportion (grey column) compared to the final phase proportion after the reaction at 1200°C (brown, orange and green columns). Red dashed lines indicate the olivine increase (+8wt%) after the reaction experiments.*

Sample	**MG10**			**MG12**			**MG14**		
Initial melt amoun (wt%)	10			25			50		
T[a]	1200			1200			1200		
P[b]	0.5			0.5			0.5		
Components	Bulk[c]	Model[d]	Residuals^2[e]	Bulk	Model	Residuals^2	Bulk	Model	Residuals^2
SiO_2	41.69	41.60	0.01	42.72	42.89	0.03	44.45	44.63	0.03
TiO_2	0.09	0.08	0.00	0.22	0.46	0.06	0.44	0.32	0.01
Al_2O_3	1.69	1.78	0.01	4.23	3.99	0.06	8.43	8.22	0.04
Cr_2O_3	0.04	0.03	0.00	0.05	0.03	0.00	0.06	0.05	0.00
FeO	9.03	10.13	1.22	9.11	8.32	0.62	9.26	9.09	0.03
MgO	45.43	45.26	0.03	39.28	39.29	0.00	29.05	28.93	0.01
NiO	0.33	0.16	0.03	0.28	0.22	0.00	0.19	0.13	0.00
CaO	1.45	1.61	0.03	3.52	3.26	0.07	6.97	6.72	0.06
Na_2O	0.24	0.21	0.00	0.58	0.81	0.05	1.15	1.10	0.00
Sum of squares of residuals	1.32			0.89			0.21		

Table 5-1 *Mass-balance output for isothermal experiments performed at 1200°C (P = 0.5 GPa with initial melt amount 10, 25 and 50wt%). [a] Temperature. [b] Pressure. [c] Starting bulk composition. [d] Model bulk composition. [e] Sum of the squares of the residuals.*

- At **1250°C**, in the MG11 run, olivine final proportion is 47wt% (***Fig. 5-2***), suggesting that high initial melt amount (IMA = 50%) led to olivine dissolution. High sums of squares of residuals (R^2), reported in ***Tab. 5-2*** show that experiments performed with 50wt%$_{IMA}$ is characterized by a Ni and Fe-loss (0.02 and 0.61, respectively), due to the formation of Ni-Fe oxides.

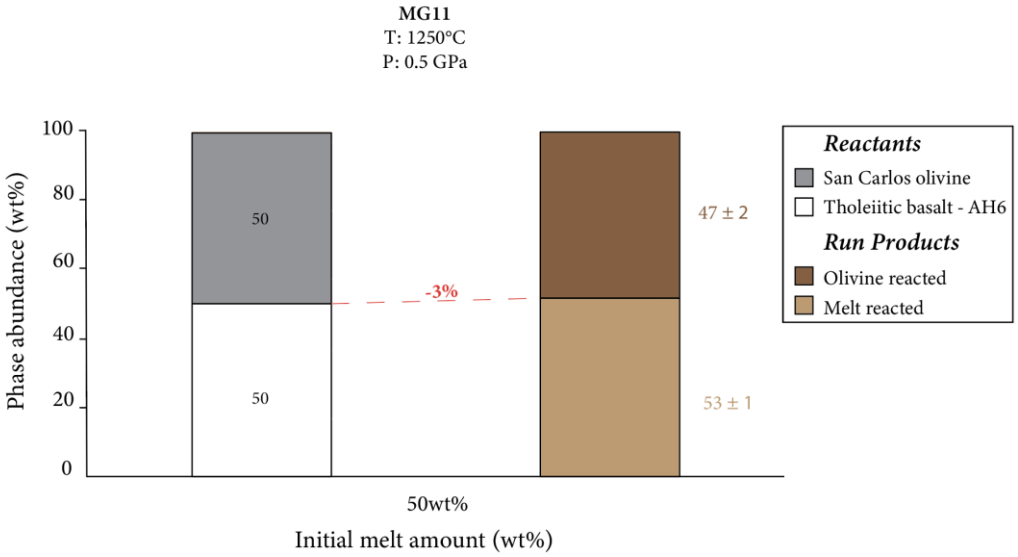

Figure 5-2 *Phases abundance in isothermal experiment performed at 0.5 GPa and 1250°C derived by mass balance calculations. The histogram shows the initial phase proportion (grey column) compared to the final phase proportion after the reaction at 1250°C (brown columns). Red dashed lines indicate the rate of olivine dissolution (-3wt%) after the reaction experiment.*

Sample	**MG11**		
Initial melt amoun (wt%)	50		
T[a]	1250		
P[b]	0.5		
Components	Bulk[c]	Model[d]	Residuals^2[e]
SiO_2	44.45	44.59	0.02
TiO_2	0.44	0.43	0.00
Al_2O_3	8.43	8.25	0.03
Cr_2O_3	0.06	0.05	0.00
FeO	9.26	8.48	0.61
MgO	29.05	29.07	0.00
NiO	0.19	0.05	0.02
CaO	6.97	7.05	0.01
Na_2O	1.15	1.13	0.00
Sum of squares of residuals	0.68		

Table 5-2 *Mass-balance output for isothermal experiment performed at 1250°C (P = 0.5 GPa with initial melt amount 50wt%). [a] Temperature. [b] Pressure. [c] Starting bulk composition. [d] Model bulk composition. [e] Sum of the squares of the residuals.*

- At **1300°C**, olivine final proportion is 45wt%, suggesting that high initial melt amount (IMA = 50wt%) led to an increase of olivine dissolution at increasing of initial melt amount (***Fig. 5-3***). High sums of squares of residuals (R^2) in ***Tab. 5-3*** show that, also in this case, experiments performed with 25, and 50wt%$_{IMA}$ are characterized by a Ni- loss of 0.06 and Ni-Fe-loss (0.03 and 2.21, respectively), due to the formation of some Ni-Fe oxides.

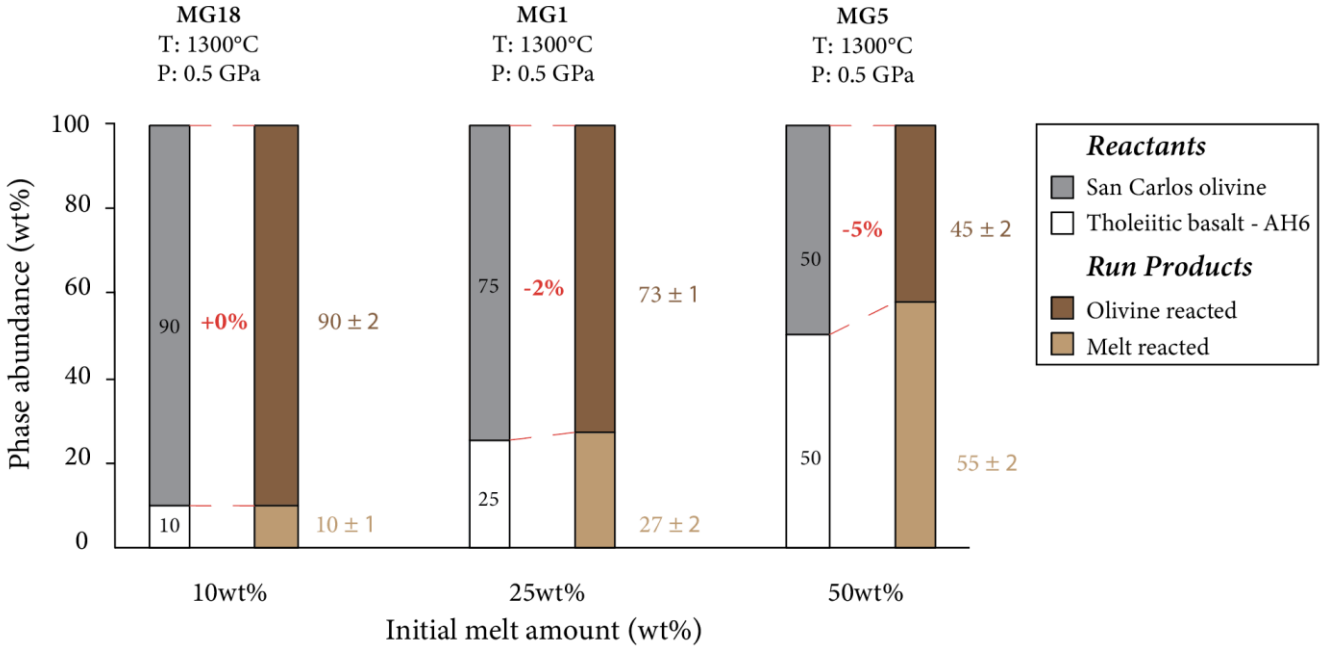

Figure 5-3 *Phases abundance in isothermal experiments performed at 0.5 GPa and 1300°C derived by mass balance calculations. The histograms show the initial phase proportion (grey column) compared to the final phase proportion after the reaction at 1300°C (brown columns). Red dashed lines indicate the increase of olivine dissolution (-5wt%) after the reaction experiments.*

Sample	**MG18**			**MG1**			**MG5**		
Initial melt amoun (wt%)	10			25			50		
T[a]	1300			1300			1300		
P[b]	0.5			0.5			0.5		
Components	Bulk[c]	Model[d]	Residuals^2[e]	Bulk	Model	Residuals^2	Bulk	Model	Residuals^2
SiO_2	41.69	41.49	0.04	42.72	42.64	0.01	44.45	44.54	0.01
TiO_2	0.09	0.09	0.00	0.22	0.24	0.00	0.44	0.46	0.00
Al_2O_3	1.69	1.53	0.03	4.23	4.30	0.00	8.43	8.55	0.01
Cr_2O_3	0.04	0.04	-6.00	0.05	0.03	0.00	0.06	0.04	0.00
FeO	9.03	10.28	1.56	9.11	9.14	0.00	9.26	7.78	2.21
MgO	45.43	45.32	0.01	39.28	39.33	0.00	29.05	29.20	0.02
NiO	0.33	0.14	0.04	0.28	0.04	0.06	0.19	0.01	0.03
CaO	1.45	1.48	0.00	3.52	3.66	0.02	6.97	7.16	0.04
Na_2O	0.24	0.21	0.00	0.58	0.58	0.00	1.15	1.12	0.00
Sum of squares of residuals	1.68			0.09			2.33		

Figure 5-3 *Mass-balance output for isothermal experiment performed at 1300°C (P = 0.5 GPa with initial melt amount 10, 25 and 50wt%). [a] Temperature. [b] Pressure. [c] Starting bulk composition. [d] Model bulk composition. [e] Sum of the squares of the residuals.*

Fig. 5-4 reports the phases abundance derived by mass-balance calculations for step-cooled experiments. Similarly to isothermal experiments, the homogenous mineral chemistry of olivine does not allow to distinguish the pre-existing olivine and the amount of new olivine (see ***Tab. 4-1***). Hence, the reactive crystallization experiments will be described in terms of total amount of olivine and interstitial phases (*i.e.*, plagioclase, clinopyroxene and glass). The histogram shows the initial phase proportion (grey column) compared to the final phase proportion after the reaction and crystallization at 1100°C (brown, orange and green columns). The crystallization of residual melt from the reaction between olivine and basaltic glass at higher initial melt amount (50wt%), results in a slightly increase of the final amount of olivine (+5wt%). Furthermore, the increase of the initial melt amount leads to a gradual appearance of the interstitial phases. Into details, the final products of the step-cooled experiment MG18 (10wt%$_{IMA}$) results only in olivine and glass but, increasing the melt amount to 25wt%, a minor content of clinopyroxene was detected. A further increase of the IMA (up to 50wt%) leads to a co-precipitation of clinopyroxene and plagioclase as can be seen in ***Fig. 5-4***. High sums of squares of residuals (R^2), reported in ***Tab. 5-4***, show that experiments performed with 10, 25 and 50wt%$_{IMA}$ are characterized by a Ni-Fe-loss (0.07 and 0.12, 0.07 and 1.45, 0.02 and 20.38, respectively), due to the formation of some Ni-Fe oxide.

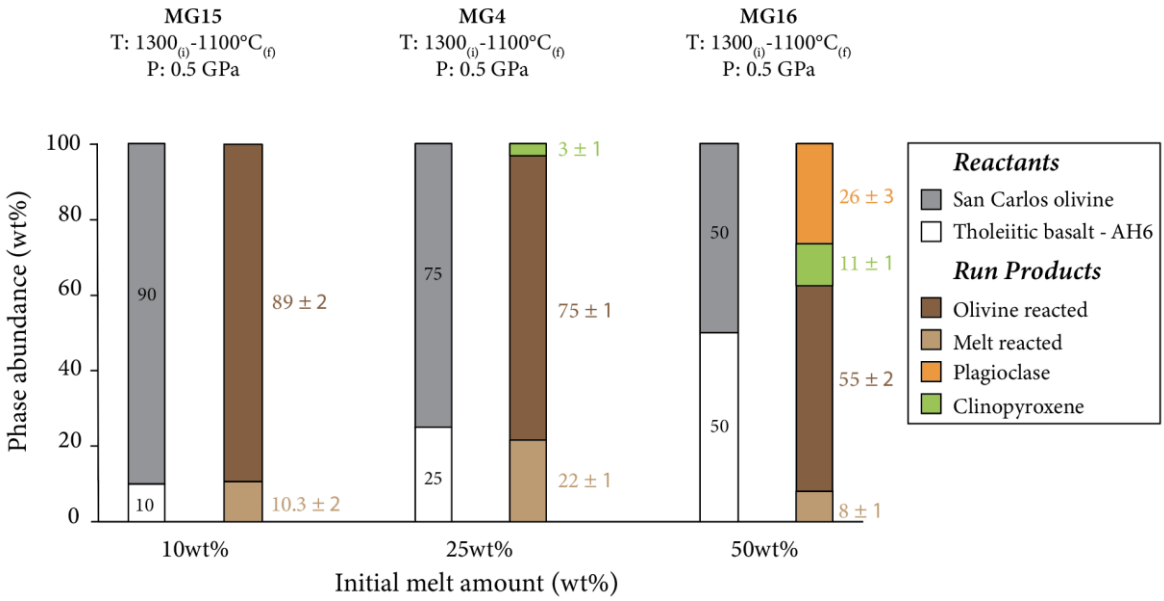

Figure 5-4 *Phases abundance in step-cooled experiments performed at 0.5 GPa (starting and final T are 1300°C and 1100°C, respectively) derived by mass balance calculations. The histogram shows the initial phase proportion (grey column) compared to the final phase proportion after the crystallization of reacted melt at 1100°C (brown, orange and green column).*

Sample	MG15			MG4			MG16		
Initial melt amoun (wt%)	10			25			50		
T[a]	$1300_{(i)}$-$1100_{(f)}$			$1300_{(i)}$-$1100_{(f)}$			$1300_{(i)}$-$1100_{(f)}$		
P[b]	0.5			0.5			0.5		
Components	Bulk[c]	Model[d]	Residuals^2[e]	Bulk	Model	Residuals^2	Bulk	Model	Residuals^2
SiO_2	41.69	41.81	0.01	42.72	42.72	0.00	44.45	43.52	0.86
TiO_2	0.09	0.09	-7.00	0.22	0.23	0.00	0.44	0.18	0.07
Al_2O_3	1.69	1.39	0.09	4.23	4.55	0.10	8.43	9.53	1.22
Cr_2O_3	0.04	0.03	0.00	0.05	0.03	0.00	0.06	0.05	0.00
FeO	9.03	8.68	0.12	9.11	7.91	1.45	9.26	4.75	20.38
MgO	45.43	45.38	0.00	39.28	39.51	0.05	29.05	30.42	1.88
NiO	0.33	0.07	0.07	0.28	0.02	0.07	0.19	0.06	0.02
CaO	1.45	1.41	0.00	3.52	3.42	0.01	6.97	8.74	3.12
Na_2O	0.24	0.20	0.00	0.58	0.62	0.00	1.15	0.96	0.03
Sum of squares of residuals	0.30			0.28	0.02	0.07	27.57		

Table 5-4 *Mass-balance output for each step-cooled experiment performed at final T 1100°C (P = 0.5 GPa with initial melt amount 10, 25 and 50wt%). [a] Temperature. [b] Pressure. [c] Starting bulk composition. [d] Model bulk composition. [e] Sum of the squares of the residuals.*

5.2 – Role of Temperature and melt/olivine ratio on final lithology

The results of mass-balance calculations revealed that temperature and initial melt amount influence the final mineral mode of the experimental assemblages originated by melt-olivine interaction and reactive crystallization. At 1200°C, increasing the IMA from 10 to 50wt% the reaction processes result in the formation of a dunite, olivine-rich troctolite and olivine-gabbro, respectively. IMA strongly affects the crystallization processes and the final phases abundance at 1200°C. In particular, high initial melt amount (to 50wt%) results in growth of olivine modal amount (+8wt%) and the crystallization of interstitial plagioclase and clinopyroxene (24wt% and 14wt%, respectively). The experiments at 1300°C describe how dunite matrix could be impregnated by a reacting MORB-type melt varying the initial melt amount. Moreover, high-*T* reaction experiments allow studying the chemical evolution of reacted melt during the reaction with mantle olivine. On the other hand, run products of step-cooled experiments describe what mineral phases it will crystallize when cooled. At 1300°C, the increase of initial melt amount (*i.e.*, 10, 25 and 50wt%) strongly enhances the olivine dissolution (-5wt% of final modal olivine, ***Fig. 5-3***).

As mentioned before in **Chapter 3**, at 1200°C, 10 and 25wt%$_{IMA}$, BSE images do not permit to recognize the grain boundaries due to the small amount of interstitial phases (***Fig. 3-2***). However, interstitial plagioclase and clinopyroxene occurred in typical *myrmekite* microstructure that suggests their co-precipitation from reacted melt. At 1300°C, the olivine grain boundaries are better visible due

to high amount of interstitial glass. In these experiments, olivine occurs as i) smaller and rounded grains (5-20 μm) or ii) large subhedral crystals (up to 100 μm) with both straight and lobate rims (***Fig. 3-5***). The increase of temperature results in a higher porosity of the matrix.

For the first time, a detailed microstructural study through EBSD analysis provided new textural insights of olivine grains derived by isothermal and step-cooled experiments on olivine matrix and impregnating melt. EBSD analysis on the experimental charges revealed that *T* and IMA play a paramount role in the development of olivine texture. At 1200°C, the olivine grains are slightly finer than those crystallized at 1300°C but also slightly more elongated. At 1300°C (IMA = 50wt%), a further decrease of the amount of small rounded grains with euhedral habit, compared to those larger with irregular habit, is observed (***Fig. 3-21***). Furthermore, at high IMA (50wt%), the reaction leads to the formation of large olivine grains with higher tortuosity grade and Shape Factor (***Figs. 3-21, 3-22, 3-23, 3-27 and 3-28***). Therefore, these results strongly indicate that the initial melt/olivine ratio (IMA) strongly affects the olivine morphology because high initial melt amounts enhance the reaction promoting the olivine crystal growth and the dissolution, resulting in the high tortuosity of olivine grain boundaries.

When a cooling path is followed and the temperature is lowered down at 1100°C, the amount of interstitial melt after the high-*T* reaction strongly affects the final modal abundance of mineral phases. As mentioned in **Section 5.1** (***Fig. 5-4***), high IMA resulted in high amount of (new) crystallized olivine and interstitial phases such as plagioclase and clinopyroxene. The reactive crystallization at relatively low interstitial melt amount (10wt%$_{IMA}$) reflects the initial proportions of olivine and basalt resulting in the formation of dunite characterized by 90wt% of olivine. Increase the initial melt amount at 25 and 50wt% results in the origin of clinopyroxene-bearing troctolite and olivine-gabbro, respectively (***Fig. 5-4*)**. In this case, the EBSD analysis reveals that the olivine matrix in step-cooled experiments is texturally more homogeneous than one in isothermal experiments. Overall, the reaction and the crystallization processes resulted in slightly larger and less tortuous olivine grains than ones in isothermal experiments (***Figs. 4-12, 4-15***). The textural differences between isothermal and step-cooled experiments could be also due to the different run duration: isothermal runs are carried out for 24 hours, whereas the step-cooled ones are performed for 72 hours.

5.2.1 – Effect of the reacted melt composition and H_2O on crystallization sequence.

It is widely known that the crystallization of mid-ocean ridge basalt (MORB) magmas is dominated by olivine (+ spinel) and plagioclase cotectic crystallization (*e.g.*, Grove et al., 1992). The increase of fractionation leads to lower MgO-contents melt due to the crystallization of olivine and to lower Al_2O_3 contents melt due to the crystallization of plagioclase. However, in the experiment **MG4** (25wt%$_{IMA}$, 0.5 GPa, 1100°C), the crystallization of the reacted melt leads to the early appearance of clinopyroxene rather than plagioclase (***Fig. 5-4***). The reacted melt composition of isothermal experiment with the same IMA at 1300°C (MG1) is considered in order to derived the composition of interstitial melt which crystallize when a cooling path is followed. Hence the olivine dissolution at 1300°C leads to the enrichment in MgO content of the reacted melt (11.05wt% ± 1.66) (***Fig. 5-6***) favoring the early clinopyroxene (high-Mg# of 0.91 ± 0.00) crystallization. As expected, in the step-cooled experiment carried out with 25wt%$_{IMA}$ (MG4) the olivine and clinopyroxene crystallization resulted in a decrease of MgO content in residual reacted melt (7.29wt% ± 0.48).

In the fractional crystallization of basalt AH6 (at 0.5 GPa), plagioclase is expected to crystallize before the clinopyroxene (*e.g.*, Husen et al., 2016). Husen et al., (2016) performed equilibrium crystallization experiments on variably evolved basalts and showed that the increase of MgO content in melt favors the early crystallization of clinopyroxene. ***Fig. 5-6*** shows the stability phase diagrams of mineral phases as a function of pressure and temperature for the step-cooled experiment performed with 25wt%$_{IMA}$. Their experimental results suggested that clinopyroxene starts to crystallize before plagioclase at 0.6 GPa for melt with MgO of 8.6wt%.

Danyushevsky et al., (2001) have experimentally demonstrated that small amount of H_2O affects the fractionation paths of MORB and BABB magmas. They inferred that the main effects of H_2O on crystallization of basaltic liquids are to decrease melt liquids temperature, extending the olivine and clinopyroxene stability field and suppressing the plagioclase crystallization. Preliminary Raman spectroscopy investigation performed at the Department of the Earth Science "Ardito Desio" (University of Milan) has revealed (not quantified) small amount of H_2O in experimental glass (MG5 with 50wt%$_{IMA}$) (***Fig. 5-5***), suggesting that experimental conditions are not perfectly dry. This could inhibit the crystallization of plagioclase (Danyushevsky et al., 2001). Hence, a combined effect of small amount of H_2O and the relatively high MgO content in reacted melt could explain the absence of plagioclase in the step-cooled experiment performed with 25wt%$_{IMA}$.

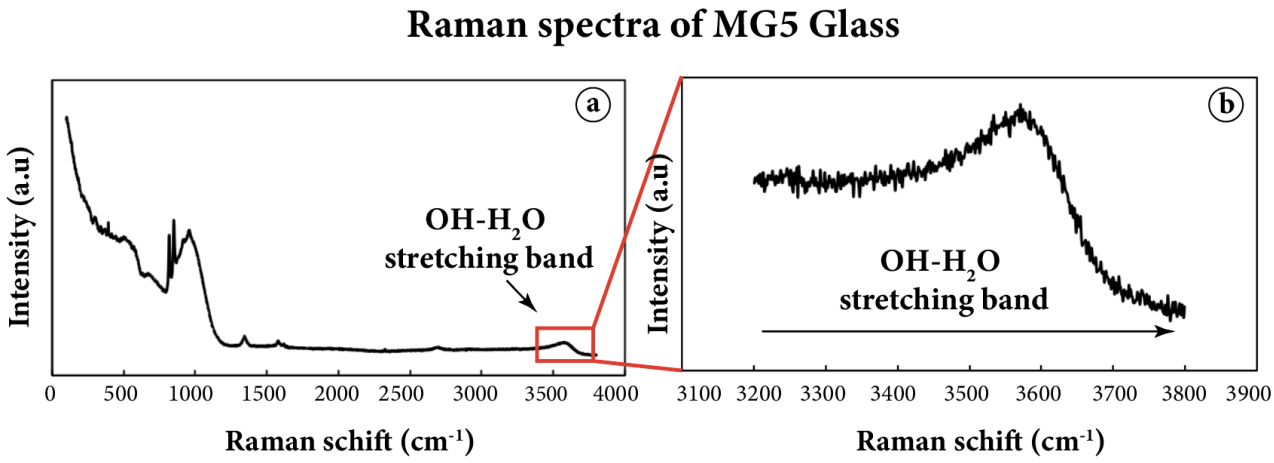

Figure 5-5 *(a) Raman spectra and detail (b) of residual glass in isothermal experiment with 50wt%IMA (MG5). The glass was analyzed by high resolution confocal (hole = 100µm) micro-Raman system (LabRam HR Evolution – Horiba) at the Department of Earth Science "Ardito Desio", University of Milan. Raman spectra were acquired using a Nd-Yag 532 nm/100mW green laser source with Ultra Low Frequency (ULF) filters. A 100x microscope objective and 600 r/mm grating were used for the analyses using a laser power of 100%. Acquisition time was set to 60s with 2 accumulations. The O-H vibrational peak is seen in the Raman spectra at range of 3500-3600 cm^{1}, suggesting the presence of H_2O.*

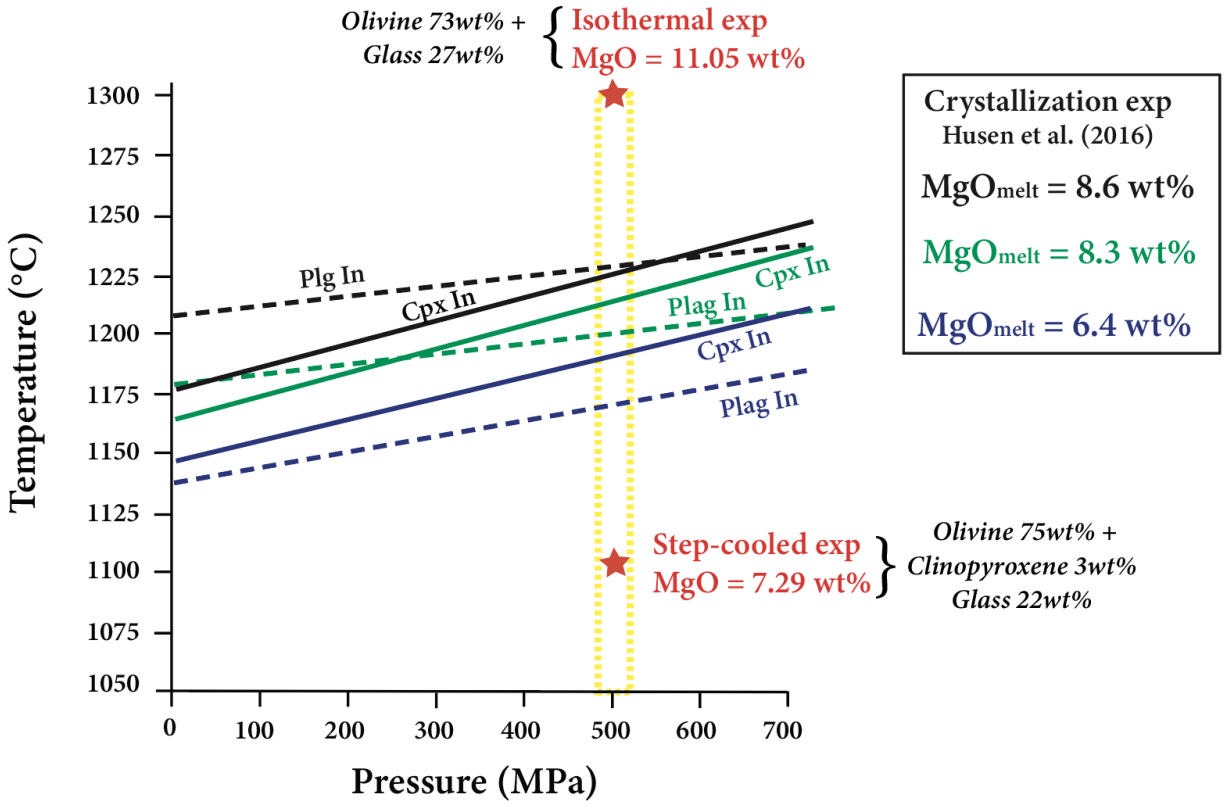

Figure 5-6 *Phase diagrams showing the stability of mineral phases as a function of pressure and temperature for the step-cooled experiment performed at 0.5 GPa and final T of 1100°C compared to experimental data from Husen et al., (2016).*

5.2.2 – The effect of melt-olivine reaction processes on olivine textural evolution

In this section, the experimental results in terms of textural features will be compared to those observed in the reaction experiments performed by Francomme, J. E., (PhD Thesis, 2016-2017), that were carried out using a melt-olivine reaction couple consisting of three layers: 1) basaltic powder, 2) olivine + 9wt%$_{IMA}$ (AH6) powder and 3) vitreous carbon spheres. Although the mobility of melt in the dunite layer was limited, Francomme, J. E., (2016-2017) showed how the textural evolution of olivine related to olivine-melt reaction is time-dependent by performing experiments at different run duration (12, 24 and 60 hours, 0.7 GPa and 1250°C).

In the experiments run for 12 and 24 hours, the olivine crystals occur both as larger grains with irregular habit and cusped rims and smaller rounded. In the run at 60 hours, olivine grain size becomes more homogenous and is characterized by olivine crystals with subhedral-smooth curvilinear and polygonal grain boundaries. In terms of equivalent diameter (µm), the main grain size increases from ~15 to ~27 µm with the run duration from 12 to 60h, which confirm the importance of the kinetic in the promotion of grain growth. These three experiments are characterized by the same main Shape Factor value of ~1.26 and PARIS Factor of ~16, independently of the run duration.

The reaction experiments performed at 1200 and 1300°C with different initial melt amount are generally characterized by larger olivine grains with higher Shape Factor and PARIS value (details in ***Tab. 3-4*, Chapter 3**) than ones performed by Francomme, J. E. (2016-2017). Hence, the comparison between the reaction experiments performed at 1200 and 1300°C with different IMA to ones carried out by Francomme, J E., suggests that two different experimental setup result in different textural features. However, the comparison revealed the importance of the kinetic and different melt/olivine ratio in affecting the olivine texture evolution.

5.2.3 – Textural evidence of melt-olivine reaction processes: comparison with natural Ol-rich troctolite

The lithologies and textures produced in the melt-olivine reaction experiments run at 1200-1300°C and the reactive crystallization experiments performed at final *T* of 1100°C, are comparable to those documented in natural rocks (*i.e.*, dunite, Ol-rich troctolite and Ol-gabbro) recovered from oceanic (*e.g.*, Suhr et al., 2008; Drouin et al., 2009, 2010; Sanfilippo & Tribuzio, 2013; Sanfilippo et al., 2015, 2016) and ophiolitic environments (*e.g.*, Renna & Tribuzio, 2011; Sanfilippo & Tribuzio, 2011, 2013a; Sanfilippo et al., 2014, 2015; Rampone et al., 2016; Renna et al., 2016). Occurrence of the interstitial plagioclase and clinopyroxene showing sharp and straight contacts, with the two different sets of olivine with regular-rounded habit and irregular-resorbed grain boundaries, were also observed in natural Ol-

rich troctolite. The presence of large olivine crystals with both straight and lobate rims in natural olivine-rich troctolite indicates the partial dissolution of olivine grains by the reactive percolated melt.

The reactive origin of olivine-rich troctolite is also supported by the detailed EBSD analysis. At decreasing modal olivine (wt%), during the transition from dunite to olivine-rich troctolite in experiments carried out at 1200°C with 10 and 25wt%$_{IMA}$, a global trend of increasing number of grains (1447 to 1512, respectively), coupled to decreasing of the Grain Area (1819.64 to 1065.77 μm^2, respectively), Shape Factor (from 1.31 to 1.30) and PARIS Factor (from 26.29 to 17.69), is observed (***Tab. 3-5*** and ***Fig. 3-29a***). These experimental results are compared with the natural occurrence of spinel-dunite and troctolite from Mt. Maggiore peridotitic body (Corsica, France) (Basch et al., 2018). At decreasing of modal olivine from spinel-dunite to troctolite, Basch et al., (2018) observed a global trend of increasing number of grains (from 12 to 59), a decreasing of the grain area (from 38mm^2 to 6 mm^2), Shape Factor (from 2.49 to 1.77) and PARIS Factor (from 179% to 105%). Although the global trend of different textural parameters between experimental results and data from Basch et al. (2018) is comparable, the textural values of olivine grains in the experiments results in lower values than ones of Basch et al., (2018). The different values are probably due to the olivine grains statistics in the selected area, elaborated through the EBSD analysis. However, the textural evidences mentioned above, supports the role of different initial melt/olivine ratio in the development of olivine texture in terms of shape and grain growth processes, usually explained through others factors such as, grade of undercooling, *PT* conditions, kinetics, melt composition and deformation.

5.3 – Role of Temperature and melt/olivine ratio on mineral chemistry

Experimental results of this work indicate that the interaction between the olivine matrix and a moderately evolved MORB-type melt strongly influences the mineral chemistry of the resulting olivine-rich lithologies. In the following section, the chemical data for each phase (*i.e.*, olivine, plagioclase, clinopyroxene and glass) constituting the isothermal and step-cooled experiments will be discussed in details. Furthermore, the experimental results will be compared to observations made on natural samples and to the experiments conducted by Francomme, J. E., (2016-2017) and Borghini et al., (2018), in order to evaluate how different experimental setup can influence the final mineral chemistry and reacted melt chemical evolution after the reaction processes.

5.3.1 – Olivine chemistry

The X_{Mg} value and NiO content in olivine have been considered potential tools to constrain the origin of olivine-rich troctolite (*e.g.*, Drouin et al., 2009; Sanfilippo et al., 2014; Rampone et al., 2016). High X_{Mg} value and NiO content in olivine have been suggested to support the hypothesis of a mantle origin of olivine matrix in some troctolites (*e.g.*, Drouin et al., 2009; Rampone et al., 2016; Sanfilippo et al., 2014). ***Figs. 5-7a-b*** show X_{Mg} value *vs.* NiO and CaO contents in olivine of the reaction experiments compared to the data from natural rocks (*e.g.*, Suhr et al., 2008; Drouin et al., 2009; Renna & Tribuzio, 2011; Sanfilippo & Tribuzio, 2013; Basch et al., 2019) and the reaction-crystallization experiments carried out in previous studies (*e.g.*, Francomme, J. E. PhD Thesis, 2016-2017; Borghini et al., 2018). The use of Ni-free starting melt in experiments resulted in olivine with lower NiO content than its natural counterpart. Reaction experiments performed at 1200°C show NiO contents comparable to those observed in natural rocks in contrast to experiments performed at 1250 and 1300°C that, instead, show very low NiO contents (0.10wt% ± 0.08 in run at 1250°C, 0.16wt%$_{IMA10}$ ± 0.08, 0.04wt%$_{IMA25}$ ± 0.08 and 0.02wt%$_{IMA50}$ ± 0.02 at 1300°C). At 1200°C, the phase assemblages are essentially constituted of olivine, plagioclase, clinopyroxene and small amount of interstitial glass in different proportions with the increase of the initial melt amount (***Tab. 3-1*** and ***Fig. 5-1***). Hence, at 1200°C the NiO content variation in olivine depends on the initial melt amount. Run with 10wt%$_{IMA}$ has olivine with NiO content (NiO = 0.17wt% ± 0.08) lower than olivines in experiments performed with 25 and 50wt%$_{IMA}$ (NiO = 0.27wt% ± 0.10 and NiO = 0.19wt% ± 0.13, respectively). The olivine-melt partition coefficients ($D_{Ni}^{ol/liq}$) (*e.g.*, Matzen et al., 2013) in reaction experiments were calculated considering the average composition of olivine (core and rim) and reacted melt. $D_{Ni}^{ol/liq}$ of isothermal experiments performed at **1200°C** are characterized by higher values for the run with 25wt%$_{IMA}$ (≈ 13.50) than ones with 10wt%$_{IMA}$ (≈ 2.42) and 50wt%$_{IMA}$ (≈ 6.33). This chemical evidence is consistent with the experimental results of

Hart & Davis (1978) who determined the partitioning of Ni between olivine and silicate melt for compositions in the system Fo-Ab-An (1 atm) and *T* from 1250 to 1450°C. They showed that the Ni content of silicate melts and coexisting olivine are strongly dependent on the composition of the melt. The intrinsic temperature dependence of the partition coefficient (D) is small and it generally affects the composition of the reacting melt.

At 1300°C, the isothermal experiments with 10 and 25wt%$_{IMA}$ (NiO = 0.16wt% ± 0.08 and NiO = 0.04wt% ± 0.08, respectively) have olivines with NiO content higher than olivines in run with 50wt%$_{IMA}$ ((0.02wt% ± 0.02). The progressively decrease of NiO content in olivine at **1300°C** leads to the conclusion that it is strongly influenced by a high initial melt amount (50wt%). $D_{Ni}^{ol/liq}$ in the run with 10wt%$_{IMA}$ is higher (≈ 16.00) than ones with 25wt%$_{IMA}$ and 50wt%$_{IMA}$ (≈ 2.00 and ≈ 2.00, respectively). Furthermore, at fixed initial melt amount, the olivine-melt Ni partition coefficient ($D_{Ni}^{ol/liq}$) increases with decreasing temperature (*e.g.*, Hart &Davis, 1978; Matzen et al., 2013), except for the reaction experiment carried out with 10wt%$_{IMA}$ at 1200°C that has lower $D_{Ni}^{ol/liq}$ (≈ 2.42) than one run at 1300°C with 10wt%$_{IMA}$ (≈ 16.00). This chemical evidence is consistent with the experimental results of Matzen et al., (2013) who calculated the partitioning of Ni between olivine and melt, through experiments on MORB encapsulated in olivine at 1 atm to 3.0 GPa and *T* from 100 to 1550°C. They showed that the $D_{Ni}^{ol/liq}$ decreases from 5.0 to 3.8 with the increase of temperature independently of the changes in liquid composition. Overall, despite Ni contents variability of the experimental data, the chemical range defined by reaction experiments run at 1200°C is more comparable to what found in natural Ol-rich troctolite (*e.g.*, Renna & Tribuzio, 2011; Sanfilippo & Tribuzio, 2013; Basch et al., 2019). On the contrary, the isothermal experiments run at 1300°C are characterized by lower Ni content than natural Ol-rich troctolites and are more comparable to the reaction experiments (*e.g.*, Francomme, J. E. PhD Thesis, 2016-2017; Borghini et al., 2018).

These results support the theory that olivine-rich troctolites can originate from the interaction between olivine-rich matrix and a migrating MORB-type melts saturated in plagioclase and clinopyroxene (*e.g.*, Suhr et al., 2008; Drouin et al., 2009, 2010). In this scenario, the chemical results revealed that the NiO content in olivine is strongly influenced by temperature (*e.g.*, 1300°C) and high initial melt amount (50wt%) during the interaction between an olivine matrix and an impregnating melt.

Fig. 5-7c-d, shows the X_{Mg} value *vs.* NiO and CaO contents in olivine of step-cooled experiments carried out at 0.5 GPa and final *T* of 1100°C with different IMA compared to data from natural rocks (*e.g.*, Renna & Tribuzio, 2011; Sanfilippo & Tribuzio, 2013; Basch et al., 2019) and reaction-

crystallization experiments (carried out at 0.5 and 0.7 GPa *e.g.*, Francomme, J. E., PhD Thesis, 2016-2017; Borghini et al., 2018). Overall, the olivine resulted from step-cooled experiments present a relatively high X_{Mg} value comparable to the reactive crystallization experiments from Borghini et al., (2018) and natural rocks. However, as already mentioned, the NiO content is lower than data from natural rocks (*e.g.*, Renna & Tribuzio, 2011; Sanfilippo & Tribuzio, 2013; Basch et al., 2019). In particular, the NiO content in the run with 25wt%$_{IMA}$ (0.03 ± 0.03) is lower than those with 10 and 50wt%$_{IMA}$ (NiO = 0.06 ± 0.07 and NiO = 0.09 ± 0.07, respectively). The partition coefficient ($D_{Ni}^{ol/liq}$) depends on the reacted melt composition (as suggested by several authors *e.g.*, Hart & Davis, 1978) (details in **Section 5.3.3**). Compared to isothermal experiment performed at 1200 and 1300°C, the step-cooled experiments have higher X_{Mg} due to the crystallization of new olivine from an MgO-enriched reacted melt as a consequence of olivine dissolution.

The Ca concentration of olivine is strongly sensitive to temperature and pressure (*e.g.*, Simkin & Smith, 1970) and it is generally used as geothermobarometer for spinel-peridotites (*e.g.*, Kohler & Brey, 1990). The relatively high diffusion of Ca in olivine results in large amounts of Ca diffusing out of olivine during cooling of mafic and ultramafic rocks (*e.g.*, Libourel, 1999). Calcium content can be used as geospeedometer to define the cooling rate of specific rocks (*e.g.*, Coogan et al., 2005; Coogan et al., 2007; Shejwalkar et al., 2013). The CaO contents in isothermal and step-cooled experiments are comparable to experimental data of previous studies (*e.g.*, Borghini et al., 2018) and higher than CaO contents in natural olivine-rich troctolites (*e.g.*, Sanfilippo & Tribuzio, 2013; Basch et al., 2019). The mismatch between experiments and natural samples is due to the high-*T* reaction processes which lead to an increase of the CaO content in olivine (*e.g.*, Coogan et al., 2005). On the contrary, the lower Ca content in olivine from natural rocks depends on Ca exchange between olivine and clinopyroxene during the cooling (*e.g.*, Coogan et al., 2005).

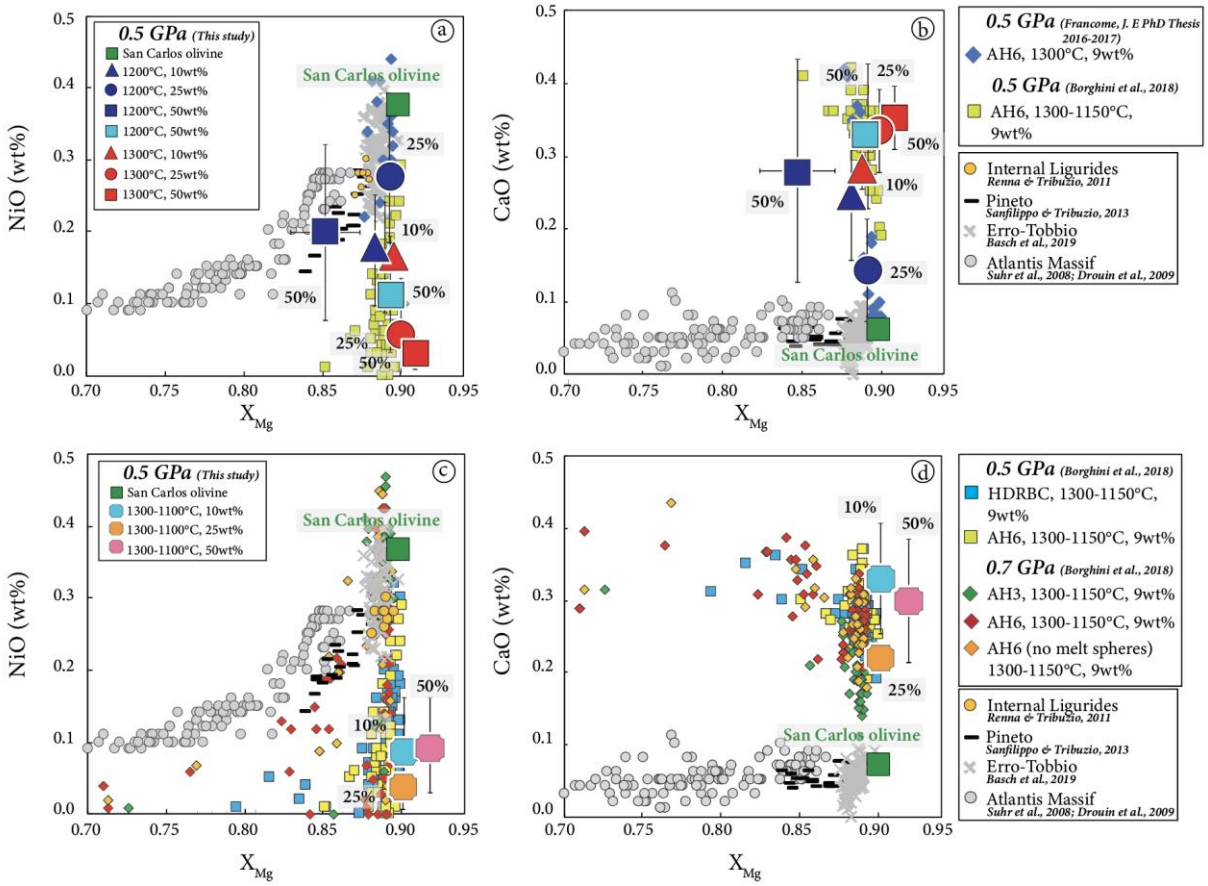

Figure 5-7 *X_{Mg} vs. NiO (a) and CaO (b) content (wt%) in olivine from isothermal reaction and step-cooled experiments compared to olivine compositions documented in previous experimental data (Francomme, J. E., 2016-2017; Borghini et al., 2018) and natural rocks (Suhr et al., 2008; Drouin et al. 2009; Renna & Tribuzio, 2011; Sanfilippo & Tribuzio, 2013; Basch et al., 2019).*

5.3.2 – Plagioclase and clinopyroxene chemistry: comparison between experiments and natural rocks

The composition of interstitial phases clinopyroxene (X_{Mg}, Cr_2O_3, and TiO_2 contents) and plagioclase (X_{An}) have been used to define the chemistry of the reacted melt. ***Fig. 5-8a-b*** shows the covariation of the X_{Mg} of olivine and clinopyroxene with X_{An} of plagioclase in the isothermal reaction experiments at 1200°C compared to data from natural olivine-rich troctolites (*e.g.*, Suhr et al., 2008; Drouin et al., 2009; Sanfilippo & Tribuzio, 2013; Basch et al., 2019). Experimental data from previous reactive crystallization experiments (Borghini et al., 2018) and equilibrium crystallization experiments (Husen et al., 2016) are also reported. No correlation between the X_{An} in plagioclase and the initial melt amount was observed. However, in ***Fig. 3-10c*** the covariation between X_{An} in plagioclase with X_{Ca} of the reacted melt, suggested that the crystallized plagioclase in reaction-crystallization experiments is in chemical equilibrium with reacted melt. Due to the crystallization from a reacted melt with lower CaO content (8.02 ± 0.20), the run with 25wt%$_{IMA}$ has lower X_{An} value (0.61 ± 0.06) than one with 50wt%$_{IMA}$ (0.66 ± 0.02). Overall, the plagioclase composition lies within the range of anorthite content in Pineto

gabbroic rocks (Sanfilippo & Tribuzio, 2013) and Erro-Tobbio troctolites (*e.g.*, Borghini et al., 2007; Rampone et al., 2016; Basch et al., 2018). Hence, the experimental data of this study agree with chemical evidences observed in natural olivine-rich troctolites and attributing to the melt-rock reaction processes involving the olivine dissolution and subsequent crystallization of interstitial plagioclase and clinopyroxene (*e.g.*, Basch et al., 2018, 2019). Further chemical evidence for a reactive origin of olivine-rich troctolite, is that anorthite content in plagioclase from isothermal experiments are not comparable to ones resulted from equilibrium crystallization experiments performed by Husen et al., (2016) (***Fig. 5-8)***. X_{An} of plagioclase in equilibrium crystallization experiments is higher than ones in reaction experiments of this study and increases with the increase of *T* from 1150 to 1200°C (X_{An} = 0.72, X_{An} = 0.72 and X_{An} = 0.77, respectively) (***Fig. 5-8***). The lower X_{An} of plagioclase in reaction experiments is probably due to the early crystallization of clinopyroxene rather than plagioclase which leads to an increase of Na/Ca ratio in the reacted melt (***Fig. 5-11***).

In step-cooled experiments (final *T* = 1100°C), plagioclase occurs only in the experiment performed with 50wt%$_{IMA}$ (***Fig. 5-8a-b***). In this case, plagioclase composition plots above the covariation range defined by X_{Mg} of olivine and clinopyroxene versus anorthite content in coexisting plagioclase from natural troctolites (*e.g.*, Sanfilippo & Tribuzio, 2013; Borghini et al., 2007; Rampone et al., 2016; Basch et al., 2018) and the reactive crystallization experiments performed by Borghini et al., (2018). It also has a lower X_{An} value (0.71 ± 0.02) compared to plagioclase composition in equilibrium experiments from Husen et al., (2016). Due to the melt-olivine interaction, the high-An plagioclase in step-cooled experiment suggests that it crystallized from a reacted melt with high CaO content (29.18 ± 6.39) and low Na_2O content (1.03 ± 0.73) than ones of isothermal experiments. Comparing the step-cooled experiment with 50wt%$_{IMA}$ to the isothermal one with the same IMA, the former has higher X_{An} as a consequence of its crystallization from a reacted melt with higher CaO content (29.18 ± 6.39) than one resulted from the reaction at 1200°C (12.39 ± 0.28).

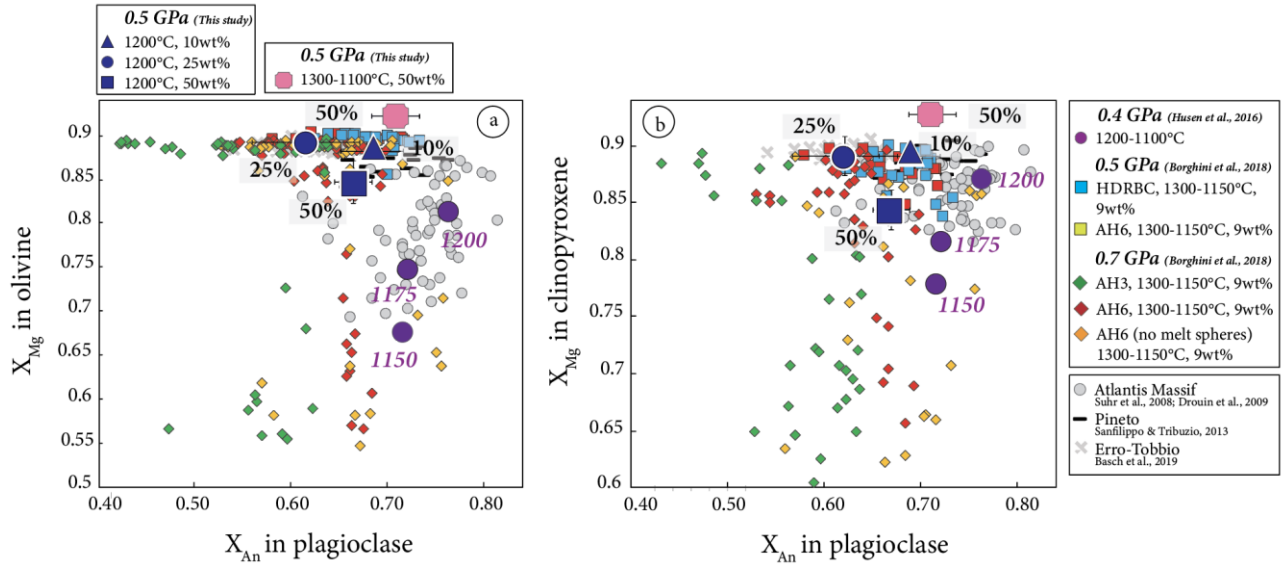

Figure 5-8 *(a) X_{Mg} in olivine vs. X_{An} in plagioclase and (b) X_{Mg} in clinopyroxene vs. X_{An} in plagioclase of isothermal and step-cooled experiments compared to data from natural troctolites and gabbroic rocks from natural rocks (Suhr et al., 2008; Drouin et al., 2009; Sanfilippo & Tribuzio, 2013; (Basch et al., 2019) and experimental data (Husen et al., 2016; Borghini et al. (2018).*

In the isothermal reaction experiments, clinopyroxene is present as interstitial phase only at 1200°C with all the adopted IMA and in step-cooled experiments with 25 and 50wt%$_{IMA}$. ***Fig. 5-9*** shows the composition of clinopyroxene in terms of X_{Mg} *vs* Cr_2O_3, Al_2O_3, Na_2O and TiO_2 in reaction experiments compared to clinopyroxenes from natural olivine-rich troctolites (*e.g.*, Suhr et al., 2008; Drouin et al., 2009; Sanfilippo & Tribuzio, 2013; Basch et al., 2019). Experimental data from previous reactive crystallization experiments (Borghini et al., 2018) and equilibrium crystallization experiments (Husen et al., 2016) are also reported. Data from the new set of experiments are comparable to previous experiments performed at 0.5 and 0.7 GPa (Borghini et al., 2018), whereas they show some differences with data from natural troctolites (*e.g.*, Suhr et al., 2008; Drouin et al., 2009; Sanfilippo & Tribuzio, 2013; Basch et al., 2019) and equilibrium experiments (Husen et al., 2016) in terms of Cr_2O_3, Al_2O_3, Na_2O and TiO_2 contents. In particular, step-cooled experiments performed at final *T* of 1100°C and isothermal run at 1200°C result in clinopyroxene with strongly lower Cr_2O_3 contents than ones observed in natural occurrences. Generally, Cr-rich clinopyroxene in troctolite is mostly related to partial dissolution of pre-existing spinel grains, promoting the Cr enrichment of the reacting melt (*e.g.*, Lissenberg & Dick, 2008; Suhr et al., 2008; Renna & Tribuzio, 2011; Sanfilippo & Tribuzio, 2013). Moreover, this chemical evidence is consistent with experimental data that point out that the reaction between tholeiitic basalt and depleted peridotite at uppermost mantle conditions enhances the increasing of Cr content in the melt through the spinel dissolution (Van den Bleeken et al., 2010). Hence, in our

experiments according to Borghini et al., (2018), the reaction between olivine and a low-Cr MORB type starting melt results in interstitial clinopyroxene with low Cr_2O_3 content (***Fig. 5-9a***), suggesting the importance of spinel dissolution in affecting the final clinopyroxene composition.

In our melt-olivine reaction and reactive crystallization experiments the Al_2O_3 content in clinopyroxene is higher than those in natural clinopyroxene (***Fig. 5-9b***). As discussed in previous experimental works, it can be related to the pressure, spinel dissolution or the extent of the reaction (*e.g.*, Borghini et al., 2009, 2018; Saper & Liang, 2014). Borghini et al., (2010) experimentally demonstrated that the Al_2O_3 content in pyroxenes in plagioclase-facies lherzolite is positively correlated with pressure. The higher Al_2O_3 contents in clinopyroxene from isothermal and step-cooled experiments are also comparable to ones observed in clinopyroxene resulted from equilibrium crystallization at 0.4 GPa (Husen et al., 2016).

The Na_2O content in clinopyroxene from isothermal experiments is slightly higher than in step-cooled ones. Clinopyroxene in isothermal experiments at 1200°C crystallized from a reacted melt more enriched in Na_2O content (*e.g.,* $2.84_{IMA10wt\%} \pm 0.18$, $5.24_{IMA25wt\%} \pm 0.12$ and $3.38_{IMA50wt\%} \pm 0.08$) than ones in step-cooled experiments (*e.g.*, $2.74_{IMA25wt\% \pm} 0.07$ and $1.03_{IMA50wt\%} \pm 0.73$). Overall, experimental data are comparable to natural olivine-rich troctolites (*e.g.*, Suhr et al., 2008; Drouin et al., 2009; Sanfilippo & Tribuzio, 2013; Basch et al., 2019) (***Fig. 5-9c***).

The TiO_2 content in clinopyroxene from experiments are generally higher than the compositional range defined by natural olivine-rich troctolites and more comparable to the reactive crystallization experiments performed by Borghini et al., (2018). Due to its slow diffusion, the TiO_2 content in reaction-crystallization experiments is mainly controlled by the melt chemical composition (*e.g.*, Van den Bleeken et al., 2010), since the TiO_2 content in San Carlos olivine is negligible. Borghini et al., (2018) suggested that a low melt/olivine ratio (9wt%) enhances Ti-enrichment in interstitial melt and, thus, in crystallizing clinopyroxene through the trapped melt effect into the impregnated dunite. Therefore, high melt/olivine ratio could explain the relatively lower TiO_2 content in experiments at 0.5 GPa. The TiO_2 content it also dependent on the amount of the fractionated melt. The lower TiO_2 content in run with 10 and $50wt\%_{IMA}$ reflect the higher amount of fractionated melt (10wt% and 46wt%, respectively) than one in run with $25wt\%_{IMA}$ (16wt%) (details in ***Fig. 5-1***). However, the experimental results of this study highlight that the titanium content in runs at 1200°C and are not melt/olivine ratio dependent. In particular, the run with $25wt\%_{IMA}$ ($TiO_2 = 2.11wt\% \pm 1.08$) has higher TiO_2 content than ones with 10 and $50wt\%_{IMA}$ ($TiO_2 = 1.58wt\% \pm 0.40$ and $TiO_2 = 1.48wt\% \pm 0.34$). Similarly, clinopyroxene in step-

cooled experiment with 50wt%$_{IMA}$ (0.95wt% ± 0.28) also shows high TiO_2 content relative to the one performed with 25wt%$_{IMA}$ (0.69wt% ± 0.15).

5.3.2.1 – Origin of high-Mg# clinopyroxene

X_{Mg} values in clinopyroxene from the experiments performed and 1200°C are comparable to natural troctolites. In particular, the isothermal reaction experiments performed at 1200°C are characterized by lower X_{Mg} value ($X_{MgIMA10}$ = 0.89 ± 0.01, $X_{MgIMA25}$ = 0.89 ± 0.02 and $X_{MgIMA50}$ = 0.84 ± 0.02) than step-cooled experiments terminated at 1100°C with 25 and 50wt%$_{IMA}$ (X_{Mg} = 0.91 ± 0.01 and X_{Mg} = 0.93 ± 0.01, respectively). Overall, the crystallization of reacted melts results in high-Mg# clinopyroxene (X_{Mg} up to 0.93) that is consistent with some natural samples recovered in mid-ocean ridge environment (*e.g.,* Atlantis Massif from Suhr et al., 2008 and Drouin et al., 2009), ophiolitic sequences (*e.g*., Pineto gabbroic sequence, from Sanfilippo & Tribuzio, 2013; Erro-Tobbio ultramafic unit, from Basch et al., 2019) and experimental data (*e.g*., Borghini et al., 2018, Yang et al., 2019) (***Fig. 5-9***). Moreover, the partition coefficient of clinopyroxene (K^{cpx}_{Fe-Mg}) (Wood & Blundy, 1997), suggests that the crystallized clinopyroxene in reaction-crystallization experiments is in chemical equilibrium with reacted melt (***Fig. 5-10***). The high-Mg# clinopyroxene (*e.g*., X_{Mg} = 86-91) is not uncommon in the lower oceanic crust as demonstrated by the rocks recovered in the Atlantic (Lissenberg & Dick, 2008; Suhr et al., 2008; Drouin et al., 2009), Pacific (Perk et al., 2007) and Indian oceans (Dick et al., 2002). The clinopyroxene with higher Mg# is chemically inconsistent with the crystallization of a MORB-type melt at low-*P*. Clinopyroxenes from equilibrium crystallization performed at 0.4 GPa and *T* from 1150 to 1200°C by Husen et al., (2016), are characterized by X_{Mg} values (from 0.78 to 0.87) lower than ones resulted from reactive crystallization processes. The more likeable hypothesis is that high-Mg# clinopyroxene forms when a relatively evolved clinopyroxene-saturated melt reacts with primitive cumulates leading to its Mg# increase after the reaction (*e.g*., Lissenberg and Dick, 2008; Lissenberg & MacLeod 2016; Sanfilippo et al., 2015; Basch et al., 2018; Borghini et al., 2018; Yang et al., 2019). High initial melt amount (50wt%) results in low-Mg# clinopyroxene with respect the clinopyroxene in runs with 10 and 25wt%$_{IMA}$. Hence, initial melt amount controls the final clinopyroxene chemical composition crystallized from the reacted melt.

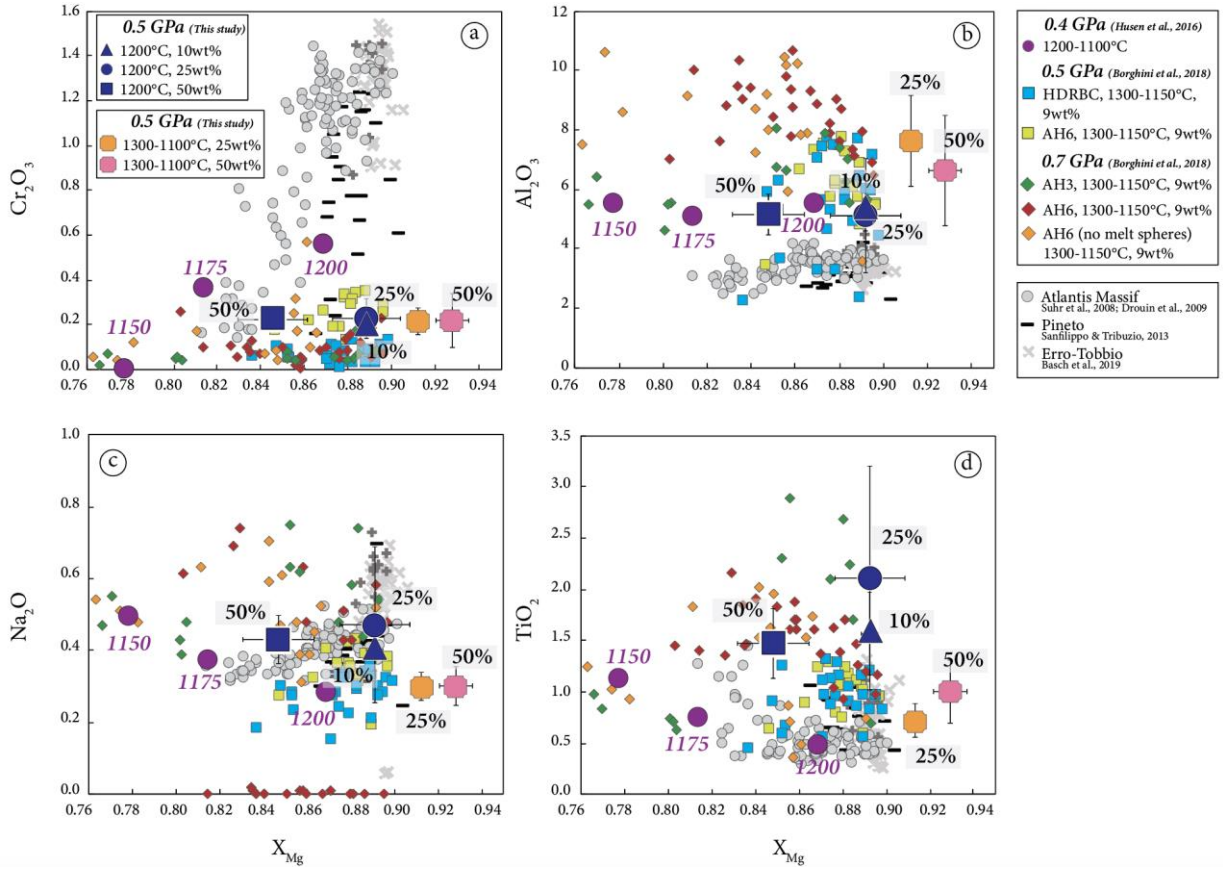

Figure 5-9 *X_{Mg} vs. Cr_2O_3 (a), Al_2O_3 (b), Na_2O (c) and TiO_2 (d) contents (wt%) in clinopyroxene from isothermal and step-cooled experiments performed at 0.5 GPa and 1100-1200°C compared to natural troctolites from natural rocks (Suhr et al., 2008; Drouin et al., 2009; Sanfilippo & Tribuzio, 2013; Basch et al., 2019) and experimental data (Husen et al., 2016; Borghini et al., 2018).*

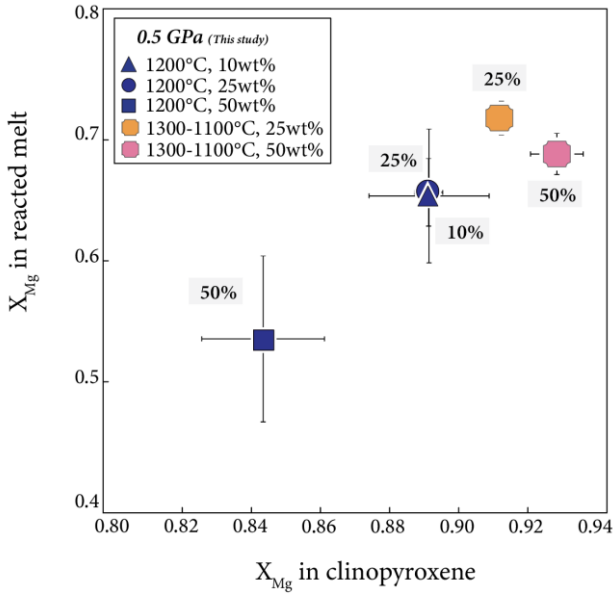

Figure 5-10 *X_{Mg} in clinopyroxene vs. X_{Mg} in reacted melt of melt-olivine reaction and reactive crystallization experiments in chemical equilibrium.*

5.3.3 – Glass chemistry

It is commonly acknowledged that an ascendant mantle source beneath the mid-ocean-ridge, undergoes decompression and partial melting. MORB chemistry mostly reflects the composition of the mantle source, degree and depth of partial melting (*e.g.*, Groove et al., 1992). In addition, the chemistry of MORB-type melt can be affected by other secondary processes, such as mixing and fractional crystallization (*e.g.*, Grove et al. 1992) and melt-rock reaction processes between an olivine-bearing rocks and reacting melt in the lower oceanic crust (*e.g.*, Lissenberg & Dick, 2008). In this regard, the chemistry of reacted melts in reaction experiments could be a powerful tool to understand how melt/rock reaction processes can affect the evolution of MORBs (*e.g.*, Collier & Kelemen, 2010; Yang et al., 2013; Paquet et al., 2016) and the origin of gabbroic rocks at the mantle-crust transition (*e.g.*, Drouin et al., 2009; Lissenberg et al., 2013).

Fig. 5-11 and ***5-12*** show the chemical composition of the residual reacted melt in isothermal experiments performed at 1200°C and step-cooled experiments runs at 1300-1100°C with different initial melt amount (*i.e.*, 10, 25 and 50wt%) compared to their initial composition (tholeiitic basalt - AH6, MgO = 8.62wt%, X_{Mg} = 0.62). Data from the reactive crystallization experiments from Borghini et al., (2018) and the compositional field of the most primitive MORB (X_{Mg} > 0.67; Gale et al., 2013), are reported for comparison. The reacted melts at 1200°C are characterized by higher values of SiO_2, Al_2O_3, Na_2O but lower MgO contents compared to those documented in primitive MORB. The CaO contents are similar to those documented in primitive MORB.

At 1300°C, the chemistry of the reacted melts is consistent to the MORB range in terms of SiO_2, Al_2O_3, Na_2O and CaO contents (***Fig. 5-11***). In particular, the run with 10wt%$_{IMA}$ has lower Al_2O_3 content (14.37wt% ± 1.02) than the MORB field (Gale et al., 203). Reactive crystallization at 1200°C results in the decreasing of the MgO content in melt coupled to a nearly constant X_{Mg}, whereas the SiO_2 and Na_2O content evolve to higher values than ones at 1300°C. Hence, this chemical evidence suggests that the fractionation of melt through reactive crystallization at lower *T* of 1200°C results in more evolved melts than those after the reaction at 1300°C (***Fig. 5-11***) (*e.g.*, Collier & Kelemen, 2010),

Fig. 5-12 shows that the residual melts in reactive crystallization experiments with 10 and 25wt%$_{IMA}$ have similar SiO_2, Na_2O and CaO contents compared to the MORB composition (X_{Mg} > 0.67, from Gale et al., 2013), except for the run with 50wt%$_{IMA}$. They show Al_2O_3 content (12.65wt% ± 1.26, 19.76wt% ± 0.48 and 12.19 ± 4.35, respectively) strongly lower than the primitive MORB. Overall, the glass composition in step-cooled experiments performed with 10 and 25wt%$_{IMA}$ have SiO_2, Na_2O and

CaO contents similar to those observed in experiments from Borghini et al., (2018), except for step-cooled with 50wt%$_{IMA}$. Compared to Borghini et al. (2018), the residual melts in the experiments with 10 and 50wt%$_{IMA}$ have a lower Al_2O_3 content (12.65wt% ± 1.26 and 12.19wt% ± 4.35, respectively) than one with 25wt%$_{IMA}$ (19.76wt% ± 0.48). Hence, the reactive crystallization with 10 and 25wt%$_{IMA}$ results in more evolved reacted melt than ones with 50wt%$_{IMA}$. This is an unexpected result if we consider the lithology resulted from the crystallization of reacted melt varying the initial melt amount. Due to the high rate of crystallization in run with 50wt%$_{IMA}$, the small amount of chemical analysis on residual glass could not reflect its real composition but it is probably affected by a quenching effect.

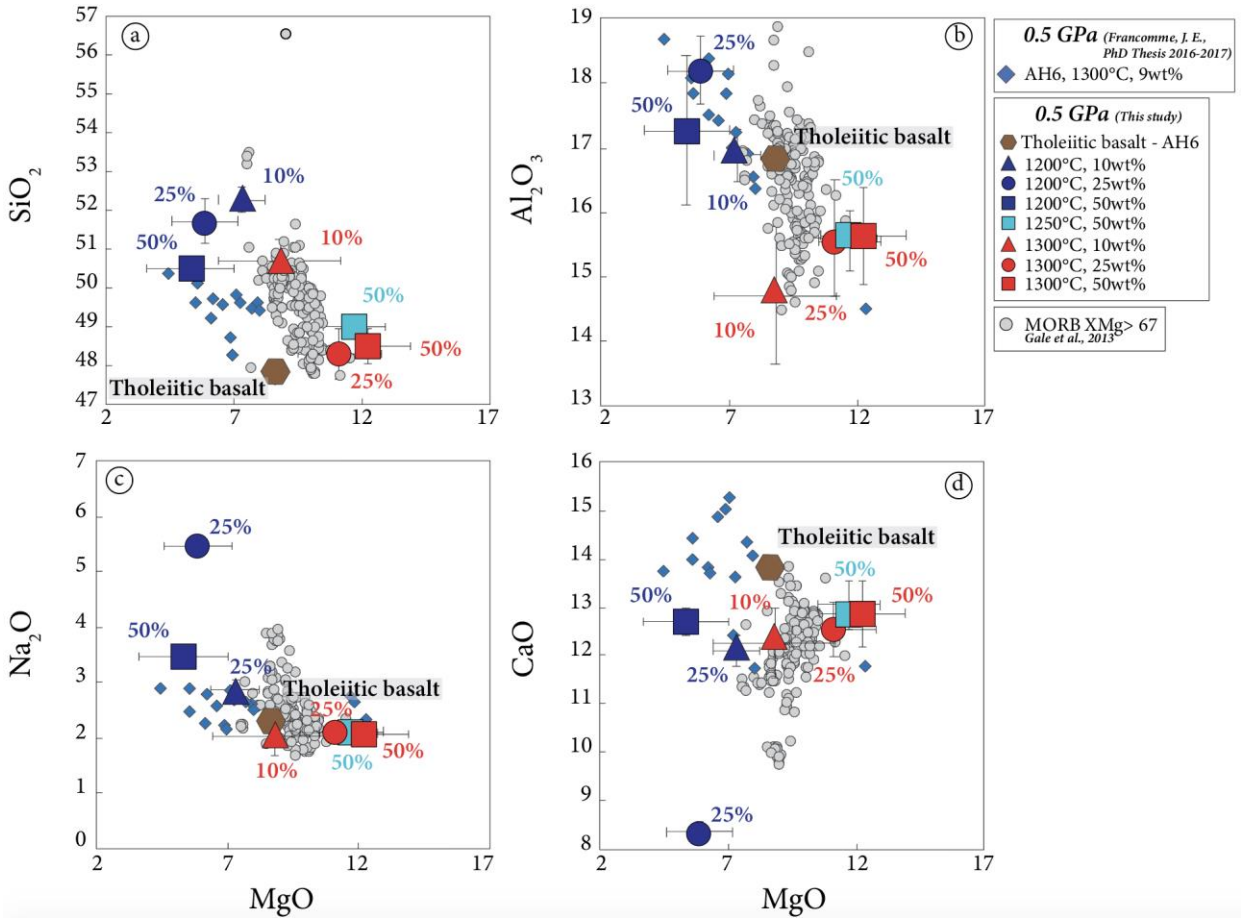

Figure 5-11 *MgO vs. SiO_2 (a), Al_2O_3 (b), Na_2O (c) and CaO (d) content in reacted melts from isothermal experiments compared to primitive MORB basalts from Gale et al., (2013). In the diagrams, the chemical compositions of reacted melts were normalized.*

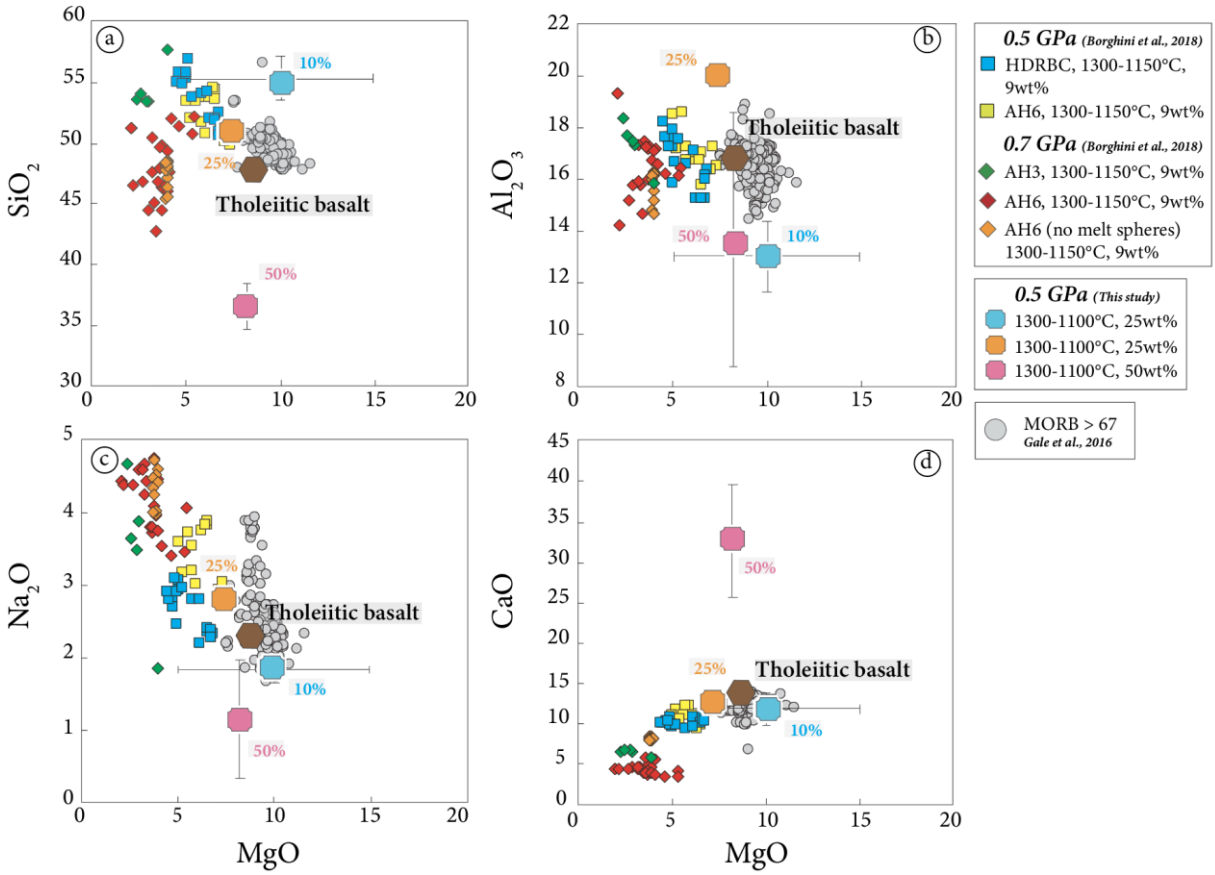

Figure 5-12 *MgO vs. SiO_2 (a), Al_2O_3 (b), Na_2O (c) and CaO (d) content in reacted residual melts from step-cooled compared to primitive MORB basalts from Gale et al., (2013) and experimental data from reactive crystallization experiments from Borghini et al., (2018). In the diagrams, the chemical compositions of reacted melts were normalized.*

Fig. 5-13 shows how the NiO content varies in reacted melt from isothermal and step-cooled experiments and with different initial melt amount (10, 25 and 50wt%, respectively) compared to the initial melt composition (AH6, NiO = 0.00wt%) and glass obtained by Francomme, J. E., (2016-2017) and Borghini et al., (2018). Experimental results are compared to NiO contents observed in natural basalts (*e.g.*, Nicholls et al., 1971; Srivastava et al., 1980; Price et al., 1986; Greene et al., 2010). High NiO contents in Hawaiian basalts are also shown (***Fig. 5-13***). They were explained as a result of melt-rock interaction between an impregnating melt and a fertile continental peridotite (Chatterjee et al., 2016).

Although the reaction with olivine modifies the chemistry of reacted melt, the latter shows a rather homogeneous chemical composition at 1200°C in terms of X_{Mg}. On the contrary, at 1300°C the reacted melt increases the X_{Mg} value with the increase of initial melt mount. The NiO contents of the reacted melts resulted from the isothermal reaction at 1200 and 1300°C, are comparable to the reactive crystallization experiments run at 0.5 and 0.7 GPa (*e.g.*, Francomme, J. E., PhD thesis 2016-2017;

Borghini et al., 2018) and natural basalts (*e.g.*, Nicholls et al., 1971; Srivastava et al., 1980; Price et al., 1986; Greene et al., 2010) except for Hawaiian basalts, which are characterized by a higher NiO content (Chatterjee et al., 2016). This suggests that lower NiO content in reacted melt derived by the reaction between an olivine matrix and reacting melt.

NiO content in experiments generally increases compared to the initial melt composition. Furthermore, in the reaction-crystallization experiments run at 1300-1100 and 1200°C, no correlation is observed between the NiO content and different IMAs. On the contrary, at 1300°C the NiO content increases proportionally to the initial melt amount (***Fig. 5-13a***). Hence, this chemical evidence suggests that melt-rock reaction processes at melt/olivine ratios play an important role in the chemical evolution of MORB in the lower oceanic crust. Although, in the experiments no sulfides crystallized after the reaction, Ciazela et al., (2017, 2018) suggested that the FeO and NiO contents in the melt can affect the sulfur concentration at sulfide saturation (SCSS). In particular, the decreasing of iron content (range of 5-15wt% FeO) and the increasing of nickel content in the melt results in the decreasing of sulfur concentration at SCSS.

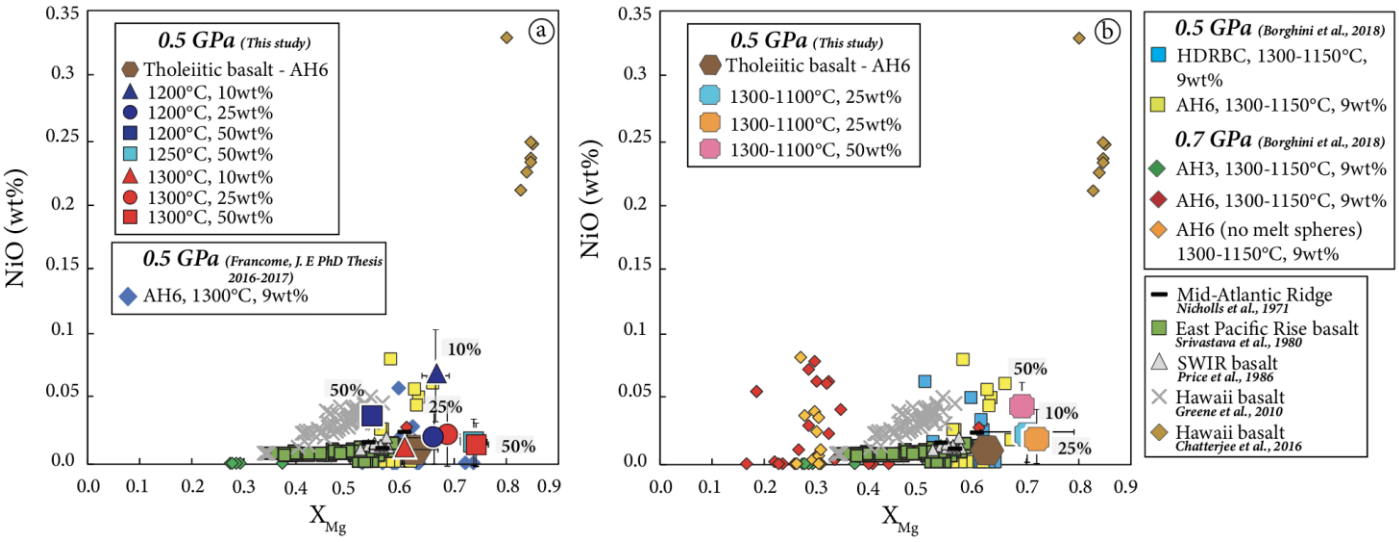

Figure 5-13 *X_{Mg} vs. NiO content (wt%) in reacted residual melts from isothermal (a) and step-cooled experiments (b) compared to experimental data (Francomme, J. E., 2016-2017; Borghini et al., 2018) and natural basalts (Nicholls et al., 1971; Srivastava et al., 1980; Price et al., 1986; Greene et al., 2010; Chatterjee et al., 2016).*

5.4 – Olivine deformation recovery

Olivine is the most abundant mineral of the Earth's upper mantle (40-80%) and it generally deforms, at low temperature and high stress, mostly along the [001] crystallographic direction (or on the (001) and (010) planes) whereas at high temperature and low stress the deformation occur mostly along the [100] crystallographic direction which glide on the (010), (021), (031) and (001) crystallographic planes (*e.g.*, Tommasi et al., 2000; Couvy et al., 2004; Burnley et al., 2013; Demouchy et al., 2013). Olivine is a key mineral in understanding the rheology of rocks in the mantle-crust transition. In order to better understand how melt-olivine reaction processes, at different temperatures (from 1100 to 1300°C, 0.5 GPa) and different initial melt amount (*i.e.*, 9, 25 and 50wt%), affect the rheology of the lower oceanic crust, a detailed microstructural study was performed. EBSD analysis aimed to provide detailed information on the intra-granular deformation of olivine grains resulted from reaction and crystallization experiments. San Carlos olivine used as starting material in reaction experiments is not naturally deformed as demonstrated by the **Grain Orientation Spread (GOS)** map displayed (***Fig.3-30a-b, 5-14a-b***) through EBSD analysis (Francomme, J. E., PhD Thesis 2016-2017). The experimental conditions (1200°C, 0.7 GPa) at which olivine was subjected for 120 hours resulted in a strongly deformed olivine grains (GOS value up to 10°), showing that the sintering process affects the olivine texture independently of other mechanisms (*e.g.*, melt impregnation).

Fig. 5-14c-d-e-f shows the occurrence of typical evidence of plastic deformation such as, *kink bands* and *subgrains* in experimentally deformed mantle olivine (*e.g.*, Raleigh, 1968; Burnley et al., 2013; Basch et al., 2018, 2019, 2021; Ferrando et al., 2018). The kinking is an important accommodation mechanism in the plastic deformation of polycrystalline olivine usually interpreted as a buckling instability that occurs when the weak planes are oriented parallel to compression (Raleigh, 1968). In details, a "*kink band*" is a part of a grain that responds to deformation by undergoing rotation with respect to the unkinked part of the grain; the axis of rotation coinciding with the line of intersection of the kink band and the slip plane, perpendicular to the slip direction (Vernon, 2004, 2018). This structural evidence was observed both in olivine experimentally and naturally deformed at low to moderate temperature (*e.g.*, Raleigh, 1968; Burnley et al., 2013; Basch et al., 2018, 2019, 2021; Ferrando et al., 2018; Ismail et al., 2021). Moreover, EBSD analysis allowed to observe that the boundaries of the kink bands are usually aligned along "*subgrains"* boundaries (***Fig. 5-14d-f***). The latter are interpreted as regions of small misorientation (phase boundaries with misorientation angle ≤ 10°, "low-angles grain boundaries") within an individual grain formed by recovery in response to the deformation. In this regard, the recovery includes all processes that attempt to return a crystal to the undeformed state without the formation of

high-angle (high-energy) boundaries; *i.e.*, no new grains are formed. Recovery involves the organization of dislocations (line defects) into regular arrays (subgrain boundaries), forming *subgrains* in deformed crystals (Vernon, 2004, 2018).

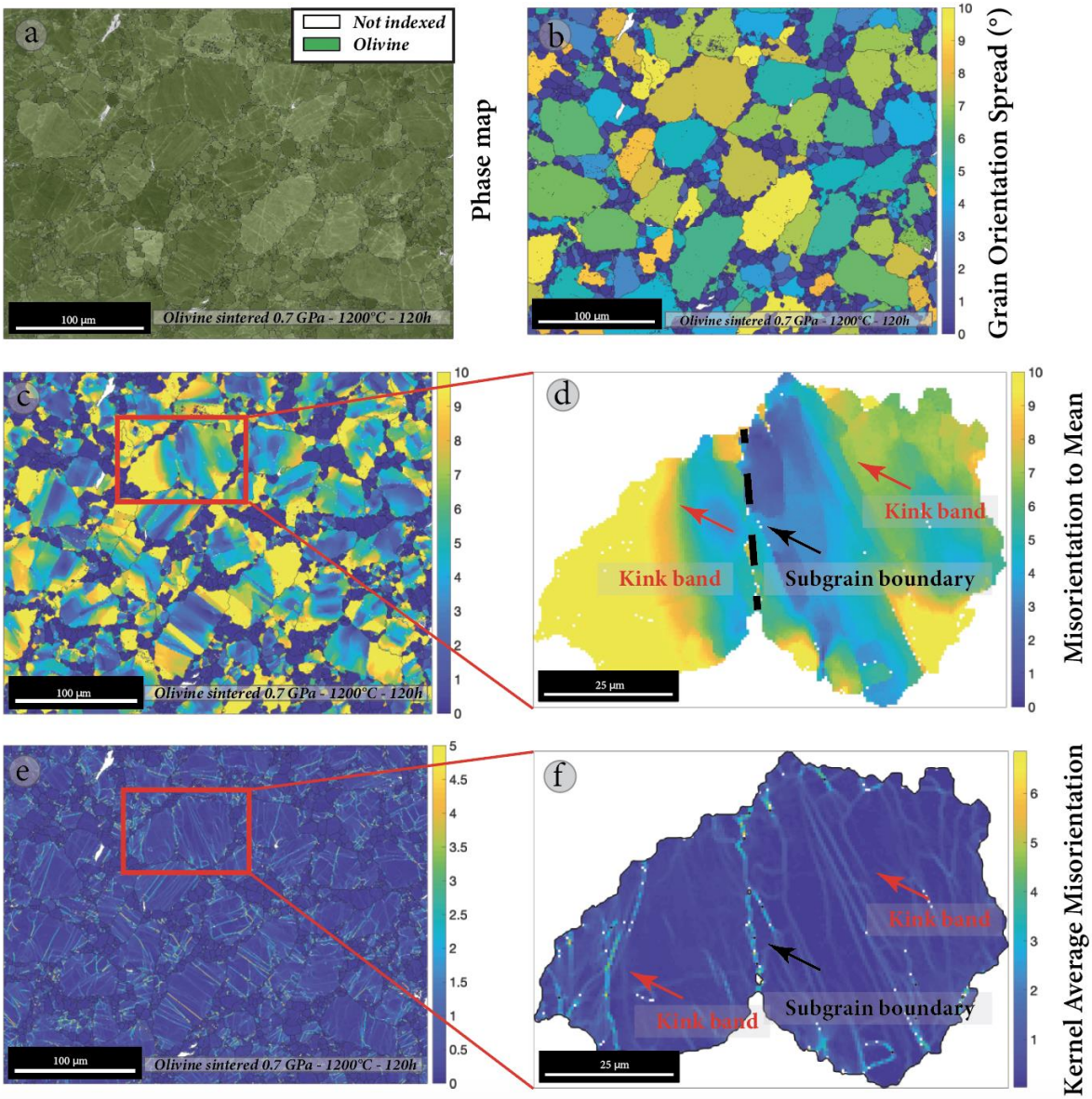

Figure 5-14 *Sintered San Carlos olivine EBSD maps: (a-b) Phase map and GOS map; (c-d) Mis2Mean map and detailed single grain map showing the kink bands (red arrows); KAM map and detailed single grain map showing subgrains (black arrows and dashed lines) (from PhD Thesis Francomme, J. E., 2016-2017).*

The olivine dissolution and re-precipitation experiments performed at 1200 and 1300°C (with IMA equal to 9, 25 and 50wt%), revealed that a higher *T* (1300°C) results more efficiently in the "recover" of the plastic deformation of the olivine grains is more efficient. ***Fig. 3-37*** **(Chapter 3)** shows that the employment of a high melt amount during the reaction with an olivine matrix, strongly enhance the "recovery" mechanism, independently of the grain size and shape (***Fig. 5-15***). Furthermore, the

deformation "recovery" is also confirmed by the disappearance of the kink bands and subgrains (***Fig. 3-38***, **Chapter 3**). The microstructural features observed in olivines resulted from the reactive crystallization experiments (at final *T* =1100°C), suggested that the reactive dissolution and crystallization processes promote the "recovery" of plastic deformation independently of the grain size (and shape) and the melt/olivine ratio. This intra-granular deformation suggests that the interaction between olivine matrix and high melt amount, strongly affects the pre-existing matrix recovering its plastic deformation, thus generating an "undeformed" matrix. Francomme, J. E., (PhD Thesis, 2016-2017), performing reaction experiments at 1250°C and 0.7 GPa ($9\%_{IMA}$), inferred that also the kinetic (*i.e.*, 12-24-60h) of the reaction influences the intensity of olivine deformation. The increase of the run duration from 12 to 60 hours favors the recovery of intra-granular deformation of olivine grains (***Fig. 5-16***). This, further highlights that the reaction processes are influenced by different parameters such as, *T*, melt/rock ratio and kinetics that contribute in modifying the rheology of rocks at mantle-crust transition.

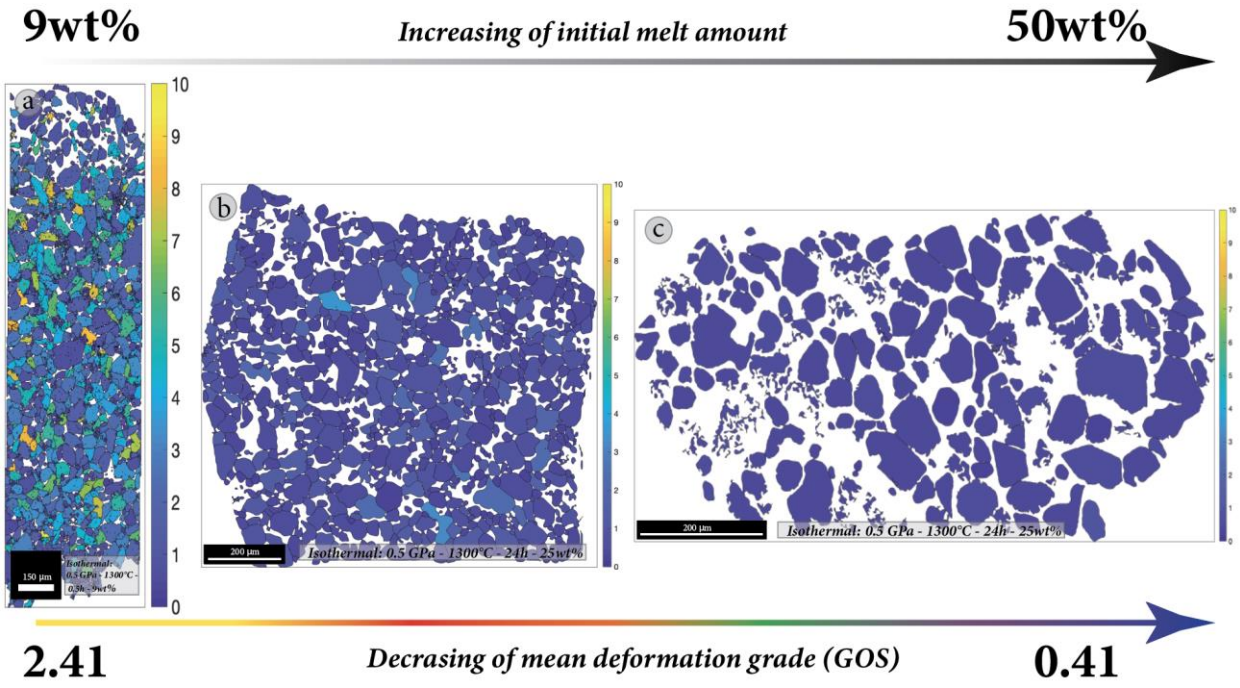

Figure 5-15 *EBSD show the decreasing of the olivine deformation grade with the increase of initial melt amount in reaction experiments performed at 1300°C and 0.5 GPa (the run with 9wt% of melt is from Francomme, J. E., PhD Thesis 2016-2017).*

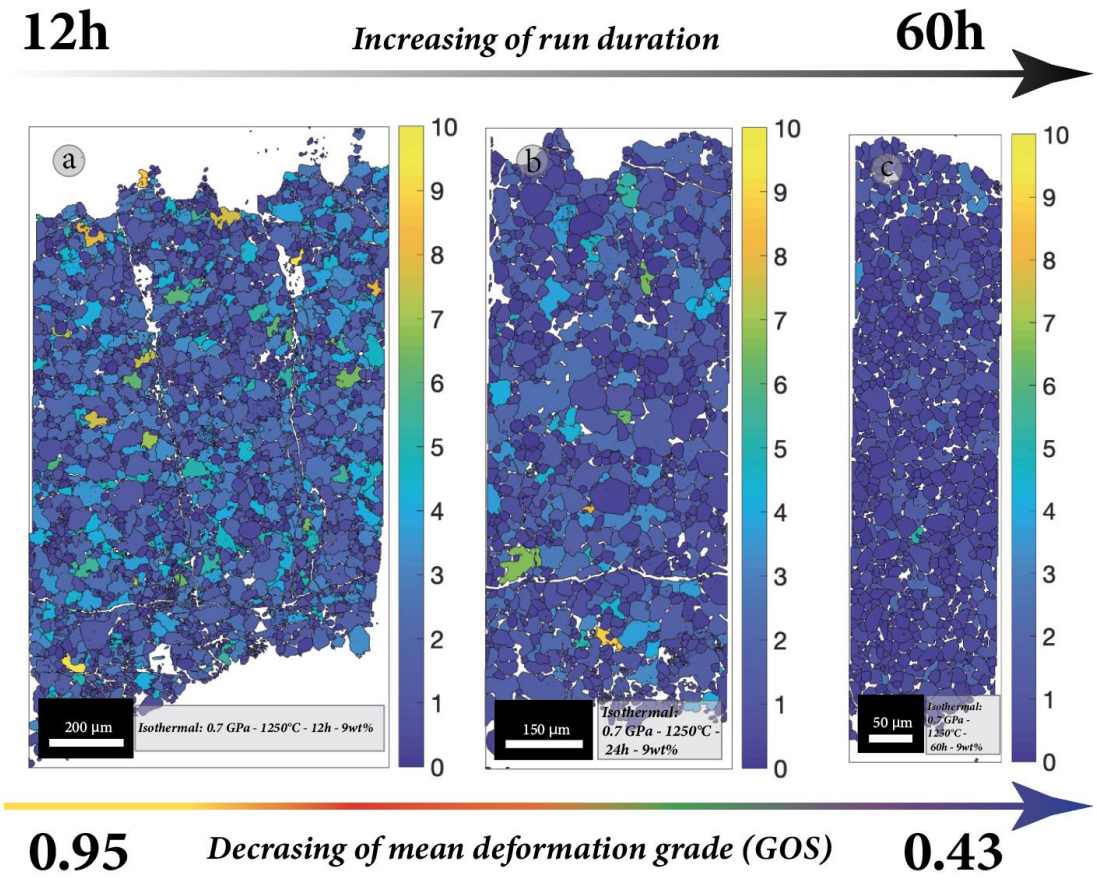

Figure 5-16 *EBSD show the decreasing of the olivine deformation grade with the increase of run duration of reaction experiments performed at 1250°C and 0.7 GPa (from Francomme, J. E., PhD Thesis 2016-2017).*

More recently Basch et al., (2018, 2019, 2021) supported the hybrid and reactive nature of some olivine-rich troctolites from Mt. Maggiore peridotitic massif (Alpine Corsica, France) and Erro-Tobbio ultramafic body (Western Alps, Italy) combining the results of microstructural (EBSD) and geochemical studies. Compared to experimental data of this study, the natural olivine-rich troctolites from Mt. Maggiore (Corsica, France) are characterized by higher value of GOS = 2.71-3.14 (Basch et al., 2018). They also suggested that the texture and crystallographic preferred orientation (CPO) of olivine are correlated and dependent on the melt/rock ratio involved in the impregnation process (*e.g.*, Drouin et al., 2010). Similarly to experimental results of this study, they inferred that the preservation of the pristine olivine matrix structure is favored by a low melt/rock ratio, whereas the disaggregation of the pre-existing matrix is favored by a high melt/rock ratio. Moreover, the authors observed two main generations of olivine: i) large subhedral and "deformed" crystals with both straight and lobate rims (generally defined as **Olivine$_1$**) and ii) smaller rounded "undeformed" grains (generally defined as **Olivine$_2$**) (*e.g.*, Rampone et al., 2016). However, the olivine resulted from the reaction-crystallization experiments demonstrated that the interpretation of the two olivine generations (*i.e.*, **Olivine$_1$** and **Olivine$_2$**) through their textural distinction based on the olivine deformation grade, is not totally correct.

Because of the GOS value approaching to zero, the olivine grains resulted from the reaction at 1200 and 1300°C with 50wt%$_{IMA}$ show that they are undeformed independently of the shape (subhedral-irregular and euhedral-regular habit, respectively) and the grain size (large and small, respectively). Hence, in this situation is difficult to define a pre-existing olivine grain (**Olivine$_1$**) and a new crystallized olivine (**Olivine$_2$**). Furthermore, no correlation is observed between olivine morphologies and their chemical composition in terms of X_{Mg}, NiO and CaO contents (*e.g.*, Basch et al., 2018, 2019). The detailed microstructural study performed through EBSD analysis revealed that an "annealing" process at 1300°C and a high melt amount (50wt%) which reacts with an olivine matrix, might totally reset the original mantle imprint independently of the grain size and shape. In this case, the evaluation of deformation grade does not allow to distinguish the two-olivine generation because the EBSD analysis demonstrated that no differences occur between the pre-existing mantle olivine (San Carlos olivine) and new olivine (*e.g.*, magmatic olivine).

Chapter 6
CONCLUSION

In order to investigate the role of temperature and melt/olivine ratio in melt-dunite reaction processes, this experimental thesis has performed a number of isothermal and step cooled experiments simulating the interaction between a **dunite matrix** and a **reacting melt.** Three starting initial melt amount (IMA) were chosen (*i.e*., 10, 25 and 50wt%). The experiments were performed at *P-T* conditions typically encountered in the mantle-crust transition zone underneath oceanic spreading centers (*i.e.,* 1100-1300°C and 0.5 GPa). Experimental results revealed that the reaction between an olivine matrix (Fo_{90}) and a relatively evolved MORB-type melt (X_{Mg} = 0.62) affects the olivine textural features and the chemistry of the mineral phases. A detailed microstructural study on olivine grains provided new insights on the origin of olivine-rich troctolite by a melt-dunite reaction process at the mantle-crust limit. The main results of isothermal experiments can be summarized as follows:

1- At 1200°C, the reaction results in the dissolution and crystallization of new olivine and interstitial phases *i.e*., plagioclase and clinopyroxene. The amount of the interstitial phases is positively correlated with the IMA.

2- At 1300°C, a relatively high initial melt amount (50wt%) enhances the reaction promoting olivine dissolution and crystal growth which leads in an increase in the olivine grain boundaries tortuosity.

3- The NiO content in reacted olivine in the experiments with $50wt\%_{IMA}$ is strongly influenced by the temperatures. It decreases with the increase of initial melt amount. $Kd_{Ni}^{ol/melt}$ decrease with the increase of temperatures from ≈ 6.33 to ≈ 2.00.

4- At 1300°C, the NiO content is affected by the different initial melt amount and decreases with the increase of IMA.

5- The composition of interstitial phases (*i.e.,* plagioclase and clinopyroxene) is mostly controlled by the chemistry of the reacted melt. In particular, high-Mg# clinopyroxene shows lower Cr_2O_3 and Al_2O_3 than natural troctolites. This further suggests the importance of spinel dissolution during the reaction processes in affecting the clinopyroxene chemical composition.

6- At 1200°C, the reacted melt compositions are more evolved than ones at 1300°C. This is due to the crystallization of olivine and interstitial phases (*i.e.,* plagioclase and clinopyroxene) and their total abundances varying with the different initial melt amount.

7- The interaction between an olivine matrix and a high melt amount (50wt%) at high temperature (*i.e.*, 1300°) strongly affects the pre-existing matrix recovering its plastic deformation, thus generating a "undeformed" matrix. In this scenario, is difficult to define a pre-existing olivine grain (**Olivine$_1$**) and a new crystallized olivine (**Olivine$_2$**).

The main results provided by the step-cooled experiments can be summarized as follows:

1- Reactive dissolution and crystallization experiments result in dunite (IMA 10wt%), olivine-rich troctolite (IMA 25wt%) and olivine-gabbro (IMA 50wt%).
2- The olivine textures result in elongated crystals with higher tortuosity of grain boundaries independently of the grain size and initial melt amount.
3- The NiO content in olivine does not depend on the initial melt amount but it depends on the reacted melt composition.
4- Differently to a normal fractional crystallization, the reactive crystallization of the interstitial melt leads to early clinopyroxene crystallization rather than plagioclase. This is presumably related to a combined effect of: i) the MgO enrichment of reacted melt due to the high extent of olivine dissolution and ii) small amounts of H_2O in reacted melts that suppress the plagioclase crystallization.
5- The reactive dissolution and crystallization processes efficiently promote the "recovery" of olivine plastic deformation independently of the grain size (and shape) and the different melt/olivine ratio.

Overall, the experimental results are comparable with textural and chemical observations documented in olivine-rich troctolite from ophiolitic massifs (*e.g.*, Sanfilippo & Tribuzio 2013; Basch et al., 2018, 2019 and 2021) supporting their origin through the reaction between a dunite and an impregnating MORB-type melt. The runs with lower and higher initial melt amount (*i.e.,* 10 and 50wt%) show that the reaction and crystallization processes at 1100 and 1200°C generally produce dunite and olivine-gabbro, respectively. The experiments performed at 1300°C indicate that high initial melt amount (50wt%) enhances the olivine dissolution and the increase of dunite matrix porosity. Moreover, contrary to the layered reaction couple experiments performed by Francomme, J. E., (2016-2017) and Borghini et al., (2018), the olivine-melt mixture used in the experiments of this study allows to better quantify the variability of modal olivine and the residual melt amount resulted from the reaction with the olivine matrix.

ACKNOWLEDGMENTS

Per la realizzazione di questa tesi vorrei ringraziare la mia Tutor, la Prof.ssa Patrizia Fumagalli ed il mio Co-Tutor il Dr. Giulio Borghini, grazie ai quali ho potuto conoscere e apprendere gli aspetti fondamentali della petrologia sperimentale e della ricerca in senso lato, occupando un ruolo importante nella mia crescita professionale e personale.

Ringrazio il mio correlatore, il Prof. Giancarlo Capitani ed il tecnico SEM Tiziano Catelani (Dipartimento di Scienze dell'Ambiente e della Terra, Università di Milano-Bicocca) per la loro professionalità ed il loro fondamentale supporto nella realizzazione ed elaborazione delle analisi EBSD.

Ringrazio anche Andrea Risplendente non solo per la sua professionalità nella realizzazione delle analisi tramite EMPA (Dipartimento di Scienze della Terra "Ardito Desio", Università degli Studi di Milano) ma anche per essersi rivelato un amico e sostegno fondamentale in questi 3 anni di dottorato. Vorrei anche ringraziare Sula Milani per avermi "soccorso" e supportata in questi 3 anni.

Un ringraziamento particolare va alla mia amica più che collega di ufficio Deborah Spartà, con cui ho avuto il piacere di instaurare un importante rapporto personale ancor prima che professionale. Ringrazio anche il mio collega di ufficio, il "Gigante Buono", Francesco Pagliaro per avermi regalato un sorriso e leggerezza nei giorni più pesanti.

Di fondamentale importanza sono stati la mia famiglia e i miei amici più cari che mi hanno sostenuta anche e soprattutto nei momenti di sconforto e debolezza sopportandomi e dandomi un motivo in più per affrontare le difficoltà.

Ultimo ma non meno importante, devo ringraziare il mio ragazzo Davide che ho avuto la fortuna di conoscere durante il mio dottorato come compagno di ufficio. Il raggiungimento ed il conseguimento di questo mio percorso professionale e accademico è anche suo. Mi ha aiutata ad affrontare i momenti difficili in modo razionale, ricordandomi che non tutto è impossibile. È il mio piccolo colpo di fortuna!

REFERENCES

Adams, B. L., Wright S. I., & Kunze, K. (1993). Orientation imaging: The emergence of a new microscopy. *Metallurgical Transactions***, 24A**, 819–831.

Almeev, R. R., Portnyagin, M., Wengorsh, T., Sano, T., Natland, J. H., & Garbe-Schönberg, D. (2011). Highly depleted melt inclusions in olivine from Shatsky Rise. *Mineralogical Magazine*, **75 (3)**, 426.

Arai, S., Matsukage, K., Isobe, E., & Vysotskiy, S. (1997). Concentration of incompatible elements in oceanic mantle: effect of melt/wall interaction in stagnant or failed melt conduits within peridotite. *Geochimica et. Cosmochimica Acta* **61**, 671-675.

Asimov, P. D., & Stolper, E. M. (1999). Steady-state mantle-melt interactions in one dimension: equilibrium, transport and melt focusing. *Journal of Petrology*, **40**, 475-494.

Bachmann, F., Hielscher, H., Jupp, P. E., Pantleon, W., Schaeben, H., & Wegert, E. (2010). Inferential statistics of electron backscatter diffraction data from within individual crystalline grains. *Journal of Applied Crystallography*, **43**, 1338-1355.

Bachmann, F., Hielscher, R., & Schaeben, H. (2011). Grain detection from 2d and 3d EBSD data – Specification of the MTEX algorithm. *Ultramicroscopy*, **111**, 1720-1733.

Basch, V., Rampone, E., Crispini, L., Ferrando, C., Ildefonse, B., & Godard, M. (2018). From mantle peridotites to hybrid troctolites: textural and chemical evolution during melt-rock interaction history (Mt. Maggiore, Corsica, France). *Lithos*, **323**, 4–23.

Basch, V., Rampone, E., Crispini, L., Ferrando, C., Ildefonse, B., & Godard, M. (2019). Multi-stage reactive formation of troctolites in slowspreading oceanic lithosphere (Erro–Tobbio, Italy): A combined field and petrochemical study. *Journal of Petrology*, **60(5),** 873–906.

Basch, V., Druey, M. R., Plumper, O., Hellebrand, E., Crispini, L., Barou, F., Godard, M., & Rampone, E. (2021). Intracrystalline melt micgration in deformed olivine revealed by trace element compositions and polyphase solid inclusions. *European Journal of Mineralogy*, **33**, 463-477.

Boistelle, R., & Astier, J. P. (1988). Crystallization mechanisms in solution. *Journal of Crystal Growth*, **90**, 14-30.

Borghini, G., & Rampone, E. (2007). Post cumulus processes in oceanic-type olivine-rich cumulates: the role of trapped melt crystallization versus melt/rock interaction. *Contributions to Mineralogy and Petrology*, **154**, 619–33.

Borghini, G., Rampone, E., Crispini, L., De Ferrari, R., & Godard, M. (2007). Origin and emplacement of ultramafic-mafic intrusions in the Erro-Tobbio manle peridotite (Ligurian Alps, Italy). *Lithos*, **94**, 210-229.

Borghini, G., Fumagalli, P., & Rampone, E. (2009) The stability of plagioclase in the upper mantle: subsolidus experiments on fertile and depleted lherzolite. *Journal of Petrology*, **51**, 229-254.

Borghini, G., Francomme, J. E., & Fumagalli, P. (2018). Melt-dunite interactions at 0.5 and 0.7 GPa: experimental constraints on the origin of olivine-rich troctolites. *Lithos*, **323**, 44-57.

Britton, T. B., Jiang, J., Guo, Y., Vilalta-Clemente, a., Wallis, D., Hansen, L. N., Winckelmann, A., & Wilkinson, A. J. (2016). Tutorial: Crystal orientations and EBSD – Or which way is up? *Materials Characterization*, **117,** 113-126.

Burnley, P. C., & Getting, I. C. (2012). Creating a high temperature environment at high pressure in a gas piston cylinder apparatus. *Review of Scientific Instruments*, **83**, 014501/1-014501/9.

Burnley, P. C., Cline II, C. J., & Drue, A. (2013). The nature and role of kinking in olivine deformation at high pressure. *American Mineralogist*, **98**, 927-931.

Cabane, H., Laporte, D., & Provost, A. (2005). An experimental study of Ostwald ripening of olivine and plagioclase in silicate melts: implications for the growth and size of crystals in magmas. *Contributions to Mineralogy and Petrology*, **150**, 37-53.

Chatterjee, R., & lassiter, J. C. (2016) 186Os/188Os variations in upper mantle peridotites: constraints on the Pt/Os ratio of primitive upper mantle, and implications for late vaneer accretion and mantle mixing timescales. *Chemical Geology*, **442**, 11-22.

Chen, Y., & Zhang, Y. (2008). Olivine dissolution in basaltic melt. *Geochimica et Cosmochimica Acta***, 72**, 4756-4777.

Ciazela, J., Dick, H. J. B., Koepke, J., Pieterek, B., Muszynki, A., Botcharnikov, R., & Kuhn, T. (2017). Thin crust and exposed mantle control sulfide differentiation in slow-spreading ridge magmas. *The Geological Society of America*, **45**, 1-4.

Ciazela, J., Koepke, J., Dick, H. J. B., Botcharnikov, R., Muszynki, A., Lazarov, M., Schuth, S., Pieterek, B., & Kuhn, T. (2018). Sulfid enrichment at an oceanic crust-mantle transition zone: Kane Megamullion (23°N, MAR). *Geochimica et Cosmochimica Acta*, **230**, 155-189.

Collier, M. L., Kelemen, P. B. (2010). The case for reactive crystallization at mid-ocean ridges. *Journal of Petrology*, **51**, 1913-1940.

Coogan, L. A., Hain, A., Stahl, S., & Chakraborty, S. (2005). Experimental determination of the diffusion coefficient for calcium in olivine between 900°C and 1500°C. *Geochimica et Cosmochimica Acta*, **69**, 3683-3694.

Coogan, L. A. (2007). The lower oceanic crust. In turekian KK, Holland KD (eds) Treatise on geochemistry. *Elsevier, Amsterdam*, **3.19,** 1-45.

Coogan, L. A., Jenkin, G. R. T., & Wilson, R. N. (2007). Contrasting cooling rates in the oceanic lithosphere at fast- and slow-spreading mid-ocean ridges derived from geospeedometry. *Journal of Petrology*, **48**, 2211-2231.

Couvy, H., Frost, D., Heidelbach, F., Nyilas, K., Ungar, T., Mackwell, S., & Cordier, P. (2004). Shear deformation experiments of forterite at 11 GPa – 1400°C in the multianvil apparatus. *European Journal of Mineralogy*, **16**, 877-889.

Daines, M. J., Kohlstedt, D. L. (1994). The transition from porous to channelized flow due to melt/rock reaction during melt migration. *Geophysical Research Letters*, **21**, 145-148.

Danyushevsky, L. V. (2001). The effect of small amounts of H2O on crystallization of mid-ocean ridge and backarc basin magmas. *Journal of volcanology and geothermal research*, **110**, 265-280.

De Haas, G. -J. L. M., Nijland, T. G., Valbracht, P. J., Maijer, C., Verschure, R., & Andersen, T. (2002). Magmatic versus methamorphic origin of olivine-plagioclase coronas. *Contributions to Mineralogy and Petrology*, **143**, 537-50.

Demouchy, S., Tommasi, A., Boffa Ballaran, T., & Cordier, P. (2013). Low strength of Earth's uppermost mantle inferred from tri-axial deformation experiments on dry olivine crystals. *Physics of the Earth and Planetary Interiors*, **220**, 37-49.

Dick, H. J. B., Ozawa, K., Meyer, P.S., Niu, Y., Robinson, P.T., Constantin, M., et al. (2002). 10. Primary silicate mineral chemistry of a 1.5 km section of very slow spreading lower ocean crust: ODP hole 735B, Southwest Indian ridge. *Proceedings of Ocean Drilling Program, Scientific Results*, **000**, 1-60.

Dick, H. J. B., Lissenberg, C. J., & Warren, J. M. (2010). Mantle Melting, Melt Transport, and Delivery Beneath a Slow-Spreading Ridge: The Paleo-MAR from 23°150N to 23°450N. *Journal of Petrology*, **51**, 425–67.

Dohmen R., Becker H. W. & Chakraborty S. (2007). Fe-Mg diffusion in olivine I: experimental determination between 700 and 1200°C as a function of composition, crystal orientation and oxygen fugacity. *Physics and Chemistry of Minerals* **34**, 389-407.

Donaldson, C. H. (1974). Olivine crystal types in harrisitic rocks of the Rhum pluton and Archean spinifex rocks. *The Geological Society of America*, **85**, 1721-1726.

Donaldson, C. H. (1976). An experimental investigation of olivine morphology. *Contributions to Mineralogy and Petrology*, **57**, 187-213.

Donaldson, C. H. (1985). The rates of dissolution of olivine, plagioclase, and quartz in a basalt melt. *Mineralogical Magazine*, **49**, 683-693.

Drouin, M., Godard, M., Ildefonse, B., Bruguier, O., & Garrido, C. J. (2009). Geochemical and petrographic evidence for magmatic impregnation in the oceanic lithosphere at Atlantis Massif, Mid-Atlantic Ridge (IODP Hole U1309D, 30 N). *Chemical Geology*, **264 (1-4),** 71–88.

Drouin, M., Ildefonse, B., & Godard M. (2010). A microstructural imprint of melt impregnation in slow-spread lithosphere: olivine-rich troctolites from the Atlantis Massif (Mid-Atlantic Ridge 30°N, IODP Hole U1309D). *Geochemistry, Geophysics, Geosystems,* **11**, 1-21.

Dygert, N., Liang, Y., & Kelemen, P. B. (2016). Formation of plagioclase lherzolite and associated dunite-harzburgite-lherzolite sequences by multiple episodes of melt percolation and melt-rock reaction: an example from the Trinity Ophiolite, California, USA. *Journal of Petrology*, **57**, 815-838.

Ferrando, C., Godard, M., Ildefonse, b., & Rampone, E. (2018). Melt transport and mantle assimilation at Atlantis Massif (IODP Site U1309) constraints from geochemical modeling. *Lithos*, **323**, 24-43.

Franck, F. C. (1949) The influence of dislocations on crystal growth. *Discussions of the Faraday Society*, **5**, 48.

Francomme, J. E. (2016-2017). Melt-rock interaction at the mantle-crust transition zone in the oceanic spreading lithosphere: an experimental study. *PhD Thesis*. University of Milan, Department of Earth Science "Ardito Desio".

Finch, G. I., & Wilman, H. (1937). The study of surface structure by electron diffraction. *Ergebnisse der Exakten Naturwissenschaften*, **16**, 353-436.

Gale, A., Dalton, C. A., Langmuir, C. H., Su, Y., & Shilling, J. (2013). The mean composition of ocean ridge basalts. *Geochemistry, Geophysics, Geosystems,* **14**, 489-518.

Godard, M., Awaji, S., & Hansen H. (2009). Geochemistry of a long in-situ section of intrusive slow-spread oceanic lithosphere: results from IODP Site U1309 (Atlantis Massif, 30°N Mid-Atlantic-Ridge). *Earth and Planetary Science Letters,* **279**, 110–22.

Grove, T. L., Kinzler, R. J., & Bryan, W. B. (1992). Fractionation of mid-ocean ridge basalt (MORB). *Geophysical Monograph Series*, **71**, 281–310.

Greene, A. R., Garcia, M. O., Weis, D., Ito, G., Kuga, M., Robinson, J., & Yamasaki, S. (2010). Low-productivity Hawaiian volcanism between Kaua'I and O'ahu. *Geochemistry, Geophysics, Geosystems,* **11**, 1-30.

Halfpenny, A. Some important practical issues for the collection and manipulation of Electron Backscatter Diffraction (EBSD) data from geological samples. *Journal of the Virtual Explorer, Electronic Edition*, **35**, 1-18.

Hart, S. R., Davis, K. E. (1978), Nickel partitioning between olivine and silicate melt. *Earth and Planetary Science Letters*, **40**, 203–219.

Husen, A., Almeev, R., & Holtz, F. (2016). The effect of H2O and pressure on multiple saturation and liquid lines of descent in basalt from Shatsky rise. *Journal of Petrology, **57**, 309-344.*

Hielscher, R., & Schaeben, H. (2008). A novel pole figure inversion method: specification of the MTEX algorithm. *Journal of Applied Crystallography*, **41**, 1024-1037.

Ismail, W. B., Tommasi, A., Lopes-Sanchez, M. A., Rutter, E. H., Barou, F., & Demouchy, S. (2021). Deformation of upper mantle rocks with contrasting initial fabrics in axial extension. Revised version submitted to *Tectonophysics*.

Kelemen, P. B., Shimizu, N., & Salters, V. J. M. (1995a) Extraction of mid-ocean-ridge basalt from the upwelling mantle by focused flow of melt in dunite channels. Nature, **375**, 747-753.

Kelemen, P. B., Whitehead, J. A., Aharonov, E., & Jordahl, K. A. (1995b). Experiments on flow focusing in soluble porous media, with application to melt extraction from the mantle. *Journal of Geophysical Research Atmospheres*, **100**, 475-496.

Kirkpatrick, R. J. (1975). Crystal growth from melt: a review. *American Mineralogist*, **60**, 798-814.

Khler, T. P., & Brey, G. P. (1990). Calcium exchange between olivine and clinopyroxene calibrated as a geothermometer for natural peridotites from 2 to 60 kb with applications. *Geochimica et Cosmochimica Acta*, **54,** 2375-2388.

Kohlstedt, D. L., & Mackwell, S. J. (1987). High-temperature stability of San Carlos olivine. *Contributions to Mineralogy and Petrology*, **95**, 226-230.

Kunze, K., Wright, S. I., Adams, B. L., & Dingley, D. J. (1993). Advances in automatic EBSP single orientation measurements. *Textures and Microstructures*, **13**, 41-45.

Lambart, S., Laporte, D., & Schiano, P. (2008). An experimental study of focused magma transport and basalt-peridotite interactions beneath mid-ocean ridges: implications for the generation of primitive MORB compositions. *Contributions to Mineralogy and Petrology*, **157**, 429-451.

Lasaga, A. C. (1998). Kinetic Theory in the Earth Sciences. Princeton, NJ: Princeton University Press.

Lasaga, A. C., & Lüttge, A. (2003) A model for crystal dissolution. *European Journal of Mineralogy*, **15**, 603-315.

Liang, Y. (1999). Diffusive dissolution in ternary systems: analysis with applications to quartz and quartzite dissolution in molten silicates. *Geochimica et Cosmochimica Acta*, **63**, 3983-3995.

Liang, Y. (2000). Dissolution in molten silicates: effects of solid solution. *Geochimica et Cosmochimica Acta*, **64**, 1617-1627.

Liang, Y. (2003). Kinetics of crystal-melt reaction in partially molten silicates: 1: Grain scale processes. *Geochemistry, Geophysics, Geosystems*, **4**, 1-27.

Liang, Y., Schiemenz, A., Hesse, M. A., Permentier, E. M., & Hesthaven, J. S. (2010). High-porosity channels for melt migration in the mantle: Top is the dunite and bottom is the harzbugite and lherzolite. *Geophysical Research Letters*, **37**, 1-5.

Libourel, G. (1999). Systematics of calcium partitioning between olivine and silicate melt: implications for melt structure and calcium content of magmatic olivines. *Contributions to Mineralogy and Petrology*, **136**, 63-80.

Lissenberg, C. J., & Dick, H. J. B. (2008). Melt-rock reaction in the lower oceanic crust and its implications for the genesis of mid-ocean ridge basalt. *Earth and Planetary Science Letters*, **271(1-4)**, 311–325.

Lissenberg, C. J., MacLeod, C. J., Howard, K. A., & Godard, M. (2013). Pervasive reactive melt migration through fast-spreading lower oceanic crust (Hess Deep, equatorial Pacific Ocean). *Earth and Planetary Science Letters*, **361**, 436–447.

Lissenberg, C. J., & MacLeod, C. J. (2016). A reactive porous flow control on mid-ocean ridge magmatic evolution. *Journal of Petrology*, **57(11-12),** 2195–2220.

Mainprice, D., Hielscher, R., & Schaeben, H., (2011). Calculating anisotropic physical properties from the texture data using the MTEX open-source package, in: Prior, D. J., Rutter, E. H. and Tatham, D. J. (eds) *Deformation mechanism, Rheology and Tectonics: Microstructures, Mechanics and Anisotropy*. Geological Society, London, Special Publications, 360, 175-192.

Mainprice, D. (2012). A personal and practical guide to the history, installation and future of the Electron Back-Scattered Diffraction (EBSD) system.

Mainprice, D., Bachmann, F., Hielscher, R., & Schaeben, H. (2014). Descriptive tools for the analysis of texture projects with large datasets using MTEX: strength, symmetry and components. Geological Society, London, Special Publications, 409(1):251.

Matzen, A. K., Baker, M. B., Beckett, J. R., Stolper, E. M. (2013). The temperature and pressure dependence of nickel partitioning between olivine and silicate melt. *Journal of Petrology*, **54,** 2521–2545.

Michael, J. R., & Goehner, R. P. (1993). Crystallographic phase identification in the scanning electron microscope: Backscatter electron Kikuchi patterns imaged with a CCD-based detector. *MSA Bull*, **23**, 168.

Morgan, Z., & Liang, Y. (2003). An experimental and numerical study of the kinetics of harzburgite reactive dissolution with applications to dunite dike formation. *Earth and Planetary Science Letters*, **214**, 59-74.

Morgan, Z., & Liang, Y. (2005). An experimental study of the kinetics of lherzolite reactive dissolution with applications to melt channel formation. *Contributions to Mineralogy and Petrology*, **150**, 369-385.

Nicholls, G. D., & Islam, M. R. (1971). Geochemical investigations of basalts and associated rocks from the ocean floor and their implications. *Mathematical, Physical and Engineering Sciences*, **268**, 469-4886.

Nishikawa, S., & Kikuchi, S. (1928). The diffraction of cathode rays by calcite. *Proceedings of the Imperial Academy*. (Japan), **4**, 475–477.

O'Driscoll, B., Donaldson, C. H., Troll, V. R., Jerram, A. D., & Emeleus, H. (2007). An origin for harrisitic and granular olivine in the Rum Layered Suite, NW Scotland: a crystal size distribution study. *Journal of Petrology*, **48**, 23-270.

Paquet, M., Cannat, M., Brunelli, D., Hamelin, C., & Humler, E. (2016). Effect of melt/mantle interactions on MORB chemistry at the easternmost Southwest Indian Ridge (61°-67° E). *Geochemistry, Geophysics, Geosystems,* **17,** 4605-4640.

Perk, N. W., Coogan, L. A., Karson, J. A., Klein, E. M., & Hanna, H. D. (2007). Petrology and geochemistry of primitive lower oceanic crust from Pito Deep: Implications for the accretion of the lower crust at the Southern East Pacific Rise. *Contributions to Mineralogy and Petrology,* **154 (5)**, 575-590.

Price, R. C., Kennedy, A. K., Riggins- Sneeringer, M., & Frey, F. A. (1986). Geochemistry of basalts from the Indian Ocean triple junction: implications for the generation and evolution of Indian Ocean ridge basalts. *Earth and Planetary Science Letters*, **78**, 379-396.

Prior, D. J., Mariani, E., & Wheeler, J. (2009). EBSD in the Earth Sciences: Applications, Common Practice and Challenges, in: Schwartz A. j., Kumar, M., Adams, B. L., Field, D. P. (Ed), *Electron Backscatter Diffraction in Materials Science. Springer Science + Business Media,* **26**, 345-360.

Rampone, E., Romairone, A., & Hofmann, A. W. (2004). Constrasting bulk and mineral chemistry in depleted peridotites: evidence for reactive porous flow. *Earth and Planetary Science Letters*, **218**, 491-506.

Rampone, E., Romairone, A., Abouchami, W., Piccardo, G. B., & Hofmann, A. W. (2005). Chronology, petrology and isotope geochemistry of the Erro-Tobbio peridotites (Ligurian Alps, Italy): records of late Paleozoic lithospheric extension. *Journal of Petrology*, **46**, 799-827.

Rampone, E., & Borghini, G. (2008). Melt migration and intrusion in the Erro-Tobbio peridotites (Ligurian Alps, Italy): insights on magmatic processes in extending lithospheric mantle. *European Journal of Mineralogy*, **20**, 573-585.

Rampone, E., Borghini, G., Godard, M., Ildefonse, B., Crispini, l., & Fumagalli, P. (2016). Melt/rock reaction at oceanic peridotite/gabbro transition as revealed by trace element chemistry of olivine. *Geochimica et Cosmochimica Acta* **190**, 390-331.

Raleigh, C. B. (1968). Mechanisms of plastic deformation of olivine. *Journal of Geophysical Research*, **73**, 5391-5406.

Reed, S. J. B. (2005). Electron microprobe analysis and scanning electron microscopy in geology. *University of Cambridge*, 1-5.

Renna, M. R., & Tribuzio R. (2011). Olivine-rich troctolites from Ligurian ophiolites (Italy): evidence for impregnation of replacive mantle conduits by MORB-type melts. *Journal of Petrology*, **52**, 1763–1790.

Renna, M. R., Tribuzio, R., & Ottolini, L. (2016). New perspectives on the origin of olivine-rich troctolites and associated harrisites from the Ligurian ophiolites (Italy). *Journal of the Geological Society*, **173**, 916-932.

Renna, M. R., Armandola, S., Becker, H., Sanfilippo, A., Tribuzio, R., & Wang, Z. (2021). Fractionation of highly siderophile and chalcogen elements in the lower oceanic crust: Insights from the troctolites of the Alpine—Appennine Jurassic ophiolites. *Lithos*, **380-381**, 1-14.

Sanfilippo, A., & Tribuzio, R. (2013a). Building of the deepest crust at a fossil slow-spreading center (Pineto gabbroic sequence, Alpine Jurassic ophiolites). *Contribution to Mineralogy and Petrology*, **165**, 705–21.

Sanfilippo, A., Dick, H. J. B., & Ohara, Y. (2013). Melt-rock reaction in the mantle: mantle troctolites from the Parece Vela ancient back-arc spreading center. *Journal of petrology*, **54**, 861-885.

Sanfilippo, A., Tribuzio, R., & Tiepolo, M. (2014). Mantle-crust interactions in the oceanic lithosphere: constraints from minor and trace elements in olivine. *Geochimica et Cosmochimica Acta*, **141**, 423-439.

Sanfilippo, A., Tribuzio, R., Tiepolo, M., & Berno, D. (2015). Reactive flow as dominant evolution process in the lowermost oceanic crust: evidence from olivine of the Pineto ophiolite (Corsica). *Contributions to Mineralogy and Petrology*, **170,** 1-12.

Sanfilippo, A., Dick H. J. B., Ohara, Y., & Tiepolo, M. (2016). New insights on the origin of troctolites from the breakaway area of the Godzilla Megamullion (Parece Vela back-arc basin): the role of melt-mantle interaction on the composition of the lower crust. *Island Arc*, **25**, 220-234.

Saper, L., & Liang, Y. (2014). Formation of plagioclase-bearing peridotite and plagioclase-bearing wehrlite and gabbro suite through reactive crystallization: an experimental study. *Contributions to Mineralogy and Petrology*, **163**, 1-16.

Schwarzer, R. A., Field, D. P., Adams, B. L., Kumar, M., & Schwartz, A., (2009). Present State of Electron Backscatter Diffraction and Perspective Developments, in: Schwartz A. j., Kumar, M., Adams, B. L., Field, D. P. (Ed), *Electron Backscatter Diffraction in Materials Science. Springer Science + Business Media*, 1-20.

Shejwalkar, A., & Coogan, L. A. (2013). Experimental calibration of the roles of temperature and composition in the Ca-in-olivine geothermometer at 0.1 MPa. *Lithos*, **177**, 54-60.

Simkin, T., & Smith, J. V. (1970). Minor-element distribution in olivine. *Journal of Geology*, **78**, 304-325.

Spiegelmen, M., Kelemen, P. B., & Aharonov, E. (2001). Causes and consequences of flow organization during melt transport: The raction infiltration instability in compactable media. *Journal of Geophysical Research Atmospheres*, **106**, 2061-2077.

Srivastava, R. K., Emmermann, R., & Pulchelt, H. (1980). Petrology and geochemistry of basalts from deep sea drilling project Leg 54. *Deep Sea Drilling Projects, Initial Reports*, **54**, 671-693.

Suhr, G., Hellebrand, E., Johnson, K., & Brunelli, D. (2008). Stacked gabbro units and intervening mantle: a detailed look at a section of IODP Leg 305, Hole U1309D. *Geochemistry, Geophysics, Geosystems,* **9**, 1-31.

Tommasi, A., Mainprice, D., Canoca, G., & Chastel, Y. (2000). Viscoplastic self-consistent and equilibrium-based modeling of olivine lattice prefereed orientations: implications for the upper mantle seismic anisotropy. *Journal of Geophysical Research Atmospheres*, **105**, 7893-7908.

Toramaru, A. (1991). Model of nucleation and growth of crystals in cooling magmas. *Contributions to Mineralogy and Petrology,* **108**, 106-117.

Tursack, E., & Liang, Y. (2011). A comparative study of melt-rock reactions in the mantle: laboratory dissolution experiments and geological field observations. *Contributions to Mineralogy and Petrology*, **163**, 861-876.

Ulmer, P., & Luth, R. (1991). The graphite-COH fluid equilibrium in P, T, fO2 space. *Contributions to Mineralogy and Petrology*, **106,** 265-272.

Van den Bleeken, G., Müntener, O., & Ulmer, P. (2010). Melt variability in percolated peridotite: an experimental study applied to reactive migration of tholeiitic basalt in the upper mantle. *Contributions to Mineralogy and Petrology,* **161**, 921-945.

Van den Bleeken, G., Müntener, O., & Ulmer, P. (2011). Reaction processes between tholeiitic melt and residual peridotite in the uppermost mantle: an experimental study at 0.8 GPa. *Journal of petrology,* **51**, 153-183.

Vernon, R. H. (2004). A practical guide to rock microstructure. *Cambridge University Press, **1nd edition***, 43-89.

Vernon, R. H. (2018). A practical guide to rock microstructure. *Cambridge University Press, **2nd edition***, 28-98.

Wood, B. J., & Blundy, J. D. (1997). A predictive model for rare earth element partitioning between clinopyroxene and anhydrous silicate melt. *Contributions to Mineralogy and Petrology*, **129,** 166-181.

Wright, S. I., & Adams, B. I. (1992). Automatic analysis of electron backscatter diffraction patterns. *Metall Trans*, **23A**, 759-767.

Yang, A. Y., Zhao, T. -P., Zhou, M. -F., Deng, X. -G., Wang, G., -Q., & Li, J. (2013). Os isotopic compositions of MORBs from the ultra-slow spreading Southwest Indian Ridge: constraints on the assimilation and fractional crystallization (AFC) processes. *Lithos*, **179**, 28-35.

Yang, A. Y., Wang, C., Liang, Y., & Lissenberg, C. J. (2019). Reaction between mid-ocean ridge basalt and lower oceanic crust: an experimental study. *Geochemistry, Geophysics, Geosystems,* **20**, 4390-4407.

Zhang, Y., Walker, D., & Lesher, C. E. (1989). Diffusive crystal dissolution. *Contributions to Mineralogy and Petrology,* **102,** 495-513.

APPENDIX

Table 7-1 shows the experimental studies, reported so far in literature, using different experimental sets-up and *T-P-t* conditions.

Table 7-2 reports the major element composition of olivine from isothermal experiments performed at 0.5 GPa, 1200, 1250 and 1300°C.

Table 7-3 reports the major element composition of olivine from step-cooled experiments performed at 0.5 GPa, from 1300 down to 1100°C.

Table 7-4 reports the major element composition of plagioclase from isothermal experiments performed at 0.5 GPa, 1200°C.

Table 7-5 reports the major element composition of plagioclase from step-cooled experiments performed at 0.5 GPa, from 1300 down to 1100°C.

Table 7-6 reports the major element composition of clinopyroxene from isothermal experiments performed at 0.5 GPa, 1200°C.

Table 7-7 reports the major element composition of clinopyroxene from step-cooled experiments performed at 0.5 GPa, from 1300 down to 1100°C.

Table 7-8 reports the major element composition of glass from isothermal experiments performed at 0.5 GPa, 1200, 1250 and 1300°C.

Table 7-9 reports the major element composition of glass from step-cooled experiments performed at 0.5 GPa, from 1300 down to 1100°C.

Table 7-10 reports textural and intra-granular deformation parameters, provided by EBSD analysis, for each class of grain size of isothermal experiment MG10 with 10wt%$_{IMA}$ run at 0.5 GPa and 1200°C for 24h.

Table 7-11 reports textural and intra-granular deformation parameters, provided by EBSD analysis, for each class of grain size of isothermal experiment MG12 with 25wt%$_{IMA}$ run at 0.5 GPa and 1200°C for 24h.

Table 7-12 reports textural and intra-granular deformation parameters, provided by EBSD analysis, for each class of grain size of isothermal experiment MG14 with 50wt%$_{IMA}$ run at 0.5 GPa and 1200°C for 24h

Table 7-13 reports textural and intra-granular deformation parameters, provided by EBSD analysis, for each class of grain size of isothermal experiment MG11 with 50wt%$_{IMA}$ run at 0.5 GPa and 1250°C for 24h.

Table 7-14 reports textural and intra-granular deformation parameters, provided by EBSD analysis, for each class of grain size of isothermal experiment OM23 with 9wt%$_{IMA}$ run at 0.5 GPa and 1300°C for 0.5h.

Table 7-15 reports textural and intra-granular deformation parameters, provided by EBSD analysis, for each class of grain size of isothermal experiment MG1 with 25wt%$_{IMA}$ run at 0.5 GPa and 1300°C for 24h.

Table 7-16 reports textural and intra-granular deformation parameters, provided by EBSD analysis, for each class of grain size of isothermal experiment MG5 with 50wt%$_{IMA}$ run at 0.5 GPa and 1300°C for 24h.

Table 7-17 reports textural and intra-granular deformation parameters, provided by EBSD analysis, for each class of grain size of step-cooled experiment MG15 with 10wt%$_{IMA}$ run at 0.5 GPa and from 1300 to 1100°C for 72h.

Table 7-18 reports textural and intra-granular deformation parameters, provided by EBSD analysis, for each class of grain size of step-cooled experiment MG4 with 25wt%$_{IMA}$ run at 0.5 GPa and from 1300 to 1100°C for 72h.

Table 7-19 reports textural and intra-granular deformation parameters, provided by EBSD analysis, for each class of grain size of step-cooled experiment MG16 with 50wt%$_{IMA}$ run at 0.5 GPa and from 1300 to 1100°C for 72h.

Table 7-1 *shows the experimental studies, reported so far in literature, using different experimental sets-up and T-P-t conditions, n.d = not definied.*

Reference	*T* (°C)	*P* (GPa)	*t* (hour)	Starting composition (wt%)	Process type	Glass ratio
Daines & Kohlstedt (1994)	1250	0.3	6	Melt sinks disk: Px = 5, 20, 50 and 95 % Glass sinks= 90% basaltic glass +10% (Ol+Px)	Reaction between disks of synthetic peridotite and basaltic glass	n.d
Daines & Kohlstedt (1994)	1250	0.3	12	Melt sinks disk: Px = 5, 20, 50 and 95 % Glass sinks= 90% basaltic glass +10% (Ol+Px)	Reaction between disks of synthetic peridotite and basaltic glass	n.d
Morgan & Liang (2003)	1290	0.6	0.0-8	Alkali basalt and harzburgite (Ol:Px= 1:1)	Dissolution of rods of basaltic and harzburgite-like compositions	n.d
Morgan & Liang (2003)	1260	0.75	4-8	Alkali basalt and harzburgite (Ol:Px= 1:1)	Dissolution of rods of basaltic and harzburgite-like compositions	n.d
Morgan & Liang (2003)	1250-1251	0.6	0.7-2	Alkali basalt and harzburgite (Ol:Px= 1:1)	Dissolution of pre-synthesized rods of basaltic and harzburgite-like compositions	n.d
Morgan & Liang (2005)	1300	1	2-8	Lherzolite (49 wt% Ol, 33% Opx, 18% Cpx) and alkali basalt (47% SiO_2)	Dissolution of pre-synthesized of lherzolite and alkali basalt	n.d
Morgan & Liang (2005)	1300	1	2-8	Lherzolite (49 wt% Ol, 33% Opx, 18% Cpx) and basaltic andesite (55% SiO_2)	Dissolution of pre-synthesized of lherzolite and basaltic andesite	n.d
Lambart et al. (2008)	1250-1310	0.5-1.25	72-113.5	Liquid 9-51% and variable amount of Ol (41-65%) Opx (0-21%), Cpx (0-11%) and Sp (0.2-0.8%)	Experiments of decompression melting of a focused magma	n.d
Van den Bleeken (2010)	1200-1320	0.8	0.17-92	Basaltic powder (49-50%SiO_2), peridotite (65% Ol, 24% Opx, 9% Cpx, 2% Spl or 63% Ol, 25% Opx, 10% Cpx, 2% Spl)	layered experimental setup between a layer of basaltic powder and one of peridotite	n.d

Reference	*T* (°C)	*P* (GPa)	*t* (hour)	Starting composition (wt%)	Process type	Glass ratio
Van den Bleeken (2011)	1170-1290	0.65-0.8	15	Basalt (49-50% SiO_2), peridotite analogue (65% ol, 24% opx, 9% cpx and 2% spl, or 63% ol, 25% opx, 10% cpx and 2% spl)	layered experimental setup between a layer of vitrified basalt and one of a peridotite analogue powder	n.d
Tursack & Liang (2012)	1300 to 1200	1 to 0.7	25+24	Mantle peridotite (Ol 57%, Opx 28%, CPx 13%, Sp 2%), alkali basalt (SiO_2 47%, Σ (Na_2O, Al_2O_3, K_2O, CaO) ~ 37%)	Reactive experiment with a unique *T* drop (*T* peak ~1300°C, final *T* ~1200°C) using an alkali basalt and a mantle peridotite	n.d
Tursack & Liang (2012)	1300 to 1200	1	29.7-49.7	Mantle peridotite (Ol 57%, Opx 28%, CPx 13%, Sp 2%), alkali basalt (SiO_2 47%, Σ (Na_2O, Al_2O_3, K_2O, CaO) ~ 37%)	Reactive step- cooled experiments (*T* peak ~1300°C, final *T* ~1200°C) using an alkali basalt and a mantle peridotite	n.d
Tursack & Liang (2012)	1320 to 1200	1	72.5	Mantle peridotite (Ol 57%, Opx 28%, CPx 13%, Sp 2%), MORB (SiO_2 50%, Σ (Na_2O, Al_2O_3, K_2O, CaO) ~ 32%)	Reactive step- cooled experiment (*T* peak ~1320°C, final *T* ~1200°C) using MORB and a mantle peridotite	n.d
Saper & Liang (2014)	1300 to 1050	1 to 0.7	24-72	Mantle peridotite (Ol 57%, Opx 28%, CPx 13%, Sp 2%), MORB (SiO_2 50%, Σ (Na_2O, Al_2O_3, K_2O, CaO) ~ 32%)	Reactive step- cooled experiments (*T* peak ~1300°C, final *T* ~1050°C) using a MORB and a mantle peridotite	n.d
Saper & Liang (2014)	1300 to 1050	1 to 0.7	24	Mantle peridotite (Ol 57%, Opx 28%, CPx 13%, Sp 2%), MORB (SiO_2 50%, Σ (Na_2O, Al_2O_3, K_2O, CaO) ~ 32%)	Reactive experiment using a MORB and a mantle peridotite at a constant *T*	n.d
Borghini et al. (2018)	1300 to 1150	0.5	72	San Carlos olivine (X_{Mg}~90), MORB glass (SiO_2~47% Σ (Na_2O, Al_2O_3, K_2O, CaO) ~ 32.5%)	Layered reactive dissolution and crystallization experiments between a MORB glass and melt -bearing dunite	n.d

Reference	*T* (°C)	*P* (GPa)	*t* (hour)	Starting composition (wt%)	Process type	Glass ratio
Borghini et al. (2018)	1300 to 1150	0.7	72	San Carlos olivine (X_{Mg}~90), MORB glass (SiO_2~47% Σ (Na_2O, Al_2O_3, K_2O, CaO) ~ 32.5%)	Layered reactive dissolution and crystallization experiments between a MORB glass and melt -bearing dunite	n.d
Borghini et al. (2018)	1250	0.7	24	San Carlos olivine (X_{Mg}~90), MORB glass (SiO_2~47% Σ (Na_2O, Al_2O_3, K_2O, CaO) ~ 32.5%)	Layered reactive dissolution and crystallization experiments between a MORB glass and melt -bearing dunite	n.d
Yang et al. (2019)	1180-1000	0.5	9-48	Troctolite mush (Ol 45%, Pl 45%, 10% primitive MORB) and evolved MORB (Mg#/An/Fo ~54)	Step-cooled reaction experiments in a layered reaction couple between a troctolite and a MORB evolved basalt	n.d
Yang et al. (2019)	1200-1050/1200	0.5	26	Troctolite mush (Ol 45%, Pl 45%, 10% primitive MORB) and primitive MORB (Mg#/An/Fo ~63)	Step-cooled reaction experiment in a layered reaction couple between a troctolite and a primitive MORB basalt	n.d
Yang et al. (2019)	1180	0.5	6	Troctolite mush (Ol 45%, Pl 45%, 10% primitive MORB) and evolved MORB (Mg#/An/Fo ~54)	Isothermal experiment in a layered reaction couple between a troctolite and an evolved MORB basalt	n.d
Yang et al. (2019)	1200	0.5	6	Troctolite mush (Ol 45%, Pl 45%, 10% primitive MORB), primitive MORB (Mg#/An/Fo ~63)	Isothermal experiment in a layered reaction couple between a troctolite and a primitive MORB basalt	n.d

Table 7-2 *Major element composition of olivine from isothermal experiments performed at 0.5 GPa, 1200, 1250 and 1300°C.*

Sample	MG10	MG10	MG10	MG10	MG10	MG10	MG10	MG10	MG10	MG10	MG10	MG10	MG10	MG10
Run duration	24	24	24	24	24	24	24	24	24	24	24	24	24	24
Melt	AH6	AH6	AH6	AH6	AH6	AH6	AH6	AH6	AH6	AH6	AH6	AH6	AH6	AH6
IMA (wt%)[a]	10	10	10	10	10	10	10	10	10	10	10	10	10	10
T[b]	1200	1200	1200	1200	1200	1200	1200	1200	1200	1200	1200	1200	1200	1200
P[c]	0.5	0.5	0.5	0.5	0.5	0.5	0.5	0.5	0.5	0.5	0.5	0.5	0.5	0.5
Point Analysis	MG10OL1	MG10OL2	MG10OL3	MG10OL4	MG10OL5	MG10OL6	MG10OL7	MG10OL8	MG10OL9	MG10OL10	MG10OL11	MG10OL12	MG10OL13	MG10OL14
Site	core	core	core	core	core	rim	core	core	rim	rim	core	core	rim	core
SiO_2	41.10	40.80	41.11	40.94	40.67	40.76	41.03	41.29	40.77	40.84	40.23	40.54	40.94	40.57
TiO_2	0.02	0.01	0.03	0.00	0.06	0.01	0.03	0.00	0.00	0.03	0.05	0.01	0.03	0.03
Al_2O_3	0.02	0.05	0.06	0.00	0.00	0.02	0.06	0.03	0.04	0.02	0.00	0.01	0.04	0.07
Cr_2O_3	0.00	0.00	0.00	0.07	0.07	0.00	0.04	0.05	0.05	0.03	0.00	0.01	0.02	0.06
FeO	10.96	10.99	10.78	10.85	10.79	11.05	10.84	11.07	10.74	11.04	10.86	11.13	11.12	11.00
MgO	48.30	48.80	48.30	48.51	48.82	48.52	47.83	48.72	48.85	47.97	48.72	48.23	48.21	48.06
MnO	0.13	0.20	0.13	0.16	0.18	0.12	0.14	0.14	0.19	0.13	0.23	0.22	0.22	0.17
NiO	0.21	0.24	0.06	0.21	0.24	0.21	0.08	0.10	0.27	0.12	0.23	0.18	0.13	0.08
CaO	0.29	0.12	0.32	0.12	0.10	0.23	0.37	0.26	0.09	0.30	0.16	0.26	0.26	0.30
Na_2O	0.00	0.03	0.00	0.00	0.00	0.02	0.00	0.00	0.00	0.04	0.03	0.00	0.01	0.00
K_2O	0.00	0.00	0.00	0.00	0.00	0.00	0.00	0.00	0.00	0.00	0.01	0.00	0.00	0.00
Total	101.03	101.24	100.78	100.86	100.93	100.93	100.43	101.66	100.99	100.53	100.53	100.59	100.98	100.34
Si	1.00	0.99	1.01	1.00	0.99	1.00	1.01	1.00	0.99	1.00	0.98	0.99	1.00	1.00
Ti	0.00	0.00	0.00	0.00	0.00	0.00	0.00	0.00	0.00	0.00	0.00	0.00	0.00	0.00
Al	0.00	0.00	0.00	0.00	0.00	0.00	0.00	0.00	0.00	0.00	0.00	0.00	0.00	0.00
Cr	0.00	0.00	0.00	0.00	0.00	0.00	0.00	0.00	0.00	0.00	0.00	0.00	0.00	0.00
Fe^{2+}	0.22	0.22	0.22	0.22	0.22	0.23	0.22	0.22	0.22	0.23	0.22	0.23	0.23	0.23
Mg	1.76	1.77	1.76	1.77	1.77	1.77	1.75	1.76	1.77	1.75	1.78	1.76	1.76	1.76
Mn	0.00	0.00	0.00	0.00	0.00	0.00	0.00	0.00	0.00	0.00	0.00	0.00	0.00	0.00
Ni	0.00	0.00	0.00	0.00	0.00	0.00	0.00	0.00	0.01	0.00	0.00	0.00	0.00	0.00
Ca	0.01	0.00	0.01	0.00	0.00	0.01	0.01	0.01	0.00	0.01	0.00	0.01	0.01	0.01
Na	0.00	0.00	0.00	0.00	0.00	0.00	0.00	0.00	0.00	0.00	0.00	0.00	0.00	0.00
K	0.00	0.00	0.00	0.00	0.00	0.00	0.00	0.00	0.00	0.00	0.00	0.00	0.00	0.00
Sum	3.00	3.00	3.00	3.00	3.00	3.00	3.00	3.00	3.00	3.00	3.00	3.00	3.00	3.00
X_{Mg}[d]	0.88	0.88	0.88	0.88	0.88	0.88	0.88	0.88	0.88	0.88	0.88	0.88	0.88	0.88

Cations are calculated with the Program NORM (version 2019) edited by Ulmer, P., and Poli, S. [a] Initial melt amount. [b] Temperature. [c] Pressure. [d] X_{Mg} = Mg/(Mg+Fe). [e] Reaction experiment performed at 0.5 GPa, 1300°C from Francomme, J. E., Phd Thesis (2016-2017).

Sample	MG10	MG10	MG10	MG10	MG10	MG10	MG10	MG10	MG10	MG10	MG10	MG10	MG10	MG10
Run duration	24	24	24	24	24	24	24	24	24	24	24	24	24	24
Melt	AH6	AH6	AH6	AH6	AH6	AH6	AH6	AH6	AH6	AH6	AH6	AH6	AH6	AH6
IMA (wt%)	10	10	10	10	10	10	10	10	10	10	10	10	10	10
T	1200	1200	1200	1200	1200	1200	1200	1200	1200	1200	1200	1200	1200	1200
P	0.5	0.5	0.5	0.5	0.5	0.5	0.5	0.5	0.5	0.5	0.5	0.5	0.5	0.5
Point Analysis	MG10OL15	MG10OL16	MG10OL17	MG10OL18	MG10OL19	MG10OL20	MG10OL21	MG10OL22	MG10OL23	MG10OL24	MG10OL25	MG10OL26	MG10OL27	MG10OL28
Site	core	core	core	core	core	core	core	core	core	core	core	core	core	core
SiO_2	40.80	40.42	40.49	41.19	40.86	40.95	40.24	40.85	41.15	40.76	40.51	40.59	40.18	40.62
TiO_2	0.00	0.05	0.02	0.00	0.02	0.00	0.01	0.00	0.05	0.03	0.04	0.04	0.03	0.02
Al_2O_3	0.05	0.04	0.02	0.03	0.08	0.01	0.04	0.04	0.07	0.02	0.11	0.04	0.00	0.03
Cr_2O_3	0.00	0.00	0.00	0.05	0.04	0.04	0.03	0.01	0.00	0.00	0.00	0.08	0.07	0.00
FeO	11.09	10.86	10.76	11.09	11.25	10.89	11.12	11.15	10.53	10.85	11.03	11.02	10.99	10.97
MgO	49.51	49.16	49.80	49.71	49.50	49.22	49.74	49.44	48.50	49.56	49.35	49.73	50.04	49.20
MnO	0.18	0.13	0.08	0.15	0.16	0.18	0.20	0.19	0.18	0.14	0.18	0.15	0.12	0.13
NiO	0.13	0.16	0.28	0.17	0.09	0.32	0.11	0.17	0.09	0.06	0.10	0.11	0.35	0.09
CaO	0.27	0.23	0.11	0.30	0.31	0.17	0.27	0.27	0.38	0.22	0.33	0.22	0.11	0.32
Na_2O	0.02	0.03	0.01	0.04	0.02	0.00	0.00	0.00	0.00	0.00	0.03	0.01	0.03	0.02
K_2O	0.00	0.00	0.00	0.01	0.00	0.00	0.01	0.02	0.00	0.02	0.00	0.00	0.00	0.00
Total	102.05	101.08	101.57	102.74	102.33	101.78	101.77	102.14	100.95	101.66	101.68	101.99	101.92	101.40
Si	0.98	0.98	0.98	0.99	0.98	0.99	0.97	0.98	1.00	0.98	0.98	0.98	0.97	0.98
Ti	0.00	0.00	0.00	0.00	0.00	0.00	0.00	0.00	0.00	0.00	0.00	0.00	0.00	0.00
Al	0.00	0.00	0.00	0.00	0.00	0.00	0.00	0.00	0.00	0.00	0.00	0.00	0.00	0.00
Cr	0.00	0.00	0.00	0.00	0.00	0.00	0.00	0.00	0.00	0.00	0.00	0.00	0.00	0.00
Fe^{2+}	0.22	0.22	0.22	0.22	0.23	0.22	0.22	0.22	0.21	0.22	0.22	0.22	0.22	0.22
Mg	1.78	1.78	1.79	1.77	1.77	1.77	1.79	1.78	1.76	1.78	1.78	1.79	1.80	1.78
Mn	0.00	0.00	0.00	0.00	0.00	0.00	0.00	0.00	0.00	0.00	0.00	0.00	0.00	0.00
Ni	0.00	0.00	0.01	0.00	0.00	0.01	0.00	0.00	0.00	0.00	0.00	0.00	0.01	0.00
Ca	0.01	0.01	0.00	0.01	0.01	0.00	0.01	0.01	0.01	0.01	0.01	0.01	0.00	0.01
Na	0.00	0.00	0.00	0.00	0.00	0.00	0.00	0.00	0.00	0.00	0.00	0.00	0.00	0.00
K	0.00	0.00	0.00	0.00	0.00	0.00	0.00	0.00	0.00	0.00	0.00	0.00	0.00	0.00
Sum	3.00	3.00	3.00	3.00	3.00	3.00	3.00	3.00	3.00	3.00	3.00	3.00	3.00	3.00
X_{Mg}	0.88	0.88	0.89	0.88	0.88	0.88	0.88	0.88	0.88	0.89	0.88	0.88	0.88	0.88

Sample	MG10	MG12	MG12	MG12	MG12	MG12	MG12	MG12	MG12	MG12	MG12	MG12	MG12	MG12
Run duration	24	24	24	24	24	24	24	24	24	24	24	24	24	24
Melt	AH6	AH6	AH6	AH6	AH6	AH6	AH6	AH6	AH6	AH6	AH6	AH6	AH6	AH6
IMA (wt%)	10	25	25	25	25	25	25	25	25	25	25	25	25	25
T	1200	1200	1200	1200	1200	1200	1200	1200	1200	1200	1200	1200	1200	1200
P	0.5	0.5	0.5	0.5	0.5	0.5	0.5	0.5	0.5	0.5	0.5	0.5	0.5	0.5
Point Analysis	MG10OL29	MG12OL1	MG12OL2	MG12OL3	MG12OL4	MG12OL5	MG12OL6	MG12OL7	MG12OL8	MG12OL9	MG12OL10	MG12OL11	MG12OL12	MG12OL13
Site	core	core	rim	core	rim	core	core	rim	core	core	rim	core	core	core
SiO_2	40.42	40.85	40.14	40.73	40.27	40.09	40.30	40.73	40.92	40.62	40.87	40.81	40.82	40.42
TiO_2	0.00	0.00	0.01	0.03	0.02	0.10	0.01	0.00	0.05	0.03	0.00	0.00	0.00	0.01
Al_2O_3	0.04	0.01	0.00	0.00	0.01	0.04	0.01	0.03	0.00	0.00	0.05	0.05	0.02	0.04
Cr_2O_3	0.05	0.00	0.04	0.02	0.00	0.03	0.05	0.02	0.00	0.05	0.00	0.03	0.00	0.00
FeO	10.88	8.88	9.48	8.98	10.30	10.73	10.07	9.17	9.08	8.98	9.17	8.88	9.32	8.89
MgO	49.52	49.92	49.46	49.70	48.60	48.39	49.35	49.89	49.48	49.41	49.53	49.28	49.95	49.71
MnO	0.14	0.14	0.16	0.09	0.19	0.21	0.11	0.10	0.14	0.12	0.13	0.13	0.21	0.14
NiO	0.24	0.37	0.28	0.32	0.28	0.24	0.24	0.33	0.37	0.26	0.40	0.31	0.28	0.31
CaO	0.28	0.10	0.13	0.09	0.15	0.20	0.12	0.11	0.07	0.10	0.11	0.10	0.09	0.10
Na_2O	0.03	0.00	0.02	0.03	0.01	0.01	0.00	0.00	0.00	0.00	0.00	0.00	0.00	0.04
K_2O	0.00	0.00	0.00	0.00	0.03	0.00	0.01	0.00	0.00	0.00	0.00	0.00	0.00	0.00
Total	101.60	100.27	99.72	99.99	99.86	100.04	100.27	100.38	100.11	99.57	100.26	99.59	100.69	99.66
Si	0.98	0.99	0.98	0.99	0.99	0.99	0.98	0.99	1.00	1.00	1.00	1.00	0.99	0.99
Ti	0.00	0.00	0.00	0.00	0.00	0.00	0.00	0.00	0.00	0.00	0.00	0.00	0.00	0.00
Al	0.00	0.00	0.00	0.00	0.00	0.00	0.00	0.00	0.00	0.00	0.00	0.00	0.00	0.00
Cr	0.00	0.00	0.00	0.00	0.00	0.00	0.00	0.00	0.00	0.00	0.00	0.00	0.00	0.00
Fe^{2+}	0.22	0.18	0.19	0.18	0.21	0.22	0.21	0.19	0.19	0.18	0.19	0.18	0.19	0.18
Mg	1.78	1.81	1.81	1.81	1.78	1.77	1.80	1.81	1.80	1.81	1.80	1.80	1.81	1.81
Mn	0.00	0.00	0.00	0.00	0.00	0.00	0.00	0.00	0.00	0.00	0.00	0.00	0.00	0.00
Ni	0.00	0.01	0.01	0.01	0.01	0.00	0.00	0.01	0.01	0.01	0.01	0.01	0.01	0.01
Ca	0.01	0.00	0.00	0.00	0.00	0.01	0.00	0.00	0.00	0.00	0.00	0.00	0.00	0.00
Na	0.00	0.00	0.00	0.00	0.00	0.00	0.00	0.00	0.00	0.00	0.00	0.00	0.00	0.00
K	0.00	0.00	0.00	0.00	0.00	0.00	0.00	0.00	0.00	0.00	0.00	0.00	0.00	0.00
Sum	3.00	3.00	3.00	3.00	3.00	3.00	3.00	3.00	3.00	3.00	3.00	3.00	3.00	3.00
X_{Mg}	0.88	0.90	0.90	0.90	0.89	0.88	0.89	0.90	0.90	0.90	0.90	0.90	0.90	0.90

Sample	MG12	MG12	MG12	MG12	MG12	MG12	MG12	MG12	MG12	MG12	MG12	MG12	MG12	MG12
Run duration	24	24	24	24	24	24	24	24	24	24	24	24	24	24
Melt	AH6	AH6	AH6	AH6	AH6	AH6	AH6	AH6	AH6	AH6	AH6	AH6	AH6	AH6
IMA (wt%)	25	25	25	25	25	25	25	25	25	25	25	25	25	25
T	1200	1200	1200	1200	1200	1200	1200	1200	1200	1200	1200	1200	1200	1200
P	0.5	0.5	0.5	0.5	0.5	0.5	0.5	0.5	0.5	0.5	0.5	0.5	0.5	0.5
Point Analysis	MG12OL14	MG12OL15	MG12OL16	MG12OL17	MG12OL18	MG12OL19	MG12OL20	MG12OL21	MG12OL22	MG12OL23	MG12OL24	MG12OL25	MG12OL26	MG12OL27
Site	rim	core	core	rim	core	core	core	core	core	core	rim	core	rim	core
SiO_2	40.23	40.55	40.81	40.56	40.28	40.85	40.65	40.36	40.66	40.32	40.55	40.63	40.47	40.30
TiO_2	0.03	0.04	0.00	0.01	0.00	0.02	0.03	0.01	0.05	0.00	0.00	0.00	0.05	0.04
Al_2O_3	0.03	0.01	0.02	0.01	0.04	0.03	0.05	0.04	0.00	0.00	0.01	0.01	0.01	0.01
Cr_2O_3	0.03	0.00	0.00	0.01	0.03	0.04	0.00	0.01	0.00	0.03	0.03	0.00	0.00	0.00
FeO	11.01	10.80	9.22	9.74	9.54	8.75	10.92	11.01	10.96	9.86	10.09	9.17	9.81	10.23
MgO	48.14	48.69	49.58	49.12	49.75	49.96	47.91	48.13	48.10	49.07	48.73	50.16	49.50	48.51
MnO	0.18	0.18	0.17	0.10	0.11	0.15	0.17	0.18	0.13	0.17	0.14	0.18	0.12	0.13
NiO	0.31	0.30	0.35	0.38	0.42	0.36	0.24	0.17	0.29	0.31	0.28	0.30	0.35	0.41
CaO	0.17	0.25	0.09	0.12	0.10	0.08	0.24	0.28	0.18	0.11	0.15	0.08	0.09	0.10
Na_2O	0.03	0.01	0.03	0.00	0.00	0.00	0.00	0.01	0.02	0.03	0.00	0.01	0.02	0.03
K_2O	0.02	0.00	0.00	0.01	0.01	0.00	0.00	0.00	0.00	0.00	0.01	0.01	0.00	0.00
Total	100.18	100.83	100.27	100.06	100.28	100.24	100.21	100.20	100.39	99.90	99.99	100.55	100.42	99.76
Si	0.99	0.99	1.00	0.99	0.98	0.99	1.00	0.99	1.00	0.99	1.00	0.99	0.99	0.99
Ti	0.00	0.00	0.00	0.00	0.00	0.00	0.00	0.00	0.00	0.00	0.00	0.00	0.00	0.00
Al	0.00	0.00	0.00	0.00	0.00	0.00	0.00	0.00	0.00	0.00	0.00	0.00	0.00	0.00
Cr	0.00	0.00	0.00	0.00	0.00	0.00	0.00	0.00	0.00	0.00	0.00	0.00	0.00	0.00
Fe^{2+}	0.23	0.22	0.19	0.20	0.19	0.18	0.22	0.23	0.23	0.20	0.21	0.19	0.20	0.21
Mg	1.77	1.77	1.80	1.79	1.81	1.81	1.76	1.76	1.76	1.79	1.78	1.81	1.80	1.78
Mn	0.00	0.00	0.00	0.00	0.00	0.00	0.00	0.00	0.00	0.00	0.00	0.00	0.00	0.00
Ni	0.01	0.01	0.01	0.01	0.01	0.01	0.00	0.00	0.01	0.01	0.01	0.01	0.01	0.01
Ca	0.00	0.01	0.00	0.00	0.00	0.00	0.01	0.01	0.00	0.00	0.00	0.00	0.00	0.00
Na	0.00	0.00	0.00	0.00	0.00	0.00	0.00	0.00	0.00	0.00	0.00	0.00	0.00	0.00
K	0.00	0.00	0.00	0.00	0.00	0.00	0.00	0.00	0.00	0.00	0.00	0.00	0.00	0.00
Sum	3.00	3.00	3.00	3.00	3.00	3.00	3.00	3.00	3.00	3.00	3.00	3.00	3.00	3.00
X_{Mg}	0.88	0.88	0.90	0.89	0.90	0.90	0.88	0.88	0.88	0.89	0.89	0.90	0.89	0.89

Sample	MG12	MG12	MG12	MG12	MG12	MG12	MG12	MG12	MG12	MG12	MG12	MG12	MG12	MG12
Run duration	24	24	24	24	24	24	24	24	24	24	24	24	24	24
Melt	AH6	AH6	AH6	AH6	AH6	AH6	AH6	AH6	AH6	AH6	AH6	AH6	AH6	AH6
IMA (wt%)	25	25	25	25	25	25	25	25	25	25	25	25	25	25
T	1200	1200	1200	1200	1200	1200	1200	1200	1200	1200	1200	1200	1200	1200
P	0.5	0.5	0.5	0.5	0.5	0.5	0.5	0.5	0.5	0.5	0.5	0.5	0.5	0.5
Point Analysis	MG12OL28	MG12OL29	MG12OL30	MG12OL31	MG12OL32	MG12OL33	MG12OL34	MG12OL35	MG12OL36	MG12OL37	MG12OL38	MG12OL39	MG12OL40	MG12OL41
Site	rim	core	rim	core	rim	core	rim	core	rim	core	rim	core	core	rim
SiO_2	40.06	40.73	40.86	40.58	40.60	40.83	40.75	40.60	40.84	40.79	40.45	40.17	40.57	40.10
TiO_2	0.00	0.00	0.05	0.08	0.00	0.01	0.00	0.05	0.00	0.02	0.03	0.00	0.01	0.03
Al_2O_3	0.05	0.03	0.00	0.02	0.00	0.05	0.03	0.01	0.01	0.00	0.00	0.08	0.03	0.01
Cr_2O_3	0.02	0.00	0.00	0.00	0.03	0.00	0.04	0.00	0.09	0.02	0.07	0.01	0.03	0.12
FeO	10.37	9.43	10.12	10.77	10.75	9.47	9.79	9.05	9.58	9.54	11.65	10.98	10.26	10.22
MgO	48.59	49.50	49.24	48.53	48.47	49.66	49.09	49.54	49.23	49.19	47.79	48.64	49.24	49.54
MnO	0.13	0.10	0.13	0.16	0.14	0.11	0.12	0.14	0.06	0.19	0.20	0.17	0.15	0.18
NiO	0.22	0.29	0.31	0.30	0.31	0.36	0.41	0.37	0.30	0.35	0.18	0.17	0.22	0.08
CaO	0.21	0.09	0.12	0.13	0.13	0.07	0.12	0.08	0.10	0.09	0.15	0.32	0.17	0.25
Na_2O	0.06	0.02	0.00	0.00	0.01	0.00	0.00	0.01	0.01	0.00	0.00	0.06	0.00	0.00
K_2O	0.00	0.00	0.00	0.00	0.00	0.00	0.02	0.00	0.01	0.00	0.00	0.00	0.00	0.00
Total	99.71	100.19	100.83	100.57	100.44	100.56	100.37	99.85	100.23	100.19	100.52	100.60	100.68	100.53
Si	0.99	0.99	0.99	0.99	1.00	0.99	1.00	0.99	1.00	1.00	0.99	0.98	0.99	0.98
Ti	0.00	0.00	0.00	0.00	0.00	0.00	0.00	0.00	0.00	0.00	0.00	0.00	0.00	0.00
Al	0.00	0.00	0.00	0.00	0.00	0.00	0.00	0.00	0.00	0.00	0.00	0.00	0.00	0.00
Cr	0.00	0.00	0.00	0.00	0.00	0.00	0.00	0.00	0.00	0.00	0.00	0.00	0.00	0.00
Fe^{2+}	0.21	0.19	0.21	0.22	0.22	0.19	0.20	0.19	0.20	0.20	0.24	0.22	0.21	0.21
Mg	1.78	1.80	1.79	1.77	1.77	1.80	1.79	1.81	1.79	1.79	1.75	1.77	1.79	1.80
Mn	0.00	0.00	0.00	0.00	0.00	0.00	0.00	0.00	0.00	0.00	0.00	0.00	0.00	0.00
Ni	0.00	0.01	0.01	0.01	0.01	0.01	0.01	0.01	0.01	0.01	0.00	0.00	0.00	0.00
Ca	0.01	0.00	0.00	0.00	0.00	0.00	0.00	0.00	0.00	0.00	0.00	0.01	0.00	0.01
Na	0.00	0.00	0.00	0.00	0.00	0.00	0.00	0.00	0.00	0.00	0.00	0.00	0.00	0.00
K	0.00	0.00	0.00	0.00	0.00	0.00	0.00	0.00	0.00	0.00	0.00	0.00	0.00	0.00
Sum	3.00	3.00	3.00	3.00	3.00	3.00	3.00	3.00	3.00	3.00	3.00	3.00	3.00	3.00
X_{Mg}	0.89	0.90	0.89	0.88	0.88	0.90	0.89	0.90	0.90	0.90	0.87	0.88	0.89	0.89

Sample	MG12	MG12	MG12	MG12	MG12	MG12	MG12	MG12	MG12	MG12	MG12	MG12	MG14	MG14
Run duration	24	24	24	24	24	24	24	24	24	24	24	24	24	24
Melt	AH6	AH6	AH6	AH6	AH6	AH6	AH6	AH6	AH6	AH6	AH6	AH6	AH6	AH6
IMA (wt%)	25	25	25	25	25	25	25	25	25	25	25	25	50	50
T	1200	1200	1200	1200	1200	1200	1200	1200	1200	1200	1200	1200	1200	1200
P	0.5	0.5	0.5	0.5	0.5	0.5	0.5	0.5	0.5	0.5	0.5	0.5	0.5	0.5
Point Analysis	MG12OL42	MG12OL43	MG12OL44	MG12OL45	MG12OL46	MG12OL47	MG12OL48	MG12OL49	MG12OL50	MG12OL51	MG12OL52	MG12OL53	MG14OL1	MG14OL2
Site	core	rim	core	core	core	rim	core	rim	core	rim	core	rim	core	core
SiO_2	40.07	40.24	40.12	40.42	40.64	40.46	40.29	40.43	40.71	40.30	40.53	40.69	39.64	40.97
TiO_2	0.00	0.00	0.00	0.06	0.00	0.03	0.03	0.01	0.05	0.00	0.01	0.02	0.06	0.00
Al_2O_3	0.05	0.03	0.04	0.06	0.02	0.01	0.06	0.03	0.00	0.04	0.01	0.04	0.04	0.03
Cr_2O_3	0.00	0.01	0.04	0.05	0.01	0.00	0.01	0.02	0.09	0.01	0.00	0.02	0.05	0.00
FeO	9.77	9.72	10.30	10.22	9.47	10.14	10.24	10.61	9.37	10.59	10.14	10.66	14.31	11.39
MgO	49.57	49.04	48.90	49.24	49.48	49.34	48.69	48.34	49.80	48.65	49.07	48.62	45.44	48.04
MnO	0.12	0.17	0.12	0.14	0.16	0.18	0.15	0.16	0.14	0.17	0.15	0.14	0.29	0.18
NiO	0.08	0.22	0.06	0.17	0.37	0.31	0.30	0.33	0.24	0.16	0.05	0.04	0.01	0.34
CaO	0.13	0.15	0.23	0.24	0.10	0.16	0.07	0.13	0.08	0.17	0.09	0.25	0.44	0.11
Na_2O	0.00	0.00	0.00	0.00	0.05	0.00	0.02	0.00	0.01	0.00	0.00	0.01	0.00	0.01
K_2O	0.00	0.00	0.00	0.00	0.00	0.00	0.00	0.00	0.00	0.00	0.00	0.00	0.00	0.01
Total	99.79	99.58	99.81	100.60	100.30	100.63	99.86	100.06	100.49	100.09	100.05	100.49	100.27	101.07
Si	0.98	0.99	0.99	0.99	0.99	0.99	0.99	0.99	0.99	0.99	0.99	1.00	0.99	1.00
Ti	0.00	0.00	0.00	0.00	0.00	0.00	0.00	0.00	0.00	0.00	0.00	0.00	0.00	0.00
Al	0.00	0.00	0.00	0.00	0.00	0.00	0.00	0.00	0.00	0.00	0.00	0.00	0.00	0.00
Cr	0.00	0.00	0.00	0.00	0.00	0.00	0.00	0.00	0.00	0.00	0.00	0.00	0.00	0.00
Fe^{2+}	0.20	0.20	0.21	0.21	0.19	0.21	0.21	0.22	0.19	0.22	0.21	0.22	0.30	0.23
Mg	1.81	1.80	1.79	1.79	1.80	1.79	1.78	1.77	1.81	1.78	1.79	1.77	1.69	1.75
Mn	0.00	0.00	0.00	0.00	0.00	0.00	0.00	0.00	0.00	0.00	0.00	0.00	0.01	0.00
Ni	0.00	0.00	0.00	0.00	0.01	0.01	0.01	0.01	0.00	0.00	0.00	0.00	0.00	0.01
Ca	0.00	0.00	0.01	0.01	0.00	0.00	0.00	0.00	0.00	0.00	0.00	0.01	0.01	0.00
Na	0.00	0.00	0.00	0.00	0.00	0.00	0.00	0.00	0.00	0.00	0.00	0.00	0.00	0.00
K	0.00	0.00	0.00	0.00	0.00	0.00	0.00	0.00	0.00	0.00	0.00	0.00	0.00	0.00
Sum	3.00	3.00	3.00	3.00	3.00	3.00	3.00	3.00	3.00	3.00	3.00	3.00	3.00	3.00
X_{Mg}	0.90	0.89	0.89	0.89	0.90	0.89	0.89	0.88	0.90	0.89	0.89	0.89	0.84	0.88

Sample	MG14	MG14	MG14	MG14	MG14	MG14	MG14	MG14	MG14	MG14	MG14	MG14	MG14	MG11
Run duration	24	24	24	24	24	24	24	24	24	24	24	24	24	24
Melt	AH6	AH6	AH6	AH6	AH6	AH6	AH6	AH6	AH6	AH6	AH6	AH6	AH6	AH6
IMA (wt%)	50	50	50	50	50	50	50	50	50	50	50	50	50	50
T	1200	1200	1200	1200	1200	1200	1200	1200	1200	1200	1200	1200	1200	1250
P	0.5	0.5	0.5	0.5	0.5	0.5	0.5	0.5	0.5	0.5	0.5	0.5	0.5	0.5
Point Analysis	MG14OL3	MG14OL4	MG14OL5	MG14OL6	MG14OL7	MG14OL8	MG14OL9	MG14OL10	MG14OL11	MG14OL12	MG14OL13	MG14OL14	MG14OL15	MG11OL1
Site	rim	core	rim	core	rim	core	rim	core	rim	core	rim	core	rim	core
SiO_2	39.87	41.29	40.40	41.22	40.46	41.29	40.07	41.04	40.05	40.62	39.85	40.69	39.63	41.03
TiO_2	0.06	0.00	0.02	0.03	0.08	0.00	0.00	0.00	0.02	0.03	0.05	0.07	0.03	0.02
Al_2O_3	0.05	0.02	0.05	0.02	0.06	0.04	0.06	0.03	0.05	0.02	0.06	0.03	0.01	0.01
Cr_2O_3	0.05	0.00	0.05	0.03	0.06	0.02	0.00	0.05	0.00	0.06	0.04	0.00	0.00	0.08
FeO	15.72	11.84	15.62	10.99	15.88	11.06	16.13	12.76	15.85	14.99	16.37	11.12	15.68	10.65
MgO	44.89	47.84	45.49	48.08	44.83	48.00	44.86	46.40	44.16	45.36	44.32	48.87	46.34	49.13
MnO	0.23	0.11	0.22	0.19	0.20	0.18	0.22	0.16	0.24	0.20	0.30	0.16	0.24	0.17
NiO	0.12	0.35	0.10	0.33	0.08	0.29	0.11	0.31	0.07	0.22	0.07	0.38	0.11	0.16
CaO	0.36	0.13	0.34	0.13	0.31	0.13	0.40	0.17	0.43	0.17	0.57	0.11	0.34	0.20
Na_2O	0.00	0.02	0.00	0.01	0.03	0.00	0.00	0.03	0.00	0.00	0.03	0.02	0.00	0.01
K_2O	0.01	0.00	0.00	0.00	0.00	0.00	0.00	0.00	0.01	0.01	0.01	0.00	0.00	0.00
Total	101.36	101.60	102.30	101.03	101.99	101.01	101.84	100.96	100.88	101.70	101.66	101.44	102.38	101.46
Si	0.99	1.01	0.99	1.01	1.00	1.01	0.99	1.01	1.00	1.00	0.99	0.99	0.97	0.99
Ti	0.00	0.00	0.00	0.00	0.00	0.00	0.00	0.00	0.00	0.00	0.00	0.00	0.00	0.00
Al	0.00	0.00	0.00	0.00	0.00	0.00	0.00	0.00	0.00	0.00	0.00	0.00	0.00	0.00
Cr	0.00	0.00	0.00	0.00	0.00	0.00	0.00	0.00	0.00	0.00	0.00	0.00	0.00	0.00
Fe^{2+}	0.33	0.24	0.32	0.22	0.33	0.23	0.33	0.26	0.33	0.31	0.34	0.23	0.32	0.22
Mg	1.66	1.74	1.67	1.75	1.65	1.75	1.66	1.71	1.65	1.67	1.64	1.77	1.69	1.78
Mn	0.00	0.00	0.00	0.00	0.00	0.00	0.00	0.00	0.01	0.00	0.01	0.00	0.00	0.00
Ni	0.00	0.01	0.00	0.01	0.00	0.01	0.00	0.01	0.00	0.00	0.00	0.01	0.00	0.00
Ca	0.01	0.00	0.01	0.00	0.01	0.00	0.01	0.00	0.01	0.00	0.02	0.00	0.01	0.01
Na	0.00	0.00	0.00	0.00	0.00	0.00	0.00	0.00	0.00	0.00	0.00	0.00	0.00	0.00
K	0.00	0.00	0.00	0.00	0.00	0.00	0.00	0.00	0.00	0.00	0.00	0.00	0.00	0.00
Sum	3.00	3.00	3.00	3.00	3.00	3.00	3.00	3.00	3.00	3.00	3.00	3.00	3.00	3.00
X_{Mg}	0.83	0.87	0.83	0.88	0.83	0.88	0.82	0.86	0.82	0.84	0.82	0.88	0.83	0.89

Sample	MG11	MG11	MG11	MG11	MG11	MG11	MG11	MG11	MG11	MG11	MG11	MG11	MG11	MG11
Run duration	24	24	24	24	24	24	24	24	24	24	24	24	24	24
Melt	AH6	AH6	AH6	AH6	AH6	AH6	AH6	AH6	AH6	AH6	AH6	AH6	AH6	AH6
IMA (wt%)	50	50	50	50	50	50	50	50	50	50	50	50	50	50
T	1250	1250	1250	1250	1250	1250	1250	1250	1250	1250	1250	1250	1250	1250
P	0.5	0.5	0.5	0.5	0.5	0.5	0.5	0.5	0.5	0.5	0.5	0.5	0.5	0.5
Point Analysis	MG11OL2	MG11OL3	MG11OL4	MG11OL5	MG11OL6	MG11OL7	MG11OL8	MG11OL9	MG11OL10	MG11OL11	MG11OL12	MG11OL13	MG11OL14	MG11OL15
Site	rim	core	rim	rim	core	rim	core	rim	core	core	rim	core	core	rim
SiO_2	40.98	40.28	40.62	41.14	40.84	41.53	40.59	40.69	40.97	40.75	41.05	40.91	40.83	40.79
TiO_2	0.04	0.07	0.07	0.06	0.01	0.01	0.00	0.00	0.03	0.00	0.04	0.00	0.02	0.05
Al_2O_3	0.03	0.03	0.05	0.07	0.02	0.05	0.04	0.05	0.07	0.01	0.07	0.07	0.04	0.00
Cr_2O_3	0.10	0.06	0.00	0.03	0.12	0.09	0.07	0.06	0.09	0.06	0.00	0.01	0.10	0.09
FeO	9.52	11.35	9.65	9.29	10.79	9.67	10.75	9.59	9.65	10.93	9.18	10.12	10.33	10.50
MgO	50.34	48.77	50.15	50.51	49.41	50.54	49.45	50.10	50.52	49.09	50.78	49.92	50.14	49.89
MnO	0.12	0.12	0.12	0.21	0.15	0.17	0.18	0.16	0.22	0.18	0.17	0.14	0.15	0.19
NiO	0.06	0.22	0.06	0.09	0.08	0.08	0.09	0.05	0.00	0.16	0.06	0.07	0.03	0.10
CaO	0.45	0.20	0.37	0.37	0.38	0.37	0.33	0.42	0.41	0.27	0.43	0.41	0.41	0.32
Na_2O	0.04	0.02	0.00	0.06	0.00	0.05	0.02	0.03	0.02	0.02	0.00	0.08	0.05	0.05
K_2O	0.02	0.01	0.00	0.00	0.00	0.01	0.01	0.00	0.00	0.01	0.00	0.02	0.00	0.02
Total	101.69	101.12	101.09	101.82	101.80	102.56	101.54	101.16	101.98	101.48	101.77	101.75	102.11	101.98
Si	0.98	0.98	0.98	0.99	0.99	0.99	0.98	0.98	0.98	0.99	0.98	0.98	0.98	0.98
Ti	0.00	0.00	0.00	0.00	0.00	0.00	0.00	0.00	0.00	0.00	0.00	0.00	0.00	0.00
Al	0.00	0.00	0.00	0.00	0.00	0.00	0.00	0.00	0.00	0.00	0.00	0.00	0.00	0.00
Cr	0.00	0.00	0.00	0.00	0.00	0.00	0.00	0.00	0.00	0.00	0.00	0.00	0.00	0.00
Fe^{2+}	0.19	0.23	0.20	0.19	0.22	0.19	0.22	0.19	0.19	0.22	0.18	0.20	0.21	0.21
Mg	1.80	1.77	1.81	1.81	1.78	1.80	1.78	1.80	1.80	1.77	1.81	1.79	1.79	1.79
Mn	0.00	0.00	0.00	0.00	0.00	0.00	0.00	0.00	0.00	0.00	0.00	0.00	0.00	0.00
Ni	0.00	0.00	0.00	0.00	0.00	0.00	0.00	0.00	0.00	0.00	0.00	0.00	0.00	0.00
Ca	0.01	0.01	0.01	0.01	0.01	0.01	0.01	0.01	0.01	0.01	0.01	0.01	0.01	0.01
Na	0.00	0.00	0.00	0.00	0.00	0.00	0.00	0.00	0.00	0.00	0.00	0.00	0.00	0.00
K	0.00	0.00	0.00	0.00	0.00	0.00	0.00	0.00	0.00	0.00	0.00	0.00	0.00	0.00
Sum	3.00	3.00	3.00	3.00	3.00	3.00	3.00	3.00	3.00	3.00	3.00	3.00	3.00	3.00
X_{Mg}	0.90	0.88	0.90	0.90	0.88	0.89	0.88	0.89	0.89	0.88	0.90	0.89	0.89	0.89

Sample	MG11	MG11	MG11	MG11	MG11	MG11	MG11	MG11	MG11	MG11	MG11	MG11	MG11	MG11
Run duration	24	24	24	24	24	24	24	24	24	24	24	24	24	24
Melt	AH6	AH6	AH6	AH6	AH6	AH6	AH6	AH6	AH6	AH6	AH6	AH6	AH6	AH6
IMA (wt%)	50	50	50	50	50	50	50	50	50	50	50	50	50	50
T	1250	1250	1250	1250	1250	1250	1250	1250	1250	1250	1250	1250	1250	1250
P	0.5	0.5	0.5	0.5	0.5	0.5	0.5	0.5	0.5	0.5	0.5	0.5	0.5	0.5
Point Analysis	MG11OL16	MG11OL17	MG11OL18	MG11OL19	MG11OL20	MG11OL21	MG11OL22	MG11OL23	MG11OL24	MG11OL25	MG11OL26	MG11OL27	MG11OL28	MG11OL29
Site	core	core	core	core	core	core	core	core	rim	rim	rim	core	core	rim
SiO_2	40.60	40.69	40.91	40.68	40.54	40.78	40.87	40.77	40.59	40.80	40.91	40.39	40.69	40.63
TiO_2	0.04	0.00	0.08	0.03	0.04	0.04	0.00	0.03	0.00	0.05	0.00	0.02	0.00	0.00
Al_2O_3	0.03	0.02	0.03	0.04	0.02	0.03	0.04	0.02	0.05	0.03	0.06	0.03	0.07	0.07
Cr_2O_3	0.00	0.04	0.02	0.04	0.04	0.08	0.00	0.01	0.09	0.12	0.02	0.05	0.07	0.06
FeO	11.14	10.95	11.13	11.18	11.13	11.02	11.14	11.03	10.17	10.00	9.12	10.99	10.69	9.86
MgO	49.22	49.63	49.39	49.37	49.21	49.16	49.24	49.38	50.62	50.01	51.02	49.54	49.62	50.41
MnO	0.20	0.14	0.09	0.16	0.11	0.17	0.15	0.13	0.15	0.15	0.16	0.19	0.19	0.19
NiO	0.28	0.30	0.23	0.20	0.26	0.27	0.27	0.28	0.07	0.11	0.15	0.21	0.22	0.07
CaO	0.15	0.10	0.12	0.15	0.14	0.13	0.13	0.23	0.25	0.23	0.38	0.23	0.35	0.43
Na_2O	0.05	0.00	0.00	0.04	0.00	0.01	0.02	0.06	0.02	0.02	0.06	0.02	0.00	0.03
K_2O	0.00	0.01	0.00	0.01	0.00	0.01	0.00	0.01	0.00	0.00	0.00	0.00	0.00	0.00
Total	101.71	101.88	102.00	101.89	101.48	101.71	101.87	101.95	102.01	101.53	101.88	101.68	101.91	101.76
Si	0.98	0.98	0.99	0.98	0.98	0.99	0.99	0.98	0.97	0.98	0.98	0.98	0.98	0.98
Ti	0.00	0.00	0.00	0.00	0.00	0.00	0.00	0.00	0.00	0.00	0.00	0.00	0.00	0.00
Al	0.00	0.00	0.00	0.00	0.00	0.00	0.00	0.00	0.00	0.00	0.00	0.00	0.00	0.00
Cr	0.00	0.00	0.00	0.00	0.00	0.00	0.00	0.00	0.00	0.00	0.00	0.00	0.00	0.00
Fe^{2+}	0.23	0.22	0.22	0.23	0.23	0.22	0.23	0.22	0.20	0.20	0.18	0.22	0.22	0.20
Mg	1.78	1.78	1.78	1.78	1.78	1.77	1.77	1.78	1.81	1.80	1.82	1.78	1.78	1.80
Mn	0.00	0.00	0.00	0.00	0.00	0.00	0.00	0.00	0.00	0.00	0.00	0.00	0.00	0.00
Ni	0.01	0.01	0.00	0.00	0.01	0.01	0.01	0.01	0.00	0.00	0.00	0.00	0.00	0.00
Ca	0.00	0.00	0.00	0.00	0.00	0.00	0.00	0.01	0.01	0.01	0.01	0.01	0.01	0.01
Na	0.00	0.00	0.00	0.00	0.00	0.00	0.00	0.00	0.00	0.00	0.00	0.00	0.00	0.00
K	0.00	0.00	0.00	0.00	0.00	0.00	0.00	0.00	0.00	0.00	0.00	0.00	0.00	0.00
Sum	3.00	3.00	3.00	3.00	3.00	3.00	3.00	3.00	3.00	3.00	3.00	3.00	3.00	3.00
X_{Mg}	0.88	0.88	0.88	0.88	0.88	0.88	0.88	0.88	0.89	0.89	0.90	0.88	0.88	0.89

Sample	MG11	MG11	MG11	MG11	MG11	MG11	MG11	MG11	MG11	MG11	MG11	MG11	MG11	MG11
Run duration	24	24	24	24	24	24	24	24	24	24	24	24	24	24
Melt	AH6	AH6	AH6	AH6	AH6	AH6	AH6	AH6	AH6	AH6	AH6	AH6	AH6	AH6
IMA (wt%)	50	50	50	50	50	50	50	50	50	50	50	50	50	50
T	1250	1250	1250	1250	1250	1250	1250	1250	1250	1250	1250	1250	1250	1250
P	0.5	0.5	0.5	0.5	0.5	0.5	0.5	0.5	0.5	0.5	0.5	0.5	0.5	0.5
Point Analysis	MG11OL30	MG11OL31	MG11OL32	MG11OL33	MG11OL34	MG11OL35	MG11OL36	MG11OL37	MG11OL38	MG11OL39	MG11OL40	MG11OL41	MG11OL42	MG11OL43
Site	rim	core	core	rim	rim	core	rim	core	rim	core	core	core	core	core
SiO_2	40.47	40.37	40.62	40.95	41.17	40.81	41.04	40.98	40.92	40.93	40.71	40.60	41.01	41.16
TiO_2	0.00	0.00	0.00	0.03	0.01	0.02	0.01	0.01	0.05	0.00	0.00	0.00	0.00	0.04
Al_2O_3	0.04	0.09	0.06	0.06	0.04	0.04	0.04	0.04	0.02	0.03	0.05	0.04	0.06	0.04
Cr_2O_3	0.03	0.03	0.04	0.03	0.01	0.04	0.02	0.02	0.08	0.10	0.02	0.08	0.00	0.00
FeO	9.99	10.45	10.97	9.55	9.27	10.41	9.45	10.85	9.82	10.71	10.72	10.50	9.84	9.29
MgO	50.01	49.38	49.19	50.48	50.61	49.33	50.57	49.71	50.39	49.39	49.41	50.08	50.37	50.59
MnO	0.15	0.16	0.15	0.18	0.15	0.17	0.13	0.15	0.16	0.22	0.14	0.18	0.17	0.17
NiO	0.05	0.16	0.09	0.05	0.02	0.16	0.07	0.24	0.06	0.17	0.11	0.08	0.06	0.01
CaO	0.33	0.37	0.34	0.37	0.39	0.21	0.41	0.19	0.17	0.17	0.35	0.37	0.34	0.37
Na_2O	0.05	0.01	0.04	0.02	0.04	0.02	0.08	0.01	0.00	0.01	0.01	0.01	0.00	0.01
K_2O	0.00	0.00	0.02	0.00	0.00	0.01	0.00	0.00	0.00	0.00	0.00	0.00	0.00	0.01
Total	101.11	101.01	101.51	101.71	101.71	101.21	101.83	102.20	101.68	101.73	101.53	101.93	101.86	101.68
Si	0.98	0.98	0.98	0.98	0.99	0.99	0.98	0.99	0.98	0.99	0.98	0.98	0.98	0.99
Ti	0.00	0.00	0.00	0.00	0.00	0.00	0.00	0.00	0.00	0.00	0.00	0.00	0.00	0.00
Al	0.00	0.00	0.00	0.00	0.00	0.00	0.00	0.00	0.00	0.00	0.00	0.00	0.00	0.00
Cr	0.00	0.00	0.00	0.00	0.00	0.00	0.00	0.00	0.00	0.00	0.00	0.00	0.00	0.00
Fe^{2+}	0.20	0.21	0.22	0.19	0.19	0.21	0.19	0.22	0.20	0.22	0.22	0.21	0.20	0.19
Mg	1.80	1.79	1.78	1.81	1.81	1.78	1.81	1.78	1.81	1.78	1.78	1.80	1.80	1.81
Mn	0.00	0.00	0.00	0.00	0.00	0.00	0.00	0.00	0.00	0.00	0.00	0.00	0.00	0.00
Ni	0.00	0.00	0.00	0.00	0.00	0.00	0.00	0.00	0.00	0.00	0.00	0.00	0.00	0.00
Ca	0.01	0.01	0.01	0.01	0.01	0.01	0.01	0.00	0.00	0.00	0.01	0.01	0.01	0.01
Na	0.00	0.00	0.00	0.00	0.00	0.00	0.00	0.00	0.00	0.00	0.00	0.00	0.00	0.00
K	0.00	0.00	0.00	0.00	0.00	0.00	0.00	0.00	0.00	0.00	0.00	0.00	0.00	0.00
Sum	3.00	3.00	3.00	3.00	3.00	3.00	3.00	3.00	3.00	3.00	3.00	3.00	3.00	3.00
X_{Mg}	0.89	0.89	0.88	0.90	0.90	0.89	0.90	0.88	0.90	0.89	0.88	0.89	0.89	0.90

Sample	MG11	MG11	MG11	MG11	MG11	MG11	MG11	MG11	MG11	MG11	MG11	MG11	MG11	MG11
Run duration	24	24	24	24	24	24	24	24	24	24	24	24	24	24
Melt	AH6	AH6	AH6	AH6	AH6	AH6	AH6	AH6	AH6	AH6	AH6	AH6	AH6	AH6
IMA (wt%)	50	50	50	50	50	50	50	50	50	50	50	50	50	50
T	1250	1250	1250	1250	1250	1250	1250	1250	1250	1250	1250	1250	1250	1250
P	0.5	0.5	0.5	0.5	0.5	0.5	0.5	0.5	0.5	0.5	0.5	0.5	0.5	0.5
Point Analysis	MG11OL44	MG11OL45	MG11OL46	MG11OL47	MG11OL48	MG11OL49	MG11OL50	MG11OL51	MG11OL52	MG11OL53	MG11OL54	MG11OL55	MG11OL56	MG11OL57
Site	rim	rim	core	core	core	core	rim	core	core	rim	rim	core	rim	core
SiO_2	40.80	40.96	40.99	40.84	41.18	40.48	41.17	41.10	41.47	41.16	41.26	40.96	41.08	40.84
TiO_2	0.00	0.01	0.00	0.00	0.00	0.07	0.00	0.03	0.00	0.00	0.00	0.00	0.02	0.07
Al_2O_3	0.02	0.05	0.06	0.02	0.06	0.05	0.09	0.05	0.05	0.08	0.08	0.03	0.18	0.04
Cr_2O_3	0.00	0.04	0.01	0.05	0.00	0.00	0.06	0.07	0.02	0.05	0.03	0.01	0.00	0.01
FeO	9.03	10.27	10.64	9.44	9.72	10.40	9.01	9.16	10.01	9.26	9.04	9.49	8.71	9.09
MgO	51.00	50.21	49.61	50.56	50.32	49.20	50.74	50.54	50.07	50.44	51.14	50.23	50.17	50.70
MnO	0.15	0.22	0.18	0.15	0.16	0.20	0.17	0.14	0.16	0.13	0.18	0.16	0.19	0.18
NiO	0.00	0.23	0.11	0.05	0.13	0.15	0.05	0.01	0.09	0.00	0.00	0.05	0.00	0.03
CaO	0.37	0.22	0.39	0.27	0.35	0.30	0.38	0.44	0.36	0.39	0.38	0.37	0.55	0.40
Na_2O	0.01	0.01	0.00	0.01	0.02	0.00	0.02	0.02	0.00	0.02	0.03	0.01	0.01	0.00
K_2O	0.01	0.00	0.00	0.01	0.00	0.00	0.00	0.01	0.01	0.01	0.00	0.00	0.00	0.01
Total	101.39	102.23	102.00	101.39	101.93	100.84	101.68	101.56	102.25	101.54	102.14	101.33	100.91	101.37
Si	0.98	0.98	0.99	0.98	0.99	0.99	0.99	0.99	0.99	0.99	0.98	0.99	0.99	0.98
Ti	0.00	0.00	0.00	0.00	0.00	0.00	0.00	0.00	0.00	0.00	0.00	0.00	0.00	0.00
Al	0.00	0.00	0.00	0.00	0.00	0.00	0.00	0.00	0.00	0.00	0.00	0.00	0.01	0.00
Cr	0.00	0.00	0.00	0.00	0.00	0.00	0.00	0.00	0.00	0.00	0.00	0.00	0.00	0.00
Fe^{2+}	0.18	0.21	0.21	0.19	0.20	0.21	0.18	0.18	0.20	0.19	0.18	0.19	0.18	0.18
Mg	1.83	1.79	1.78	1.81	1.80	1.79	1.81	1.81	1.79	1.81	1.82	1.81	1.81	1.82
Mn	0.00	0.00	0.00	0.00	0.00	0.00	0.00	0.00	0.00	0.00	0.00	0.00	0.00	0.00
Ni	0.00	0.00	0.00	0.00	0.00	0.00	0.00	0.00	0.00	0.00	0.00	0.00	0.00	0.00
Ca	0.01	0.01	0.01	0.01	0.01	0.01	0.01	0.01	0.01	0.01	0.01	0.01	0.01	0.01
Na	0.00	0.00	0.00	0.00	0.00	0.00	0.00	0.00	0.00	0.00	0.00	0.00	0.00	0.00
K	0.00	0.00	0.00	0.00	0.00	0.00	0.00	0.00	0.00	0.00	0.00	0.00	0.00	0.00
Sum	3.00	3.00	3.00	3.00	3.00	3.00	3.00	3.00	3.00	3.00	3.00	3.00	3.00	3.00
X_{Mg}	0.90	0.89	0.89	0.90	0.90	0.89	0.90	0.90	0.89	0.90	0.90	0.90	0.90	0.90

Sample	MG11	MG11	MG11	MG11	MG11	MG11	MG11	MG11	MG11	MG11	MG11	MG11	MG11	MG11
Run duration	24	24	24	24	24	24	24	24	24	24	24	24	24	24
Melt	AH6	AH6	AH6	AH6	AH6	AH6	AH6	AH6	AH6	AH6	AH6	AH6	AH6	AH6
IMA (wt%)	50	50	50	50	50	50	50	50	50	50	50	50	50	50
T	1250	1250	1250	1250	1250	1250	1250	1250	1250	1250	1250	1250	1250	1250
P	0.5	0.5	0.5	0.5	0.5	0.5	0.5	0.5	0.5	0.5	0.5	0.5	0.5	0.5
Point Analysis	MG11OL58	MG11OL59	MG11OL60	MG11OL61	MG11OL62	MG11OL63	MG11OL64	MG11OL65	MG11OL66	MG11OL67	MG11OL68	MG11OL69	MG11OL70	MG11OL71
Site	core	core	core	core	core	core	rim	core	core	core	core	core	rim	core
SiO_2	40.74	40.81	41.16	40.90	40.52	40.79	41.18	40.92	41.12	41.07	40.24	40.68	41.41	40.94
TiO_2	0.00	0.02	0.00	0.02	0.05	0.00	0.00	0.00	0.00	0.01	0.05	0.00	0.00	0.00
Al_2O_3	0.05	0.07	0.05	0.07	0.05	0.06	0.05	0.02	0.03	0.03	0.03	0.05	0.07	0.04
Cr_2O_3	0.03	0.02	0.07	0.01	0.08	0.00	0.05	0.03	0.03	0.09	0.06	0.00	0.07	0.04
FeO	9.00	9.19	9.38	9.08	9.03	9.21	8.59	8.95	8.44	9.04	9.71	10.35	8.67	10.98
MgO	50.66	50.59	50.74	50.99	51.21	51.15	51.06	50.74	50.95	50.61	50.67	50.16	50.57	49.43
MnO	0.17	0.16	0.16	0.14	0.18	0.18	0.13	0.15	0.18	0.17	0.16	0.13	0.15	0.14
NiO	0.10	0.00	0.09	0.06	0.05	0.08	0.02	0.01	0.03	0.05	0.02	0.03	0.00	0.25
CaO	0.38	0.37	0.35	0.39	0.39	0.28	0.39	0.36	0.40	0.39	0.40	0.34	0.36	0.20
Na_2O	0.00	0.04	0.00	0.00	0.01	0.01	0.00	0.05	0.03	0.00	0.01	0.00	0.00	0.02
K_2O	0.00	0.00	0.00	0.00	0.00	0.00	0.00	0.01	0.01	0.00	0.00	0.00	0.00	0.00
Total	101.13	101.26	102.01	101.65	101.55	101.76	101.48	101.23	101.23	101.46	101.35	101.74	101.31	102.03
Si	0.98	0.98	0.99	0.98	0.97	0.98	0.99	0.98	0.99	0.99	0.97	0.98	1.00	0.99
Ti	0.00	0.00	0.00	0.00	0.00	0.00	0.00	0.00	0.00	0.00	0.00	0.00	0.00	0.00
Al	0.00	0.00	0.00	0.00	0.00	0.00	0.00	0.00	0.00	0.00	0.00	0.00	0.00	0.00
Cr	0.00	0.00	0.00	0.00	0.00	0.00	0.00	0.00	0.00	0.00	0.00	0.00	0.00	0.00
Fe^{2+}	0.18	0.19	0.19	0.18	0.18	0.18	0.17	0.18	0.17	0.18	0.20	0.21	0.17	0.22
Mg	1.82	1.82	1.81	1.82	1.83	1.82	1.82	1.82	1.82	1.81	1.82	1.80	1.81	1.78
Mn	0.00	0.00	0.00	0.00	0.00	0.00	0.00	0.00	0.00	0.00	0.00	0.00	0.00	0.00
Ni	0.00	0.00	0.00	0.00	0.00	0.00	0.00	0.00	0.00	0.00	0.00	0.00	0.00	0.00
Ca	0.01	0.01	0.01	0.01	0.01	0.01	0.01	0.01	0.01	0.01	0.01	0.01	0.01	0.01
Na	0.00	0.00	0.00	0.00	0.00	0.00	0.00	0.00	0.00	0.00	0.00	0.00	0.00	0.00
K	0.00	0.00	0.00	0.00	0.00	0.00	0.00	0.00	0.00	0.00	0.00	0.00	0.00	0.00
Sum	3.00	3.00	3.00	3.00	3.00	3.00	3.00	3.00	3.00	3.00	3.00	3.00	3.00	3.00
X_{Mg}	0.90	0.90	0.90	0.90	0.90	0.90	0.91	0.90	0.91	0.90	0.90	0.89	0.91	0.88

Sample	MG11	MG11	MG18	MG18	MG18	MG18	MG18	MG18	MG18	MG18	MG18	MG18	MG18	MG18
Run duration	24	24	24	24	24	24	24	24	24	24	24	24	24	24
Melt	AH6	AH6	AH6	AH6	AH6	AH6	AH6	AH6	AH6	AH6	AH6	AH6	AH6	AH6
IMA (wt%)	50	50	10	10	10	10	10	10	10	10	10	10	10	10
T	1250	1250	1300	1300	1300	1300	1300	1300	1300	1300	1300	1300	1300	1300
P	0.5	0.5	0.5	0.5	0.5	0.5	0.5	0.5	0.5	0.5	0.5	0.5	0.5	0.5
Point Analysis	MG11OL72	MG11OL73	MG18OL1	MG18OL2	MG18OL3	MG18OL4	MG18OL5	MG18OL6	MG18OL7	MG18OL8	MG18OL9	MG18OL10	MG18OL11	MG18OL12
Site	rim	core	core	rim	core	core	core	rim	core	rim	core	rim	core	rim
SiO_2	40.79	40.89	40.44	40.21	40.68	40.42	40.33	40.50	40.63	40.66	40.49	40.65	40.63	40.91
TiO_2	0.01	0.00	0.00	0.00	0.00	0.00	0.00	0.00	0.00	0.01	0.01	0.00	0.03	0.00
Al_2O_3	0.05	0.01	0.06	0.06	0.05	0.07	0.04	0.05	0.06	0.05	0.05	0.07	0.06	0.05
Cr_2O_3	0.02	0.06	0.05	0.05	0.01	0.03	0.00	0.06	0.04	0.03	0.00	0.03	0.06	0.08
FeO	9.24	10.36	10.51	10.59	10.53	10.53	10.80	10.34	10.60	10.61	10.65	10.53	10.67	10.57
MgO	51.10	49.22	49.21	50.10	49.03	49.11	49.23	49.23	49.10	49.10	49.43	49.26	49.41	49.08
MnO	0.15	0.17	0.10	0.14	0.15	0.08	0.14	0.12	0.17	0.17	0.08	0.17	0.16	0.17
NiO	0.10	0.16	0.24	0.26	0.16	0.24	0.21	0.18	0.11	0.23	0.25	0.24	0.17	0.16
CaO	0.35	0.26	0.27	0.30	0.27	0.28	0.27	0.28	0.27	0.27	0.28	0.27	0.27	0.30
Na_2O	0.00	0.00	0.00	0.00	0.02	0.00	0.00	0.00	0.00	0.04	0.02	0.00	0.00	0.03
K_2O	0.00	0.01	0.00	0.00	0.00	0.00	0.00	0.00	0.01	0.00	0.00	0.00	0.00	0.01
Total	101.81	101.13	100.88	101.73	100.91	100.76	101.02	100.77	100.98	101.17	101.26	101.22	101.47	101.35
Si	0.98	0.99	0.98	0.97	0.99	0.99	0.98	0.99	0.99	0.99	0.98	0.99	0.98	0.99
Ti	0.00	0.00	0.00	0.00	0.00	0.00	0.00	0.00	0.00	0.00	0.00	0.00	0.00	0.00
Al	0.00	0.00	0.00	0.00	0.00	0.00	0.00	0.00	0.00	0.00	0.00	0.00	0.00	0.00
Cr	0.00	0.00	0.00	0.00	0.00	0.00	0.00	0.00	0.00	0.00	0.00	0.00	0.00	0.00
Fe^{2+}	0.18	0.21	0.21	0.21	0.21	0.21	0.22	0.21	0.22	0.22	0.22	0.21	0.22	0.21
Mg	1.82	1.78	1.79	1.80	1.78	1.78	1.78	1.79	1.78	1.78	1.79	1.78	1.78	1.77
Mn	0.00	0.00	0.00	0.00	0.00	0.00	0.00	0.00	0.00	0.00	0.00	0.00	0.00	0.00
Ni	0.00	0.00	0.00	0.01	0.00	0.00	0.00	0.00	0.00	0.00	0.00	0.00	0.00	0.00
Ca	0.01	0.01	0.01	0.01	0.01	0.01	0.01	0.01	0.01	0.01	0.01	0.01	0.01	0.01
Na	0.00	0.00	0.00	0.00	0.00	0.00	0.00	0.00	0.00	0.00	0.00	0.00	0.00	0.00
K	0.00	0.00	0.00	0.00	0.00	0.00	0.00	0.00	0.00	0.00	0.00	0.00	0.00	0.00
Sum	3.00	3.00	3.00	3.00	3.00	3.00	3.00	3.00	3.00	3.00	3.00	3.00	3.00	3.00
X_{Mg}	0.90	0.89	0.89	0.89	0.89	0.89	0.88	0.89	0.89	0.88	0.89	0.89	0.88	0.88

Sample	MG18	MG18	MG18	MG18	MG18	MG18	MG18	MG18	MG18	MG18	MG18	MG18	MG18	OM23[d]
Run duration	24	24	24	24	24	24	24	24	24	24	24	24	24	0.5
Melt	AH6	AH6	AH6	AH6	AH6	AH6	AH6	AH6	AH6	AH6	AH6	AH6	AH6	AH6
IMA (wt%)	10	10	10	10	10	10	10	10	10	10	10	10	10	9
T	1300	1300	1300	1300	1300	1300	1300	1300	1300	1300	1300	1300	1300	1300
P	0.5	0.5	0.5	0.5	0.5	0.5	0.5	0.5	0.5	0.5	0.5	0.5	0.5	0.5
Point Analysis	MG18OL13	MG18OL14	MG18OL15	MG18OL16	MG18OL17	MG18OL18	MG18OL19	MG18OL20	MG18OL21	MG18OL22	MG18OL23	MG18OL24	MG18OL25	OM23OL1
Site	core	rim	core	core	rim	core	core	rim	core	rim	core	core	rim	rim
SiO_2	40.96	40.90	40.06	40.63	40.88	40.21	40.75	40.49	40.93	40.64	41.16	40.61	40.58	40.85
TiO_2	0.02	0.00	0.03	0.00	0.00	0.04	0.03	0.01	0.02	0.04	0.01	0.03	0.00	0.00
Al_2O_3	0.05	0.06	0.03	0.04	0.07	0.05	0.04	0.03	0.07	0.07	0.05	0.06	0.08	0.05
Cr_2O_3	0.00	0.07	0.05	0.07	0.06	0.01	0.00	0.06	0.00	0.08	0.04	0.04	0.04	0.02
FeO	10.57	10.74	10.19	10.60	10.50	10.67	9.96	9.63	9.47	9.52	9.36	10.17	9.47	9.97
MgO	49.16	49.32	48.67	49.76	49.10	49.64	50.35	51.41	50.08	51.09	50.37	49.46	50.79	48.29
MnO	0.18	0.10	0.14	0.18	0.12	0.09	0.12	0.10	0.15	0.10	0.16	0.11	0.10	0.18
NiO	0.19	0.14	0.19	0.12	0.17	0.25	0.15	0.00	0.10	0.04	0.00	0.10	0.01	0.28
CaO	0.28	0.27	0.27	0.29	0.27	0.28	0.19	0.31	0.26	0.29	0.29	0.25	0.26	0.28
Na_2O	0.00	0.01	0.00	0.01	0.00	0.03	0.00	0.00	0.00	0.00	0.00	0.01	0.00	0.01
K_2O	0.00	0.00	0.00	0.00	0.00	0.01	0.00	0.00	0.00	0.00	0.00	0.00	0.03	0.01
Total	101.40	101.61	99.63	101.71	101.16	101.28	101.59	102.05	101.08	101.87	101.45	100.85	101.35	99.94
Si	0.99	0.99	0.99	0.98	0.99	0.97	0.98	0.97	0.99	0.97	0.99	0.99	0.98	1.00
Ti	0.00	0.00	0.00	0.00	0.00	0.00	0.00	0.00	0.00	0.00	0.00	0.00	0.00	0.00
Al	0.00	0.00	0.00	0.00	0.00	0.00	0.00	0.00	0.00	0.00	0.00	0.00	0.00	0.00
Cr	0.00	0.00	0.00	0.00	0.00	0.00	0.00	0.00	0.00	0.00	0.00	0.00	0.00	0.00
Fe^{2+}	0.21	0.22	0.21	0.21	0.21	0.22	0.20	0.19	0.19	0.19	0.19	0.21	0.19	0.21
Mg	1.78	1.78	1.79	1.79	1.78	1.79	1.81	1.83	1.80	1.82	1.81	1.79	1.82	1.77
Mn	0.00	0.00	0.00	0.00	0.00	0.00	0.00	0.00	0.00	0.00	0.00	0.00	0.00	0.00
Ni	0.00	0.00	0.00	0.00	0.00	0.00	0.00	0.00	0.00	0.00	0.00	0.00	0.00	0.01
Ca	0.01	0.01	0.01	0.01	0.01	0.01	0.01	0.01	0.01	0.01	0.01	0.01	0.01	0.01
Na	0.00	0.00	0.00	0.00	0.00	0.00	0.00	0.00	0.00	0.00	0.00	0.00	0.00	0.00
K	0.00	0.00	0.00	0.00	0.00	0.00	0.00	0.00	0.00	0.00	0.00	0.00	0.00	0.00
Sum	3.00	3.00	3.00	3.00	3.00	3.00	3.00	3.00	3.00	3.00	3.00	3.00	3.00	3.00
X_{Mg}	0.89	0.88	0.89	0.89	0.89	0.88	0.90	0.90	0.90	0.90	0.90	0.89	0.90	0.89

Sample	OM23	OM23	OM23	OM23	OM23	OM23	OM23	OM23	OM23	OM23	OM23	OM23	OM23	OM23
Run duration	0.5	0.5	0.5	0.5	0.5	0.5	0.5	0.5	0.5	0.5	0.5	0.5	0.5	0.5
Melt	AH6	AH6	AH6	AH6	AH6	AH6	AH6	AH6	AH6	AH6	AH6	AH6	AH6	AH6
IMA (wt%)	9	9	9	9	9	9	9	9	9	9	9	9	9	9
T	1300	1300	1300	1300	1300	1300	1300	1300	1300	1300	1300	1300	1300	1300
P	0.5	0.5	0.5	0.5	0.5	0.5	0.5	0.5	0.5	0.5	0.5	0.5	0.5	0.5
Point Analysis	OM23OL2	OM23OL3	OM23OL4	OM23OL5	OM23OL6	OM23OL7	OM23OL8	OM23OL9	OM23OL10	OM23OL11	OM23OL12	OM23OL13	OM23OL14	OM23OL15
Site	rim	core	rim	rim	core	rim	core	core	core	rim	core	core	rim	rim
SiO_2	40.42	40.85	40.86	40.63	40.75	40.96	40.51	40.84	41.26	40.86	40.80	40.82	40.70	40.64
TiO_2	0.02	0.00	0.05	0.01	0.00	0.00	0.00	0.00	0.00	0.01	0.02	0.07	0.00	0.03
Al_2O_3	0.05	0.03	0.09	0.07	0.03	0.04	0.02	0.02	0.01	0.05	0.00	0.01	0.03	0.08
Cr_2O_3	0.09	0.00	0.02	0.00	0.00	0.01	0.00	0.00	0.06	0.00	0.02	0.00	0.01	0.00
FeO	10.61	9.72	10.09	10.48	9.70	10.09	9.17	9.59	9.13	9.44	9.64	9.31	8.80	9.99
MgO	47.93	48.83	48.51	48.29	48.88	48.71	49.36	49.25	49.11	48.80	49.17	49.33	49.77	48.38
MnO	0.17	0.14	0.17	0.09	0.14	0.15	0.15	0.13	0.14	0.15	0.18	0.14	0.15	0.13
NiO	0.34	0.35	0.24	0.41	0.36	0.30	0.38	0.34	0.38	0.36	0.44	0.37	0.10	0.38
CaO	0.41	0.11	0.28	0.35	0.08	0.16	0.08	0.09	0.10	0.18	0.08	0.08	0.35	0.37
Na_2O	0.00	0.05	0.00	0.00	0.01	0.01	0.00	0.03	0.01	0.00	0.01	0.00	0.02	0.04
K_2O	0.00	0.01	0.00	0.00	0.00	0.00	0.00	0.02	0.01	0.01	0.00	0.01	0.00	0.01
Total	100.04	100.09	100.31	100.33	99.95	100.43	99.67	100.31	100.21	99.86	100.36	100.14	99.93	100.05
Si	1.00	1.00	1.00	1.00	1.00	1.00	0.99	1.00	1.01	1.00	1.00	1.00	0.99	1.00
Ti	0.00	0.00	0.00	0.00	0.00	0.00	0.00	0.00	0.00	0.00	0.00	0.00	0.00	0.00
Al	0.00	0.00	0.00	0.00	0.00	0.00	0.00	0.00	0.00	0.00	0.00	0.00	0.00	0.00
Cr	0.00	0.00	0.00	0.00	0.00	0.00	0.00	0.00	0.00	0.00	0.00	0.00	0.00	0.00
Fe^{2+}	0.22	0.20	0.21	0.22	0.20	0.21	0.19	0.20	0.19	0.19	0.20	0.19	0.18	0.21
Mg	1.76	1.78	1.77	1.77	1.79	1.78	1.80	1.79	1.79	1.79	1.79	1.80	1.81	1.77
Mn	0.00	0.00	0.00	0.00	0.00	0.00	0.00	0.00	0.00	0.00	0.00	0.00	0.00	0.00
Ni	0.01	0.01	0.00	0.01	0.01	0.01	0.01	0.01	0.01	0.01	0.01	0.01	0.00	0.01
Ca	0.01	0.00	0.01	0.01	0.00	0.00	0.00	0.00	0.00	0.00	0.00	0.00	0.01	0.01
Na	0.00	0.00	0.00	0.00	0.00	0.00	0.00	0.00	0.00	0.00	0.00	0.00	0.00	0.00
K	0.00	0.00	0.00	0.00	0.00	0.00	0.00	0.00	0.00	0.00	0.00	0.00	0.00	0.00
Sum	3.00	3.00	3.00	3.00	3.00	3.00	3.00	3.00	3.00	3.00	3.00	3.00	3.00	3.00
X_{Mg}	0.88	0.89	0.89	0.88	0.89	0.89	0.90	0.90	0.90	0.89	0.89	0.90	0.90	0.89

Sample	OM23	OM23	MG1	MG1	MG1	MG1	MG1	MG1	MG1	MG1	MG1	MG1	MG1	MG1
Run duration	0.5	0.5	24	24	24	24	24	24	24	24	24	24	24	24
Melt	AH6	AH6	AH6	AH6	AH6	AH6	AH6	AH6	AH6	AH6	AH6	AH6	AH6	AH6
IMA (wt%)	9	9	25	25	25	25	25	25	25	25	25	25	25	25
T	1300	1300	1300	1300	1300	1300	1300	1300	1300	1300	1300	1300	1300	1300
P	0.5	0.5	0.5	0.5	0.5	0.5	0.5	0.5	0.5	0.5	0.5	0.5	0.5	0.5
Point Analysis	OM23OL16	OM23OL17	MG1OL1	MG1OL2	MG1OL3	MG1OL4	MG1OL5	MG1OL6	MG1OL7	MG1OL8	MG1OL9	MG1OL10	MG1OL11	MG1OL12
Site	rim	rim	core	core	core	core	core	core	core	core	core	core	core	core
SiO_2	40.98	40.65	41.88	42.24	41.48	41.71	41.71	41.92	42.14	42.14	42.05	41.91	40.24	40.94
TiO_2	0.00	0.04	0.07	0.02	0.05	0.01	0.00	0.00	0.06	0.04	0.00	0.00	0.05	0.03
Al_2O_3	0.12	0.00	0.03	0.08	0.03	0.05	0.05	0.05	0.02	0.03	0.08	0.07	0.04	0.06
Cr_2O_3	0.00	0.05	0.00	0.05	0.01	0.03	0.03	0.05	0.01	0.06	0.03	0.07	0.06	0.03
FeO	9.86	9.58	9.58	9.27	9.29	9.38	9.57	9.56	9.14	9.15	9.01	8.80	9.14	9.11
MgO	48.68	48.69	49.28	49.41	49.83	48.76	49.54	49.18	49.63	49.40	49.85	49.89	50.01	48.88
MnO	0.13	0.12	0.13	0.09	0.14	0.13	0.18	0.11	0.15	0.19	0.15	0.15	0.08	0.10
NiO	0.41	0.30	0.04	0.02	0.02	0.04	0.09	0.16	0.00	0.01	0.00	0.00	0.11	0.02
CaO	0.36	0.19	0.34	0.34	0.33	0.35	0.31	0.17	0.34	0.32	0.30	0.31	0.20	0.34
Na_2O	0.01	0.00	0.00	0.00	0.02	0.04	0.04	0.00	0.03	0.00	0.02	0.03	0.00	0.01
K_2O	0.00	0.00	0.02	0.00	0.01	0.01	0.01	0.00	0.01	0.00	0.00	0.00	0.00	0.01
Total	100.55	99.62	101.38	101.51	101.21	100.51	101.53	101.21	101.53	101.34	101.49	101.23	99.93	99.53
Si	1.00	1.00	1.01	1.02	1.00	1.02	1.01	1.02	1.02	1.02	1.01	1.01	0.98	1.01
Ti	0.00	0.00	0.00	0.00	0.00	0.00	0.00	0.00	0.00	0.00	0.00	0.00	0.00	0.00
Al	0.00	0.00	0.00	0.00	0.00	0.00	0.00	0.00	0.00	0.00	0.00	0.00	0.00	0.00
Cr	0.00	0.00	0.00	0.00	0.00	0.00	0.00	0.00	0.00	0.00	0.00	0.00	0.00	0.00
Fe^{2+}	0.20	0.20	0.19	0.19	0.19	0.19	0.19	0.19	0.18	0.19	0.18	0.18	0.19	0.19
Mg	1.77	1.79	1.78	1.78	1.79	1.77	1.78	1.78	1.78	1.78	1.79	1.79	1.82	1.79
Mn	0.00	0.00	0.00	0.00	0.00	0.00	0.00	0.00	0.00	0.00	0.00	0.00	0.00	0.00
Ni	0.01	0.01	0.00	0.00	0.00	0.00	0.00	0.00	0.00	0.00	0.00	0.00	0.00	0.00
Ca	0.01	0.01	0.01	0.01	0.01	0.01	0.01	0.00	0.01	0.01	0.01	0.01	0.01	0.01
Na	0.00	0.00	0.00	0.00	0.00	0.00	0.00	0.00	0.00	0.00	0.00	0.00	0.00	0.00
K	0.00	0.00	0.00	0.00	0.00	0.00	0.00	0.00	0.00	0.00	0.00	0.00	0.00	0.00
Sum	3.00	3.00	3.00	3.00	3.00	3.00	3.00	3.00	3.00	3.00	3.00	3.00	3.00	3.00
X_{Mg}	0.89	0.89	0.90	0.90	0.90	0.90	0.89	0.90	0.90	0.90	0.90	0.90	0.90	0.90

Sample	MG1	MG1	MG1	MG1	MG1	MG1	MG1	MG1	MG1	MG1	MG1	MG1	MG1	MG1
Run duration	24	24	24	24	24	24	24	24	24	24	24	24	24	24
Melt	AH6	AH6	AH6	AH6	AH6	AH6	AH6	AH6	AH6	AH6	AH6	AH6	AH6	AH6
IMA (wt%)	25	25	25	25	25	25	25	25	25	25	25	25	25	25
T	1300	1300	1300	1300	1300	1300	1300	1300	1300	1300	1300	1300	1300	1300
P	0.5	0.5	0.5	0.5	0.5	0.5	0.5	0.5	0.5	0.5	0.5	0.5	0.5	0.5
Point Analysis	MG1OL13	MG1OL14	MG1OL15	MG1OL16	MG1OL17	MG1OL18	MG1OL19	MG1OL20	MG1OL21	MG1OL22	MG1OL23	MG1OL24	MG1OL25	MG1OL26
Site	core	core	core	core	core	core	core	core	core	core	core	core	core	core
SiO_2	39.89	39.95	39.91	40.17	40.43	40.11	40.46	40.47	39.58	40.57	40.14	40.42	40.51	40.41
TiO_2	0.05	0.03	0.00	0.01	0.05	0.07	0.02	0.00	0.04	0.03	0.00	0.01	0.00	0.00
Al_2O_3	0.06	0.12	0.06	0.08	0.06	0.08	0.02	0.03	0.07	0.05	0.08	0.09	0.08	0.05
Cr_2O_3	0.04	0.05	0.06	0.00	0.00	0.04	0.03	0.01	0.00	0.02	0.05	0.00	0.02	0.07
FeO	9.08	9.31	9.05	9.19	8.81	9.15	9.22	8.83	10.18	9.07	9.07	9.00	9.04	9.19
MgO	50.48	50.30	50.15	49.90	49.77	49.21	50.10	49.85	49.39	49.70	49.98	49.64	50.73	50.78
MnO	0.14	0.18	0.11	0.17	0.06	0.14	0.09	0.10	0.18	0.15	0.10	0.14	0.13	0.19
NiO	0.01	0.37	0.08	0.00	0.03	0.15	0.12	0.05	0.77	0.00	0.00	0.00	0.00	0.02
CaO	0.33	0.37	0.26	0.35	0.35	0.20	0.14	0.34	0.28	0.33	0.35	0.36	0.33	0.32
Na_2O	0.02	0.02	0.00	0.00	0.02	0.06	0.00	0.02	0.03	0.01	0.01	0.04	0.01	0.00
K_2O	0.00	0.01	0.01	0.00	0.01	0.04	0.02	0.02	0.02	0.01	0.01	0.01	0.01	0.01
Total	100.09	100.70	99.68	99.86	99.59	99.25	100.23	99.72	100.54	99.94	99.79	99.71	100.86	101.03
Si	0.97	0.97	0.98	0.98	0.99	0.99	0.98	0.99	0.97	0.99	0.98	0.99	0.98	0.97
Ti	0.00	0.00	0.00	0.00	0.00	0.00	0.00	0.00	0.00	0.00	0.00	0.00	0.00	0.00
Al	0.00	0.00	0.00	0.00	0.00	0.00	0.00	0.00	0.00	0.00	0.00	0.00	0.00	0.00
Cr	0.00	0.00	0.00	0.00	0.00	0.00	0.00	0.00	0.00	0.00	0.00	0.00	0.00	0.00
Fe^{2+}	0.18	0.19	0.18	0.19	0.18	0.19	0.19	0.18	0.21	0.19	0.19	0.18	0.18	0.19
Mg	1.83	1.82	1.83	1.82	1.82	1.81	1.82	1.82	1.80	1.81	1.82	1.81	1.83	1.83
Mn	0.00	0.00	0.00	0.00	0.00	0.00	0.00	0.00	0.00	0.00	0.00	0.00	0.00	0.00
Ni	0.00	0.01	0.00	0.00	0.00	0.00	0.00	0.00	0.02	0.00	0.00	0.00	0.00	0.00
Ca	0.01	0.01	0.01	0.01	0.01	0.01	0.00	0.01	0.01	0.01	0.01	0.01	0.01	0.01
Na	0.00	0.00	0.00	0.00	0.00	0.00	0.00	0.00	0.00	0.00	0.00	0.00	0.00	0.00
K	0.00	0.00	0.00	0.00	0.00	0.00	0.00	0.00	0.00	0.00	0.00	0.00	0.00	0.00
Sum	3.00	3.00	3.00	3.00	3.00	3.00	3.00	3.00	3.00	3.00	3.00	3.00	3.00	3.00
X_{Mg}	0.90	0.89	0.90	0.90	0.90	0.90	0.90	0.90	0.88	0.90	0.90	0.90	0.90	0.90

Sample	MG1	MG1	MG1	MG1	MG1	MG1	MG1	MG1	MG1	MG1	MG1	MG1	MG1	MG1
Run duration	24	24	24	24	24	24	24	24	24	24	24	24	24	24
Melt	AH6	AH6	AH6	AH6	AH6	AH6	AH6	AH6	AH6	AH6	AH6	AH6	AH6	AH6
IMA (wt%)	25	25	25	25	25	25	25	25	25	25	25	25	25	25
T	1300	1300	1300	1300	1300	1300	1300	1300	1300	1300	1300	1300	1300	1300
P	0.5	0.5	0.5	0.5	0.5	0.5	0.5	0.5	0.5	0.5	0.5	0.5	0.5	0.5
Point Analysis	MG1OL27	MG1OL28	MG1OL29	MG1OL30	MG1OL31	MG1OL32	MG1OL33	MG1OL34	MG1OL35	MG1OL36	MG1OL37	MG1OL38	MG1OL39	MG1OL40
Site	core	core	core	core	core	core	core	core	core	core	core	core	core	core
SiO_2	40.46	40.55	40.70	40.54	40.61	40.54	40.86	40.25	40.62	40.89	40.77	40.42	40.79	40.57
TiO_2	0.00	0.03	0.06	0.00	0.04	0.03	0.13	0.01	0.03	0.02	0.03	0.01	0.00	0.02
Al_2O_3	0.05	0.04	0.06	0.04	0.05	0.10	0.55	0.08	0.07	0.10	0.11	0.06	0.05	0.06
Cr_2O_3	0.07	0.04	0.08	0.00	0.01	0.04	0.02	0.02	0.04	0.02	0.09	0.00	0.10	0.01
FeO	9.10	9.30	9.13	9.35	9.25	9.20	9.26	8.97	9.20	9.08	9.18	9.24	9.40	9.52
MgO	50.76	50.68	50.49	50.29	50.46	49.91	49.05	50.53	51.04	50.79	50.27	50.39	50.13	50.59
MnO	0.12	0.14	0.12	0.12	0.13	0.14	0.20	0.12	0.14	0.14	0.14	0.09	0.16	0.14
NiO	0.04	0.02	0.00	0.00	0.00	0.09	0.04	0.03	0.04	0.02	0.02	0.05	0.00	0.04
CaO	0.34	0.34	0.38	0.32	0.32	0.30	0.75	0.35	0.31	0.37	0.42	0.31	0.33	0.31
Na_2O	0.01	0.02	0.03	0.01	0.00	0.01	0.18	0.02	0.02	0.00	0.01	0.02	0.02	0.04
K_2O	0.01	0.02	0.00	0.02	0.02	0.00	0.03	0.00	0.02	0.02	0.02	0.01	0.01	0.01
Total	100.96	101.17	101.06	100.68	100.89	100.35	101.07	100.37	101.52	101.45	101.05	100.59	100.98	101.30
Si	0.98	0.98	0.98	0.98	0.98	0.99	0.99	0.98	0.97	0.98	0.98	0.98	0.99	0.98
Ti	0.00	0.00	0.00	0.00	0.00	0.00	0.00	0.00	0.00	0.00	0.00	0.00	0.00	0.00
Al	0.00	0.00	0.00	0.00	0.00	0.00	0.02	0.00	0.00	0.00	0.00	0.00	0.00	0.00
Cr	0.00	0.00	0.00	0.00	0.00	0.00	0.00	0.00	0.00	0.00	0.00	0.00	0.00	0.00
Fe^{2+}	0.18	0.19	0.18	0.19	0.19	0.19	0.19	0.18	0.18	0.18	0.19	0.19	0.19	0.19
Mg	1.83	1.82	1.82	1.82	1.82	1.81	1.77	1.83	1.82	1.82	1.81	1.82	1.81	1.82
Mn	0.00	0.00	0.00	0.00	0.00	0.00	0.00	0.00	0.00	0.00	0.00	0.00	0.00	0.00
Ni	0.00	0.00	0.00	0.00	0.00	0.00	0.00	0.00	0.00	0.00	0.00	0.00	0.00	0.00
Ca	0.01	0.01	0.01	0.01	0.01	0.01	0.02	0.01	0.01	0.01	0.01	0.01	0.01	0.01
Na	0.00	0.00	0.00	0.00	0.00	0.00	0.01	0.00	0.00	0.00	0.00	0.00	0.00	0.00
K	0.00	0.00	0.00	0.00	0.00	0.00	0.00	0.00	0.00	0.00	0.00	0.00	0.00	0.00
Sum	3.00	3.00	3.00	3.00	3.00	3.00	3.00	3.00	3.00	3.00	3.00	3.00	3.00	3.00
X_{Mg}	0.90	0.90	0.90	0.90	0.90	0.90	0.88	0.90	0.90	0.90	0.90	0.90	0.90	0.90

Sample	MG1	MG1	MG1	MG1	MG1	MG1	MG1	MG1	MG1	MG1	MG1	MG1	MG1	MG1
Run duration	24	24	24	24	24	24	24	24	24	24	24	24	24	24
Melt	AH6	AH6	AH6	AH6	AH6	AH6	AH6	AH6	AH6	AH6	AH6	AH6	AH6	AH6
IMA (wt%)	25	25	25	25	25	25	25	25	25	25	25	25	25	25
T	1300	1300	1300	1300	1300	1300	1300	1300	1300	1300	1300	1300	1300	1300
P	0.5	0.5	0.5	0.5	0.5	0.5	0.5	0.5	0.5	0.5	0.5	0.5	0.5	0.5
Point Analysis	MG1OL41	MG1OL42	MG1OL43	MG1OL44	MG1OL45	MG1OL46	MG1OL47	MG1OL48	MG1OL49	MG1OL50	MG1OL51	MG1OL52	MG1OL53	MG1OL54
Site	core	core	core	core	core	core	core	core	core	core	core	core	core	core
SiO_2	40.57	40.77	40.78	40.29	40.44	40.56	40.37	40.52	40.47	39.44	39.71	39.93	40.31	41.01
TiO_2	0.02	0.03	0.03	0.06	0.04	0.01	0.00	0.00	0.02	0.00	0.04	0.00	0.03	0.02
Al_2O_3	0.05	0.03	0.03	0.07	0.07	0.07	0.06	0.05	0.03	0.10	0.05	0.04	0.05	0.09
Cr_2O_3	0.05	0.00	0.02	0.00	0.02	0.02	0.00	0.07	0.00	0.02	0.02	0.08	0.00	0.00
FeO	9.45	9.27	9.22	9.42	9.14	9.21	9.38	9.16	9.34	8.14	8.35	8.57	8.31	8.90
MgO	50.85	50.28	50.69	50.49	50.49	50.19	49.98	49.95	50.52	46.71	48.92	48.24	47.64	50.30
MnO	0.13	0.12	0.16	0.12	0.13	0.09	0.12	0.16	0.14	0.15	0.15	0.12	0.14	0.18
NiO	0.03	0.03	0.02	0.00	0.06	0.00	0.03	0.00	0.03	0.00	0.00	0.00	0.06	0.00
CaO	0.36	0.32	0.33	0.31	0.37	0.34	0.29	0.34	0.36	0.32	0.35	0.32	0.29	0.30
Na_2O	0.03	0.04	0.01	0.00	0.02	0.04	0.06	0.02	0.00	0.03	0.01	0.02	0.01	0.06
K_2O	0.01	0.00	0.00	0.00	0.01	0.03	0.04	0.01	0.01	0.03	0.01	0.02	0.01	0.00
Total	101.55	100.88	101.29	100.75	100.79	100.55	100.33	100.28	100.93	94.93	97.62	97.35	96.86	100.86
Si	0.97	0.99	0.98	0.97	0.98	0.98	0.98	0.99	0.98	1.02	0.99	1.00	1.02	0.99
Ti	0.00	0.00	0.00	0.00	0.00	0.00	0.00	0.00	0.00	0.00	0.00	0.00	0.00	0.00
Al	0.00	0.00	0.00	0.00	0.00	0.00	0.00	0.00	0.00	0.00	0.00	0.00	0.00	0.00
Cr	0.00	0.00	0.00	0.00	0.00	0.00	0.00	0.00	0.00	0.00	0.00	0.00	0.00	0.00
Fe^{2+}	0.19	0.19	0.19	0.19	0.18	0.19	0.19	0.19	0.19	0.18	0.17	0.18	0.18	0.18
Mg	1.82	1.81	1.82	1.82	1.82	1.81	1.81	1.81	1.82	1.79	1.82	1.80	1.79	1.81
Mn	0.00	0.00	0.00	0.00	0.00	0.00	0.00	0.00	0.00	0.00	0.00	0.00	0.00	0.00
Ni	0.00	0.00	0.00	0.00	0.00	0.00	0.00	0.00	0.00	0.00	0.00	0.00	0.00	0.00
Ca	0.01	0.01	0.01	0.01	0.01	0.01	0.01	0.01	0.01	0.01	0.01	0.01	0.01	0.01
Na	0.00	0.00	0.00	0.00	0.00	0.00	0.00	0.00	0.00	0.00	0.00	0.00	0.00	0.00
K	0.00	0.00	0.00	0.00	0.00	0.00	0.00	0.00	0.00	0.00	0.00	0.00	0.00	0.00
Sum	3.00	3.00	3.00	3.00	3.00	3.00	3.00	3.00	3.00	3.00	3.00	3.00	3.00	3.00
X_{Mg}	0.90	0.90	0.90	0.90	0.90	0.90	0.90	0.90	0.90	0.90	0.91	0.90	0.90	0.90

Sample	MG1	MG1	MG1	MG1	MG1	MG1	MG1	MG1	MG1	MG1	MG1	MG1	MG1	MG1
Run duration	24	24	24	24	24	24	24	24	24	24	24	24	24	24
Melt	AH6	AH6	AH6	AH6	AH6	AH6	AH6	AH6	AH6	AH6	AH6	AH6	AH6	AH6
IMA (wt%)	25	25	25	25	25	25	25	25	25	25	25	25	25	25
T	1300	1300	1300	1300	1300	1300	1300	1300	1300	1300	1300	1300	1300	1300
P	0.5	0.5	0.5	0.5	0.5	0.5	0.5	0.5	0.5	0.5	0.5	0.5	0.5	0.5
Point Analysis	MG1OL55	MG1OL56	MG1OL57	MG1OL58	MG1OL59	MG1OL60	MG1OL61	MG1OL62	MG1OL63	MG1OL64	MG1OL65	MG1OL66	MG1OL67	MG1OL68
Site	core	core	core	core	core	core	core	core	core	core	core	core	core	core
SiO_2	40.40	40.95	40.72	40.50	39.92	39.63	40.47	40.78	40.28	40.42	40.55	40.48	40.36	40.60
TiO_2	0.01	0.04	0.03	0.00	0.02	0.05	0.02	0.00	0.05	0.02	0.03	0.00	0.01	0.04
Al_2O_3	0.09	0.07	0.06	0.07	0.09	0.04	0.08	0.01	0.07	0.11	0.04	0.06	0.04	0.02
Cr_2O_3	0.04	0.04	0.00	0.02	0.05	0.06	0.06	0.04	0.04	0.05	0.00	0.01	0.04	0.03
FeO	9.44	9.31	9.30	9.01	9.21	8.79	9.25	9.18	9.08	8.99	9.27	9.23	9.46	9.43
MgO	50.32	50.89	50.48	50.69	50.66	50.04	51.76	50.80	50.83	50.20	50.32	50.45	50.13	50.98
MnO	0.17	0.11	0.13	0.13	0.11	0.11	0.17	0.15	0.14	0.16	0.18	0.13	0.16	0.10
NiO	0.12	0.05	0.11	0.00	0.00	0.04	0.06	0.04	0.03	0.01	0.08	0.10	0.19	0.07
CaO	0.34	0.32	0.24	0.35	0.35	0.31	0.35	0.25	0.32	0.33	0.39	0.34	0.28	0.28
Na_2O	0.05	0.02	0.00	0.03	0.02	0.02	0.00	0.02	0.02	0.04	0.01	0.02	0.00	0.02
K_2O	0.01	0.01	0.00	0.00	0.04	0.02	0.02	0.02	0.00	0.01	0.00	0.01	0.01	0.01
Total	101.00	101.81	101.08	100.81	100.47	99.11	102.24	101.30	100.85	100.34	100.88	100.83	100.67	101.58
Si	0.98	0.98	0.98	0.98	0.97	0.97	0.96	0.98	0.97	0.98	0.98	0.98	0.98	0.97
Ti	0.00	0.00	0.00	0.00	0.00	0.00	0.00	0.00	0.00	0.00	0.00	0.00	0.00	0.00
Al	0.00	0.00	0.00	0.00	0.00	0.00	0.00	0.00	0.00	0.00	0.00	0.00	0.00	0.00
Cr	0.00	0.00	0.00	0.00	0.00	0.00	0.00	0.00	0.00	0.00	0.00	0.00	0.00	0.00
Fe^{2+}	0.19	0.19	0.19	0.18	0.19	0.18	0.18	0.18	0.18	0.18	0.19	0.19	0.19	0.19
Mg	1.81	1.82	1.82	1.82	1.83	1.83	1.84	1.82	1.83	1.82	1.81	1.82	1.81	1.82
Mn	0.00	0.00	0.00	0.00	0.00	0.00	0.00	0.00	0.00	0.00	0.00	0.00	0.00	0.00
Ni	0.00	0.00	0.00	0.00	0.00	0.00	0.00	0.00	0.00	0.00	0.00	0.00	0.00	0.00
Ca	0.01	0.01	0.01	0.01	0.01	0.01	0.01	0.01	0.01	0.01	0.01	0.01	0.01	0.01
Na	0.00	0.00	0.00	0.00	0.00	0.00	0.00	0.00	0.00	0.00	0.00	0.00	0.00	0.00
K	0.00	0.00	0.00	0.00	0.00	0.00	0.00	0.00	0.00	0.00	0.00	0.00	0.00	0.00
Sum	3.00	3.00	3.00	3.00	3.00	3.00	3.00	3.00	3.00	3.00	3.00	3.00	3.00	3.00
X_{Mg}	0.90	0.90	0.90	0.90	0.90	0.90	0.90	0.90	0.90	0.90	0.90	0.90	0.90	0.90

Sample	MG1	MG1	MG1	MG1	MG1	MG1	MG1	MG1	MG1	MG1	MG1	MG1	MG1	MG1
Run duration	24	24	24	24	24	24	24	24	24	24	24	24	24	24
Melt	AH6	AH6	AH6	AH6	AH6	AH6	AH6	AH6	AH6	AH6	AH6	AH6	AH6	AH6
IMA (wt%)	25	25	25	25	25	25	25	25	25	25	25	25	25	25
T	1300	1300	1300	1300	1300	1300	1300	1300	1300	1300	1300	1300	1300	1300
P	0.5	0.5	0.5	0.5	0.5	0.5	0.5	0.5	0.5	0.5	0.5	0.5	0.5	0.5
Point Analysis	MG1OL69	MG1OL70	MG1OL71	MG1OL72	MG1OL73	MG1OL74	MG1OL75	MG1OL76	MG1OL77	MG1OL78	MG1OL79	MG1OL80	MG1OL81	MG1OL82
Site	core	core	core	core	rim	rim	rim	rim	rim	rim	rim	rim	rim	rim
SiO_2	40.78	40.30	40.46	40.39	41.68	42.12	41.81	41.73	42.39	42.02	41.80	41.99	41.63	41.66
TiO_2	0.03	0.03	0.06	0.00	0.04	0.00	0.00	0.00	0.03	0.00	0.04	0.08	0.01	0.10
Al_2O_3	0.04	0.08	0.04	0.04	0.07	0.08	0.05	0.05	0.04	0.08	0.07	0.08	0.08	0.06
Cr_2O_3	0.06	0.05	0.00	0.01	0.03	0.00	0.00	0.09	0.06	0.00	0.02	0.00	0.05	0.10
FeO	9.28	9.11	9.16	9.44	9.43	9.06	8.98	9.05	9.35	9.04	9.21	9.14	9.05	8.91
MgO	49.79	50.76	50.59	50.75	49.13	49.67	49.33	49.39	49.69	50.36	50.20	49.47	50.05	49.78
MnO	0.13	0.18	0.09	0.17	0.15	0.11	0.11	0.14	0.13	0.14	0.16	0.14	0.14	0.11
NiO	0.04	0.05	0.06	0.03	0.04	0.08	0.03	0.01	0.00	0.06	0.00	0.02	0.06	0.00
CaO	0.31	0.37	0.32	0.31	0.32	0.36	0.36	0.34	0.37	0.35	0.33	0.35	0.35	0.34
Na_2O	0.03	0.00	0.02	0.02	0.02	0.05	0.00	0.00	0.01	0.01	0.00	0.00	0.01	0.01
K_2O	0.05	0.00	0.02	0.01	0.00	0.02	0.00	0.00	0.00	0.01	0.01	0.00	0.00	0.00
Total	100.54	100.94	100.81	101.16	100.90	101.56	100.67	100.80	102.06	102.06	101.84	101.27	101.43	101.07
Si	0.99	0.97	0.98	0.97	1.01	1.01	1.02	1.01	1.02	1.01	1.00	1.02	1.00	1.01
Ti	0.00	0.00	0.00	0.00	0.00	0.00	0.00	0.00	0.00	0.00	0.00	0.00	0.00	0.00
Al	0.00	0.00	0.00	0.00	0.00	0.00	0.00	0.00	0.00	0.00	0.00	0.00	0.00	0.00
Cr	0.00	0.00	0.00	0.00	0.00	0.00	0.00	0.00	0.00	0.00	0.00	0.00	0.00	0.00
Fe^{2+}	0.19	0.18	0.19	0.19	0.19	0.18	0.18	0.18	0.19	0.18	0.18	0.18	0.18	0.18
Mg	1.80	1.83	1.82	1.82	1.78	1.78	1.79	1.79	1.78	1.80	1.80	1.78	1.80	1.80
Mn	0.00	0.00	0.00	0.00	0.00	0.00	0.00	0.00	0.00	0.00	0.00	0.00	0.00	0.00
Ni	0.00	0.00	0.00	0.00	0.00	0.00	0.00	0.00	0.00	0.00	0.00	0.00	0.00	0.00
Ca	0.01	0.01	0.01	0.01	0.01	0.01	0.01	0.01	0.01	0.01	0.01	0.01	0.01	0.01
Na	0.00	0.00	0.00	0.00	0.00	0.00	0.00	0.00	0.00	0.00	0.00	0.00	0.00	0.00
K	0.00	0.00	0.00	0.00	0.00	0.00	0.00	0.00	0.00	0.00	0.00	0.00	0.00	0.00
Sum	3.00	3.00	3.00	3.00	3.00	3.00	3.00	3.00	3.00	3.00	3.00	3.00	3.00	3.00
X_{Mg}	0.90	0.90	0.90	0.90	0.90	0.90	0.90	0.90	0.90	0.90	0.90	0.90	0.90	0.90

Sample	MG1	MG1	MG1	MG1	MG1	MG1	MG1	MG1	MG1	MG1	MG1	MG1	MG1	MG1
Run duration	24	24	24	24	24	24	24	24	24	24	24	24	24	24
Melt	AH6	AH6	AH6	AH6	AH6	AH6	AH6	AH6	AH6	AH6	AH6	AH6	AH6	AH6
IMA (wt%)	25	25	25	25	25	25	25	25	25	25	25	25	25	25
T	1300	1300	1300	1300	1300	1300	1300	1300	1300	1300	1300	1300	1300	1300
P	0.5	0.5	0.5	0.5	0.5	0.5	0.5	0.5	0.5	0.5	0.5	0.5	0.5	0.5
Point Analysis	MG1OL83	MG1OL84	MG1OL85	MG1OL86	MG1OL87	MG1OL88	MG1OL89	MG1OL90	MG1OL91	MG1OL92	MG1OL93	MG1OL94	MG1OL95	MG1OL96
Site	rim	rim	rim	rim	rim	rim	rim	rim	rim	rim	rim	rim	rim	rim
SiO_2	40.33	40.52	40.38	40.37	40.23	40.14	40.25	40.14	40.26	40.27	40.27	40.37	40.68	40.43
TiO_2	0.00	0.00	0.04	0.00	0.00	0.02	0.03	0.00	0.00	0.00	0.00	0.04	0.03	0.00
Al_2O_3	0.05	0.05	0.04	0.04	0.09	0.05	0.06	0.06	0.07	0.06	0.06	0.09	0.07	0.07
Cr_2O_3	0.02	0.00	0.01	0.07	0.08	0.05	0.00	0.02	0.01	0.00	0.01	0.02	0.01	0.03
FeO	9.14	9.22	9.04	9.15	9.17	9.31	9.08	9.02	9.01	9.13	8.99	9.31	9.30	9.19
MgO	50.11	50.05	50.26	49.96	49.84	49.80	50.09	50.22	50.42	50.87	50.73	50.48	50.59	50.56
MnO	0.14	0.22	0.07	0.12	0.12	0.20	0.16	0.15	0.16	0.10	0.18	0.18	0.11	0.19
NiO	0.09	0.02	0.00	0.04	0.00	0.07	0.07	0.04	0.00	0.00	0.05	0.03	0.04	0.03
CaO	0.28	0.33	0.35	0.32	0.33	0.31	0.30	0.34	0.37	0.33	0.32	0.33	0.31	0.32
Na_2O	0.02	0.01	0.03	0.00	0.01	0.02	0.00	0.00	0.00	0.01	0.01	0.00	0.00	0.04
K_2O	0.01	0.02	0.00	0.00	0.01	0.01	0.00	0.01	0.00	0.02	0.01	0.00	0.02	0.01
Total	100.20	100.44	100.22	100.08	99.89	99.99	100.04	100.02	100.30	100.80	100.63	100.85	101.17	100.86
Si	0.98	0.98	0.98	0.98	0.98	0.98	0.98	0.98	0.98	0.97	0.97	0.98	0.98	0.98
Ti	0.00	0.00	0.00	0.00	0.00	0.00	0.00	0.00	0.00	0.00	0.00	0.00	0.00	0.00
Al	0.00	0.00	0.00	0.00	0.00	0.00	0.00	0.00	0.00	0.00	0.00	0.00	0.00	0.00
Cr	0.00	0.00	0.00	0.00	0.00	0.00	0.00	0.00	0.00	0.00	0.00	0.00	0.00	0.00
Fe^{2+}	0.19	0.19	0.18	0.19	0.19	0.19	0.19	0.18	0.18	0.18	0.18	0.19	0.19	0.19
Mg	1.82	1.81	1.82	1.82	1.81	1.81	1.82	1.82	1.82	1.83	1.83	1.82	1.82	1.82
Mn	0.00	0.00	0.00	0.00	0.00	0.00	0.00	0.00	0.00	0.00	0.00	0.00	0.00	0.00
Ni	0.00	0.00	0.00	0.00	0.00	0.00	0.00	0.00	0.00	0.00	0.00	0.00	0.00	0.00
Ca	0.01	0.01	0.01	0.01	0.01	0.01	0.01	0.01	0.01	0.01	0.01	0.01	0.01	0.01
Na	0.00	0.00	0.00	0.00	0.00	0.00	0.00	0.00	0.00	0.00	0.00	0.00	0.00	0.00
K	0.00	0.00	0.00	0.00	0.00	0.00	0.00	0.00	0.00	0.00	0.00	0.00	0.00	0.00
Sum	3.00	3.00	3.00	3.00	3.00	3.00	3.00	3.00	3.00	3.00	3.00	3.00	3.00	3.00
X_{Mg}	0.90	0.90	0.90	0.90	0.90	0.90	0.90	0.90	0.90	0.90	0.90	0.90	0.90	0.90

Sample	MG1	MG1	MG1	MG1	MG1	MG1	MG1	MG1	MG1	MG1	MG1	MG1	MG1	MG1
Run duration	24	24	24	24	24	24	24	24	24	24	24	24	24	24
Melt	AH6	AH6	AH6	AH6	AH6	AH6	AH6	AH6	AH6	AH6	AH6	AH6	AH6	AH6
IMA (wt%)	25	25	25	25	25	25	25	25	25	25	25	25	25	25
T	1300	1300	1300	1300	1300	1300	1300	1300	1300	1300	1300	1300	1300	1300
P	0.5	0.5	0.5	0.5	0.5	0.5	0.5	0.5	0.5	0.5	0.5	0.5	0.5	0.5
Point Analysis	MG1OL97	MG1OL98	MG1OL99	MG1OL100	MG1OL101	MG1OL102	MG1OL103	MG1OL104	MG1OL105	MG1OL106	MG1OL107	MG1OL108	MG1OL109	MG1OL110
Site	rim	rim	rim	rim	rim	rim	rim	rim	rim	rim	rim	rim	rim	rim
SiO_2	40.46	40.72	40.37	40.96	40.55	40.59	40.92	40.09	40.71	40.57	40.95	40.72	40.63	40.50
TiO_2	0.06	0.00	0.04	0.00	0.04	0.00	0.02	0.00	0.00	0.01	0.00	0.00	0.00	0.00
Al_2O_3	0.10	0.06	0.09	0.09	0.04	0.05	0.07	0.05	0.07	0.06	0.04	0.10	0.08	0.07
Cr_2O_3	0.00	0.00	0.04	0.04	0.03	0.00	0.00	0.00	0.00	0.04	0.03	0.11	0.04	0.03
FeO	9.09	9.03	9.00	9.21	9.06	9.38	9.21	9.19	9.23	8.93	9.31	8.98	9.09	9.11
MgO	50.36	50.43	50.62	50.71	50.69	50.23	50.36	50.09	50.28	50.12	50.37	49.86	49.79	49.78
MnO	0.14	0.07	0.18	0.12	0.11	0.08	0.16	0.12	0.16	0.15	0.14	0.15	0.13	0.13
NiO	0.02	0.09	0.00	0.04	0.00	0.00	0.04	0.02	0.01	0.10	0.06	0.00	0.00	0.01
CaO	0.32	0.32	0.33	0.32	0.34	0.36	0.31	0.34	0.35	0.33	0.35	0.36	0.31	0.40
Na_2O	0.02	0.03	0.00	0.00	0.02	0.00	0.02	0.00	0.05	0.00	0.00	0.00	0.03	0.00
K_2O	0.01	0.01	0.00	0.00	0.00	0.02	0.00	0.02	0.02	0.01	0.00	0.02	0.04	0.00
Total	100.59	100.76	100.67	101.50	100.88	100.71	101.11	99.92	100.88	100.31	101.25	100.30	100.14	100.03
Si	0.98	0.98	0.98	0.98	0.98	0.98	0.99	0.98	0.98	0.99	0.99	0.99	0.99	0.99
Ti	0.00	0.00	0.00	0.00	0.00	0.00	0.00	0.00	0.00	0.00	0.00	0.00	0.00	0.00
Al	0.00	0.00	0.00	0.00	0.00	0.00	0.00	0.00	0.00	0.00	0.00	0.00	0.00	0.00
Cr	0.00	0.00	0.00	0.00	0.00	0.00	0.00	0.00	0.00	0.00	0.00	0.00	0.00	0.00
Fe^{2+}	0.18	0.18	0.18	0.19	0.18	0.19	0.19	0.19	0.19	0.18	0.19	0.18	0.19	0.19
Mg	1.82	1.82	1.83	1.82	1.82	1.81	1.81	1.82	1.81	1.82	1.81	1.81	1.81	1.81
Mn	0.00	0.00	0.00	0.00	0.00	0.00	0.00	0.00	0.00	0.00	0.00	0.00	0.00	0.00
Ni	0.00	0.00	0.00	0.00	0.00	0.00	0.00	0.00	0.00	0.00	0.00	0.00	0.00	0.00
Ca	0.01	0.01	0.01	0.01	0.01	0.01	0.01	0.01	0.01	0.01	0.01	0.01	0.01	0.01
Na	0.00	0.00	0.00	0.00	0.00	0.00	0.00	0.00	0.00	0.00	0.00	0.00	0.00	0.00
K	0.00	0.00	0.00	0.00	0.00	0.00	0.00	0.00	0.00	0.00	0.00	0.00	0.00	0.00
Sum	3.00	3.00	3.00	3.00	3.00	3.00	3.00	3.00	3.00	3.00	3.00	3.00	3.00	3.00
X_{Mg}	0.90	0.90	0.90	0.90	0.90	0.90	0.90	0.90	0.90	0.90	0.90	0.90	0.90	0.90

Sample	MG1	MG1	MG1	MG1	MG1	MG1	MG1	MG1	MG1	MG1	MG5	MG5	MG5	MG5
Run duration	24	24	24	24	24	24	24	24	24	24	24	24	24	24
Melt	AH6	AH6	AH6	AH6	AH6	AH6	AH6	AH6	AH6	AH6	AH6	AH6	AH6	AH6
IMA (wt%)	25	25	25	25	25	25	25	25	25	25	50	50	50	50
T	1300	1300	1300	1300	1300	1300	1300	1300	1300	1300	1300	1300	1300	1300
P	0.5	0.5	0.5	0.5	0.5	0.5	0.5	0.5	0.5	0.5	0.5	0.5	0.5	0.5
Point Analysis	MG1OL111	MG1OL112	MG1OL113	MG1OL114	MG1OL115	MG1OL116	MG1OL117	MG1OL118	MG1OL119	MG1OL120	MG5OL1	MG5OL2	MG5OL3	MG5OL4
Site	rim	rim	rim	rim	rim	rim	rim	rim	rim	rim	core	core	core	core
SiO_2	40.66	40.61	40.28	39.84	40.55	40.77	40.43	40.37	41.00	41.12	40.83	40.96	41.27	40.27
TiO_2	0.04	0.00	0.00	0.02	0.04	0.07	0.00	0.00	0.04	0.00	0.00	0.00	0.00	0.02
Al_2O_3	0.05	0.09	0.07	0.07	0.10	0.05	0.06	0.04	0.06	0.08	0.05	0.06	0.10	0.06
Cr_2O_3	0.03	0.02	0.00	0.07	0.09	0.04	0.00	0.07	0.01	0.06	0.00	0.01	0.02	0.03
FeO	9.09	9.09	9.37	9.38	9.30	9.34	9.32	9.35	9.31	9.04	9.41	8.56	7.95	7.95
MgO	50.10	49.37	50.63	50.54	50.26	50.75	50.54	50.92	49.98	50.29	49.45	50.66	50.64	50.74
MnO	0.13	0.15	0.15	0.13	0.17	0.21	0.11	0.13	0.09	0.12	0.13	0.14	0.10	0.12
NiO	0.00	0.07	0.00	0.00	0.05	0.00	0.03	0.04	0.05	0.00	0.00	0.04	0.00	0.02
CaO	0.33	0.26	0.34	0.34	0.40	0.33	0.33	0.30	0.33	0.34	0.31	0.33	0.37	0.34
Na_2O	0.03	0.07	0.01	0.01	0.00	0.01	0.00	0.04	0.01	0.00	0.04	0.05	0.00	0.02
K_2O	0.02	0.05	0.02	0.02	0.01	0.01	0.01	0.00	0.01	0.00	0.02	0.00	0.02	0.01
Total	100.48	99.77	100.86	100.42	100.96	101.59	100.83	101.26	100.88	101.05	100.24	100.80	100.46	99.59
Si	0.99	0.99	0.97	0.97	0.98	0.98	0.98	0.97	0.99	0.99	1.00	0.99	1.00	0.98
Ti	0.00	0.00	0.00	0.00	0.00	0.00	0.00	0.00	0.00	0.00	0.00	0.00	0.00	0.00
Al	0.00	0.00	0.00	0.00	0.00	0.00	0.00	0.00	0.00	0.00	0.00	0.00	0.00	0.00
Cr	0.00	0.00	0.00	0.00	0.00	0.00	0.00	0.00	0.00	0.00	0.00	0.00	0.00	0.00
Fe^{2+}	0.18	0.19	0.19	0.19	0.19	0.19	0.19	0.19	0.19	0.18	0.19	0.17	0.16	0.16
Mg	1.81	1.80	1.82	1.83	1.81	1.82	1.82	1.83	1.80	1.81	1.80	1.82	1.83	1.84
Mn	0.00	0.00	0.00	0.00	0.00	0.00	0.00	0.00	0.00	0.00	0.00	0.00	0.00	0.00
Ni	0.00	0.00	0.00	0.00	0.00	0.00	0.00	0.00	0.00	0.00	0.00	0.00	0.00	0.00
Ca	0.01	0.01	0.01	0.01	0.01	0.01	0.01	0.01	0.01	0.01	0.01	0.01	0.01	0.01
Na	0.00	0.00	0.00	0.00	0.00	0.00	0.00	0.00	0.00	0.00	0.00	0.00	0.00	0.00
K	0.00	0.00	0.00	0.00	0.00	0.00	0.00	0.00	0.00	0.00	0.00	0.00	0.00	0.00
Sum	3.00	3.00	3.00	3.00	3.00	3.00	3.00	3.00	3.00	3.00	3.00	3.00	3.00	3.00
X_{Mg}	0.90	0.90	0.90	0.90	0.90	0.90	0.90	0.90	0.90	0.90	0.90	0.91	0.91	0.91

Sample	MG5	MG5	MG5	MG5	MG5	MG5	MG5	MG5	MG5	MG5	MG5	MG5	MG5	MG5
Run duration	24	24	24	24	24	24	24	24	24	24	24	24	24	24
Melt	AH6	AH6	AH6	AH6	AH6	AH6	AH6	AH6	AH6	AH6	AH6	AH6	AH6	AH6
IMA (wt%)	50	50	50	50	50	50	50	50	50	50	50	50	50	50
T	1300	1300	1300	1300	1300	1300	1300	1300	1300	1300	1300	1300	1300	1300
P	0.5	0.5	0.5	0.5	0.5	0.5	0.5	0.5	0.5	0.5	0.5	0.5	0.5	0.5
Point Analysis	MG5OL5	MG5OL6	MG5OL7	MG5OL8	MG5OL9	MG5OL10	MG5OL11	MG5OL12	MG5OL13	MG5OL14	MG5OL15	MG5OL16	MG5OL17	MG5OL18
Site	core	core	core	core	core	core	core	core	core	core	core	core	core	core
SiO_2	40.79	40.77	40.86	40.30	41.15	40.78	41.12	40.66	41.20	41.06	41.14	41.02	40.95	40.26
TiO_2	0.00	0.02	0.00	0.00	0.01	0.06	0.01	0.04	0.02	0.00	0.01	0.00	0.04	0.03
Al_2O_3	0.05	0.02	0.11	0.05	0.10	0.10	0.06	0.07	0.07	0.06	0.06	0.04	0.06	0.07
Cr_2O_3	0.02	0.09	0.01	0.00	0.09	0.04	0.03	0.05	0.03	0.03	0.06	0.03	0.00	0.05
FeO	8.13	9.03	9.36	8.27	8.08	8.08	8.59	9.16	8.12	8.71	9.03	8.24	8.66	7.61
MgO	50.87	50.62	50.20	51.16	50.79	50.66	50.49	49.90	50.63	50.64	50.16	51.51	50.64	50.84
MnO	0.17	0.14	0.21	0.14	0.11	0.14	0.17	0.15	0.14	0.18	0.11	0.14	0.15	0.12
NiO	0.08	0.07	0.03	0.00	0.00	0.00	0.00	0.00	0.00	0.01	0.03	0.00	0.02	0.03
CaO	0.36	0.26	0.31	0.31	0.39	0.36	0.35	0.40	0.35	0.36	0.31	0.30	0.34	0.54
Na_2O	0.00	0.00	0.01	0.01	0.00	0.05	0.02	0.06	0.03	0.02	0.01	0.02	0.01	0.01
K_2O	0.01	0.00	0.00	0.01	0.01	0.03	0.00	0.02	0.01	0.01	0.01	0.00	0.01	0.00
Total	100.48	101.03	101.10	100.26	100.71	100.30	100.84	100.50	100.61	101.08	100.92	101.31	100.87	99.56
Si	0.99	0.98	0.99	0.97	0.99	0.99	0.99	0.99	1.00	0.99	0.99	0.98	0.99	0.98
Ti	0.00	0.00	0.00	0.00	0.00	0.00	0.00	0.00	0.00	0.00	0.00	0.00	0.00	0.00
Al	0.00	0.00	0.00	0.00	0.00	0.00	0.00	0.00	0.00	0.00	0.00	0.00	0.00	0.00
Cr	0.00	0.00	0.00	0.00	0.00	0.00	0.00	0.00	0.00	0.00	0.00	0.00	0.00	0.00
Fe^{2+}	0.16	0.18	0.19	0.17	0.16	0.16	0.17	0.19	0.16	0.18	0.18	0.17	0.17	0.15
Mg	1.83	1.82	1.81	1.84	1.83	1.83	1.82	1.81	1.82	1.82	1.81	1.84	1.82	1.84
Mn	0.00	0.00	0.00	0.00	0.00	0.00	0.00	0.00	0.00	0.00	0.00	0.00	0.00	0.00
Ni	0.00	0.00	0.00	0.00	0.00	0.00	0.00	0.00	0.00	0.00	0.00	0.00	0.00	0.00
Ca	0.01	0.01	0.01	0.01	0.01	0.01	0.01	0.01	0.01	0.01	0.01	0.01	0.01	0.01
Na	0.00	0.00	0.00	0.00	0.00	0.00	0.00	0.00	0.00	0.00	0.00	0.00	0.00	0.00
K	0.00	0.00	0.00	0.00	0.00	0.00	0.00	0.00	0.00	0.00	0.00	0.00	0.00	0.00
Sum	3.00	3.00	3.00	3.00	3.00	3.00	3.00	3.00	3.00	3.00	3.00	3.00	3.00	3.00
X_{Mg}	0.91	0.90	0.90	0.91	0.91	0.91	0.91	0.90	0.91	0.90	0.90	0.91	0.91	0.91

Sample	MG5	MG5	MG5	MG5	MG5	MG5	MG5	MG5	MG5	MG5	MG5	MG5	MG5	MG5
Run duration	24	24	24	24	24	24	24	24	24	24	24	24	24	24
Melt	AH6	AH6	AH6	AH6	AH6	AH6	AH6	AH6	AH6	AH6	AH6	AH6	AH6	AH6
Initial melt amo	50	50	50	50	50	50	50	50	50	50	50	50	50	50
T	1300	1300	1300	1300	1300	1300	1300	1300	1300	1300	1300	1300	1300	1300
P	0.5	0.5	0.5	0.5	0.5	0.5	0.5	0.5	0.5	0.5	0.5	0.5	0.5	0.5
Point Analysis	MG5OL19	MG5OL20	MG5OL21	MG5OL22	MG5OL23	MG5OL24	MG5OL25	MG5OL26	MG5OL27	MG5OL28	MG5OL29	MG5OL30	MG5OL31	MG5OL32
Site	core	core	core	core	core	core	core	core	core	rim	rim	rim	rim	rim
SiO_2	41.11	40.88	40.92	41.14	40.91	41.21	40.79	40.38	41.37	41.13	41.29	41.21	40.74	41.08
TiO_2	0.02	0.03	0.00	0.03	0.05	0.02	0.02	0.04	0.01	0.01	0.00	0.04	0.09	0.05
Al_2O_3	0.09	0.05	0.10	0.08	0.09	0.08	0.08	0.07	0.08	0.09	0.08	0.06	0.07	0.07
Cr_2O_3	0.03	0.03	0.05	0.08	0.00	0.06	0.04	0.01	0.00	0.09	0.04	0.06	0.06	0.10
FeO	7.85	8.99	8.72	7.87	8.86	8.49	7.71	8.67	7.99	7.93	8.29	7.89	7.81	7.90
MgO	51.49	50.11	50.65	51.57	50.51	51.53	51.94	50.84	51.87	50.78	50.61	50.90	50.98	51.28
MnO	0.08	0.08	0.17	0.15	0.14	0.11	0.11	0.11	0.13	0.14	0.16	0.14	0.10	0.13
NiO	0.00	0.05	0.04	0.03	0.05	0.01	0.00	0.01	0.01	0.01	0.02	0.09	0.00	0.00
CaO	0.37	0.27	0.30	0.33	0.32	0.32	0.34	0.34	0.35	0.37	0.35	0.37	0.36	0.35
Na_2O	0.00	0.00	0.00	0.00	0.00	0.01	0.00	0.00	0.01	0.02	0.03	0.01	0.00	0.00
K_2O	0.00	0.00	0.01	0.00	0.00	0.02	0.00	0.00	0.00	0.00	0.01	0.01	0.02	0.00
Total	101.05	100.49	100.95	101.29	100.92	101.86	101.02	100.47	101.82	100.57	100.88	100.78	100.22	100.95
Si	0.99	0.99	0.99	0.99	0.99	0.98	0.98	0.98	0.99	0.99	1.00	0.99	0.99	0.99
Ti	0.00	0.00	0.00	0.00	0.00	0.00	0.00	0.00	0.00	0.00	0.00	0.00	0.00	0.00
Al	0.00	0.00	0.00	0.00	0.00	0.00	0.00	0.00	0.00	0.00	0.00	0.00	0.00	0.00
Cr	0.00	0.00	0.00	0.00	0.00	0.00	0.00	0.00	0.00	0.00	0.00	0.00	0.00	0.00
Fe^{2+}	0.16	0.18	0.18	0.16	0.18	0.17	0.15	0.18	0.16	0.16	0.17	0.16	0.16	0.16
Mg	1.84	1.81	1.82	1.84	1.82	1.83	1.85	1.83	1.84	1.83	1.82	1.83	1.84	1.84
Mn	0.00	0.00	0.00	0.00	0.00	0.00	0.00	0.00	0.00	0.00	0.00	0.00	0.00	0.00
Ni	0.00	0.00	0.00	0.00	0.00	0.00	0.00	0.00	0.00	0.00	0.00	0.00	0.00	0.00
Ca	0.01	0.01	0.01	0.01	0.01	0.01	0.01	0.01	0.01	0.01	0.01	0.01	0.01	0.01
Na	0.00	0.00	0.00	0.00	0.00	0.00	0.00	0.00	0.00	0.00	0.00	0.00	0.00	0.00
K	0.00	0.00	0.00	0.00	0.00	0.00	0.00	0.00	0.00	0.00	0.00	0.00	0.00	0.00
Sum	3.00	3.00	3.00	3.00	3.00	3.00	3.00	3.00	3.00	3.00	3.00	3.00	3.00	3.00
X_{Mg}	0.91	0.90	0.91	0.91	0.90	0.91	0.92	0.91	0.91	0.91	0.91	0.91	0.91	0.91

Sample	MG5	MG5	MG5	MG5	MG5	MG5	MG5	MG5	MG5	MG5	MG5	MG5	MG5	MG5
Run duration	24	24	24	24	24	24	24	24	24	24	24	24	24	24
Melt	AH6	AH6	AH6	AH6	AH6	AH6	AH6	AH6	AH6	AH6	AH6	AH6	AH6	AH6
IMA (wt%)	50	50	50	50	50	50	50	50	50	50	50	50	50	50
T	1300	1300	1300	1300	1300	1300	1300	1300	1300	1300	1300	1300	1300	1300
P	0.5	0.5	0.5	0.5	0.5	0.5	0.5	0.5	0.5	0.5	0.5	0.5	0.5	0.5
Point Analysis	MG5OL33	MG5OL34	MG5OL35	MG5OL36	MG5OL37	MG5OL38	MG5OL39	MG5OL40	MG5OL41	MG5OL42	MG5OL43	MG5OL44	MG5OL45	MG5OL46
Site	rim	rim	rim	rim	rim	rim	rim	rim	rim	rim	rim	rim	rim	rim
SiO_2	41.26	40.60	41.09	41.39	41.33	40.98	41.09	40.84	41.04	41.10	41.07	41.01	41.29	41.26
TiO_2	0.00	0.03	0.05	0.02	0.06	0.02	0.01	0.00	0.01	0.00	0.01	0.00	0.04	0.02
Al_2O_3	0.09	0.07	0.07	0.20	0.06	0.05	0.04	0.08	0.07	0.08	0.04	0.10	0.07	0.06
Cr_2O_3	0.08	0.10	0.00	0.03	0.03	0.05	0.08	0.02	0.01	0.01	0.02	0.05	0.06	0.07
FeO	8.05	7.84	7.77	7.64	7.67	8.50	7.57	8.61	8.04	8.41	8.41	7.67	7.89	8.19
MgO	50.48	51.26	51.32	50.97	51.09	51.36	51.78	51.05	51.86	51.00	51.63	51.83	52.24	51.44
MnO	0.19	0.13	0.09	0.14	0.14	0.13	0.12	0.15	0.17	0.09	0.14	0.07	0.09	0.15
NiO	0.00	0.00	0.00	0.00	0.00	0.00	0.00	0.00	0.04	0.05	0.00	0.03	0.01	0.04
CaO	0.34	0.38	0.37	0.43	0.38	0.34	0.33	0.33	0.35	0.34	0.36	0.35	0.31	0.32
Na_2O	0.05	0.01	0.00	0.06	0.03	0.00	0.00	0.02	0.00	0.00	0.03	0.00	0.02	0.00
K_2O	0.00	0.00	0.00	0.01	0.02	0.00	0.01	0.00	0.01	0.00	0.00	0.00	0.00	0.00
Total	100.52	100.42	100.75	100.89	100.81	101.43	101.03	101.10	101.59	101.09	101.72	101.12	102.03	101.55
Si	1.00	0.98	0.99	1.00	0.99	0.98	0.98	0.98	0.98	0.99	0.98	0.98	0.98	0.99
Ti	0.00	0.00	0.00	0.00	0.00	0.00	0.00	0.00	0.00	0.00	0.00	0.00	0.00	0.00
Al	0.00	0.00	0.00	0.01	0.00	0.00	0.00	0.00	0.00	0.00	0.00	0.00	0.00	0.00
Cr	0.00	0.00	0.00	0.00	0.00	0.00	0.00	0.00	0.00	0.00	0.00	0.00	0.00	0.00
Fe^{2+}	0.16	0.16	0.16	0.15	0.15	0.17	0.15	0.17	0.16	0.17	0.17	0.15	0.16	0.16
Mg	1.82	1.84	1.84	1.83	1.83	1.83	1.85	1.83	1.84	1.83	1.84	1.85	1.85	1.83
Mn	0.00	0.00	0.00	0.00	0.00	0.00	0.00	0.00	0.00	0.00	0.00	0.00	0.00	0.00
Ni	0.00	0.00	0.00	0.00	0.00	0.00	0.00	0.00	0.00	0.00	0.00	0.00	0.00	0.00
Ca	0.01	0.01	0.01	0.01	0.01	0.01	0.01	0.01	0.01	0.01	0.01	0.01	0.01	0.01
Na	0.00	0.00	0.00	0.00	0.00	0.00	0.00	0.00	0.00	0.00	0.00	0.00	0.00	0.00
K	0.00	0.00	0.00	0.00	0.00	0.00	0.00	0.00	0.00	0.00	0.00	0.00	0.00	0.00
Sum	3.00	3.00	3.00	3.00	3.00	3.00	3.00	3.00	3.00	3.00	3.00	3.00	3.00	3.00
X_{Mg}	0.91	0.91	0.92	0.91	0.91	0.91	0.92	0.91	0.91	0.91	0.91	0.92	0.92	0.91

Sample	MG5
Run duration	24
Melt	AH6
IMA (wt%)	50
T	1300
P	0.5
Point Analysis	MG5OL47
Site	rim
SiO_2	41.54
TiO_2	0.03
Al_2O_3	0.09
Cr_2O_3	0.02
FeO	7.84
MgO	51.71
MnO	0.15
NiO	0.00
CaO	0.35
Na_2O	0.00
K_2O	0.00
Total	101.74
Si	0.99
Ti	0.00
Al	0.00
Cr	0.00
Fe^{2+}	0.16
Mg	1.84
Mn	0.00
Ni	0.00
Ca	0.01
Na	0.00
K	0.00
Sum	3.00
X_{Mg}	0.91

Table 7-3 *Major element composition of olivine from step-cooled experiments performed at 0.5 GPa, from 1300 down to 1100°C.*

Sample	MG15	MG15	MG15	MG15	MG15	MG15	MG15	MG15	MG15	MG15	MG15	MG15	MG15	MG15
Run duration	72	72	72	72	72	72	72	72	72	72	72	72	72	72
Melt	AH6	AH6	AH6	AH6	AH6	AH6	AH6	AH6	AH6	AH6	AH6	AH6	AH6	AH6
IMA (wt%)[a]	10	10	10	10	10	10	10	10	10	10	10	10	10	10
T[b]	$1300_{(i)}$-$1100_{(f)}$	$1300_{(i)}$-$1100_{(f)}$	$1300_{(i)}$-$1100_{(f)}$	$1300_{(i)}$-$1100_{(f}$	$1300_{(i)}$-$1100_{(f)}$	$1300_{(i)}$-$1100_{(f)}$	$1300_{(i)}$-$1100_{(f)}$	$1300_{(i)}$-$1100_{(f)}$	$1300_{(i)}$-$1100_{(f)}$	$1300_{(i)}$-$1100_{(f)}$	$1300_{(i)}$-$1100_{(f)}$	$1300_{(i)}$-$1100_{(f)}$	$1300_{(i)}$-$1100_{(f)}$	$1300_{(i)}$-$1100_{(f)}$
P[c]	0.5	0.5	0.5	0.5	0.5	0.5	0.5	0.5	0.5	0.5	0.5	0.5	0.5	0.5
Point Analysis	MG15OL1	MG15OL2	MG15OL3	MG15OL4	MG15OL5	MG15OL6	MG15OL7	MG15OL8	MG15OL9	MG15OL10	MG15OL11	MG15OL12	MG15OL13	MG15OL14
Site	core	rim	core	core	rim	core	core	rim	core	core	rim	core	core	rim
SiO_2	40.38	40.82	40.77	40.97	43.54	40.30	40.87	40.51	40.63	41.19	41.30	41.39	41.21	41.11
TiO_2	0.00	0.00	0.02	0.00	0.02	0.00	0.00	0.00	0.00	0.00	0.09	0.00	0.02	0.00
Al_2O_3	0.04	0.07	0.04	0.03	0.21	0.02	0.08	0.01	0.05	0.03	0.03	0.08	0.05	0.00
Cr_2O_3	0.08	0.06	0.04	0.00	0.00	0.04	0.05	0.03	0.06	0.05	0.06	0.02	0.01	0.03
FeO	9.75	9.64	9.72	9.34	9.35	9.73	9.67	9.64	10.15	10.14	10.17	9.40	9.73	9.64
MgO	49.56	49.52	49.49	49.77	47.34	49.88	49.74	49.62	49.09	49.81	49.91	49.77	49.54	49.63
MnO	0.12	0.13	0.16	0.17	0.11	0.10	0.15	0.13	0.18	0.13	0.13	0.16	0.18	0.14
NiO	0.16	0.12	0.10	0.09	0.08	0.06	0.18	0.15	0.27	0.24	0.27	0.09	0.20	0.20
CaO	0.21	0.23	0.21	0.23	0.26	0.22	0.21	0.22	0.21	0.23	0.18	0.23	0.20	0.22
Na_2O	0.00	0.01	0.00	0.00	0.00	0.00	0.03	0.02	0.01	0.00	0.03	0.02	0.06	0.02
K_2O	0.00	0.00	0.00	0.01	0.00	0.01	0.00	0.01	0.00	0.00	0.01	0.00	0.01	0.01
Total	100.30	100.60	100.55	100.61	100.91	100.36	100.98	100.34	100.65	101.82	102.18	101.16	101.21	101.00
Si	0.99	0.99	0.99	1.00	1.07	0.98	0.99	0.99	0.99	0.99	0.99	1.00	1.00	1.00
Ti	0.00	0.00	0.00	0.00	0.00	0.00	0.00	0.00	0.00	0.00	0.00	0.00	0.00	0.00
Al	0.00	0.00	0.00	0.00	0.01	0.00	0.00	0.00	0.00	0.00	0.00	0.00	0.00	0.00
Cr	0.00	0.00	0.00	0.00	0.00	0.00	0.00	0.00	0.00	0.00	0.00	0.00	0.00	0.00
Fe^{2+}	0.20	0.20	0.20	0.19	0.19	0.20	0.20	0.20	0.21	0.20	0.20	0.19	0.20	0.20
Mg	1.80	1.80	1.80	1.80	1.73	1.81	1.80	1.80	1.78	1.79	1.79	1.79	1.79	1.79
Mn	0.00	0.00	0.00	0.00	0.00	0.00	0.00	0.00	0.00	0.00	0.00	0.00	0.00	0.00
Ni	0.00	0.00	0.00	0.00	0.00	0.00	0.00	0.00	0.01	0.00	0.01	0.00	0.00	0.00
Ca	0.01	0.01	0.01	0.01	0.01	0.01	0.01	0.01	0.01	0.01	0.00	0.01	0.01	0.01
Na	0.00	0.00	0.00	0.00	0.00	0.00	0.00	0.00	0.00	0.00	0.00	0.00	0.00	0.00
K	0.00	0.00	0.00	0.00	0.00	0.00	0.00	0.00	0.00	0.00	0.00	0.00	0.00	0.00
Sum	3.00	3.00	3.00	3.00	3.00	3.00	3.00	3.00	3.00	3.00	3.00	3.00	3.00	3.00
X_{Mg}[d]	0.89	0.90	0.90	0.90	0.89	0.90	0.89	0.90	0.89	0.89	0.89	0.90	0.89	0.90

Cations are calculated with the Program NORM (version 2019) edited by Ulmer, P., and Poli, S. [a] Initial melt amount. [b] Temperature. [c] Pressure. [d] X_{Mg} = Mg/(Mg+Fe).

Sample	MG15	MG15	MG15	MG15	MG15	MG15	MG15	MG15	MG15	MG15	MG15	MG15	MG15	MG15
Run duration	72	72	72	72	72	72	72	72	72	72	72	72	72	72
Melt	AH6	AH6	AH6	AH6	AH6	AH6	AH6	AH6	AH6	AH6	AH6	AH6	AH6	AH6
IMA (wt%)	10	10	10	10	10	10	10	10	10	10	10	10	10	10
T	$1300_{(i)}$-$1100_{(f)}$	$1300_{(i)}$-$1100_{(f)}$	$1300_{(i)}$-$1100_{(f)}$	$1300_{(i)}$-$1100_{(f}$	$1300_{(i)}$-$1100_{(f)}$	$1300_{(i)}$-$1100_{(f)}$	$1300_{(i)}$-$1100_{(f)}$	$1300_{(i)}$-$1100_{(f)}$	$1300_{(i)}$-$1100_{(f)}$	$1300_{(i)}$-$1100_{(f)}$	$1300_{(i)}$-$1100_{(f)}$	$1300_{(i)}$-$1100_{(f)}$	$1300_{(i)}$-$1100_{(f)}$	$1300_{(i)}$-$1100_{(f)}$
P	0.5	0.5	0.5	0.5	0.5	0.5	0.5	0.5	0.5	0.5	0.5	0.5	0.5	0.5
Point Analysis	MG15OL15	MG15OL16	MG15OL17	MG15OL18	MG15OL19	MG15OL20	MG15OL21	MG15OL22	MG15OL23	MG15OL24	MG15OL25	MG15OL26	MG15OL27	MG15OL28
Site	core	rim	core	rim	core	rim	core	rim	core	rim	core	core	rim	core
SiO_2	41.17	41.45	40.93	41.40	41.18	41.32	41.63	38.11	41.26	41.36	41.15	41.03	40.81	41.20
TiO_2	0.02	0.03	0.03	0.02	0.00	0.04	0.00	0.00	0.05	0.03	0.02	0.00	0.01	0.02
Al_2O_3	0.05	0.04	0.03	0.04	0.06	0.05	0.04	0.24	0.05	0.05	0.05	0.04	0.07	0.06
Cr_2O_3	0.00	0.00	0.01	0.05	0.02	0.04	0.09	0.04	0.01	0.08	0.00	0.05	0.03	0.03
FeO	8.93	8.68	9.30	8.78	8.78	8.78	9.18	8.70	9.19	8.80	8.89	8.93	9.13	8.53
MgO	50.63	50.85	50.49	50.94	50.58	50.97	50.96	53.79	50.51	50.65	50.76	50.69	50.15	50.84
MnO	0.15	0.12	0.17	0.13	0.12	0.16	0.13	0.16	0.16	0.18	0.13	0.18	0.17	0.16
NiO	0.09	0.01	0.05	0.09	0.04	0.05	0.04	0.07	0.01	0.00	0.04	0.00	0.03	0.05
CaO	0.24	0.21	0.22	0.20	0.23	0.20	0.24	0.24	0.24	0.21	0.22	0.23	0.21	0.24
Na_2O	0.00	0.02	0.00	0.01	0.01	0.02	0.00	0.00	0.04	0.02	0.02	0.00	0.00	0.00
K_2O	0.01	0.01	0.00	0.00	0.01	0.00	0.00	0.00	0.00	0.01	0.00	0.00	0.00	0.00
Total	101.29	101.42	101.23	101.66	101.03	101.63	102.31	101.35	101.52	101.39	101.28	101.15	100.61	101.13
Si	0.99	1.00	0.99	0.99	0.99	0.99	0.99	0.91	0.99	0.99	0.99	0.99	0.99	0.99
Ti	0.00	0.00	0.00	0.00	0.00	0.00	0.00	0.00	0.00	0.00	0.00	0.00	0.00	0.00
Al	0.00	0.00	0.00	0.00	0.00	0.00	0.00	0.01	0.00	0.00	0.00	0.00	0.00	0.00
Cr	0.00	0.00	0.00	0.00	0.00	0.00	0.00	0.00	0.00	0.00	0.00	0.00	0.00	0.00
Fe^{2+}	0.18	0.17	0.19	0.18	0.18	0.18	0.18	0.17	0.18	0.18	0.18	0.18	0.19	0.17
Mg	1.82	1.82	1.81	1.82	1.82	1.82	1.81	1.90	1.81	1.82	1.82	1.82	1.81	1.82
Mn	0.00	0.00	0.00	0.00	0.00	0.00	0.00	0.00	0.00	0.00	0.00	0.00	0.00	0.00
Ni	0.00	0.00	0.00	0.00	0.00	0.00	0.00	0.00	0.00	0.00	0.00	0.00	0.00	0.00
Ca	0.01	0.01	0.01	0.01	0.01	0.01	0.01	0.01	0.01	0.01	0.01	0.01	0.01	0.01
Na	0.00	0.00	0.00	0.00	0.00	0.00	0.00	0.00	0.00	0.00	0.00	0.00	0.00	0.00
K	0.00	0.00	0.00	0.00	0.00	0.00	0.00	0.00	0.00	0.00	0.00	0.00	0.00	0.00
Sum	3.00	3.00	3.00	3.00	3.00	3.00	3.00	3.00	3.00	3.00	3.00	3.00	3.00	3.00
X_{Mg}	0.90	0.91	0.90	0.91	0.91	0.91	0.90	0.91	0.90	0.91	0.91	0.91	0.90	0.91

Sample	MG15	MG15	MG15	MG15	MG15	MG15	MG15	MG15	MG15	MG15	MG15	MG15	MG15	MG15
Run duration	72	72	72	72	72	72	72	72	72	72	72	72	72	72
Melt	AH6	AH6	AH6	AH6	AH6	AH6	AH6	AH6	AH6	AH6	AH6	AH6	AH6	AH6
IMA (wt%)	10	10	10	10	10	10	10	10	10	10	10	10	10	10
T	$1300_{(i)}$-$1100_{(f)}$	$1300_{(i)}$-$1100_{(f)}$	$1300_{(i)}$-$1100_{(f)}$	$1300_{(i)}$-$1100_{(f}$	$1300_{(i)}$-$1100_{(f)}$	$1300_{(i)}$-$1100_{(f)}$	$1300_{(i)}$-$1100_{(f)}$	$1300_{(i)}$-$1100_{(f)}$	$1300_{(i)}$-$1100_{(f)}$	$1300_{(i)}$-$1100_{(f)}$	$1300_{(i)}$-$1100_{(f)}$	$1300_{(i)}$-$1100_{(f)}$	$1300_{(i)}$-$1100_{(f)}$	$1300_{(i)}$-$1100_{(f)}$
P	0.5	0.5	0.5	0.5	0.5	0.5	0.5	0.5	0.5	0.5	0.5	0.5	0.5	0.5
Point Analysis	MG15OL29	MG15OL30	MG15OL31	MG15OL32	MG15OL33	MG15OL34	MG15OL35	MG15OL36	MG15OL37	MG15OL38	MG15OL39	MG15OL40	MG15OL41	MG15OL42
Site	core	rim	core	core	core	rim	core	rim	core	core	core	rim	core	core
SiO_2	41.21	41.66	41.33	41.39	40.80	41.13	41.03	41.18	41.13	41.26	41.12	41.23	40.89	41.11
TiO_2	0.04	0.00	0.01	0.04	0.00	0.02	0.04	0.02	0.00	0.01	0.00	0.00	0.06	0.00
Al_2O_3	0.04	0.05	0.03	0.04	0.04	0.06	0.05	0.06	0.07	0.06	0.05	0.06	0.04	0.06
Cr_2O_3	0.03	0.04	0.04	0.03	0.00	0.00	0.00	0.02	0.02	0.00	0.00	0.04	0.02	0.03
FeO	8.64	8.71	8.91	8.79	8.88	8.56	9.20	8.70	8.63	8.53	8.31	8.44	8.58	8.09
MgO	51.10	51.43	50.47	50.85	50.38	50.74	50.48	51.01	51.02	51.22	50.76	51.26	51.03	51.24
MnO	0.18	0.15	0.10	0.20	0.09	0.13	0.15	0.17	0.13	0.16	0.15	0.15	0.17	0.09
NiO	0.05	0.06	0.02	0.09	0.00	0.01	0.10	0.00	0.07	0.03	0.00	0.08	0.00	0.08
CaO	0.19	0.23	0.22	0.20	0.25	0.26	0.24	0.22	0.22	0.22	0.26	0.22	0.23	0.23
Na_2O	0.01	0.00	0.00	0.03	0.03	0.02	0.00	0.00	0.00	0.00	0.00	0.00	0.00	0.04
K_2O	0.01	0.00	0.00	0.00	0.01	0.00	0.01	0.00	0.01	0.00	0.01	0.00	0.00	0.02
Total	101.50	102.33	101.13	101.66	100.48	100.93	101.30	101.38	101.30	101.49	100.66	101.48	101.02	100.99
Si	0.99	0.99	1.00	0.99	0.99	0.99	0.99	0.99	0.99	0.99	0.99	0.99	0.98	0.99
Ti	0.00	0.00	0.00	0.00	0.00	0.00	0.00	0.00	0.00	0.00	0.00	0.00	0.00	0.00
Al	0.00	0.00	0.00	0.00	0.00	0.00	0.00	0.00	0.00	0.00	0.00	0.00	0.00	0.00
Cr	0.00	0.00	0.00	0.00	0.00	0.00	0.00	0.00	0.00	0.00	0.00	0.00	0.00	0.00
Fe^{2+}	0.17	0.17	0.18	0.18	0.18	0.17	0.19	0.17	0.17	0.17	0.17	0.17	0.17	0.16
Mg	1.83	1.82	1.81	1.82	1.82	1.82	1.81	1.83	1.83	1.83	1.83	1.83	1.83	1.84
Mn	0.00	0.00	0.00	0.00	0.00	0.00	0.00	0.00	0.00	0.00	0.00	0.00	0.00	0.00
Ni	0.00	0.00	0.00	0.00	0.00	0.00	0.00	0.00	0.00	0.00	0.00	0.00	0.00	0.00
Ca	0.00	0.01	0.01	0.01	0.01	0.01	0.01	0.01	0.01	0.01	0.01	0.01	0.01	0.01
Na	0.00	0.00	0.00	0.00	0.00	0.00	0.00	0.00	0.00	0.00	0.00	0.00	0.00	0.00
K	0.00	0.00	0.00	0.00	0.00	0.00	0.00	0.00	0.00	0.00	0.00	0.00	0.00	0.00
Sum	3.00	3.00	3.00	3.00	3.00	3.00	3.00	3.00	3.00	3.00	3.00	3.00	3.00	3.00
X_{Mg}	0.91	0.91	0.91	0.91	0.91	0.91	0.90	0.91	0.91	0.91	0.91	0.91	0.91	0.91

Sample	MG15	MG15	MG15	MG15	MG15	MG15	MG15	MG15	MG15	MG15	MG15	MG15	MG15	MG15
Run duration	72	72	72	72	72	72	72	72	72	72	72	72	72	72
Melt	AH6	AH6	AH6	AH6	AH6	AH6	AH6	AH6	AH6	AH6	AH6	AH6	AH6	AH6
IMA (wt%)	10	10	10	10	10	10	10	10	10	10	10	10	10	10
T	$1300_{(i)}$-$1100_{(f)}$	$1300_{(i)}$-$1100_{(f)}$	$1300_{(i)}$-$1100_{(f)}$	$1300_{(i)}$-$1100_{(f}$	$1300_{(i)}$-$1100_{(f)}$	$1300_{(i)}$-$1100_{(f)}$	$1300_{(i)}$-$1100_{(f)}$	$1300_{(i)}$-$1100_{(f)}$	$1300_{(i)}$-$1100_{(f)}$	$1300_{(i)}$-$1100_{(f)}$	$1300_{(i)}$-$1100_{(f)}$	$1300_{(i)}$-$1100_{(f)}$	$1300_{(i)}$-$1100_{(f)}$	$1300_{(i)}$-$1100_{(f)}$
P	0.5	0.5	0.5	0.5	0.5	0.5	0.5	0.5	0.5	0.5	0.5	0.5	0.5	0.5
Point Analysis	MG15OL43	MG15OL44	MG15OL45	MG15OL46	MG15OL47	MG15OL48	MG15OL49	MG15OL50	MG15OL51	MG15OL52	MG15OL53	MG15OL54	MG15OL55	MG15OL56
Site	core	core	core	core	core	core	core	core	rim	core	rim	core	rim	core
SiO_2	41.37	41.61	41.61	41.40	41.26	41.57	41.68	41.93	41.68	41.55	41.91	42.00	41.73	41.47
TiO_2	0.03	0.04	0.00	0.00	0.00	0.00	0.03	0.00	0.01	0.00	0.00	0.00	0.00	0.00
Al_2O_3	0.08	0.03	0.04	0.04	0.06	0.04	0.02	0.04	0.06	0.05	0.07	0.03	0.05	0.05
Cr_2O_3	0.04	0.07	0.02	0.09	0.00	0.03	0.01	0.05	0.00	0.02	0.02	0.00	0.00	0.00
FeO	9.02	8.46	8.62	8.17	8.27	8.11	5.81	6.68	6.67	6.44	6.17	5.79	5.77	5.79
MgO	51.42	51.34	51.20	51.18	50.86	51.29	52.01	52.29	52.69	51.81	52.82	52.85	52.91	52.64
MnO	0.15	0.13	0.13	0.19	0.13	0.16	0.12	0.17	0.17	0.14	0.10	0.16	0.10	0.15
NiO	0.11	0.00	0.06	0.03	0.03	0.00	0.00	0.00	0.03	0.04	0.00	0.05	0.01	0.01
CaO	0.25	0.21	0.21	0.23	0.24	0.23	0.22	0.23	0.23	0.23	0.23	0.23	0.22	0.21
Na_2O	0.03	0.00	0.00	0.00	0.00	0.00	0.07	0.01	0.00	0.00	0.00	0.02	0.01	0.00
K_2O	0.00	0.00	0.01	0.02	0.00	0.00	0.00	0.00	0.01	0.00	0.00	0.00	0.00	0.00
Total	102.50	101.89	101.90	101.35	100.85	101.43	99.97	101.40	101.55	100.28	101.32	101.13	100.80	100.32
Si	0.98	0.99	0.99	0.99	0.99	1.00	1.00	1.00	0.99	1.00	1.00	1.00	1.00	0.99
Ti	0.00	0.00	0.00	0.00	0.00	0.00	0.00	0.00	0.00	0.00	0.00	0.00	0.00	0.00
Al	0.00	0.00	0.00	0.00	0.00	0.00	0.00	0.00	0.00	0.00	0.00	0.00	0.00	0.00
Cr	0.00	0.00	0.00	0.00	0.00	0.00	0.00	0.00	0.00	0.00	0.00	0.00	0.00	0.00
Fe^{2+}	0.18	0.17	0.17	0.16	0.17	0.16	0.12	0.13	0.13	0.13	0.12	0.12	0.12	0.12
Mg	1.82	1.83	1.82	1.83	1.83	1.83	1.87	1.86	1.87	1.86	1.87	1.87	1.88	1.88
Mn	0.00	0.00	0.00	0.00	0.00	0.00	0.00	0.00	0.00	0.00	0.00	0.00	0.00	0.00
Ni	0.00	0.00	0.00	0.00	0.00	0.00	0.00	0.00	0.00	0.00	0.00	0.00	0.00	0.00
Ca	0.01	0.01	0.01	0.01	0.01	0.01	0.01	0.01	0.01	0.01	0.01	0.01	0.01	0.01
Na	0.00	0.00	0.00	0.00	0.00	0.00	0.00	0.00	0.00	0.00	0.00	0.00	0.00	0.00
K	0.00	0.00	0.00	0.00	0.00	0.00	0.00	0.00	0.00	0.00	0.00	0.00	0.00	0.00
Sum	3.00	3.00	3.00	3.00	3.00	3.00	3.00	3.00	3.00	3.00	3.00	3.00	3.00	3.00
X_{Mg}	0.90	0.91	0.91	0.91	0.91	0.91	0.94	0.93	0.93	0.93	0.93	0.94	0.94	0.94

Sample	MG15	MG15	MG15	MG15	MG15	MG15	MG15	MG15	MG15	MG15	MG15	MG15	MG15	MG15
Run duration	72	72	72	72	72	72	72	72	72	72	72	72	72	72
Melt	AH6	AH6	AH6	AH6	AH6	AH6	AH6	AH6	AH6	AH6	AH6	AH6	AH6	AH6
IMA (wt%)	10	10	10	10	10	10	10	10	10	10	10	10	10	10
T	$1300_{(i)}$-$1100_{(f)}$	$1300_{(i)}$-$1100_{(f)}$	$1300_{(i)}$-$1100_{(f)}$	$1300_{(i)}$-$1100_{(f}$	$1300_{(i)}$-$1100_{(f)}$	$1300_{(i)}$-$1100_{(f)}$	$1300_{(i)}$-$1100_{(f)}$	$1300_{(i)}$-$1100_{(f)}$	$1300_{(i)}$-$1100_{(f)}$	$1300_{(i)}$-$1100_{(f)}$	$1300_{(i)}$-$1100_{(f)}$	$1300_{(i)}$-$1100_{(f)}$	$1300_{(i)}$-$1100_{(f)}$	$1300_{(i)}$-$1100_{(f)}$
P	0.5	0.5	0.5	0.5	0.5	0.5	0.5	0.5	0.5	0.5	0.5	0.5	0.5	0.5
Point Analysis	MG15OL57	MG15OL58	MG15OL59	MG15OL60	MG15OL61	MG15OL62	MG15OL63	MG15OL64	MG15OL65	MG15OL66	MG15OL67	MG15OL68	MG15OL69	MG15OL70
Site	core	rim	core	core	rim	core	rim	core	core	core	core	rim	rim	core
SiO_2	41.74	41.63	42.24	41.91	41.96	41.70	41.97	41.91	41.94	41.53	41.35	41.55	41.99	41.61
TiO_2	0.04	0.00	0.01	0.01	0.04	0.02	0.00	0.01	0.01	0.01	0.04	0.00	0.03	0.00
Al_2O_3	0.05	0.02	0.05	0.05	0.05	0.05	0.05	0.07	0.06	0.05	0.03	0.02	0.09	0.08
Cr_2O_3	0.03	0.06	0.02	0.00	0.00	0.00	0.06	0.00	0.05	0.02	0.03	0.00	0.04	0.00
FeO	5.93	5.75	5.62	5.91	5.56	6.76	6.14	5.38	5.97	5.81	6.40	5.98	5.86	8.34
MgO	52.76	53.34	53.33	52.65	53.34	52.26	52.51	53.58	52.76	53.24	52.71	53.30	52.93	51.03
MnO	0.12	0.15	0.14	0.15	0.10	0.15	0.17	0.13	0.16	0.14	0.13	0.12	0.13	0.12
NiO	0.01	0.00	0.01	0.01	0.04	0.09	0.16	0.00	0.07	0.02	0.00	0.04	0.01	0.12
CaO	0.22	0.23	0.21	0.23	0.23	0.22	0.22	0.25	0.20	0.19	0.25	0.23	0.26	0.24
Na_2O	0.01	0.00	0.02	0.00	0.00	0.04	0.00	0.02	0.00	0.03	0.00	0.00	0.00	0.00
K_2O	0.00	0.01	0.00	0.00	0.00	0.00	0.00	0.00	0.00	0.00	0.00	0.00	0.00	0.00
Total	100.91	101.19	101.65	100.92	101.32	101.29	101.28	101.35	101.22	101.04	100.94	101.24	101.34	101.54
Si	1.00	0.99	1.00	1.00	0.99	0.99	1.00	0.99	1.00	0.99	0.99	0.99	1.00	1.00
Ti	0.00	0.00	0.00	0.00	0.00	0.00	0.00	0.00	0.00	0.00	0.00	0.00	0.00	0.00
Al	0.00	0.00	0.00	0.00	0.00	0.00	0.00	0.00	0.00	0.00	0.00	0.00	0.00	0.00
Cr	0.00	0.00	0.00	0.00	0.00	0.00	0.00	0.00	0.00	0.00	0.00	0.00	0.00	0.00
Fe^{2+}	0.12	0.11	0.11	0.12	0.11	0.13	0.12	0.11	0.12	0.12	0.13	0.12	0.12	0.17
Mg	1.88	1.89	1.88	1.87	1.88	1.86	1.86	1.89	1.87	1.89	1.87	1.89	1.87	1.82
Mn	0.00	0.00	0.00	0.00	0.00	0.00	0.00	0.00	0.00	0.00	0.00	0.00	0.00	0.00
Ni	0.00	0.00	0.00	0.00	0.00	0.00	0.00	0.00	0.00	0.00	0.00	0.00	0.00	0.00
Ca	0.01	0.01	0.01	0.01	0.01	0.01	0.01	0.01	0.01	0.00	0.01	0.01	0.01	0.01
Na	0.00	0.00	0.00	0.00	0.00	0.00	0.00	0.00	0.00	0.00	0.00	0.00	0.00	0.00
K	0.00	0.00	0.00	0.00	0.00	0.00	0.00	0.00	0.00	0.00	0.00	0.00	0.00	0.00
Sum	3.00	3.00	3.00	3.00	3.00	3.00	3.00	3.00	3.00	3.00	3.00	3.00	3.00	3.00
X_{Mg}	0.94	0.94	0.94	0.94	0.94	0.93	0.93	0.94	0.93	0.94	0.93	0.94	0.94	0.91

Sample	MG15	MG15	MG4	MG4	MG4	MG4	MG4	MG4	MG4	MG4	MG4	MG4	MG4	MG4
Run duration	72	72	72	72	72	72	72	72	72	72	72	72	72	72
Melt	AH6	AH6	AH6	AH6	AH6	AH6	AH6	AH6	AH6	AH6	AH6	AH6	AH6	AH6
IMA (wt%)	10	10	25	25	25	25	25	25	25	25	25	25	25	25
T	$1300_{(i)}$-$1100_{(f)}$	$1300_{(i)}$-$1100_{(f)}$	$1300_{(i)}$-$1100_{(f)}$	$1300_{(i)}$-$1100_{(f}$	$1300_{(i)}$-$1100_{(f)}$	$1300_{(i)}$-$1100_{(f)}$	$1300_{(i)}$-$1100_{(f)}$	$1300_{(i)}$-$1100_{(f)}$	$1300_{(i)}$-$1100_{(f)}$	$1300_{(i)}$-$1100_{(f)}$	$1300_{(i)}$-$1100_{(f)}$	$1300_{(i)}$-$1100_{(f)}$	$1300_{(i)}$-$1100_{(f)}$	$1300_{(i)}$-$1100_{(f)}$
P	0.5	0.5	0.5	0.5	0.5	0.5	0.5	0.5	0.5	0.5	0.5	0.5	0.5	0.5
Point Analysis	MG15OL71	MG15OL72	MG4OL1	MG4OL2	MG4OL3	MG4OL4	MG4OL5	MG4OL6	MG4OL7	MG4OL8	MG4OL9	MG4OL10	MG4OL11	MG4OL12
Site	core	core	core	core	core	core	core	core	core	core	core	core	core	core
SiO_2	41.37	40.76	40.50	40.57	40.79	40.73	40.60	40.69	40.49	39.96	39.82	39.88	39.82	40.21
TiO_2	0.00	0.05	0.00	0.02	0.03	0.00	0.03	0.02	0.00	0.00	0.02	0.02	0.06	0.00
Al_2O_3	0.04	0.03	0.05	0.03	0.01	0.06	0.05	0.06	0.07	0.07	0.04	0.06	0.07	0.04
Cr_2O_3	0.07	0.09	0.01	0.00	0.05	0.00	0.03	0.06	0.07	0.05	0.00	0.00	0.03	0.09
FeO	8.46	7.72	9.08	9.32	8.13	9.26	9.46	9.15	9.24	9.36	9.15	9.43	9.24	9.43
MgO	50.55	51.22	50.26	50.31	50.44	49.70	50.15	50.46	49.59	50.01	50.23	50.12	50.41	49.99
MnO	0.14	0.10	0.16	0.16	0.15	0.13	0.16	0.12	0.16	0.05	0.16	0.20	0.14	0.19
NiO	0.19	0.07	0.07	0.07	0.00	0.00	0.00	0.02	0.07	0.00	0.05	0.07	0.02	0.01
CaO	0.22	0.29	0.29	0.32	0.30	0.35	0.34	0.31	0.47	0.40	0.35	0.32	0.32	0.28
Na_2O	0.00	0.00	0.02	0.00	0.00	0.03	0.03	0.00	0.00	0.03	0.02	0.01	0.03	0.02
K_2O	0.01	0.00	0.01	0.00	0.01	0.01	0.00	0.00	0.00	0.00	0.00	0.01	0.00	0.00
Total	101.05	100.33	100.46	100.81	99.91	100.27	100.85	100.89	100.15	99.93	99.84	100.12	100.14	100.26
Si	1.00	0.98	0.98	0.98	0.99	0.99	0.98	0.98	0.99	0.97	0.97	0.97	0.97	0.98
Ti	0.00	0.00	0.00	0.00	0.00	0.00	0.00	0.00	0.00	0.00	0.00	0.00	0.00	0.00
Al	0.00	0.00	0.00	0.00	0.00	0.00	0.00	0.00	0.00	0.00	0.00	0.00	0.00	0.00
Cr	0.00	0.00	0.00	0.00	0.00	0.00	0.00	0.00	0.00	0.00	0.00	0.00	0.00	0.00
Fe^{2+}	0.17	0.16	0.18	0.19	0.17	0.19	0.19	0.18	0.19	0.19	0.19	0.19	0.19	0.19
Mg	1.82	1.84	1.82	1.82	1.83	1.80	1.81	1.82	1.80	1.82	1.83	1.82	1.83	1.81
Mn	0.00	0.00	0.00	0.00	0.00	0.00	0.00	0.00	0.00	0.00	0.00	0.00	0.00	0.00
Ni	0.00	0.00	0.00	0.00	0.00	0.00	0.00	0.00	0.00	0.00	0.00	0.00	0.00	0.00
Ca	0.01	0.01	0.01	0.01	0.01	0.01	0.01	0.01	0.01	0.01	0.01	0.01	0.01	0.01
Na	0.00	0.00	0.00	0.00	0.00	0.00	0.00	0.00	0.00	0.00	0.00	0.00	0.00	0.00
K	0.00	0.00	0.00	0.00	0.00	0.00	0.00	0.00	0.00	0.00	0.00	0.00	0.00	0.00
Sum	3.00	3.00	3.00	3.00	3.00	3.00	3.00	3.00	3.00	3.00	3.00	3.00	3.00	3.00
X_{Mg}	0.91	0.92	0.90	0.90	0.91	0.90	0.90	0.90	0.90	0.90	0.90	0.90	0.90	0.90

Sample	MG4	MG4	MG4	MG4	MG4	MG4	MG4	MG4	MG4	MG4	MG4	MG4	MG4	MG4
Run duration	72	72	72	72	72	72	72	72	72	72	72	72	72	72
Melt	AH6	AH6	AH6	AH6	AH6	AH6	AH6	AH6	AH6	AH6	AH6	AH6	AH6	AH6
IMA (wt%)	25	25	25	25	25	25	25	25	25	25	25	25	25	25
T	$1300_{(i)}$-$1100_{(f)}$	$1300_{(i)}$-$1100_{(f)}$	$1300_{(i)}$-$1100_{(f)}$	$1300_{(i)}$-$1100_{(f}$	$1300_{(i)}$-$1100_{(f)}$	$1300_{(i)}$-$1100_{(f)}$	$1300_{(i)}$-$1100_{(f)}$	$1300_{(i)}$-$1100_{(f)}$	$1300_{(i)}$-$1100_{(f)}$	$1300_{(i)}$-$1100_{(f)}$	$1300_{(i)}$-$1100_{(f)}$	$1300_{(i)}$-$1100_{(f)}$	$1300_{(i)}$-$1100_{(f)}$	$1300_{(i)}$-$1100_{(f)}$
P	0.5	0.5	0.5	0.5	0.5	0.5	0.5	0.5	0.5	0.5	0.5	0.5	0.5	0.5
Point Analysis	MG4OL13	MG4OL14	MG4OL15	MG4OL16	MG4OL17	MG4OL18	MG4OL19	MG4OL20	MG4OL21	MG4OL22	MG4OL23	MG4OL24	MG4OL25	MG4OL26
Site	core	core	core	core	core	core	core	core	core	core	core	core	core	core
SiO_2	40.35	40.78	40.18	40.30	40.00	39.43	39.82	39.82	39.84	40.30	40.32	40.26	40.59	40.53
TiO_2	0.01	0.03	0.00	0.02	0.00	0.04	0.05	0.00	0.00	0.06	0.00	0.01	0.01	0.00
Al_2O_3	0.04	0.15	0.02	0.11	0.04	0.08	0.01	0.06	0.07	0.03	0.06	0.06	0.04	0.05
Cr_2O_3	0.02	0.00	0.04	0.06	0.10	0.08	0.00	0.06	0.01	0.06	0.06	0.02	0.01	0.01
FeO	8.89	8.99	8.90	8.88	8.58	9.07	8.92	8.77	8.77	8.49	8.28	8.29	8.52	8.50
MgO	50.34	50.08	50.37	50.30	50.14	50.69	50.66	50.39	50.36	50.64	50.02	50.71	50.24	49.36
MnO	0.18	0.13	0.10	0.18	0.13	0.10	0.17	0.13	0.14	0.09	0.13	0.12	0.14	0.14
NiO	0.00	0.01	0.03	0.02	0.06	0.01	0.01	0.01	0.04	0.00	0.00	0.03	0.00	0.03
CaO	0.33	0.39	0.35	0.38	0.32	0.34	0.30	0.33	0.32	0.33	0.32	0.25	0.32	0.29
Na_2O	0.01	0.03	0.00	0.00	0.01	0.00	0.00	0.00	0.00	0.02	0.00	0.00	0.00	0.00
K_2O	0.01	0.00	0.00	0.00	0.00	0.01	0.00	0.00	0.00	0.01	0.00	0.01	0.00	0.00
Total	100.17	100.59	100.00	100.24	99.38	99.84	99.95	99.57	99.55	100.02	99.19	99.77	99.88	98.92
Si	0.98	0.99	0.98	0.98	0.98	0.96	0.97	0.97	0.97	0.98	0.99	0.98	0.99	1.00
Ti	0.00	0.00	0.00	0.00	0.00	0.00	0.00	0.00	0.00	0.00	0.00	0.00	0.00	0.00
Al	0.00	0.00	0.00	0.00	0.00	0.00	0.00	0.00	0.00	0.00	0.00	0.00	0.00	0.00
Cr	0.00	0.00	0.00	0.00	0.00	0.00	0.00	0.00	0.00	0.00	0.00	0.00	0.00	0.00
Fe^{2+}	0.18	0.18	0.18	0.18	0.18	0.18	0.18	0.18	0.18	0.17	0.17	0.17	0.17	0.18
Mg	1.82	1.81	1.83	1.82	1.83	1.84	1.84	1.83	1.83	1.83	1.83	1.84	1.82	1.81
Mn	0.00	0.00	0.00	0.00	0.00	0.00	0.00	0.00	0.00	0.00	0.00	0.00	0.00	0.00
Ni	0.00	0.00	0.00	0.00	0.00	0.00	0.00	0.00	0.00	0.00	0.00	0.00	0.00	0.00
Ca	0.01	0.01	0.01	0.01	0.01	0.01	0.01	0.01	0.01	0.01	0.01	0.01	0.01	0.01
Na	0.00	0.00	0.00	0.00	0.00	0.00	0.00	0.00	0.00	0.00	0.00	0.00	0.00	0.00
K	0.00	0.00	0.00	0.00	0.00	0.00	0.00	0.00	0.00	0.00	0.00	0.00	0.00	0.00
Sum	3.00	3.00	3.00	3.00	3.00	3.00	3.00	3.00	3.00	3.00	3.00	3.00	3.00	3.00
X_{Mg}	0.90	0.90	0.90	0.90	0.91	0.90	0.90	0.91	0.91	0.91	0.91	0.91	0.91	0.91

Sample	MG4	MG4	MG4	MG4	MG4	MG4	MG4	MG4	MG4	MG4	MG4	MG4	MG4	MG4
Run duration	72	72	72	72	72	72	72	72	72	72	72	72	72	72
Melt	AH6	AH6	AH6	AH6	AH6	AH6	AH6	AH6	AH6	AH6	AH6	AH6	AH6	AH6
IMA (wt%)	25	25	25	25	25	25	25	25	25	25	25	25	25	25
T	$1300_{(i)}$-$1100_{(f)}$	$1300_{(i)}$-$1100_{(f)}$	$1300_{(i)}$-$1100_{(f)}$	$1300_{(i)}$-$1100_{(f}$	$1300_{(i)}$-$1100_{(f)}$	$1300_{(i)}$-$1100_{(f)}$	$1300_{(i)}$-$1100_{(f)}$	$1300_{(i)}$-$1100_{(f)}$	$1300_{(i)}$-$1100_{(f)}$	$1300_{(i)}$-$1100_{(f)}$	$1300_{(i)}$-$1100_{(f)}$	$1300_{(i)}$-$1100_{(f)}$	$1300_{(i)}$-$1100_{(f)}$	$1300_{(i)}$-$1100_{(f)}$
P	0.5	0.5	0.5	0.5	0.5	0.5	0.5	0.5	0.5	0.5	0.5	0.5	0.5	0.5
Point Analysis	MG4OL27	MG4OL28	MG4OL29	MG4OL30	MG4OL31	MG4OL32	MG4OL33	MG4OL34	MG4OL35	MG4OL36	MG4OL37	MG4OL38	MG4OL39	MG4OL40
Site	core	core	core	core	core	core	core	core	core	core	core	core	core	core
SiO_2	40.56	40.78	40.65	40.65	41.12	40.60	40.40	40.83	40.79	40.69	40.78	40.81	40.84	40.73
TiO_2	0.06	0.00	0.00	0.04	0.02	0.02	0.00	0.00	0.02	0.03	0.05	0.02	0.00	0.01
Al_2O_3	0.07	0.07	0.04	0.02	0.04	0.03	0.05	0.03	0.08	0.02	0.10	0.05	0.05	0.05
Cr_2O_3	0.09	0.04	0.01	0.04	0.01	0.05	0.00	0.08	0.08	0.02	0.00	0.00	0.04	0.09
FeO	8.45	8.51	8.47	8.67	8.39	8.58	8.35	8.51	8.73	8.67	8.86	8.67	8.72	8.73
MgO	49.56	49.54	49.35	49.72	48.81	49.22	49.20	49.93	49.74	49.91	49.57	49.83	49.78	50.15
MnO	0.17	0.15	0.14	0.08	0.17	0.17	0.13	0.16	0.14	0.14	0.12	0.13	0.12	0.11
NiO	0.00	0.02	0.01	0.00	0.00	0.08	0.00	0.04	0.02	0.00	0.00	0.00	0.07	0.00
CaO	0.32	0.31	0.32	0.30	0.31	0.31	0.31	0.30	0.27	0.31	0.29	0.32	0.34	0.32
Na_2O	0.00	0.05	0.01	0.02	0.00	0.04	0.00	0.00	0.01	0.00	0.00	0.00	0.00	0.00
K_2O	0.00	0.00	0.00	0.00	0.00	0.00	0.00	0.01	0.00	0.00	0.00	0.02	0.00	0.01
Total	99.28	99.47	99.00	99.54	98.87	99.10	98.44	99.89	99.87	99.79	99.77	99.84	99.96	100.19
Si	1.00	1.00	1.00	1.00	1.02	1.00	1.00	1.00	1.00	0.99	1.00	1.00	1.00	0.99
Ti	0.00	0.00	0.00	0.00	0.00	0.00	0.00	0.00	0.00	0.00	0.00	0.00	0.00	0.00
Al	0.00	0.00	0.00	0.00	0.00	0.00	0.00	0.00	0.00	0.00	0.00	0.00	0.00	0.00
Cr	0.00	0.00	0.00	0.00	0.00	0.00	0.00	0.00	0.00	0.00	0.00	0.00	0.00	0.00
Fe^{2+}	0.17	0.17	0.17	0.18	0.17	0.18	0.17	0.17	0.18	0.18	0.18	0.18	0.18	0.18
Mg	1.81	1.81	1.81	1.81	1.80	1.81	1.82	1.82	1.81	1.82	1.81	1.81	1.81	1.82
Mn	0.00	0.00	0.00	0.00	0.00	0.00	0.00	0.00	0.00	0.00	0.00	0.00	0.00	0.00
Ni	0.00	0.00	0.00	0.00	0.00	0.00	0.00	0.00	0.00	0.00	0.00	0.00	0.00	0.00
Ca	0.01	0.01	0.01	0.01	0.01	0.01	0.01	0.01	0.01	0.01	0.01	0.01	0.01	0.01
Na	0.00	0.00	0.00	0.00	0.00	0.00	0.00	0.00	0.00	0.00	0.00	0.00	0.00	0.00
K	0.00	0.00	0.00	0.00	0.00	0.00	0.00	0.00	0.00	0.00	0.00	0.00	0.00	0.00
Sum	3.00	3.00	3.00	3.00	3.00	3.00	3.00	3.00	3.00	3.00	3.00	3.00	3.00	3.00
X_{Mg}	0.91	0.90	0.91	0.91	0.91	0.90	0.91	0.91	0.90	0.91	0.90	0.91	0.90	0.91

Sample	MG4	MG4	MG4	MG4	MG4	MG4	MG4	MG4	MG4	MG4	MG4	MG4	MG4	MG4
Run duration	72	72	72	72	72	72	72	72	72	72	72	72	72	72
Melt	AH6	AH6	AH6	AH6	AH6	AH6	AH6	AH6	AH6	AH6	AH6	AH6	AH6	AH6
IMA (wt%)	25	25	25	25	25	25	25	25	25	25	25	25	25	25
T	$1300_{(i)}$-$1100_{(f)}$	$1300_{(i)}$-$1100_{(f)}$	$1300_{(i)}$-$1100_{(f)}$	$1300_{(i)}$-$1100_{(f}$	$1300_{(i)}$-$1100_{(f)}$	$1300_{(i)}$-$1100_{(f)}$	$1300_{(i)}$-$1100_{(f)}$	$1300_{(i)}$-$1100_{(f)}$	$1300_{(i)}$-$1100_{(f)}$	$1300_{(i)}$-$1100_{(f)}$	$1300_{(i)}$-$1100_{(f)}$	$1300_{(i)}$-$1100_{(f)}$	$1300_{(i)}$-$1100_{(f)}$	$1300_{(i)}$-$1100_{(f)}$
P	0.5	0.5	0.5	0.5	0.5	0.5	0.5	0.5	0.5	0.5	0.5	0.5	0.5	0.5
Point Analysis	MG4OL41	MG4OL42	MG4OL43	MG4OL44	MG4OL45	MG4OL46	MG4OL47	MG4OL48	MG4OL49	MG4OL50	MG4OL51	MG4OL52	MG4OL53	MG4OL54
Site	core	core	core	core	core	core	core	core	core	core	core	core	core	core
SiO_2	40.60	40.46	40.65	40.83	40.43	40.57	40.42	40.76	40.57	40.45	40.64	41.05	40.66	40.96
TiO_2	0.03	0.01	0.04	0.02	0.00	0.04	0.00	0.02	0.00	0.04	0.00	0.03	0.03	0.02
Al_2O_3	0.01	0.02	0.03	0.08	0.03	0.04	0.07	0.06	0.08	0.03	0.02	0.06	0.09	0.08
Cr_2O_3	0.07	0.00	0.04	0.02	0.06	0.01	0.07	0.07	0.01	0.00	0.10	0.04	0.00	0.02
FeO	8.81	8.87	8.88	9.06	9.37	8.91	9.11	8.89	9.14	9.30	9.11	8.94	9.10	9.38
MgO	49.38	49.26	49.41	49.50	49.18	49.27	49.28	48.98	49.19	49.51	49.91	49.71	49.62	49.23
MnO	0.21	0.14	0.16	0.16	0.16	0.13	0.12	0.14	0.12	0.13	0.19	0.15	0.16	0.10
NiO	0.00	0.04	0.05	0.02	0.00	0.03	0.06	0.02	0.02	0.07	0.02	0.01	0.02	0.00
CaO	0.42	0.31	0.34	0.31	0.31	0.30	0.32	0.32	0.34	0.35	0.34	0.33	0.32	0.35
Na_2O	0.03	0.02	0.00	0.00	0.01	0.01	0.00	0.03	0.01	0.00	0.00	0.01	0.00	0.02
K_2O	0.01	0.00	0.00	0.00	0.00	0.00	0.00	0.00	0.00	0.00	0.00	0.00	0.00	0.00
Total	99.58	99.13	99.60	100.01	99.55	99.31	99.45	99.29	99.47	99.87	100.33	100.33	99.99	100.15
Si	1.00	1.00	1.00	1.00	0.99	1.00	0.99	1.00	1.00	0.99	0.99	1.00	0.99	1.00
Ti	0.00	0.00	0.00	0.00	0.00	0.00	0.00	0.00	0.00	0.00	0.00	0.00	0.00	0.00
Al	0.00	0.00	0.00	0.00	0.00	0.00	0.00	0.00	0.00	0.00	0.00	0.00	0.00	0.00
Cr	0.00	0.00	0.00	0.00	0.00	0.00	0.00	0.00	0.00	0.00	0.00	0.00	0.00	0.00
Fe^{2+}	0.18	0.18	0.18	0.19	0.19	0.18	0.19	0.18	0.19	0.19	0.19	0.18	0.19	0.19
Mg	1.80	1.81	1.81	1.80	1.80	1.81	1.80	1.80	1.80	1.81	1.81	1.80	1.81	1.79
Mn	0.00	0.00	0.00	0.00	0.00	0.00	0.00	0.00	0.00	0.00	0.00	0.00	0.00	0.00
Ni	0.00	0.00	0.00	0.00	0.00	0.00	0.00	0.00	0.00	0.00	0.00	0.00	0.00	0.00
Ca	0.01	0.01	0.01	0.01	0.01	0.01	0.01	0.01	0.01	0.01	0.01	0.01	0.01	0.01
Na	0.00	0.00	0.00	0.00	0.00	0.00	0.00	0.00	0.00	0.00	0.00	0.00	0.00	0.00
K	0.00	0.00	0.00	0.00	0.00	0.00	0.00	0.00	0.00	0.00	0.00	0.00	0.00	0.00
Sum	3.00	3.00	3.00	3.00	3.00	3.00	3.00	3.00	3.00	3.00	3.00	3.00	3.00	3.00
X_{Mg}	0.90	0.90	0.90	0.90	0.90	0.90	0.90	0.90	0.90	0.90	0.90	0.90	0.90	0.90

Sample	MG4	MG4	MG4	MG4	MG4	MG4	MG4	MG4	MG4	MG4	MG4	MG4	MG4	MG4
Run duration	72	72	72	72	72	72	72	72	72	72	72	72	72	72
Melt	AH6	AH6	AH6	AH6	AH6	AH6	AH6	AH6	AH6	AH6	AH6	AH6	AH6	AH6
IMA (wt%)	25	25	25	25	25	25	25	25	25	25	25	25	25	25
T	$1300_{(i)}$-$1100_{(f)}$	$1300_{(i)}$-$1100_{(f)}$	$1300_{(i)}$-$1100_{(f)}$	$1300_{(i)}$-$1100_{(f}$	$1300_{(i)}$-$1100_{(f)}$	$1300_{(i)}$-$1100_{(f)}$	$1300_{(i)}$-$1100_{(f)}$	$1300_{(i)}$-$1100_{(f)}$	$1300_{(i)}$-$1100_{(f)}$	$1300_{(i)}$-$1100_{(f)}$	$1300_{(i)}$-$1100_{(f)}$	$1300_{(i)}$-$1100_{(f)}$	$1300_{(i)}$-$1100_{(f)}$	$1300_{(i)}$-$1100_{(f)}$
P	0.5	0.5	0.5	0.5	0.5	0.5	0.5	0.5	0.5	0.5	0.5	0.5	0.5	0.5
Point Analysis	MG4OL55	MG4OL56	MG4OL57	MG4OL58	MG4OL59	MG4OL60	MG4OL61	MG4OL62	MG4OL63	MG4OL64	MG4OL65	MG4OL66	MG4OL67	MG4OL68
Site	core	core	core	core	core	core	core	rim	rim	rim	rim	rim	rim	rim
SiO_2	41.00	40.68	40.35	40.55	40.27	40.68	40.33	40.59	40.73	40.33	40.78	40.23	40.65	40.44
TiO_2	0.02	0.00	0.02	0.00	0.00	0.01	0.00	0.01	0.00	0.06	0.05	0.00	0.02	0.04
Al_2O_3	0.06	0.04	0.06	0.07	0.08	0.05	0.05	0.05	0.35	0.07	0.08	0.08	0.07	0.70
Cr_2O_3	0.06	0.04	0.00	0.07	0.01	0.02	0.00	0.01	0.03	0.06	0.00	0.06	0.03	0.04
FeO	9.23	9.31	9.01	9.07	9.35	9.06	9.18	9.30	8.41	8.48	8.60	8.47	8.60	8.57
MgO	49.59	49.76	49.80	49.30	49.65	49.99	49.14	50.41	49.10	49.94	49.04	49.12	49.04	48.83
MnO	0.14	0.17	0.10	0.15	0.15	0.19	0.20	0.11	0.16	0.10	0.13	0.12	0.13	0.13
NiO	0.01	0.08	0.03	0.00	0.11	0.02	0.02	0.02	0.00	0.00	0.03	0.04	0.07	0.00
CaO	0.31	0.30	0.29	0.35	0.26	0.31	0.28	0.37	0.95	0.30	0.32	0.29	0.29	0.37
Na_2O	0.03	0.01	0.00	0.01	0.01	0.00	0.00	0.04	0.02	0.01	0.01	0.00	0.00	0.02
K_2O	0.00	0.00	0.01	0.01	0.00	0.00	0.00	0.00	0.00	0.00	0.01	0.00	0.00	0.00
Total	100.45	100.39	99.67	99.58	99.90	100.34	99.21	100.91	99.75	99.35	99.04	98.41	98.90	99.15
Si	1.00	0.99	0.99	0.99	0.98	0.99	0.99	0.98	1.00	0.99	1.01	1.00	1.00	1.00
Ti	0.00	0.00	0.00	0.00	0.00	0.00	0.00	0.00	0.00	0.00	0.00	0.00	0.00	0.00
Al	0.00	0.00	0.00	0.00	0.00	0.00	0.00	0.00	0.01	0.00	0.00	0.00	0.00	0.02
Cr	0.00	0.00	0.00	0.00	0.00	0.00	0.00	0.00	0.00	0.00	0.00	0.00	0.00	0.00
Fe^{2+}	0.19	0.19	0.18	0.19	0.19	0.18	0.19	0.19	0.17	0.17	0.18	0.18	0.18	0.18
Mg	1.80	1.81	1.82	1.80	1.81	1.81	1.80	1.82	1.79	1.82	1.80	1.81	1.80	1.79
Mn	0.00	0.00	0.00	0.00	0.00	0.00	0.00	0.00	0.00	0.00	0.00	0.00	0.00	0.00
Ni	0.00	0.00	0.00	0.00	0.00	0.00	0.00	0.00	0.00	0.00	0.00	0.00	0.00	0.00
Ca	0.01	0.01	0.01	0.01	0.01	0.01	0.01	0.01	0.02	0.01	0.01	0.01	0.01	0.01
Na	0.00	0.00	0.00	0.00	0.00	0.00	0.00	0.00	0.00	0.00	0.00	0.00	0.00	0.00
K	0.00	0.00	0.00	0.00	0.00	0.00	0.00	0.00	0.00	0.00	0.00	0.00	0.00	0.00
Sum	3.00	3.00	3.00	3.00	3.00	3.00	3.00	3.00	3.00	3.00	3.00	3.00	3.00	3.00
X_{Mg}	0.90	0.90	0.90	0.90	0.90	0.90	0.90	0.90	0.89	0.91	0.90	0.91	0.90	0.89

Sample	MG4	MG4	MG4	MG4	MG4	MG4	MG4	MG4	MG4	MG4	MG4	MG4	MG4	MG4
Run duration	72	72	72	72	72	72	72	72	72	72	72	72	72	72
Melt	AH6	AH6	AH6	AH6	AH6	AH6	AH6	AH6	AH6	AH6	AH6	AH6	AH6	AH6
IMA (wt%)	25	25	25	25	25	25	25	25	25	25	25	25	25	25
T	$1300_{(i)}$-$1100_{(f)}$	$1300_{(i)}$-$1100_{(f)}$	$1300_{(i)}$-$1100_{(f)}$	$1300_{(i)}$-$1100_{(f}$	$1300_{(i)}$-$1100_{(f)}$	$1300_{(i)}$-$1100_{(f)}$	$1300_{(i)}$-$1100_{(f)}$	$1300_{(i)}$-$1100_{(f)}$	$1300_{(i)}$-$1100_{(f)}$	$1300_{(i)}$-$1100_{(f)}$	$1300_{(i)}$-$1100_{(f)}$	$1300_{(i)}$-$1100_{(f)}$	$1300_{(i)}$-$1100_{(f)}$	$1300_{(i)}$-$1100_{(f)}$
P	0.5	0.5	0.5	0.5	0.5	0.5	0.5	0.5	0.5	0.5	0.5	0.5	0.5	0.5
Point Analysis	MG4OL69	MG4OL70	MG4OL71	MG4OL72	MG4OL73	MG4OL74	MG4OL75	MG4OL76	MG4OL77	MG4OL78	MG4OL79	MG4OL80	MG4OL81	MG4OL82
Site	rim	rim	rim	rim	rim	rim	rim	rim	rim	rim	rim	rim	rim	rim
SiO_2	41.00	40.80	41.06	40.51	40.86	40.90	40.66	40.87	40.66	40.67	41.58	41.15	40.72	40.83
TiO_2	0.04	0.00	0.00	0.02	0.06	0.00	0.01	0.02	0.00	0.00	0.06	0.02	0.00	0.01
Al_2O_3	0.07	0.11	0.10	0.06	0.05	0.07	0.05	0.04	0.09	0.07	0.43	0.04	0.06	0.07
Cr_2O_3	0.00	0.00	0.00	0.00	0.03	0.00	0.00	0.04	0.00	0.02	0.03	0.03	0.03	0.00
FeO	8.59	8.82	8.77	8.81	8.72	8.90	8.55	8.79	8.83	9.15	9.18	8.91	9.18	8.89
MgO	49.54	49.40	50.18	49.77	50.23	50.14	50.19	49.65	49.36	49.06	48.01	49.01	49.41	49.24
MnO	0.13	0.18	0.14	0.09	0.13	0.14	0.15	0.19	0.16	0.09	0.09	0.11	0.20	0.15
NiO	0.02	0.07	0.06	0.00	0.01	0.04	0.08	0.00	0.01	0.03	0.00	0.18	0.00	0.03
CaO	0.31	0.32	0.30	0.33	0.37	0.32	0.36	0.30	0.35	0.31	0.56	0.27	0.32	0.31
Na_2O	0.00	0.02	0.00	0.01	0.02	0.01	0.02	0.00	0.02	0.00	0.20	0.00	0.00	0.03
K_2O	0.00	0.01	0.00	0.00	0.00	0.00	0.00	0.01	0.01	0.01	0.01	0.00	0.01	0.00
Total	99.69	99.74	100.60	99.60	100.48	100.51	100.09	99.92	99.48	99.42	100.15	99.73	99.92	99.55
Si	1.00	1.00	1.00	0.99	0.99	0.99	0.99	1.00	1.00	1.00	1.02	1.01	1.00	1.00
Ti	0.00	0.00	0.00	0.00	0.00	0.00	0.00	0.00	0.00	0.00	0.00	0.00	0.00	0.00
Al	0.00	0.00	0.00	0.00	0.00	0.00	0.00	0.00	0.00	0.00	0.01	0.00	0.00	0.00
Cr	0.00	0.00	0.00	0.00	0.00	0.00	0.00	0.00	0.00	0.00	0.00	0.00	0.00	0.00
Fe^{2+}	0.18	0.18	0.18	0.18	0.18	0.18	0.17	0.18	0.18	0.19	0.19	0.18	0.19	0.18
Mg	1.81	1.80	1.81	1.82	1.82	1.81	1.82	1.81	1.80	1.80	1.75	1.79	1.80	1.80
Mn	0.00	0.00	0.00	0.00	0.00	0.00	0.00	0.00	0.00	0.00	0.00	0.00	0.00	0.00
Ni	0.00	0.00	0.00	0.00	0.00	0.00	0.00	0.00	0.00	0.00	0.00	0.00	0.00	0.00
Ca	0.01	0.01	0.01	0.01	0.01	0.01	0.01	0.01	0.01	0.01	0.01	0.01	0.01	0.01
Na	0.00	0.00	0.00	0.00	0.00	0.00	0.00	0.00	0.00	0.00	0.01	0.00	0.00	0.00
K	0.00	0.00	0.00	0.00	0.00	0.00	0.00	0.00	0.00	0.00	0.00	0.00	0.00	0.00
Sum	3.00	3.00	3.00	3.00	3.00	3.00	3.00	3.00	3.00	3.00	3.00	3.00	3.00	3.00
X_{Mg}	0.91	0.90	0.90	0.90	0.90	0.90	0.91	0.90	0.90	0.90	0.89	0.90	0.90	0.90

Sample	MG4	MG4	MG4	MG4	MG4	MG4	MG4	MG4	MG4	MG4	MG4	MG16	MG16	MG16
Run duration	72	72	72	72	72	72	72	72	72	72	72	72	72	72
Melt	AH6	AH6	AH6	AH6	AH6	AH6	AH6	AH6	AH6	AH6	AH6	AH6	AH6	AH6
IMA (wt%)	25	25	25	25	25	25	25	25	25	25	25	50	50	50
T	$1300_{(i)}$-$1100_{(f)}$	$1300_{(i)}$-$1100_{(f)}$	$1300_{(i)}$-$1100_{(f)}$	$1300_{(i)}$-$1100_{(f}$	$1300_{(i)}$-$1100_{(f)}$	$1300_{(i)}$-$1100_{(f)}$	$1300_{(i)}$-$1100_{(f)}$	$1300_{(i)}$-$1100_{(f)}$	$1300_{(i)}$-$1100_{(f)}$	$1300_{(i)}$-$1100_{(f)}$	$1300_{(i)}$-$1100_{(f)}$	$1300_{(i)}$-$1100_{(f)}$	$1300_{(i)}$-$1100_{(f)}$	$1300_{(i)}$-$1100_{(f)}$
P	0.5	0.5	0.5	0.5	0.5	0.5	0.5	0.5	0.5	0.5	0.5	0.5	0.5	0.5
Point Analysis	MG4OL83	MG4OL84	MG4OL85	MG4OL86	MG4OL87	MG4OL88	MG4OL89	MG4OL90	MG4OL91	MG4OL92	MG4OL93	MG16OL1	MG16OL2	MG16OL3
Site	rim	rim	rim	rim	rim	rim	rim	rim	rim	rim	rim	core	core	core
SiO_2	40.61	40.66	40.60	40.75	40.62	40.63	40.77	40.45	40.35	40.43	40.83	41.19	40.85	40.78
TiO_2	0.00	0.02	0.02	0.01	0.07	0.05	0.00	0.03	0.08	0.08	0.04	0.00	0.03	0.00
Al_2O_3	0.04	0.02	0.05	0.06	0.03	0.05	0.05	0.06	0.05	0.06	0.05	0.03	0.02	0.05
Cr_2O_3	0.05	0.06	0.00	0.06	0.03	0.11	0.04	0.11	0.00	0.00	0.04	0.06	0.00	0.04
FeO	8.99	9.30	9.24	9.09	9.07	9.19	9.04	8.97	9.07	9.11	9.31	6.37	8.07	8.21
MgO	49.47	49.64	49.92	49.63	49.67	49.21	49.26	49.38	49.97	49.79	49.35	52.13	50.63	50.57
MnO	0.14	0.11	0.18	0.15	0.15	0.12	0.17	0.12	0.14	0.15	0.11	0.12	0.14	0.19
NiO	0.05	0.01	0.07	0.00	0.04	0.00	0.06	0.03	0.05	0.00	0.00	0.00	0.00	0.14
CaO	0.35	0.30	0.30	0.31	0.31	0.34	0.31	0.33	0.28	0.28	0.32	0.53	0.46	0.29
Na_2O	0.00	0.01	0.02	0.00	0.00	0.03	0.01	0.00	0.00	0.01	0.02	0.01	0.00	0.00
K_2O	0.02	0.02	0.01	0.01	0.02	0.01	0.01	0.00	0.00	0.00	0.00	0.00	0.00	0.00
Total	99.73	100.15	100.41	100.08	100.01	99.73	99.73	99.47	99.99	99.91	100.07	100.44	100.20	100.27
Si	0.99	0.99	0.99	0.99	0.99	1.00	1.00	0.99	0.98	0.99	1.00	0.99	0.99	0.99
Ti	0.00	0.00	0.00	0.00	0.00	0.00	0.00	0.00	0.00	0.00	0.00	0.00	0.00	0.00
Al	0.00	0.00	0.00	0.00	0.00	0.00	0.00	0.00	0.00	0.00	0.00	0.00	0.00	0.00
Cr	0.00	0.00	0.00	0.00	0.00	0.00	0.00	0.00	0.00	0.00	0.00	0.00	0.00	0.00
Fe^{2+}	0.18	0.19	0.19	0.19	0.19	0.19	0.19	0.18	0.19	0.19	0.19	0.13	0.16	0.17
Mg	1.81	1.80	1.81	1.81	1.81	1.80	1.80	1.81	1.82	1.81	1.80	1.87	1.83	1.83
Mn	0.00	0.00	0.00	0.00	0.00	0.00	0.00	0.00	0.00	0.00	0.00	0.00	0.00	0.00
Ni	0.00	0.00	0.00	0.00	0.00	0.00	0.00	0.00	0.00	0.00	0.00	0.00	0.00	0.00
Ca	0.01	0.01	0.01	0.01	0.01	0.01	0.01	0.01	0.01	0.01	0.01	0.01	0.01	0.01
Na	0.00	0.00	0.00	0.00	0.00	0.00	0.00	0.00	0.00	0.00	0.00	0.00	0.00	0.00
K	0.00	0.00	0.00	0.00	0.00	0.00	0.00	0.00	0.00	0.00	0.00	0.00	0.00	0.00
Sum	3.00	3.00	3.00	3.00	3.00	3.00	3.00	3.00	3.00	3.00	3.00	3.00	3.00	3.00
X_{Mg}	0.90	0.90	0.90	0.90	0.90	0.90	0.90	0.90	0.90	0.90	0.90	0.93	0.91	0.91

Sample	MG16	MG16	MG16	MG16	MG16	MG16	MG16	MG16	MG16	MG16	MG16	MG16	MG16	MG16
Run duration	72	72	72	72	72	72	72	72	72	72	72	72	72	72
Melt	AH6	AH6	AH6	AH6	AH6	AH6	AH6	AH6	AH6	AH6	AH6	AH6	AH6	AH6
IMA (wt%)	50	50	50	50	50	50	50	50	50	50	50	50	50	50
T	$1300_{(i)}$-$1100_{(f)}$	$1300_{(i)}$-$1100_{(f)}$	$1300_{(i)}$-$1100_{(f)}$	$1300_{(i)}$-$1100_{(f}$	$1300_{(i)}$-$1100_{(f)}$	$1300_{(i)}$-$1100_{(f)}$	$1300_{(i)}$-$1100_{(f)}$	$1300_{(i)}$-$1100_{(f)}$	$1300_{(i)}$-$1100_{(f)}$	$1300_{(i)}$-$1100_{(f)}$	$1300_{(i)}$-$1100_{(f)}$	$1300_{(i)}$-$1100_{(f)}$	$1300_{(i)}$-$1100_{(f)}$	$1300_{(i)}$-$1100_{(f)}$
P	0.5	0.5	0.5	0.5	0.5	0.5	0.5	0.5	0.5	0.5	0.5	0.5	0.5	0.5
Point Analysis	MG16OL4	MG16OL5	MG16OL6	MG16OL7	MG16OL8	MG16OL9	MG16OL10	MG16OL11	MG16OL12	MG16OL13	MG16OL14	MG16OL15	MG16OL16	MG16OL17
Site	rim	core	rim	core	core	rim	core	rim	core	rim	core	rim	core	core
SiO_2	40.82	41.17	41.06	40.75	40.66	40.95	41.01	41.46	41.21	41.50	41.24	40.81	40.76	41.06
TiO_2	0.02	0.01	0.03	0.00	0.03	0.00	0.03	0.00	0.00	0.01	0.00	0.01	0.03	0.03
Al_2O_3	0.01	0.02	0.01	0.03	0.04	0.04	0.05	0.03	0.03	0.05	0.01	0.03	0.05	0.01
Cr_2O_3	0.00	0.05	0.00	0.08	0.04	0.05	0.01	0.05	0.06	0.09	0.08	0.03	0.00	0.04
FeO	7.35	7.78	7.68	8.61	8.26	6.96	7.86	6.71	7.49	6.51	7.57	7.06	6.89	6.90
MgO	50.45	51.08	50.67	50.55	49.94	51.00	50.59	51.96	51.35	52.12	50.61	51.26	51.26	51.64
MnO	0.10	0.13	0.11	0.15	0.12	0.12	0.18	0.16	0.09	0.11	0.14	0.14	0.16	0.15
NiO	0.04	0.17	0.21	0.17	0.13	0.06	0.13	0.07	0.06	0.00	0.10	0.02	0.05	0.05
CaO	0.32	0.15	0.18	0.31	0.26	0.37	0.34	0.26	0.34	0.36	0.15	0.38	0.35	0.26
Na_2O	0.00	0.00	0.02	0.02	0.00	0.02	0.00	0.01	0.00	0.03	0.00	0.00	0.02	0.00
K_2O	0.00	0.00	0.01	0.00	0.01	0.00	0.02	0.00	0.00	0.00	0.00	0.00	0.01	0.00
Total	99.11	100.56	99.98	100.67	99.49	99.57	100.22	100.71	100.63	100.78	99.90	99.74	99.58	100.14
Si	1.00	0.99	1.00	0.99	0.99	1.00	0.99	0.99	0.99	0.99	1.00	0.99	0.99	0.99
Ti	0.00	0.00	0.00	0.00	0.00	0.00	0.00	0.00	0.00	0.00	0.00	0.00	0.00	0.00
Al	0.00	0.00	0.00	0.00	0.00	0.00	0.00	0.00	0.00	0.00	0.00	0.00	0.00	0.00
Cr	0.00	0.00	0.00	0.00	0.00	0.00	0.00	0.00	0.00	0.00	0.00	0.00	0.00	0.00
Fe^{2+}	0.15	0.16	0.16	0.17	0.17	0.14	0.16	0.13	0.15	0.13	0.15	0.14	0.14	0.14
Mg	1.84	1.84	1.83	1.82	1.82	1.85	1.83	1.86	1.84	1.86	1.83	1.85	1.85	1.86
Mn	0.00	0.00	0.00	0.00	0.00	0.00	0.00	0.00	0.00	0.00	0.00	0.00	0.00	0.00
Ni	0.00	0.00	0.00	0.00	0.00	0.00	0.00	0.00	0.00	0.00	0.00	0.00	0.00	0.00
Ca	0.01	0.00	0.00	0.01	0.01	0.01	0.01	0.01	0.01	0.01	0.00	0.01	0.01	0.01
Na	0.00	0.00	0.00	0.00	0.00	0.00	0.00	0.00	0.00	0.00	0.00	0.00	0.00	0.00
K	0.00	0.00	0.00	0.00	0.00	0.00	0.00	0.00	0.00	0.00	0.00	0.00	0.00	0.00
Sum	3.00	3.00	3.00	3.00	3.00	3.00	3.00	3.00	3.00	3.00	3.00	3.00	3.00	3.00
X_{Mg}	0.92	0.92	0.92	0.91	0.91	0.92	0.91	0.93	0.92	0.93	0.92	0.92	0.92	0.93

Sample	MG16	MG16	MG16	MG16	MG16	MG16	MG16	MG16	MG16	MG16	MG16	MG16	MG16	MG16
Run duration	72	72	72	72	72	72	72	72	72	72	72	72	72	72
Melt	AH6	AH6	AH6	AH6	AH6	AH6	AH6	AH6	AH6	AH6	AH6	AH6	AH6	AH6
IMA (wt%)	50	50	50	50	50	50	50	50	50	50	50	50	50	50
T	$1300_{(i)}$-$1100_{(f)}$	$1300_{(i)}$-$1100_{(f)}$	$1300_{(i)}$-$1100_{(f)}$	$1300_{(i)}$-$1100_{(f}$	$1300_{(i)}$-$1100_{(f)}$	$1300_{(i)}$-$1100_{(f)}$	$1300_{(i)}$-$1100_{(f)}$	$1300_{(i)}$-$1100_{(f)}$	$1300_{(i)}$-$1100_{(f)}$	$1300_{(i)}$-$1100_{(f)}$	$1300_{(i)}$-$1100_{(f)}$	$1300_{(i)}$-$1100_{(f)}$	$1300_{(i)}$-$1100_{(f)}$	$1300_{(i)}$-$1100_{(f)}$
P	0.5	0.5	0.5	0.5	0.5	0.5	0.5	0.5	0.5	0.5	0.5	0.5	0.5	0.5
Point Analysis	MG16OL18	MG16OL19	MG16OL20	MG16OL21	MG16OL22	MG16OL23	MG16OL24	MG16OL25	MG16OL26	MG16OL27	MG16OL28	MG16OL29	MG16OL30	MG16OL31
Site	core	core	rim	core	rim	core	rim	core	core	core	core	core	core	core
SiO_2	40.98	41.49	41.23	41.28	41.55	41.45	41.45	40.98	40.91	41.06	41.19	41.67	40.85	40.78
TiO_2	0.03	0.00	0.01	0.09	0.00	0.00	0.00	0.03	0.04	0.00	0.00	0.00	0.03	0.00
Al_2O_3	0.03	0.03	0.05	0.01	0.03	0.01	0.03	0.04	0.07	0.05	0.03	0.04	0.02	0.05
Cr_2O_3	0.10	0.05	0.05	0.04	0.05	0.00	0.04	0.04	0.04	0.02	0.06	0.01	0.00	0.04
FeO	7.57	7.31	6.37	8.01	6.46	7.36	6.51	6.49	6.44	5.89	6.37	3.26	8.07	8.21
MgO	51.53	51.10	52.15	50.88	51.48	51.00	51.47	51.11	51.46	52.33	52.13	53.37	50.63	50.57
MnO	0.21	0.13	0.13	0.12	0.13	0.15	0.08	0.21	0.20	0.16	0.12	0.10	0.14	0.19
NiO	0.05	0.12	0.06	0.24	0.21	0.13	0.04	0.08	0.03	0.04	0.00	0.03	0.00	0.14
CaO	0.31	0.25	0.34	0.19	0.24	0.23	0.28	0.27	0.32	0.33	0.53	1.50	0.46	0.29
Na_2O	0.02	0.01	0.00	0.03	0.01	0.00	0.00	0.00	0.00	0.00	0.01	0.02	0.00	0.00
K_2O	0.00	0.00	0.01	0.00	0.00	0.00	0.00	0.01	0.00	0.00	0.00	0.00	0.00	0.00
Total	100.83	100.49	100.40	100.89	100.16	100.33	99.90	99.26	99.51	99.88	100.44	100.00	100.20	100.27
Si	0.98	1.00	0.99	0.99	1.00	1.00	1.00	1.00	0.99	0.99	0.99	0.99	0.99	0.99
Ti	0.00	0.00	0.00	0.00	0.00	0.00	0.00	0.00	0.00	0.00	0.00	0.00	0.00	0.00
Al	0.00	0.00	0.00	0.00	0.00	0.00	0.00	0.00	0.00	0.00	0.00	0.00	0.00	0.00
Cr	0.00	0.00	0.00	0.00	0.00	0.00	0.00	0.00	0.00	0.00	0.00	0.00	0.00	0.00
Fe^{2+}	0.15	0.15	0.13	0.16	0.13	0.15	0.13	0.13	0.13	0.12	0.13	0.07	0.16	0.17
Mg	1.85	1.84	1.87	1.83	1.85	1.84	1.85	1.85	1.86	1.88	1.87	1.90	1.83	1.83
Mn	0.00	0.00	0.00	0.00	0.00	0.00	0.00	0.00	0.00	0.00	0.00	0.00	0.00	0.00
Ni	0.00	0.00	0.00	0.00	0.00	0.00	0.00	0.00	0.00	0.00	0.00	0.00	0.00	0.00
Ca	0.01	0.01	0.01	0.00	0.01	0.01	0.01	0.01	0.01	0.01	0.01	0.04	0.01	0.01
Na	0.00	0.00	0.00	0.00	0.00	0.00	0.00	0.00	0.00	0.00	0.00	0.00	0.00	0.00
K	0.00	0.00	0.00	0.00	0.00	0.00	0.00	0.00	0.00	0.00	0.00	0.00	0.00	0.00
Sum	3.00	3.00	3.00	3.00	3.00	3.00	3.00	3.00	3.00	3.00	3.00	3.00	3.00	3.00
X_{Mg}	0.92	0.92	0.93	0.91	0.93	0.92	0.93	0.93	0.93	0.93	0.93	0.95	0.91	0.91

Sample	MG16	MG16	MG16	MG16	MG16	MG16	MG16	MG16	MG16	MG16	MG16	MG16	MG16	MG16
Run duration	72	72	72	72	72	72	72	72	72	72	72	72	72	72
Melt	AH6	AH6	AH6	AH6	AH6	AH6	AH6	AH6	AH6	AH6	AH6	AH6	AH6	AH6
IMA (wt%)	50	50	50	50	50	50	50	50	50	50	50	50	50	50
T	$1300_{(i)}$-$1100_{(f)}$	$1300_{(i)}$-$1100_{(f)}$	$1300_{(i)}$-$1100_{(f)}$	$1300_{(i)}$-$1100_{(f}$	$1300_{(i)}$-$1100_{(f)}$	$1300_{(i)}$-$1100_{(f)}$	$1300_{(i)}$-$1100_{(f)}$	$1300_{(i)}$-$1100_{(f)}$	$1300_{(i)}$-$1100_{(f)}$	$1300_{(i)}$-$1100_{(f)}$	$1300_{(i)}$-$1100_{(f)}$	$1300_{(i)}$-$1100_{(f)}$	$1300_{(i)}$-$1100_{(f)}$	$1300_{(i)}$-$1100_{(f)}$
P	0.5	0.5	0.5	0.5	0.5	0.5	0.5	0.5	0.5	0.5	0.5	0.5	0.5	0.5
Point Analysis	MG16OL32	MG16OL33	MG16OL34	MG16OL35	MG16OL36	MG16OL37	MG16OL38	MG16OL39	MG16OL40	MG16OL41	MG16OL42	MG16OL43	MG16OL44	MG16OL45
Site	rim	core	rim	core	core	core	rim	core	rim	core	rim	core	rim	core
SiO_2	40.82	41.17	41.06	40.75	41.02	40.66	40.95	41.01	41.46	41.21	41.50	41.24	40.81	40.76
TiO_2	0.02	0.01	0.03	0.00	0.00	0.03	0.00	0.03	0.00	0.00	0.01	0.00	0.01	0.03
Al_2O_3	0.01	0.02	0.01	0.03	0.00	0.04	0.04	0.05	0.03	0.03	0.05	0.01	0.03	0.05
Cr_2O_3	0.00	0.05	0.00	0.08	0.00	0.04	0.05	0.01	0.05	0.06	0.09	0.08	0.03	0.00
FeO	7.35	7.78	7.68	8.61	5.46	8.26	6.96	7.86	6.71	7.49	6.51	7.57	7.06	6.89
MgO	50.45	51.08	50.67	50.55	51.80	49.94	51.00	50.59	51.96	51.35	52.12	50.61	51.26	51.26
MnO	0.10	0.13	0.11	0.15	0.10	0.12	0.12	0.18	0.16	0.09	0.11	0.14	0.14	0.16
NiO	0.04	0.17	0.21	0.17	0.00	0.13	0.06	0.13	0.07	0.06	0.00	0.10	0.02	0.05
CaO	0.32	0.15	0.18	0.31	1.38	0.26	0.37	0.34	0.26	0.34	0.36	0.15	0.38	0.35
Na_2O	0.00	0.00	0.02	0.02	0.02	0.00	0.02	0.00	0.01	0.00	0.03	0.00	0.00	0.02
K_2O	0.00	0.00	0.01	0.00	0.00	0.01	0.00	0.02	0.00	0.00	0.00	0.00	0.00	0.01
Total	99.11	100.56	99.98	100.67	99.78	99.49	99.57	100.22	100.71	100.63	100.78	99.90	99.74	99.58
Si	1.00	0.99	1.00	0.99	0.99	0.99	1.00	0.99	0.99	0.99	0.99	1.00	0.99	0.99
Ti	0.00	0.00	0.00	0.00	0.00	0.00	0.00	0.00	0.00	0.00	0.00	0.00	0.00	0.00
Al	0.00	0.00	0.00	0.00	0.00	0.00	0.00	0.00	0.00	0.00	0.00	0.00	0.00	0.00
Cr	0.00	0.00	0.00	0.00	0.00	0.00	0.00	0.00	0.00	0.00	0.00	0.00	0.00	0.00
Fe^{2+}	0.15	0.16	0.16	0.17	0.11	0.17	0.14	0.16	0.13	0.15	0.13	0.15	0.14	0.14
Mg	1.84	1.84	1.83	1.82	1.86	1.82	1.85	1.83	1.86	1.84	1.86	1.83	1.85	1.85
Mn	0.00	0.00	0.00	0.00	0.00	0.00	0.00	0.00	0.00	0.00	0.00	0.00	0.00	0.00
Ni	0.00	0.00	0.00	0.00	0.00	0.00	0.00	0.00	0.00	0.00	0.00	0.00	0.00	0.00
Ca	0.01	0.00	0.00	0.01	0.04	0.01	0.01	0.01	0.01	0.01	0.01	0.00	0.01	0.01
Na	0.00	0.00	0.00	0.00	0.00	0.00	0.00	0.00	0.00	0.00	0.00	0.00	0.00	0.00
K	0.00	0.00	0.00	0.00	0.00	0.00	0.00	0.00	0.00	0.00	0.00	0.00	0.00	0.00
Sum	3.00	3.00	3.00	3.00	3.00	3.00	3.00	3.00	3.00	3.00	3.00	3.00	3.00	3.00
X_{Mg}	0.92	0.92	0.92	0.91	0.93	0.91	0.92	0.91	0.93	0.92	0.93	0.92	0.92	0.92

Sample	MG16	MG16	MG16	MG16	MG16	MG16	MG16	MG16	MG16	MG16	MG16
Run duration	72	72	72	72	72	72	72	72	72	72	72
Melt	AH6	AH6	AH6	AH6	AH6	AH6	AH6	AH6	AH6	AH6	AH6
IMA (wt%)	50	50	50	50	50	50	50	50	50	50	50
T	$1300_{(i)}$-$1100_{(f)}$	$1300_{(i)}$-$1100_{(f)}$	$1300_{(i)}$-$1100_{(f)}$	$1300_{(i)}$-$1100_{(f}$	$1300_{(i)}$-$1100_{(f)}$	$1300_{(i)}$-$1100_{(f)}$	$1300_{(i)}$-$1100_{(f)}$	$1300_{(i)}$-$1100_{(f)}$	$1300_{(i)}$-$1100_{(f)}$	$1300_{(i)}$-$1100_{(f)}$	$1300_{(i)}$-$1100_{(f)}$
P	0.5	0.5	0.5	0.5	0.5	0.5	0.5	0.5	0.5	0.5	0.5
Point Analysis	MG16OL46	MG16OL47	MG16OL48	MG16OL49	MG16OL50	MG16OL51	MG16OL52	MG16OL53	MG16OL54	MG16OL55	MG16OL56
Site	core	core	core	rim	core	rim	core	rim	core	core	core
SiO_2	41.06	40.98	41.49	41.23	41.28	41.55	41.45	41.45	40.98	40.91	41.06
TiO_2	0.03	0.03	0.00	0.01	0.09	0.00	0.00	0.00	0.03	0.04	0.00
Al_2O_3	0.01	0.03	0.03	0.05	0.01	0.03	0.01	0.03	0.04	0.07	0.05
Cr_2O_3	0.04	0.10	0.05	0.05	0.04	0.05	0.00	0.04	0.04	0.04	0.02
FeO	6.90	7.57	7.31	6.37	8.01	6.46	7.36	6.51	6.49	6.44	5.89
MgO	51.64	51.53	51.10	52.15	50.88	51.48	51.00	51.47	51.11	51.46	52.33
MnO	0.15	0.21	0.13	0.13	0.12	0.13	0.15	0.08	0.21	0.20	0.16
NiO	0.05	0.05	0.12	0.06	0.24	0.21	0.13	0.04	0.08	0.03	0.04
CaO	0.26	0.31	0.25	0.34	0.19	0.24	0.23	0.28	0.27	0.32	0.33
Na_2O	0.00	0.02	0.01	0.00	0.03	0.01	0.00	0.00	0.00	0.00	0.00
K_2O	0.00	0.00	0.00	0.01	0.00	0.00	0.00	0.00	0.01	0.00	0.00
Total	100.14	100.83	100.49	100.40	100.89	100.16	100.33	99.90	99.26	99.51	99.88
Si	0.99	0.98	1.00	0.99	0.99	1.00	1.00	1.00	1.00	0.99	0.99
Ti	0.00	0.00	0.00	0.00	0.00	0.00	0.00	0.00	0.00	0.00	0.00
Al	0.00	0.00	0.00	0.00	0.00	0.00	0.00	0.00	0.00	0.00	0.00
Cr	0.00	0.00	0.00	0.00	0.00	0.00	0.00	0.00	0.00	0.00	0.00
Fe^{2+}	0.14	0.15	0.15	0.13	0.16	0.13	0.15	0.13	0.13	0.13	0.12
Mg	1.86	1.85	1.84	1.87	1.83	1.85	1.84	1.85	1.85	1.86	1.88
Mn	0.00	0.00	0.00	0.00	0.00	0.00	0.00	0.00	0.00	0.00	0.00
Ni	0.00	0.00	0.00	0.00	0.00	0.00	0.00	0.00	0.00	0.00	0.00
Ca	0.01	0.01	0.01	0.01	0.00	0.01	0.01	0.01	0.01	0.01	0.01
Na	0.00	0.00	0.00	0.00	0.00	0.00	0.00	0.00	0.00	0.00	0.00
K	0.00	0.00	0.00	0.00	0.00	0.00	0.00	0.00	0.00	0.00	0.00
Sum	3.00	3.00	3.00	3.00	3.00	3.00	3.00	3.00	3.00	3.00	3.00
X_{Mg}	0.93	0.92	0.92	0.93	0.91	0.93	0.92	0.93	0.93	0.93	0.93

Table 7-4 *Major element composition of plagioclase from isothermal experiments performed at 0.5 GPa, 1200°C.*

Sample	MG10	MG10	MG10	MG10	MG10	MG10	MG10	MG10	MG10	MG10	MG10	MG10	MG12	MG12
Run duration	24	24	24	24	24	24	24	24	24	24	24	24	24	24
Melt	AH6	AH6	AH6	AH6	AH6	AH6	AH6	AH6	AH6	AH6	AH6	AH6	AH6	AH6
IMA (wt%)[a]	10	10	10	10	10	10	10	10	10	10	10	10	25	25
T[b]	1200	1200	1200	1200	1200	1200	1200	1200	1200	1200	1200	1200	1200	1200
P[c]	0.5	0.5	0.5	0.5	0.5	0.5	0.5	0.5	0.5	0.5	0.5	0.5	0.5	0.5
Point Analysis	MG10Plg1	MG10Plg2	MG10Plg3	MG10Plg4	MG10Plg5	MG10Plg6	MG10Plg7	MG10Plg8	MG10Plg9	MG10Plg10	MG10Plg11	MG10Plg12	MG12Plg1	MG12Plg2
SiO_2	51.33	50.67	51.02	51.54	51.52	51.50	51.88	51.82	51.67	52.38	50.75	50.16	51.65	53.54
TiO_2	0.11	0.01	0.02	0.00	0.17	0.06	0.13	0.13	0.13	0.18	0.07	0.08	0.35	0.35
Al_2O_3	29.46	29.96	30.81	29.31	28.67	28.36	29.36	30.13	28.53	26.53	30.76	29.68	26.22	27.02
Cr_2O_3	0.02	0.02	0.01	0.02	0.00	0.00	0.02	0.00	0.01	0.01	0.03	0.00	0.02	0.00
FeO	0.63	0.61	0.63	0.58	0.62	0.53	0.21	0.00	0.00	0.00	0.02	0.00	0.00	0.00
MgO	0.40	0.42	0.35	0.40	0.40	0.82	0.47	0.37	1.84	2.54	0.32	1.01	4.30	1.30
MnO	0.01	0.06	0.00	0.00	0.01	0.00	0.00	0.00	0.00	0.00	0.07	0.00	0.00	0.01
NiO	0.07	0.00	0.03	0.03	0.16	0.00	0.15	0.04	0.24	0.00	0.00	0.11	0.07	0.00
CaO	13.95	14.54	14.16	13.50	13.23	13.49	13.18	13.56	12.65	11.71	14.37	13.99	11.52	11.11
Na_2O	3.22	2.82	3.06	3.38	3.49	3.52	3.76	3.72	3.72	3.97	3.26	3.22	4.14	4.83
K_2O	0.07	0.07	0.08	0.08	0.08	0.06	0.13	0.13	0.13	0.17	0.08	0.13	0.26	0.27
Total	99.26	99.19	100.17	98.84	98.35	98.49	100.07	100.59	100.25	98.73	100.51	99.36	100.03	99.20
Si	2.36	2.34	2.33	2.38	2.39	2.38	2.36	2.35	2.34	2.40	2.31	2.30	2.32	2.44
Ti	0.00	0.00	0.00	0.00	0.01	0.00	0.00	0.00	0.00	0.01	0.00	0.00	0.01	0.01
Al	1.60	1.63	1.66	1.59	1.57	1.55	1.58	1.61	1.52	1.43	1.65	1.61	1.39	1.45
Cr	0.00	0.00	0.00	0.00	0.00	0.00	0.00	0.00	0.00	0.00	0.00	0.00	0.00	0.00
Fe^{2+}	0.02	0.02	0.02	0.02	0.02	0.02	0.01	0.00	0.00	0.00	0.00	0.00	0.00	0.00
Mg	0.03	0.03	0.02	0.03	0.03	0.06	0.03	0.03	0.12	0.17	0.02	0.07	0.29	0.09
Mn	0.00	0.00	0.00	0.00	0.00	0.00	0.00	0.00	0.00	0.00	0.00	0.00	0.00	0.00
Ni	0.00	0.00	0.00	0.00	0.01	0.00	0.01	0.00	0.01	0.00	0.00	0.00	0.00	0.00
Ca	0.69	0.72	0.69	0.67	0.66	0.67	0.64	0.66	0.61	0.58	0.70	0.69	0.56	0.54
Na	0.29	0.25	0.27	0.30	0.31	0.32	0.33	0.33	0.33	0.35	0.29	0.29	0.36	0.43
K	0.00	0.00	0.00	0.00	0.00	0.00	0.01	0.01	0.01	0.01	0.00	0.01	0.01	0.02
Na+Ca	0.98	0.97	0.96	0.97	0.97	0.98	0.98	0.98	0.94	0.93	0.99	0.97	0.92	0.97
X_{An}[d]	0.70	0.74	0.72	0.69	0.67	0.68	0.65	0.66	0.65	0.61	0.71	0.70	0.60	0.55

Cations are calculated with the Program NORM (version 2019) edited by Ulmer, P., and Poli, S. [a] Initial melt amount. [b] Temperature. [c] Pressure. [d] X_{An} = Ca/(Ca+Na).

Sample	MG12	MG12	MG12	MG12	MG12	MG12	MG12	MG14	MG14	MG14	MG14	MG14	MG14	MG14
Run duration	24	24	24	24	24	24	24	24	24	24	24	24	24	24
Melt	AH6	AH6	AH6	AH6	AH6	AH6	AH6	AH6	AH6	AH6	AH6	AH6	AH6	AH6
IMA (wt%)	25	25	25	25	25	25	25	50	50	50	50	50	50	50
T	1200	1200	1200	1200	1200	1200	1200	1200	1200	1200	1200	1200	1200	1200
P	0.5	0.5	0.5	0.5	0.5	0.5	0.5	0.5	0.5	0.5	0.5	0.5	0.5	0.5
Point Analysis	MG12Plg3	MG12Plg4	MG12Plg5	MG12Plg6	MG12Plg7	MG12Plg8	MG12Plg9	MG14Plg1	MG14Plg2	MG14Plg3	MG14Plg4	MG14Plg5	MG14Plg6	MG14Plg7
SiO_2	51.72	52.50	51.33	52.73	49.40	51.60	49.77	51.77	52.60	52.33	51.99	51.82	51.14	52.00
TiO_2	0.09	0.23	0.09	0.18	0.12	0.14	0.09	0.07	0.09	0.08	0.12	0.15	0.24	0.11
Al_2O_3	28.55	27.30	27.67	28.43	29.32	28.97	30.42	29.27	28.69	29.25	29.19	27.89	26.57	27.30
Cr_2O_3	0.00	0.04	0.00	0.00	0.00	0.00	0.03	0.02	0.00	0.00	0.07	0.03	0.00	0.02
FeO	0.00	0.00	0.00	0.00	0.00	0.61	0.00	0.48	0.57	0.49	0.50	0.00	0.00	0.35
MgO	1.22	2.90	2.01	0.52	1.83	0.65	0.79	0.20	0.31	0.15	0.29	0.60	0.92	0.40
MnO	0.00	0.00	0.00	0.00	0.01	0.02	0.00	0.04	0.00	0.04	0.00	0.00	0.00	0.04
NiO	0.01	0.01	0.10	0.08	0.05	0.05	0.05	0.05	0.08	0.00	0.00	0.06	0.05	0.00
CaO	11.60	10.09	11.52	11.24	13.17	12.66	13.33	13.04	13.57	13.41	13.75	13.59	13.91	12.67
Na_2O	4.26	4.70	3.99	4.59	3.02	3.70	3.35	3.73	3.64	3.60	3.42	3.76	3.64	4.10
K_2O	0.20	0.22	0.15	0.19	0.08	0.12	0.10	0.08	0.06	0.10	0.07	0.09	0.09	0.11
Total	98.36	98.99	97.70	98.56	97.77	98.52	98.71	98.76	99.62	99.46	99.39	98.74	97.57	97.33
Si	2.38	2.38	2.38	2.42	2.30	2.38	2.30	2.39	2.41	2.40	2.39	2.39	2.39	2.43
Ti	0.00	0.01	0.00	0.01	0.00	0.00	0.00	0.00	0.00	0.00	0.00	0.01	0.01	0.00
Al	1.55	1.46	1.51	1.54	1.61	1.58	1.65	1.59	1.55	1.58	1.58	1.52	1.46	1.50
Cr	0.00	0.00	0.00	0.00	0.00	0.00	0.00	0.00	0.00	0.00	0.00	0.00	0.00	0.00
Fe^{2+}	0.00	0.00	0.00	0.00	0.00	0.02	0.00	0.02	0.02	0.02	0.02	0.00	0.00	0.01
Mg	0.08	0.20	0.14	0.04	0.13	0.04	0.05	0.01	0.02	0.01	0.02	0.04	0.06	0.03
Mn	0.00	0.00	0.00	0.00	0.00	0.00	0.00	0.00	0.00	0.00	0.00	0.00	0.00	0.00
Ni	0.00	0.00	0.00	0.00	0.00	0.00	0.00	0.00	0.00	0.00	0.00	0.00	0.00	0.00
Ca	0.57	0.49	0.57	0.55	0.66	0.63	0.66	0.64	0.67	0.66	0.68	0.67	0.70	0.63
Na	0.38	0.41	0.36	0.41	0.27	0.33	0.30	0.33	0.32	0.32	0.30	0.34	0.33	0.37
K	0.01	0.01	0.01	0.01	0.00	0.01	0.01	0.00	0.00	0.01	0.00	0.01	0.01	0.01
Na+Ca	0.95	0.90	0.93	0.96	0.93	0.96	0.96	0.98	0.99	0.98	0.98	1.01	1.03	1.01
X_{An}	0.59	0.54	0.61	0.57	0.70	0.65	0.68	0.66	0.67	0.67	0.69	0.66	0.68	0.63

Sample	MG14	MG14
Run duration	24	24
Melt	AH6	AH6
IMA (wt%)	50	50
T	1200	1200
P	0.5	0.5
Point Analysis	MG14Plg8	MG14Plg9
SiO_2	51.55	51.76
TiO_2	0.09	0.07
Al_2O_3	27.20	28.42
Cr_2O_3	0.00	0.02
FeO	0.00	0.16
MgO	0.24	0.45
MnO	0.04	0.07
NiO	0.00	0.07
CaO	12.84	13.72
Na_2O	4.10	3.68
K_2O	0.11	0.09
Total	96.85	98.92
Si	2.42	2.39
Ti	0.00	0.00
Al	1.51	1.54
Cr	0.00	0.00
Fe^{2+}	0.00	0.01
Mg	0.02	0.03
Mn	0.00	0.00
Ni	0.00	0.00
Ca	0.65	0.68
Na	0.37	0.33
K	0.01	0.01
Na+Ca	1.02	1.01
X_{An}	0.63	0.67

Table 7-5 *Major element composition of plagioclase from step-cooled experiments performed at 0.5 GPa, from 1300 down to 1100°C.*

Sample	MG16	MG16	MG16
Run duration	72	72	72
Melt	AH6	AH6	AH6
IMA (wt%)[a]	50	50	50
T[b]	$1300_{(i)}$-$1100_{(f)}$	$1300_{(i)}$-$1100_{(f)}$	$1300_{(i)}$-$1100_{(f)}$
P[c]	0.5	0.5	0.5
Point Analysis	MG16Plg1	MG16Plg2	MG16Plg3
SiO_2	49.95	51.46	51.35
TiO_2	0.01	0.03	0.11
Al_2O_3	30.91	30.18	30.51
Cr_2O_3	0.03	0.00	0.00
FeO	0.00	0.12	0.34
MgO	0.31	0.25	0.33
MnO	0.00	0.00	0.04
NiO	0.03	0.04	0.00
CaO	15.18	14.00	14.39
Na_2O	3.00	3.59	3.31
K_2O	0.08	0.04	0.03
Total	99.97	99.97	100.41
Si	2.28	2.34	2.33
Ti	0.00	0.00	0.00
Al	1.66	1.62	1.63
Cr	0.00	0.00	0.00
Fe^{2+}	0.00	0.00	0.01
Mg	0.02	0.02	0.02
Mn	0.00	0.00	0.00
Ni	0.00	0.00	0.00
Ca	0.74	0.68	0.70
Na	0.27	0.32	0.29
K	0.00	0.00	0.00
X_{An}[d]	0.73	0.68	0.71

Cations are calculated with the Program NORM (version 2019) edited by Ulmer, P., and Poli, S. [a] Initial melt amount. [b] Temperature. [c] Pressure. [d] X_{An} = Ca/(Ca+Na).

Table 7-6 *Major element composition of clinopyroxene from isothermal experiments performed at 0.5 GPa, 1200°C.*

Sample	MG10	MG10	MG10	MG10	MG10	MG10	MG10	MG10	MG10	MG10	MG12	MG12	MG12	MG12
Run duration	24	24	24	24	24	24	24	24	24	24	24	24	24	24
Melt	AH6	AH6	AH6	AH6	AH6	AH6	AH6	AH6	AH6	AH6	AH6	AH6	AH6	AH6
IMA (wt%)[a]	10	10	10	10	10	10	10	10	10	10	25	25	25	25
T[b]	1200	1200	1200	1200	1200	1200	1200	1200	1200	1200	1200	1200	1200	1200
P[c]	0.5	0.5	0.5	0.5	0.5	0.5	0.5	0.5	0.5	0.5	0.5	0.5	0.5	0.5
Point Analysis	MG10Cpx1	MG10Cpx2	MG10Cpx3	MG10Cpx4	MG10Cpx5	MG10Cpx6	MG10Cpx7	MG10Cpx8	MG10Cpx9	MG10Cpx10	MG12Cpx1	MG12Cpx2	MG12Cpx3	MG12Cpx4
SiO_2	51.88	51.52	51.69	51.66	50.70	51.09	50.15	51.64	51.38	51.01	50.73	50.15	46.40	48.74
TiO_2	1.46	1.21	1.02	1.45	2.16	1.81	2.25	1.27	1.49	1.65	2.24	2.65	4.24	2.99
Al_2O_3	5.20	4.48	4.48	4.66	5.26	5.75	6.25	4.76	5.39	5.95	3.73	4.45	8.89	6.64
Cr_2O_3	0.11	0.12	0.15	0.17	0.21	0.16	0.22	0.17	0.14	0.10	0.11	0.32	0.12	0.20
FeO	3.78	3.78	4.00	3.92	3.73	3.81	3.62	3.84	3.62	3.54	3.16	3.37	4.43	3.29
MgO	16.97	17.28	17.90	16.88	16.73	17.67	16.23	19.15	17.12	17.11	16.80	16.39	12.98	15.41
MnO	0.10	0.04	0.12	0.10	0.12	0.13	0.14	0.05	0.13	0.10	0.08	0.07	0.07	0.09
NiO	0.06	0.06	0.03	0.05	0.07	0.06	0.02	0.10	0.03	0.01	0.03	0.01	0.04	0.10
CaO	20.63	20.43	19.94	20.56	20.53	20.51	21.06	18.87	20.70	20.64	20.59	21.09	21.52	20.34
Na_2O	0.31	0.35	0.34	0.42	0.49	0.41	0.46	0.39	0.42	0.40	0.66	0.36	0.65	0.65
K_2O	0.00	0.01	0.00	0.01	0.00	0.00	0.00	0.03	0.01	0.02	0.01	0.01	0.01	0.00
Total	100.50	99.28	99.67	99.88	100.00	101.40	100.40	100.27	100.43	100.53	98.14	98.87	99.35	98.45
Si	1.87	1.88	1.88	1.88	1.85	1.83	1.82	1.86	1.86	1.84	1.88	1.85	1.72	1.80
Ti	0.04	0.03	0.03	0.04	0.06	0.05	0.06	0.03	0.04	0.04	0.06	0.07	0.12	0.08
Al	0.22	0.19	0.19	0.20	0.23	0.24	0.27	0.20	0.23	0.25	0.16	0.19	0.39	0.29
Cr	0.00	0.00	0.00	0.00	0.01	0.00	0.01	0.00	0.00	0.00	0.00	0.01	0.00	0.01
Fe^{2+}	0.11	0.12	0.12	0.12	0.11	0.11	0.11	0.12	0.11	0.11	0.10	0.10	0.14	0.10
Mg	0.91	0.94	0.97	0.92	0.91	0.94	0.88	1.03	0.92	0.92	0.93	0.90	0.72	0.85
Mn	0.00	0.00	0.00	0.00	0.00	0.00	0.00	0.00	0.00	0.00	0.00	0.00	0.00	0.00
Ni	0.00	0.00	0.00	0.00	0.00	0.00	0.00	0.00	0.00	0.00	0.00	0.00	0.00	0.00
Ca	0.80	0.80	0.78	0.80	0.80	0.79	0.82	0.73	0.80	0.80	0.82	0.83	0.85	0.81
Na	0.02	0.02	0.02	0.03	0.03	0.03	0.03	0.03	0.03	0.03	0.05	0.03	0.05	0.05
K	0.00	0.00	0.00	0.00	0.00	0.00	0.00	0.00	0.00	0.00	0.00	0.00	0.00	0.00
Sum	3.99	4.00	4.00	3.99	4.00	4.01	4.00	4.01	4.00	4.00	4.00	3.99	3.99	3.99
X_{Mg}[d]	0.89	0.89	0.89	0.89	0.89	0.89	0.89	0.90	0.89	0.90	0.91	0.90	0.84	0.89

Cations are calculated with the Program NORM (version 2019) edited by Ulmer, P., and Poli, S. [a] Initial melt amount. [b] Temperature. [c] Pressure. [d] X_{Mg} = Mg/(Mg+Fe).

Sample	MG12	MG12	MG12	MG12	MG12	MG12	MG12	MG12	MG14	MG14	MG14	MG14	MG14	MG14
Run duration	24	24	24	24	24	24	24	24	24	24	24	24	24	24
Melt	AH6	AH6	AH6	AH6	AH6	AH6	AH6	AH6	AH6	AH6	AH6	AH6	AH6	AH6
IMA (wt%)	25	25	25	25	25	25	25	25	50	50	50	50	50	50
T	1200	1200	1200	1200	1200	1200	1200	1200	1200	1200	1200	1200	1200	1200
P	0.5	0.5	0.5	0.5	0.5	0.5	0.5	0.5	0.5	0.5	0.5	0.5	0.5	0.5
Point Analysis	MG12Cpx5	MG12Cpx6	MG12Cpx7	MG12Cpx8	MG12Cpx9	MG12Cpx10	MG12Cpx11	MG12Cpx12	MG14Cpx1	MG14Cpx2	MG14Cpx3	MG14Cpx4	MG14Cpx5	MG14Cpx6
SiO_2	48.46	50.56	49.05	51.76	51.24	51.24	51.65	51.21	50.84	51.27	52.09	52.54	51.27	51.79
TiO_2	3.24	1.69	2.84	1.03	1.22	1.29	0.94	1.00	1.30	0.81	1.32	1.15	1.59	1.67
Al_2O_3	5.90	7.69	5.52	3.43	4.33	4.24	2.80	3.45	6.52	4.96	5.03	3.95	4.92	5.23
Cr_2O_3	0.13	0.15	0.10	0.28	0.29	0.27	0.06	0.28	0.20	0.18	0.15	0.16	0.18	0.23
FeO	3.32	3.43	3.66	3.62	3.27	3.31	3.79	3.74	6.38	5.58	4.65	4.87	5.08	4.59
MgO	15.69	15.06	16.29	17.63	17.13	16.93	18.98	17.77	14.96	19.51	15.89	16.16	15.31	15.61
MnO	0.09	0.05	0.11	0.18	0.06	0.05	0.09	0.15	0.20	0.14	0.17	0.10	0.10	0.09
NiO	0.06	0.14	0.03	0.00	0.07	0.07	0.06	0.03	0.12	0.00	0.12	0.00	0.05	0.08
CaO	20.52	20.50	20.06	20.52	20.73	20.90	18.83	20.31	20.92	18.86	21.16	21.14	21.46	21.44
Na_2O	0.62	0.84	0.59	0.21	0.30	0.30	0.24	0.25	0.38	0.38	0.45	0.30	0.49	0.50
K_2O	0.00	0.03	0.01	0.00	0.00	0.00	0.01	0.00	0.01	0.00	0.02	0.01	0.02	0.01
Total	98.03	100.14	98.26	98.66	98.64	98.60	97.45	98.19	101.83	101.69	101.05	100.39	100.47	101.24
Si	1.80	1.83	1.82	1.90	1.88	1.89	1.92	1.90	1.84	1.84	1.88	1.91	1.87	1.87
Ti	0.09	0.05	0.08	0.03	0.03	0.04	0.03	0.03	0.04	0.02	0.04	0.03	0.04	0.05
Al	0.26	0.33	0.24	0.15	0.19	0.18	0.12	0.15	0.28	0.21	0.21	0.17	0.21	0.22
Cr	0.00	0.00	0.00	0.01	0.01	0.01	0.00	0.01	0.01	0.01	0.00	0.00	0.01	0.01
Fe^{2+}	0.10	0.10	0.11	0.11	0.10	0.10	0.12	0.12	0.19	0.17	0.14	0.15	0.15	0.14
Mg	0.87	0.81	0.90	0.97	0.94	0.93	1.05	0.98	0.81	1.04	0.86	0.87	0.83	0.84
Mn	0.00	0.00	0.00	0.01	0.00	0.00	0.00	0.00	0.01	0.00	0.01	0.00	0.00	0.00
Ni	0.00	0.00	0.00	0.00	0.00	0.00	0.00	0.00	0.00	0.00	0.00	0.00	0.00	0.00
Ca	0.82	0.80	0.80	0.81	0.82	0.82	0.75	0.81	0.81	0.73	0.82	0.82	0.84	0.83
Na	0.04	0.06	0.04	0.02	0.02	0.02	0.02	0.02	0.03	0.03	0.03	0.02	0.03	0.03
K	0.00	0.00	0.00	0.00	0.00	0.00	0.00	0.00	0.00	0.00	0.00	0.00	0.00	0.00
Sum	4.00	3.99	4.00	4.00	3.99	3.99	4.00	4.01	4.00	4.04	3.99	3.98	4.00	3.99
X_{Mg}	0.89	0.89	0.89	0.90	0.90	0.90	0.90	0.89	0.81	0.86	0.86	0.86	0.84	0.86

Sample	MG14	MG14	MG14	MG14
Run duration	24	24	24	24
Melt	AH6	AH6	AH6	AH6
IMA (wt%)	50	50	50	50
T	1200	1200	1200	1200
P	0.5	0.5	0.5	0.5
Point Analysis	MG14Cpx7	MG14Cpx8	MG14Cpx9	MG14Cpx10
SiO_2	49.95	51.13	51.15	50.92
TiO_2	1.82	1.69	1.58	1.91
Al_2O_3	5.37	4.82	4.78	5.71
Cr_2O_3	0.16	0.21	0.16	0.24
FeO	5.68	5.52	5.07	4.82
MgO	14.95	15.22	15.51	15.31
MnO	0.12	0.14	0.17	0.15
NiO	0.00	0.03	0.09	0.03
CaO	21.50	21.42	21.12	21.12
Na_2O	0.39	0.44	0.50	0.48
K_2O	0.01	0.01	0.00	0.03
Total	99.95	100.64	100.14	100.71
Si	1.84	1.87	1.87	1.85
Ti	0.05	0.05	0.04	0.05
Al	0.23	0.21	0.21	0.24
Cr	0.00	0.01	0.00	0.01
Fe^{2+}	0.18	0.17	0.16	0.15
Mg	0.82	0.83	0.85	0.83
Mn	0.00	0.00	0.01	0.00
Ni	0.00	0.00	0.00	0.00
Ca	0.85	0.84	0.83	0.82
Na	0.03	0.03	0.04	0.03
K	0.00	0.00	0.00	0.00
Sum	4.00	4.00	4.00	3.99
X_{Mg}	0.82	0.83	0.85	0.85

Table 7-7 *Major element composition of clinopyroxene from step-cooled experiments performed at 0.5 GPa, from 1300 down to 1100°C.*

Sample	MG4	MG4	MG4	MG4	MG4	MG4	MG4	MG4	MG4	MG4	MG4	MG4	MG4	MG4
Run duration	72	72	72	72	72	72	72	72	72	72	72	72	72	72
Melt	AH6	AH6	AH6	AH6	AH6	AH6	AH6	AH6	AH6	AH6	AH6	AH6	AH6	AH6
IMA (wt%)[a]	25	25	25	25	25	25	25	25	25	25	25	25	25	25
T[b]	$1300_{(i)}$-$1100_{(f)}$	$1300_{(i)}$-$1100_{(f)}$	$1300_{(i)}$-$1100_{(f)}$	$1300_{(i)}$-$1100_{(f)}$	$1300_{(i)}$-$1100_{(f)}$	$1300_{(i)}$-$1100_{(f)}$	$1300_{(i)}$-$1100_{(f)}$	$1300_{(i)}$-$1100_{(f)}$	$1300_{(i)}$-$1100_{(f)}$	$1300_{(i)}$-$1100_{(f)}$	$1300_{(i)}$-$1100_{(f)}$	$1300_{(i)}$-$1100_{(f)}$	$1300_{(i)}$-$1100_{(f)}$	$1300_{(i)}$-$1100_{(f)}$
P[c]	0.5	0.5	0.5	0.5	0.5	0.5	0.5	0.5	0.5	0.5	0.5	0.5	0.5	0.5
Point Analysis	MG4Cpx1	MG4Cpx2	MG4Cpx3	MG4Cpx4	MG4Cpx5	MG4Cpx6	MG4Cpx7	MG4Cpx8	MG4Cpx9	MG4Cpx10	MG4Cpx11	MG4Cpx12	MG4Cpx13	MG4Cpx14
SiO_2	49.73	49.01	49.05	49.64	49.24	49.01	47.77	51.08	51.50	49.40	50.30	50.45	51.07	50.60
TiO_2	0.72	0.78	0.80	0.80	0.70	0.84	0.97	0.65	0.60	0.89	0.80	0.84	0.65	0.88
Al_2O_3	8.79	8.31	8.90	8.43	8.08	8.66	8.97	7.58	7.20	9.01	7.71	7.68	7.20	7.35
Cr_2O_3	0.31	0.24	0.17	0.20	0.23	0.10	0.19	0.16	0.23	0.18	0.20	0.25	0.21	0.17
FeO	2.88	2.96	2.92	2.77	2.96	2.91	2.76	2.80	2.74	2.80	2.63	2.78	2.82	2.93
MgO	16.20	16.47	15.94	16.39	16.51	16.49	15.98	17.32	17.31	16.40	16.34	16.61	16.87	16.82
MnO	0.10	0.13	0.08	0.04	0.09	0.07	0.08	0.10	0.10	0.10	0.13	0.11	0.09	0.07
NiO	0.00	0.06	0.00	0.00	0.00	0.00	0.05	0.03	0.10	0.00	0.04	0.00	0.06	0.00
CaO	21.67	21.79	21.46	21.50	21.84	21.09	21.27	20.39	19.98	20.69	20.56	20.46	20.41	20.22
Na_2O	0.33	0.35	0.26	0.28	0.31	0.32	0.26	0.30	0.28	0.34	0.31	0.25	0.34	0.30
K_2O	0.00	0.01	0.01	0.01	0.01	0.00	0.02	0.00	0.01	0.00	0.00	0.00	0.00	0.00
Total	100.72	100.11	99.59	100.05	99.97	99.50	98.32	100.42	100.04	99.81	99.03	99.44	99.72	99.34
Si	1.79	1.78	1.79	1.80	1.79	1.79	1.77	1.83	1.85	1.79	1.83	1.83	1.85	1.84
Ti	0.02	0.02	0.02	0.02	0.02	0.02	0.03	0.02	0.02	0.02	0.02	0.02	0.02	0.02
Al	0.37	0.36	0.38	0.36	0.35	0.37	0.39	0.32	0.31	0.38	0.33	0.33	0.31	0.31
Cr	0.01	0.01	0.00	0.01	0.01	0.00	0.01	0.00	0.01	0.01	0.01	0.01	0.01	0.00
Fe^{2+}	0.09	0.09	0.09	0.08	0.09	0.09	0.09	0.08	0.08	0.08	0.08	0.08	0.09	0.09
Mg	0.87	0.89	0.87	0.88	0.90	0.90	0.88	0.93	0.93	0.89	0.89	0.90	0.91	0.91
Mn	0.00	0.00	0.00	0.00	0.00	0.00	0.00	0.00	0.00	0.00	0.00	0.00	0.00	0.00
Ni	0.00	0.00	0.00	0.00	0.00	0.00	0.00	0.00	0.00	0.00	0.00	0.00	0.00	0.00
Ca	0.84	0.85	0.84	0.83	0.85	0.82	0.84	0.78	0.77	0.80	0.80	0.80	0.79	0.79
Na	0.02	0.03	0.02	0.02	0.02	0.02	0.02	0.02	0.02	0.02	0.02	0.02	0.02	0.02
K	0.00	0.00	0.00	0.00	0.00	0.00	0.00	0.00	0.00	0.00	0.00	0.00	0.00	0.00
Sum	4.01	4.03	4.01	4.01	4.02	4.02	4.02	4.00	3.99	4.00	3.99	3.99	3.99	3.99
X_{Mg}[d]	0.91	0.91	0.91	0.91	0.91	0.91	0.91	0.92	0.92	0.91	0.92	0.91	0.91	0.91

Cations are calculated with the Program NORM (version 2019) edited by Ulmer, P., and Poli, S. [a] Initial melt amount. [b] Temperature. [c] Pressure. [d] X_{Mg} = Mg/(Mg+Fe).

Sample	MG4	MG4	MG4	MG4	MG4	MG4	MG4	MG4	MG4	MG4	MG4	MG4	MG4	MG4
Run duration	72	72	72	72	72	72	72	72	72	72	72	72	72	72
Melt	AH6	AH6	AH6	AH6	AH6	AH6	AH6	AH6	AH6	AH6	AH6	AH6	AH6	AH6
IMA (wt%)	25	25	25	25	25	25	25	25	25	25	25	25	25	25
T	$1300_{(i)}$-$1100_{(f)}$	$1300_{(i)}$-$1100_{(f)}$	$1300_{(i)}$-$1100_{(f}$	$1300_{(i)}$-$1100_{(f)}$	$1300_{(i)}$-$1100_{(f)}$	$1300_{(i)}$-$1100_{(f}$	$1300_{(i)}$-$1100_{(f}$	$1300_{(i)}$-$1100_{(f)}$	$1300_{(i)}$-$1100_{(f}$	$1300_{(i)}$-$1100_{(f}$	$1300_{(i)}$-$1100_{(f}$	$1300_{(i)}$-$1100_{(f)}$	$1300_{(i)}$-$1100_{(f)}$	$1300_{(i)}$-$1100_{(f)}$
P	0.5	0.5	0.5	0.5	0.5	0.5	0.5	0.5	0.5	0.5	0.5	0.5	0.5	0.5
Point Analysis	MG4Cpx15	MG4Cpx16	MG4Cpx17	MG4Cpx18	MG4Cpx19	MG4Cpx20	MG4Cpx21	MG4Cpx22	MG4Cpx23	MG4Cpx24	MG4Cpx25	MG4Cpx26	MG4Cpx27	MG4Cpx28
SiO_2	50.39	50.65	53.02	50.62	52.75	51.03	50.37	50.27	50.81	50.43	53.12	51.43	49.52	49.30
TiO_2	0.74	0.64	0.41	0.68	0.37	0.59	0.75	0.58	0.59	0.57	0.43	0.54	0.75	0.87
Al_2O_3	7.45	8.05	4.13	7.48	4.09	7.49	7.28	7.64	7.33	7.31	3.77	6.60	8.89	8.66
Cr_2O_3	0.23	0.22	0.09	0.30	0.19	0.20	0.29	0.21	0.19	0.24	0.14	0.15	0.21	0.24
FeO	2.67	2.66	2.98	3.00	3.19	2.89	2.83	2.97	2.73	2.80	3.62	3.13	2.89	2.86
MgO	16.70	16.84	18.68	17.32	18.94	16.69	16.62	16.83	17.07	17.23	19.63	17.48	16.08	15.83
MnO	0.07	0.08	0.07	0.07	0.11	0.08	0.10	0.11	0.07	0.07	0.09	0.13	0.06	0.12
NiO	0.11	0.00	0.00	0.00	0.00	0.02	0.00	0.00	0.05	0.00	0.00	0.03	0.08	0.02
CaO	20.69	20.85	19.97	20.20	19.64	20.61	20.42	20.64	20.41	20.25	18.48	20.12	20.98	21.24
Na_2O	0.30	0.30	0.27	0.32	0.19	0.27	0.27	0.31	0.33	0.32	0.22	0.27	0.29	0.31
K_2O	0.00	0.00	0.00	0.00	0.00	0.00	0.00	0.01	0.00	0.01	0.01	0.00	0.00	0.01
Total	99.36	100.30	99.63	99.99	99.47	99.86	98.93	99.56	99.60	99.23	99.51	99.89	99.75	99.45
Si	1.83	1.82	1.92	1.83	1.91	1.84	1.84	1.83	1.84	1.83	1.92	1.86	1.80	1.80
Ti	0.02	0.02	0.01	0.02	0.01	0.02	0.02	0.02	0.02	0.02	0.01	0.01	0.02	0.02
Al	0.32	0.34	0.18	0.32	0.17	0.32	0.31	0.33	0.31	0.31	0.16	0.28	0.38	0.37
Cr	0.01	0.01	0.00	0.01	0.01	0.01	0.01	0.01	0.01	0.01	0.00	0.00	0.01	0.01
Fe^{2+}	0.08	0.08	0.09	0.09	0.10	0.09	0.09	0.09	0.08	0.09	0.11	0.09	0.09	0.09
Mg	0.90	0.90	1.01	0.93	1.02	0.90	0.90	0.91	0.92	0.93	1.06	0.94	0.87	0.86
Mn	0.00	0.00	0.00	0.00	0.00	0.00	0.00	0.00	0.00	0.00	0.00	0.00	0.00	0.00
Ni	0.00	0.00	0.00	0.00	0.00	0.00	0.00	0.00	0.00	0.00	0.00	0.00	0.00	0.00
Ca	0.81	0.80	0.77	0.78	0.76	0.80	0.80	0.80	0.79	0.79	0.72	0.78	0.82	0.83
Na	0.02	0.02	0.02	0.02	0.01	0.02	0.02	0.02	0.02	0.02	0.02	0.02	0.02	0.02
K	0.00	0.00	0.00	0.00	0.00	0.00	0.00	0.00	0.00	0.00	0.00	0.00	0.00	0.00
Sum	4.00	4.00	3.99	4.00	4.00	3.99	3.99	4.00	4.00	4.00	4.00	4.00	4.00	4.00
X_{Mg}	0.92	0.92	0.92	0.91	0.91	0.91	0.91	0.91	0.92	0.92	0.91	0.91	0.91	0.91

Sample	MG4	MG16	MG16	MG16	MG16	MG16	MG16	MG16
Run duration	72	72	72	72	72	72	72	72
Melt	AH6	AH6	AH6	AH6	AH6	AH6	AH6	AH6
IMA (wt%)	25	50	50	50	50	50	50	50
T	$1300_{(i)}$-$1100_{(f)}$	$1300_{(i)}$-$1100_{(f)}$	$1300_{(i)}$-$1100_{(f)}$	$1300_{(i)}$-$1100_{(f)}$	$1300_{(i)}$-$1100_{(f)}$	$1300_{(i)}$-$1100_{(f)}$	$1300_{(i)}$-$1100_{(f)}$	$1300_{(i)}$-$1100_{(f)}$
P	0.5	0.5	0.5	0.5	0.5	0.5	0.5	0.5
Point Analysis	MG4Cpx29	MG16Cpx1	MG16Cpx2	MG16Cpx3	MG16Cpx4	MG16Cpx5	MG16Cpx6	MG16Cpx7
SiO_2	50.50	51.18	50.09	51.19	52.42	51.22	51.00	50.81
TiO_2	0.71	0.68	0.93	0.63	0.75	1.09	1.22	1.35
Al_2O_3	7.50	6.44	9.51	7.28	3.88	5.98	6.43	6.72
Cr_2O_3	0.32	0.21	0.34	0.27	0.00	0.27	0.14	0.26
FeO	3.08	2.33	2.03	1.97	3.17	2.24	2.32	2.17
MgO	17.13	16.56	15.50	16.85	18.57	16.75	16.94	16.27
MnO	0.09	0.11	0.08	0.12	0.11	0.07	0.05	0.09
NiO	0.00	0.02	0.06	0.00	0.00	0.06	0.00	0.05
CaO	20.17	23.00	21.96	22.34	21.20	22.03	21.60	22.32
Na_2O	0.31	0.34	0.29	0.27	0.20	0.31	0.30	0.35
K_2O	0.01	0.02	0.01	0.00	0.00	0.00	0.00	0.00
Total	99.83	100.89	100.80	100.92	100.30	100.02	100.00	100.39
Si	1.83	1.84	1.79	1.83	1.89	1.85	1.84	1.83
Ti	0.02	0.02	0.03	0.02	0.02	0.03	0.03	0.04
Al	0.32	0.27	0.40	0.31	0.17	0.26	0.27	0.29
Cr	0.01	0.01	0.01	0.01	0.00	0.01	0.00	0.01
Fe^{2+}	0.09	0.07	0.06	0.06	0.10	0.07	0.07	0.07
Mg	0.92	0.89	0.83	0.90	1.00	0.90	0.91	0.88
Mn	0.00	0.00	0.00	0.00	0.00	0.00	0.00	0.00
Ni	0.00	0.00	0.00	0.00	0.00	0.00	0.00	0.00
Ca	0.78	0.89	0.84	0.86	0.82	0.85	0.84	0.86
Na	0.02	0.02	0.02	0.02	0.01	0.02	0.02	0.02
K	0.00	0.00	0.00	0.00	0.00	0.00	0.00	0.00
Sum	4.00	4.01	3.99	4.00	4.01	4.00	4.00	4.00
X_{Mg}	0.91	0.93	0.93	0.94	0.91	0.93	0.93	0.93

Table 7-8 *Major element composition of glass from isothermal experiments performed at 0.5 GPa, 1200, 1250 and 1300°C.*

Sample	MG10	MG10	MG10	MG10	MG10	MG12	MG12	MG12	MG14	MG14	MG11M1	MG11M1	MG11M1	MG11M1
Run duration	24	24	24	24	24	24	24	24	24	24	24	24	24	24
Melt	AH6	AH6	AH6	AH6	AH6	AH6	AH6	AH6	AH6	AH6	AH6	AH6	AH6	AH6
IMA (wt%)[a]	10	10	10	10	10	25	25	25	50	50	50	50	50	50
T[b]	1200	1200	1200	1200	1200	1200	1200	1200	1200	1200	1250	1250	1250	1250
P[c]	0.5	0.5	0.5	0.5	0.5	0.5	0.5	0.5	0.5	0.5	0.5	0.5	0.5	0.5
Point Analysis	MG10M1	MG10M2	MG10M3	MG10M4	MG10M8	MG12M1	MG12M2	MG12M4	MG14M1	MG14M2	MG11M1	MG11M2	MG11M3	MG11M4
SiO_2	51.71	51.89	51.29	51.56	52.01	50.17	49.63	49.05	49.04	49.52	48.33	48.65	48.95	48.54
TiO_2	1.25	1.17	1.18	1.27	1.43	2.97	2.75	2.94	1.93	2.34	0.83	0.77	0.92	0.83
Al_2O_3	16.69	16.25	16.93	16.36	17.28	18.03	17.11	17.25	16.05	17.67	15.22	15.94	16.96	15.50
Cr_2O_3	0.04	0.00	0.02	0.00	0.00	0.00	0.04	0.04	0.01	0.00	0.09	0.12	0.05	0.03
FeO	6.76	6.50	6.83	6.84	6.38	5.20	5.26	5.09	8.03	7.55	7.78	7.60	7.15	7.53
MgO	7.52	7.99	7.47	7.43	5.62	4.20	6.29	6.35	6.32	4.02	11.39	10.10	7.90	11.43
MnO	0.10	0.11	0.15	0.13	0.18	0.13	0.17	0.11	0.20	0.16	0.15	0.15	0.13	0.13
NiO	0.02	0.04	0.07	0.11	0.09	0.00	0.01	0.04	0.06	0.00	0.00	0.00	0.02	0.00
CaO	11.74	12.04	12.04	11.55	12.45	8.25	7.86	7.96	12.19	12.59	13.17	13.82	14.25	13.30
Na_2O	2.70	2.69	2.86	2.79	3.14	5.13	5.22	5.36	3.32	3.43	2.15	2.32	2.45	2.08
K_2O	0.37	0.35	0.34	0.38	0.37	1.79	1.66	1.73	0.35	0.43	0.14	0.15	0.15	0.14
Total	98.91	99.03	99.18	98.42	98.95	95.87	96.00	95.92	97.50	97.71	99.26	99.61	98.93	99.51
X_{Mg}[d]	0.67	0.69	0.66	0.66	0.61	0.59	0.68	0.69	0.58	0.49	0.72	0.70	0.66	0.73
X_{Ca}[e]	0.81	0.82	0.81	0.81	0.80	0.62	0.60	0.60	0.79	0.79	0.86	0.86	0.85	0.86

[a] Initial melt amount. [b] Temperature. [c] Pressure. [d] X_{Mg} = Mg/(Mg+Fe). [e] X_{Ca} = Ca/(Ca+Na). [f] Reaction experiment performed at 0.5 GPa, 1300°C from Francomme, J. E., Phd Thesis (2016-2017).

Sample	MG11M1	MG11M1	MG11M1	MG11M1	MG11M1	MG11M1	MG11M1	MG11M1	MG11M1	MG11M1	MG11M1	MG11M1	MG11M1	MG11M1
Run duration	24	24	24	24	24	24	24	24	24	24	24	24	24	24
Melt	AH6	AH6	AH6	AH6	AH6	AH6	AH6	AH6	AH6	AH6	AH6	AH6	AH6	AH6
IMA (wt%)	50	50	50	50	50	50	50	50	50	50	50	50	50	50
T	1250	1250	1250	1250	1250	1250	1250	1250	1250	1250	1250	1250	1250	1250
P	0.5	0.5	0.5	0.5	0.5	0.5	0.5	0.5	0.5	0.5	0.5	0.5	0.5	0.5
Point Analysis	MG11M5	MG11M6	MG11M7	MG11M8	MG11M9	MG11M10	MG11M11	MG11M12	MG11M13	MG11M14	MG11M15	MG11M16	MG11M17	MG11M18
SiO_2	48.36	48.30	49.21	48.40	48.89	48.41	48.67	49.12	48.91	48.46	48.59	48.42	48.53	48.58
TiO_2	0.79	0.89	0.84	0.88	0.76	0.76	0.77	0.88	0.80	0.77	0.81	0.76	0.86	0.74
Al_2O_3	15.25	15.58	16.99	15.65	15.54	15.55	15.22	15.37	14.97	14.75	15.27	15.31	15.13	15.54
Cr_2O_3	0.08	0.05	0.07	0.04	0.07	0.01	0.07	0.00	0.08	0.04	0.04	0.05	0.11	0.04
FeO	7.72	7.05	7.23	7.49	7.86	7.87	7.63	7.71	7.84	7.21	6.76	6.81	6.81	6.81
MgO	11.65	11.55	8.40	10.64	10.31	10.89	12.12	11.50	11.54	12.72	13.01	12.92	12.68	12.73
MnO	0.11	0.14	0.21	0.14	0.09	0.09	0.13	0.15	0.15	0.18	0.13	0.20	0.09	0.17
NiO	0.03	0.00	0.00	0.00	0.00	0.04	0.02	0.03	0.04	0.01	0.01	0.04	0.03	0.00
CaO	13.08	13.04	13.72	13.41	13.69	13.52	12.87	13.15	13.10	12.70	12.55	12.65	12.51	12.46
Na_2O	2.12	2.11	2.47	2.19	2.19	2.01	2.14	2.11	2.00	2.12	2.18	2.02	2.16	2.12
K_2O	0.13	0.14	0.17	0.16	0.14	0.12	0.13	0.13	0.12	0.11	0.12	0.14	0.13	0.13
Total	99.32	98.84	99.31	98.99	99.55	99.28	99.77	100.15	99.55	99.06	99.47	99.32	99.06	99.33
X_{Mg}	0.73	0.75	0.67	0.72	0.70	0.71	0.74	0.73	0.72	0.76	0.77	0.77	0.77	0.77
X_{Ca}	0.86	0.86	0.85	0.86	0.86	0.87	0.86	0.86	0.87	0.86	0.85	0.86	0.85	0.85

Sample	MG11M1	MG11M1	MG11M1	MG11M1	MG11M1	MG11M1	MG11M1	MG11M1	MG11M1	MG11M1	MG11M1	MG11M1	MG11M1	MG11M1
Run duration	24	24	24	24	24	24	24	24	24	24	24	24	24	24
Melt	AH6	AH6	AH6	AH6	AH6	AH6	AH6	AH6	AH6	AH6	AH6	AH6	AH6	AH6
IMA (wt%)	50	50	50	50	50	50	50	50	50	50	50	50	50	50
T	1250	1250	1250	1250	1250	1250	1250	1250	1250	1250	1250	1250	1250	1250
P	0.5	0.5	0.5	0.5	0.5	0.5	0.5	0.5	0.5	0.5	0.5	0.5	0.5	0.5
Point Analysis	MG11M19	MG11M20	MG11M21	MG11M22	MG11M23	MG11M24	MG11M25	MG11M26	MG11M27	MG11M28	MG11M29	MG11M30	MG11M31	MG11M32
SiO_2	49.15	48.23	48.78	48.65	48.70	49.34	48.61	48.49	49.12	49.12	49.21	48.60	48.67	49.23
TiO_2	0.77	0.71	0.73	0.74	0.71	0.80	0.87	0.80	0.84	0.79	0.80	0.81	0.73	0.79
Al_2O_3	15.58	15.12	15.32	15.24	15.28	15.67	15.32	15.67	15.29	15.45	15.41	15.01	15.36	15.54
Cr_2O_3	0.03	0.04	0.01	0.07	0.01	0.05	0.07	0.12	0.06	0.09	0.03	0.08	0.04	0.03
FeO	6.66	7.45	7.60	7.49	7.59	7.66	7.66	7.55	7.61	7.48	7.72	7.65	6.69	7.54
MgO	12.64	12.64	12.51	12.68	12.25	11.09	12.51	11.55	11.52	11.16	10.58	12.61	12.96	11.65
MnO	0.16	0.20	0.13	0.15	0.19	0.16	0.19	0.15	0.14	0.22	0.18	0.18	0.19	0.15
NiO	0.00	0.00	0.00	0.02	0.01	0.02	0.01	0.00	0.00	0.00	0.08	0.02	0.00	0.00
CaO	12.68	12.60	12.46	12.42	12.61	13.10	12.46	12.86	12.92	12.96	13.35	12.54	12.14	12.91
Na_2O	2.20	1.95	2.01	2.07	2.00	2.05	1.93	2.03	1.95	2.06	1.90	1.92	2.10	2.06
K_2O	0.13	0.11	0.09	0.12	0.12	0.12	0.11	0.11	0.12	0.12	0.09	0.13	0.12	0.10
Total	100.00	99.06	99.64	99.65	99.47	100.06	99.74	99.33	99.57	99.45	99.35	99.55	99.00	100.00
X_{Mg}	0.77	0.75	0.75	0.75	0.74	0.72	0.74	0.73	0.73	0.73	0.71	0.75	0.78	0.73
X_{Ca}	0.85	0.87	0.86	0.86	0.86	0.86	0.87	0.86	0.87	0.86	0.88	0.87	0.85	0.86

Sample	MG18	MG18	MG18	MG18	MG18	MG18	MG18	MG18	OM23[f]	OM23	OM23	OM23	OM23	OM23
Run duration	24	24	24	24	24	24	24	24	0.5	0.5	0.5	0.5	0.5	0.5
Melt	AH6	AH6	AH6	AH6	AH6	AH6	AH6	AH6	AH6	AH6	AH6	AH6	AH6	AH6
IMA (wt%)	10	10	10	10	10	10	10	10	9	9	9	9	9	9
T	1300	1300	1300	1300	1300	1300	1300	1300	1300	1300	1300	1300	1300	1300
P	0.5	0.5	0.5	0.5	0.5	0.5	0.5	0.5	0.5	0.5	0.5	0.5	0.5	0.5
Point Analysis	MG18M1	MG18M2	MG18M3	MG18M4	MG18M5	MG18M6	MG18M7	MG18M8	OM23M1	OM23M2	OM23M3	OM23M4	OM23M5	OM23M6
SiO_2	49.31	49.62	50.62	49.43	49.28	49.53	49.58	48.90	48.68	48.23	49.22	49.60	49.61	49.69
TiO_2	0.75	0.94	0.81	0.74	0.84	0.83	0.86	0.74	0.64	0.62	0.93	1.06	1.06	1.19
Al_2O_3	14.88	15.46	16.11	14.04	13.60	14.00	13.72	13.12	17.83	18.15	18.38	18.08	17.22	17.50
Cr_2O_3	0.00	0.10	0.00	0.05	0.00	0.00	0.07	0.10	0.11	0.02	0.10	0.08	0.07	0.04
FeO	9.96	10.20	9.40	10.00	10.31	10.30	10.35	10.30	8.30	8.48	7.74	7.67	8.03	7.98
MgO	6.96	5.66	4.91	10.47	10.26	10.00	9.99	10.43	6.84	6.95	6.12	5.51	7.20	6.19
MnO	0.17	0.19	0.20	0.21	0.25	0.20	0.20	0.22	0.16	0.15	0.12	0.16	0.16	0.08
NiO	0.00	0.00	0.03	0.00	0.00	0.00	0.03	0.00	0.06	0.02	0.00	0.00	0.01	0.00
CaO	12.49	12.87	12.93	11.21	11.63	11.47	11.58	11.59	15.07	15.14	15.04	15.28	13.82	14.42
Na_2O	2.37	2.25	2.45	1.84	1.61	1.69	1.84	1.73	2.25	2.16	2.28	2.48	2.67	2.79
K_2O	0.09	0.12	0.12	0.11	0.09	0.08	0.08	0.06	0.05	0.07	0.07	0.09	0.15	0.13
Total	96.98	97.41	97.59	98.11	97.87	98.11	98.30	97.20	100.00	100.00	100.00	100.00	100.00	100.00
X_{Mg}	0.56	0.50	0.48	0.65	0.64	0.63	0.63	0.64	0.59	0.59	0.59	0.56	0.61	0.58
X_{Ca}	0.84	0.85	0.84	0.86	0.88	0.87	0.86	0.87	0.87	0.87	0.87	0.86	0.84	0.84

Sample	OM23	OM23	OM23	OM23	OM23	OM23	OM23	OM23	OM23	OM23	MG1	MG1	MG1	MG1
Run duration	0.5	0.5	0.5	0.5	0.5	0.5	0.5	0.5	0.5	0.5	24	24	24	24
Melt	AH6	AH6	AH6	AH6	AH6	AH6	AH6	AH6	AH6	AH6	AH6	AH6	AH6	AH6
IMA (wt%)	9	9	9	9	9	9	9	9	9	9	25	25	25	25
T	1300	1300	1300	1300	1300	1300	1300	1300	1300	1300	1300	1300	1300	1300
P	0.5	0.5	0.5	0.5	0.5	0.5	0.5	0.5	0.5	0.5	0.5	0.5	0.5	0.5
Point Analysis	OM23M7	OM23M8	OM23M9	OM23M10	OM23M11	OM23M12	OM23M13	OM23M14	OM23M15	OM23M16	MG1M1	MG1M2	MG1M3	MG1M4
SiO_2	49.59	49.43	49.54	50.10	50.32	49.78	49.40	48.60	48.96	48.94	49.61	49.68	49.78	49.65
TiO_2	1.18	1.07	1.27	1.27	1.40	1.18	1.29	0.94	1.13	1.20	0.85	0.80	0.75	0.83
Al_2O_3	16.54	16.90	17.41	17.84	18.66	17.00	16.37	14.50	15.57	15.63	15.73	14.68	14.82	15.00
Cr_2O_3	0.00	0.00	0.04	0.11	0.00	0.04	0.09	0.06	0.03	0.00	0.05	0.02	0.01	0.03
FeO	8.20	8.26	8.19	7.65	7.14	7.71	8.38	8.58	7.90	7.67	8.52	9.01	9.26	9.17
MgO	7.90	7.68	6.55	5.56	4.41	7.10	7.96	12.27	11.65	11.81	11.02	13.08	11.96	10.96
MnO	0.20	0.14	0.21	0.11	0.14	0.17	0.11	0.19	0.10	0.13	0.20	0.20	0.15	0.20
NiO	0.00	0.02	0.00	0.00	0.00	0.03	0.00	0.00	0.01	0.00	0.04	0.02	0.00	0.01
CaO	13.62	13.68	14.07	14.33	14.87	13.99	13.73	12.40	11.72	11.79	12.13	11.78	12.21	12.53
Na_2O	2.64	2.64	2.58	2.89	2.89	2.86	2.53	2.34	2.77	2.66	2.21	1.94	1.98	2.04
K_2O	0.13	0.17	0.15	0.15	0.16	0.15	0.15	0.13	0.14	0.16	0.15	0.14	0.13	0.13
Total	100.00	100.00	100.00	100.00	100.00	100.00	100.00	100.00	100.00	100.00	100.51	101.35	101.05	100.55
X_{Mg}	0.63	0.62	0.59	0.56	0.52	0.62	0.63	0.72	0.72	0.73	0.70	0.72	0.70	0.68
X_{Ca}	0.84	0.84	0.85	0.83	0.84	0.83	0.84	0.84	0.81	0.82	0.85	0.86	0.86	0.86

Sample	MG1	MG1	MG1	MG1	MG1	MG1	MG1	MG1	MG1	MG1	MG1	MG1	MG1	MG1
Run duration	24	24	24	24	24	24	24	24	24	24	24	24	24	24
Melt	AH6	AH6	AH6	AH6	AH6	AH6	AH6	AH6	AH6	AH6	AH6	AH6	AH6	AH6
IMA (wt%)	25	25	25	25	25	25	25	25	25	25	25	25	25	25
T	1300	1300	1300	1300	1300	1300	1300	1300	1300	1300	1300	1300	1300	1300
P	0.5	0.5	0.5	0.5	0.5	0.5	0.5	0.5	0.5	0.5	0.5	0.5	0.5	0.5
Point Analysis	MG1M5	MG1M6	MG1M7	MG1M8	MG1M9	MG1M10	MG1M11	MG1M12	MG1M13	MG1M14	MG1M15	MG1M16	MG1M17	MG1M18
SiO_2	50.35	49.85	49.47	49.25	48.22	48.36	48.46	47.44	47.53	48.06	48.29	47.43	47.72	47.20
TiO_2	0.74	0.75	0.78	0.75	0.82	0.83	0.83	0.74	0.81	0.81	0.87	0.88	0.76	0.75
Al_2O_3	14.93	14.23	14.11	14.37	16.19	16.02	17.11	15.44	14.38	16.11	16.27	15.90	15.12	15.09
Cr_2O_3	0.00	0.04	0.03	0.01	0.00	0.10	0.04	0.03	0.02	0.00	0.01	0.07	0.03	0.05
FeO	9.19	9.43	9.50	9.37	8.68	8.64	8.39	8.88	9.67	8.98	9.00	8.81	9.24	9.22
MgO	11.47	13.59	13.35	11.97	9.25	9.46	8.18	11.73	12.14	8.66	8.57	9.74	11.73	12.06
MnO	0.19	0.18	0.20	0.17	0.19	0.22	0.23	0.20	0.21	0.20	0.24	0.24	0.22	0.21
NiO	0.06	0.00	0.00	0.01	0.00	0.04	0.07	0.00	0.08	0.00	0.00	0.05	0.00	0.00
CaO	12.38	11.77	11.75	12.28	13.00	12.62	13.11	12.12	12.40	13.42	13.17	12.88	12.26	12.01
Na_2O	2.07	1.84	1.86	1.87	2.33	2.22	2.45	2.03	1.76	2.09	2.07	2.09	2.01	2.05
K_2O	0.12	0.14	0.15	0.14	0.18	0.15	0.20	0.17	0.14	0.16	0.16	0.15	0.14	0.14
Total	101.50	101.82	101.19	100.20	98.86	98.67	99.07	98.79	99.15	98.49	98.65	98.23	99.23	98.78
X_{Mg}	0.69	0.72	0.72	0.70	0.66	0.66	0.64	0.70	0.69	0.63	0.63	0.66	0.69	0.70
X_{Ca}	0.86	0.86	0.86	0.87	0.85	0.85	0.84	0.86	0.88	0.87	0.86	0.86	0.86	0.85

Sample	MG1	MG1	MG1	MG1	MG1	MG1	MG1	MG1	MG1	MG1	MG1	MG1	MG1	MG1
Run duration	24	24	24	24	24	24	24	24	24	24	24	24	24	24
Melt	AH6	AH6	AH6	AH6	AH6	AH6	AH6	AH6	AH6	AH6	AH6	AH6	AH6	AH6
IMA (wt%)	25	25	25	25	25	25	25	25	25	25	25	25	25	25
T	1300	1300	1300	1300	1300	1300	1300	1300	1300	1300	1300	1300	1300	1300
P	0.5	0.5	0.5	0.5	0.5	0.5	0.5	0.5	0.5	0.5	0.5	0.5	0.5	0.5
Point Analysis	MG1M19	MG1M20	MG1M21	MG1M22	MG1M23	MG1M24	MG1M25	MG1M26	MG1M27	MG1M28	MG1M29	MG1M30	MG1M31	MG1M32
SiO_2	47.23	47.69	47.24	47.83	47.04	47.83	48.70	47.12	48.31	47.33	47.16	48.13	47.21	48.36
TiO_2	0.85	0.79	0.68	0.89	0.70	0.84	0.94	0.79	0.93	0.82	0.81	0.82	0.77	0.87
Al_2O_3	14.52	15.67	14.75	16.04	14.86	15.69	16.79	15.32	17.01	14.85	14.99	16.69	14.97	16.49
Cr_2O_3	0.09	0.00	0.05	0.04	0.07	0.03	0.02	0.03	0.00	0.06	0.05	0.05	0.04	0.08
FeO	9.18	8.90	9.43	9.02	9.33	9.36	8.55	9.42	8.88	9.72	9.21	8.50	9.38	8.82
MgO	12.48	10.54	12.67	9.84	12.62	10.79	9.45	11.63	8.41	12.69	13.30	9.01	12.22	9.37
MnO	0.15	0.14	0.22	0.23	0.16	0.16	0.17	0.16	0.15	0.19	0.12	0.09	0.19	0.22
NiO	0.00	0.00	0.05	0.00	0.04	0.00	0.01	0.06	0.00	0.00	0.04	0.00	0.00	0.00
CaO	12.01	12.52	12.21	12.86	12.11	12.84	13.04	12.27	13.30	12.07	11.78	13.04	12.26	12.67
Na_2O	2.01	2.19	1.93	2.05	2.06	2.07	2.26	1.93	2.25	1.92	2.02	2.29	1.95	2.35
K_2O	0.13	0.17	0.11	0.15	0.18	0.12	0.16	0.13	0.17	0.12	0.14	0.15	0.15	0.19
Total	98.65	98.61	99.34	98.96	99.17	99.73	100.09	98.87	99.41	99.77	99.62	98.78	99.14	99.42
X_{Mg}	0.71	0.68	0.71	0.66	0.71	0.67	0.66	0.69	0.63	0.70	0.72	0.65	0.70	0.65
X_{Ca}	0.86	0.85	0.86	0.86	0.85	0.86	0.85	0.86	0.86	0.86	0.85	0.85	0.86	0.84

Sample	MG1	MG1	MG1	MG1	MG1	MG1	MG1	MG1	MG1	MG1	MG1	MG1	MG1	MG5
Run duration	24	24	24	24	24	24	24	24	24	24	24	24	24	24
Melt	AH6	AH6	AH6	AH6	AH6	AH6	AH6	AH6	AH6	AH6	AH6	AH6	AH6	AH6
IMA (wt%)	25	25	25	25	25	25	25	25	25	25	25	25	25	50
T	1300	1300	1300	1300	1300	1300	1300	1300	1300	1300	1300	1300	1300	1300
P	0.5	0.5	0.5	0.5	0.5	0.5	0.5	0.5	0.5	0.5	0.5	0.5	0.5	0.5
Point Analysis	MG1M33	MG1M34	MG1M35	MG1M36	MG1M37	MG1M38	MG1M39	MG1M40	MG1M41	MG1M42	MG1M43	MG1M44	MG1M45	MG5M1
SiO_2	47.76	47.56	47.19	48.26	47.72	46.99	47.65	47.42	47.01	47.78	47.57	48.31	47.89	47.94
TiO_2	0.81	0.79	0.69	0.87	0.77	0.75	0.80	0.84	0.80	0.79	0.75	0.91	0.85	0.75
Al_2O_3	15.99	15.07	15.14	16.86	15.06	14.70	15.68	15.57	15.43	15.33	15.18	17.14	16.95	14.48
Cr_2O_3	0.07	0.01	0.03	0.04	0.07	0.09	0.00	0.02	0.08	0.09	0.05	0.02	0.07	0.00
FeO	8.87	9.38	9.34	8.89	8.99	9.47	9.19	9.32	10.10	9.01	9.23	8.79	8.69	7.77
MgO	10.67	12.95	12.45	7.92	10.90	13.51	10.73	11.66	11.65	11.99	12.00	8.30	8.49	13.25
MnO	0.22	0.22	0.19	0.23	0.22	0.21	0.22	0.17	0.18	0.18	0.18	0.13	0.18	0.20
NiO	0.07	0.04	0.05	0.00	0.01	0.00	0.00	0.00	0.04	0.04	0.00	0.05	0.00	0.00
CaO	12.53	11.81	12.07	13.69	12.28	11.79	12.67	12.44	12.20	12.07	12.18	13.53	13.31	12.66
Na_2O	2.10	2.04	2.02	2.34	2.14	1.87	2.03	2.07	2.11	1.87	2.00	2.23	2.14	1.98
K_2O	0.16	0.14	0.16	0.15	0.17	0.13	0.14	0.14	0.20	0.16	0.16	0.17	0.15	0.10
Total	99.25	100.01	99.34	99.24	98.34	99.51	99.11	99.65	99.79	99.30	99.30	99.58	98.73	99.14
X_{Mg}	0.68	0.71	0.70	0.61	0.68	0.72	0.68	0.69	0.67	0.70	0.70	0.63	0.64	0.75
X_{Ca}	0.86	0.85	0.86	0.85	0.85	0.86	0.86	0.86	0.85	0.87	0.86	0.86	0.86	0.86

Sample	MG5	MG5	MG5	MG5	MG5	MG5	MG5	MG5	MG5	MG5	MG5	MG5	MG5	MG5
Run duration	24	24	24	24	24	24	24	24	24	24	24	24	24	24
Melt	AH6	AH6	AH6	AH6	AH6	AH6	AH6	AH6	AH6	AH6	AH6	AH6	AH6	AH6
IMA (wt%)	50	50	50	50	50	50	50	50	50	50	50	50	50	50
T	1300	1300	1300	1300	1300	1300	1300	1300	1300	1300	1300	1300	1300	1300
P	0.5	0.5	0.5	0.5	0.5	0.5	0.5	0.5	0.5	0.5	0.5	0.5	0.5	0.5
Point Analysis	MG5M2	MG5M3	MG5M4	MG5M5	MG5M6	MG5M7	MG5M8	MG5M9	MG5M10	MG5M11	MG5M12	MG5M13	MG5M14	MG5M15
SiO_2	48.07	48.56	48.13	48.17	49.83	48.62	47.65	48.71	49.14	48.47	48.25	48.59	47.99	48.54
TiO_2	0.66	0.78	0.80	0.86	0.96	0.78	0.87	0.81	0.91	0.84	0.84	0.79	0.81	0.84
Al_2O_3	14.65	14.99	15.35	15.15	17.43	16.29	15.57	16.03	17.44	16.24	15.85	15.82	15.12	15.57
Cr_2O_3	0.09	0.00	0.02	0.06	0.06	0.07	0.04	0.08	0.02	0.02	0.03	0.00	0.11	0.03
FeO	7.81	7.57	7.63	7.72	7.08	7.32	7.29	7.43	6.79	7.41	7.46	7.55	7.67	7.64
MgO	12.68	12.66	11.24	11.95	7.59	11.50	12.64	11.96	8.53	11.36	10.69	11.65	13.85	12.76
MnO	0.14	0.17	0.13	0.16	0.15	0.16	0.17	0.14	0.14	0.15	0.14	0.15	0.24	0.14
NiO	0.03	0.00	0.00	0.03	0.00	0.00	0.00	0.00	0.01	0.00	0.05	0.01	0.00	0.05
CaO	12.87	12.90	13.32	13.23	14.64	12.93	12.84	13.11	13.74	13.31	13.61	13.25	12.23	12.56
Na_2O	1.91	2.13	2.09	2.09	2.33	2.20	2.00	2.15	2.57	2.12	2.09	2.10	1.89	1.87
K_2O	0.11	0.11	0.09	0.09	0.10	0.12	0.11	0.13	0.16	0.11	0.12	0.11	0.09	0.10
Total	99.03	99.87	98.81	99.51	100.17	99.99	99.18	100.54	99.46	100.02	99.13	100.02	100.00	100.10
X_{Mg}	0.74	0.75	0.72	0.73	0.66	0.74	0.76	0.74	0.69	0.73	0.72	0.73	0.76	0.75
X_{Ca}	0.87	0.86	0.86	0.86	0.86	0.85	0.87	0.86	0.84	0.86	0.87	0.86	0.87	0.87

Sample	MG5	MG5	MG5	MG5	MG5	MG5	MG5	MG5	MG5
Run duration	24	24	24	24	24	24	24	24	24
Melt	AH6	AH6	AH6	AH6	AH6	AH6	AH6	AH6	AH6
IMA (wt%)	50	50	50	50	50	50	50	50	50
T	1300	1300	1300	1300	1300	1300	1300	1300	1300
P	0.5	0.5	0.5	0.5	0.5	0.5	0.5	0.5	0.5
Point Analysis	MG5M16	MG5M17	MG5M18	MG5M19	MG5M20	MG5M21	MG5M22	MG5M23	MG5M24
SiO_2	49.28	48.44	48.21	48.27	49.02	47.96	48.29	48.57	47.80
TiO_2	0.92	0.75	0.84	0.82	0.86	0.77	0.77	0.84	0.80
Al_2O_3	16.19	15.32	15.98	15.71	15.83	14.96	14.80	15.20	14.99
Cr_2O_3	0.10	0.05	0.01	0.06	0.03	0.03	0.10	0.06	0.07
FeO	7.44	7.90	7.56	7.84	7.53	7.62	7.79	7.88	7.93
MgO	12.16	13.22	11.82	12.14	11.69	14.91	15.14	12.99	14.35
MnO	0.16	0.18	0.16	0.18	0.14	0.20	0.12	0.17	0.19
NiO	0.00	0.03	0.02	0.00	0.00	0.04	0.00	0.00	0.00
CaO	12.66	12.31	12.57	12.93	13.06	11.72	11.75	12.48	11.88
Na_2O	2.10	1.95	2.03	1.97	1.96	1.93	1.87	1.98	1.89
K_2O	0.08	0.09	0.11	0.09	0.09	0.09	0.11	0.11	0.10
Total	101.09	100.23	99.31	100.00	100.21	100.24	100.74	100.28	100.00
X_{Mg}	0.74	0.75	0.74	0.73	0.74	0.78	0.78	0.75	0.76
X_{Ca}	0.86	0.86	0.86	0.87	0.87	0.86	0.86	0.86	0.86

Table 7-9 *Major element composition of glass from step-cooled experiments performed at 0.5 GPa, from 1300 down to 1100°C.*

Sample	MG15	MG15	MG15	MG15	MG15	MG15	MG15	MG15	MG15	MG15	MG15	MG15	MG15	MG15
Run duration	72	72	72	72	72	72	72	72	72	72	72	72	72	72
Melt	AH6	AH6	AH6	AH6	AH6	AH6	AH6	AH6	AH6	AH6	AH6	AH6	AH6	AH6
IMA (wt%)[a]	10	10	10	10	10	10	10	10	10	10	10	10	10	10
T[b]	$1300_{(i)}$-$1100_{(f)}$	$1300_{(i)}$-$1100_{(f)}$	$1300_{(i)}$-$1100_{(f)}$	$1300_{(i)}$-$1100_{(f)}$	$1300_{(i)}$-$1100_{(f)}$	$1300_{(i)}$-$1100_{(f)}$	$1300_{(i)}$-$1100_{(f)}$	$1300_{(i)}$-$1100_{(f)}$	$1300_{(i)}$-$1100_{(f)}$	$1300_{(i)}$-$1100_{(f)}$	$1300_{(i)}$-$1100_{(f)}$	$1300_{(i)}$-$1100_{(f)}$	$1300_{(i)}$-$1100_{(f)}$	$1300_{(i)}$-$1100_{(f)}$
P[c]	0.5	0.5	0.5	0.5	0.5	0.5	0.5	0.5	0.5	0.5	0.5	0.5	0.5	0.5
Point Analysis	MG15M1	MG15M2	MG15M3	MG15M4	MG15M5	MG15M6	MG15M7	MG15M8	MG15M9	MG15M10	MG15M11	MG15M12	MG15M13	MG15M14
SiO_2	52.99	54.15	54.13	52.24	52.13	54.73	49.46	54.24	54.18	54.76	53.00	55.01	54.31	54.57
TiO_2	0.85	0.78	0.78	0.70	0.53	0.74	0.36	0.78	0.77	0.79	0.73	0.70	0.77	0.76
Al_2O_3	12.08	12.86	12.76	11.78	11.34	13.82	8.44	12.47	13.08	13.10	11.84	13.93	13.13	13.86
Cr_2O_3	0.01	0.07	0.04	0.04	0.02	0.04	0.08	0.01	0.07	0.02	0.09	0.04	0.05	0.01
FeO	7.97	7.67	7.54	8.61	7.88	6.43	8.50	7.63	7.20	7.25	7.86	6.47	6.90	6.48
MgO	0.20	0.18	0.20	0.16	0.20	0.19	0.12	0.20	0.15	0.20	0.14	0.14	0.17	0.15
MnO	0.04	0.00	0.00	0.04	0.00	0.01	0.00	0.00	0.00	0.00	0.08	0.04	0.00	0.06
NiO	7.34	6.10	4.75	10.76	12.33	7.42	26.08	6.97	6.62	5.72	9.52	8.66	6.36	8.00
CaO	12.50	12.95	12.86	11.39	11.11	11.48	5.06	12.54	12.28	12.85	11.86	11.09	12.36	11.44
Na_2O	1.76	1.88	1.72	1.67	1.55	2.01	1.41	1.65	1.80	1.80	1.60	2.00	1.83	2.09
K_2O	0.09	0.11	0.10	0.08	0.08	0.11	0.08	0.07	0.11	0.07	0.10	0.12	0.10	0.10
Total	95.83	96.75	94.88	97.47	97.17	96.98	99.59	96.56	96.26	96.56	96.82	98.20	95.98	97.52
X_{Mg}[d]	0.62	0.59	0.53	0.69	0.74	0.67	0.85	0.62	0.62	0.58	0.68	0.71	0.62	0.69
X_{Ca}[e]	0.80	0.79	0.80	0.79	0.80	0.76	0.66	0.81	0.79	0.80	0.80	0.75	0.79	0.75

[a] Initial melt amount. [b] Temperature. [c] Pressure. [d] X_{Mg} = Mg/(Mg+Fe). [e] X_{Ca} = Ca/(Ca+Na).

Sample	MG15	MG15	MG15	MG15	MG15	MG15	MG15	MG4	MG4	MG4	MG4	MG4	MG4	MG4
Run duration	72	72	72	72	72	72	72	72	72	72	72	72	72	72
Melt	AH6	AH6	AH6	AH6	AH6	AH6	AH6	AH6	AH6	AH6	AH6	AH6	AH6	AH6
IMA (wt%)	10	10	10	10	10	10	10	25	25	25	25	25	25	25
T	$1300_{(i)}$-$1100_{(f)}$	$1300_{(i)}$-$1100_{(f}$	$1300_{(i)}$-$1100_{(f}$	$1300_{(i)}$-$1100_{(f}$	$1300_{(i)}$-$1100_{(f)}$	$1300_{(i)}$-$1100_{(f}$	$1300_{(i)}$-$1100_{(f}$	$1300_{(i)}$-$1100_{(f)}$	$1300_{(i)}$-$1100_{(f}$	$1300_{(i)}$-$1100_{(f}$	$1300_{(i)}$-$1100_{(f}$	$1300_{(i)}$-$1100_{(f}$	$1300_{(i)}$-$1100_{(f)}$	$1300_{(i)}$-$1100_{(f)}$
P	0.5	0.5	0.5	0.5	0.5	0.5	0.5	0.5	0.5	0.5	0.5	0.5	0.5	0.5
Point Analysis	MG15M15	MG15M16	MG15M17	MG15M18	MG15M19	MG15M20	MG15M21	MG4M1	MG4M2	MG4M3	MG4M4	MG4M5	MG4M6	MG4M7
SiO_2	54.02	53.05	53.85	54.97	54.15	55.15	55.14	49.49	49.62	49.56	50.11	49.56	48.79	50.05
TiO_2	0.72	0.56	0.82	0.69	0.70	0.70	0.76	0.94	0.87	0.95	0.91	0.90	0.97	0.90
Al_2O_3	12.54	11.70	12.49	13.73	12.86	13.88	14.04	20.02	20.45	19.96	20.22	20.06	20.46	19.60
Cr_2O_3	0.06	0.07	0.00	0.00	0.05	0.01	0.02	0.03	0.04	0.04	0.00	0.03	0.01	0.02
FeO	7.05	5.01	5.34	4.68	4.89	4.71	4.53	5.34	5.25	5.28	4.96	5.08	5.26	5.06
MgO	0.12	0.12	0.13	0.09	0.18	0.15	0.14	0.11	0.13	0.13	0.13	0.09	0.06	0.21
MnO	0.03	0.00	0.01	0.01	0.03	0.00	0.04	0.04	0.02	0.00	0.03	0.00	0.00	0.01
NiO	7.49	20.44	11.84	9.65	11.76	8.70	8.82	7.65	7.75	7.88	7.09	7.06	7.57	7.52
CaO	12.35	8.18	11.59	11.91	11.51	12.07	11.67	12.48	12.60	12.55	12.73	12.95	12.59	12.60
Na_2O	1.71	1.81	1.68	1.81	1.70	1.87	2.10	2.76	2.78	2.75	2.69	2.70	2.67	2.66
K_2O	0.08	0.10	0.09	0.09	0.09	0.12	0.12	0.15	0.15	0.18	0.18	0.20	0.19	0.18
Total	96.17	101.04	97.84	97.63	97.92	97.36	97.38	99.02	99.66	99.27	99.04	98.63	98.57	98.80
X_{Mg}	0.65	0.88	0.80	0.79	0.81	0.77	0.78	0.72	0.73	0.73	0.72	0.71	0.72	0.73
X_{Ca}	0.80	0.71	0.79	0.78	0.79	0.78	0.75	0.71	0.71	0.72	0.72	0.73	0.72	0.72

Sample	MG4	MG4	MG4	MG4	MG4	MG4	MG4	MG4	MG4	MG4	MG4	MG4	MG4	MG4
Run duration	72	72	72	72	72	72	72	72	72	72	72	72	72	72
Melt	AH6	AH6	AH6	AH6	AH6	AH6	AH6	AH6	AH6	AH6	AH6	AH6	AH6	AH6
IMA (wt%)	25	25	25	25	25	25	25	25	25	25	25	25	25	25
T	$1300_{(i)}$-$1100_{(f)}$	$1300_{(i)}$-$1100_{(f}$	$1300_{(i)}$-$1100_{(f}$	$1300_{(i)}$-$1100_{(f}$	$1300_{(i)}$-$1100_{(f)}$	$1300_{(i)}$-$1100_{(f}$	$1300_{(i)}$-$1100_{(f}$	$1300_{(i)}$-$1100_{(f)}$	$1300_{(i)}$-$1100_{(f}$	$1300_{(i)}$-$1100_{(f}$	$1300_{(i)}$-$1100_{(f}$	$1300_{(i)}$-$1100_{(f}$	$1300_{(i)}$-$1100_{(f)}$	$1300_{(i)}$-$1100_{(f)}$
P	0.5	0.5	0.5	0.5	0.5	0.5	0.5	0.5	0.5	0.5	0.5	0.5	0.5	0.5
Point Analysis	MG4M8	MG4M9	MG4M10	MG4M11	MG4M12	MG4M13	MG4M14	MG4M15	MG4M16	MG4M17	MG4M18	MG4M19	MG4M20	MG4M21
SiO_2	48.53	48.81	50.11	50.22	50.63	51.13	50.82	51.19	50.95	51.04	50.54	49.88	49.93	50.66
TiO_2	0.92	0.97	0.82	0.89	0.95	0.86	0.92	0.97	0.89	0.90	0.85	0.97	0.92	0.90
Al_2O_3	19.42	20.54	20.40	20.05	19.63	19.05	19.02	19.25	19.51	19.69	19.49	19.78	19.85	20.74
Cr_2O_3	0.00	0.02	0.01	0.00	0.00	0.09	0.00	0.01	0.04	0.04	0.00	0.00	0.01	0.03
FeO	4.67	4.84	4.85	4.75	5.05	4.97	5.00	4.93	5.07	4.99	4.94	5.13	5.02	4.88
MgO	0.08	0.13	0.09	0.10	0.13	0.12	0.16	0.12	0.10	0.13	0.07	0.02	0.12	0.11
MnO	0.00	0.03	0.07	0.00	0.03	0.00	0.02	0.01	0.05	0.00	0.04	0.00	0.01	0.00
NiO	7.52	6.96	7.04	7.35	7.10	7.56	7.17	7.33	7.28	6.76	6.96	7.63	7.58	5.31
CaO	12.50	12.75	12.26	11.77	12.22	12.15	12.20	12.12	12.29	12.37	12.42	12.13	12.18	13.00
Na_2O	2.70	2.68	2.74	2.89	2.75	2.75	2.77	2.96	2.76	2.83	2.75	2.71	2.81	2.85
K_2O	0.20	0.21	0.21	0.24	0.18	0.20	0.21	0.20	0.19	0.19	0.20	0.17	0.20	0.16
Total	96.55	97.93	98.60	98.26	98.67	98.87	98.29	99.09	99.13	98.94	98.26	98.42	98.63	98.64
X_{Mg}	0.74	0.72	0.72	0.73	0.72	0.73	0.72	0.73	0.72	0.71	0.72	0.73	0.73	0.66
X_{Ca}	0.72	0.72	0.71	0.69	0.71	0.71	0.71	0.69	0.71	0.71	0.71	0.71	0.71	0.72

Sample	MG4	MG4	MG4	MG4	MG4	MG4	MG4	MG4	MG4	MG16	MG16	MG16
Run duration	72	72	72	72	72	72	72	72	72	72	72	72
Melt	AH6	AH6	AH6	AH6	AH6	AH6	AH6	AH6	AH6	AH6	AH6	AH6
IMA (wt%)	25	25	25	25	25	25	25	25	25	50	50	50
T	$1300_{(i)}$-$1100_{(f)}$	$1300_{(i)}$-$1100_{(f)}$	$1300_{(i)}$-$1100_{(f)}$	$1300_{(i)}$-$1100_{(f)}$	$1300_{(i)}$-$1100_{(f)}$	$1300_{(i)}$-$1100_{(f)}$	$1300_{(i)}$-$1100_{(f)}$	$1300_{(i)}$-$1100_{(f)}$	$1300_{(i)}$-$1100_{(f)}$	$1300_{(i)}$-$1100_{(f)}$	$1300_{(i)}$-$1100_{(f)}$	$1300_{(i)}$-$1100_{(f)}$
P	0.5	0.5	0.5	0.5	0.5	0.5	0.5	0.5	0.5	0.5	0.5	0.5
Point Analysis	MG4M22	MG4M23	MG4M24	MG4M25	MG4M26	MG4M27	MG4M28	MG4M29	MG4M30	MG16M1	MG16M2	MG16M3
SiO_2	50.03	50.08	50.44	49.84	49.86	50.09	50.05	49.91	50.00	34.45	31.67	31.62
TiO_2	0.93	1.05	0.98	0.99	0.89	0.95	0.94	0.85	0.98	0.37	0.85	0.84
Al_2O_3	19.01	18.89	19.31	19.67	19.70	19.91	19.83	19.85	19.50	17.21	9.43	9.94
Cr_2O_3	0.00	0.00	0.01	0.01	0.06	0.00	0.00	0.00	0.02	0.00	0.08	0.01
FeO	5.22	5.43	5.40	5.26	5.31	5.27	5.18	5.06	5.33	5.90	5.88	5.97
MgO	0.12	0.10	0.09	0.09	0.09	0.10	0.15	0.12	0.15	0.15	0.17	0.14
MnO	0.00	0.00	0.00	0.00	0.00	0.02	0.00	0.07	0.00	0.02	0.03	0.06
NiO	7.82	7.51	7.46	7.83	7.30	7.38	7.24	6.87	7.32	6.99	8.00	7.05
CaO	11.95	12.42	12.13	12.29	12.33	12.31	12.33	12.45	12.34	21.81	32.76	32.98
Na_2O	2.70	2.70	2.64	2.69	2.60	2.71	2.70	2.74	2.77	1.87	0.62	0.59
K_2O	0.19	0.19	0.16	0.19	0.18	0.15	0.19	0.18	0.16	0.35	0.07	0.08
Total	97.97	98.37	98.62	98.86	98.32	98.89	98.60	98.10	98.57	89.13	89.56	89.28
X_{Mg}	0.73	0.71	0.71	0.73	0.71	0.71	0.71	0.71	0.71	0.68	0.71	0.68
X_{Ca}	0.71	0.72	0.72	0.72	0.72	0.72	0.72	0.72	0.71	0.87	0.97	0.97

Table 7-10 *Textural and intra-granular deformation parameters, provided by EBSD analysis, for each class of grain size of isothermal experiment MG10 with 10wt%$_{IMA}$ run at 0.5 GPa and 1200°C for 24h.*

CLASS	Grain area (micron^2)	Equivalent diameter (micron)	Aspect Ratio	Shape Factor	PARIS Factor (%)	GOS (°)	KAM
5-10 micron	49.27	7.77	1.46	1.13	1.63	0.75	1.00
10-15 micron	136.00	13.09	1.52	1.18	6.25	1.16	1.10
15-20 micron	258.40	18.08	1.55	1.22	10.62	1.45	1.01
20-25 micron	419.41	23.08	1.69	1.25	14.81	1.97	1.00
25-30 micron	626.30	28.20	1.59	1.35	25.80	2.19	1.11
30-35 micron	877.49	33.39	1.55	1.29	19.31	2.40	1.00
35-40 micron	1140.17	38.08	1.44	1.31	26.39	2.74	1.09
40-45 micron	1437.29	42.76	1.38	1.24	18.94	2.80	0.87
45-50 micron	1788.17	47.70	1.38	1.40	41.90	3.15	0.87
50-55 micron	2248.22	53.48	1.65	1.40	31.80	2.70	0.95
55-60 micron	2688.55	58.50	1.38	1.54	59.46	3.19	0.85
60-65 micron	3046.55	62.28	1.30	1.30	24.36	3.16	0.44
65-70 micron	3664.57	68.29	1.29	1.41	48.38	3.13	0.84
70-75 micron	4133.39	72.53	1.41	1.41	41.47	2.14	0.60
75-80 micron	4780.84	78.02	1.46	1.26	23.25	2.53	0.94

Table 7-11 *Textural and intra-granular deformation parameters, provided by EBSD analysis, for each class of grain size of isothermal experiment MG12 with 25wt%$_{IMA}$ run at 0.5 GPa and 1200°C for 24h.*

CLASS	Grain area (micron^2)	Equivalent diameter (micron)	Aspect Ratio	Shape Factor	PARIS Factor (%)	GOS (°)	KAM
5-10 micron	42.28	7.15	1.52	1.15	2.93	0.96	0.96
10-15 micron	137.74	13.16	1.63	1.23	10.29	1.38	1.01
15-20 micron	264.84	18.30	1.69	1.29	15.25	1.57	1.00
20-25 micron	433.15	23.44	1.73	1.31	18.29	1.70	0.87
25-30 micron	637.51	28.44	1.90	1.33	19.02	1.63	1.12
30-35 micron	867.72	33.21	1.82	1.35	21.03	1.52	1.02
35-40 micron	1166.60	38.52	1.94	1.39	22.63	1.79	0.82
40-45 micron	1468.32	43.21	1.79	1.39	29.78	1.44	1.09
45-50 micron	1838.18	48.36	1.77	1.30	18.38	1.37	0.99
50-55 micron	2198.95	52.90	1.59	1.24	15.88	0.91	0.61
55-60 micron	2668.16	58.26	1.80	1.36	21.12	1.65	1.11

Table 7-12 *Textural and intra-granular deformation parameters, provided by EBSD analysis, for each class of grain size of isothermal experiment MG14 with 50wt%$_{IMA}$ run at 0.5 GPa and 1200°C for 24h.*

CLASS	Grain area (micron^2)	Equivalent diameter (micron)	Aspect Ratio	Shape Factor	PARIS Factor (%)	GOS (°)	KAM
5-10 micron	48.75	7.72	1.55	1.15	1.82	0.75	0.99
10-15 micron	140.57	13.30	1.70	1.24	7.75	0.92	1.02
15-20 micron	248.62	17.73	1.70	1.27	11.98	0.81	0.95
20-25 micron	415.94	22.97	1.88	1.33	15.24	1.08	1.03
25-30 micron	632.87	28.35	1.88	1.38	21.95	0.89	0.87
30-35 micron	886.14	33.56	1.79	1.40	28.62	0.75	1.07
35-40 micron	1097.99	37.37	1.61	1.43	34.12	0.77	1.18
40-45 micron	1542.94	44.31	1.86	1.50	40.87	0.78	0.87
45-50 micron	1885.59	48.98	1.26	1.29	29.98	1.77	0.72
55-60 micron	2785.27	59.55	1.52	1.27	21.56	3.34	0.71
65-70 micron	3611.67	67.81	1.26	1.63	102.68	0.69	1.14

Table 7-13 *Textural and intra-granular deformation parameters, provided by EBSD analysis, for each class of grain size of isothermal experiment MG11 with 50wt%$_{IMA}$ run at 0.5 GPa and 1250°C for 24h.*

CLASS	Grain area (micron^2)	Equivalent diameter (micron)	Aspect Ratio	Shape Factor	PARIS Factor (%)	GOS (°)	KAM
10-15 micron	136.28	13.05	1.63	1.27	13.36	0.44	0.46
15-20 micron	136.28	13.05	1.63	1.27	13.36	0.44	0.46
20-25 micron	440.42	23.64	1.60	1.21	9.37	0.41	0.34
25-30 micron	644.39	28.60	1.71	1.21	7.72	0.35	0.44
30-35 micron	891.49	33.65	1.58	1.28	18.01	0.42	0.39
35-40 micron	1186.61	38.85	1.60	1.20	8.90	0.44	0.50
40-45 micron	1479.48	43.37	1.64	1.21	8.94	0.41	0.43
45-50 micron	1832.73	48.29	1.62	1.30	23.47	0.45	0.50
50-55 micron	2308.30	54.20	1.77	1.33	19.95	0.47	0.41
55-60 micron	2694.81	58.56	1.61	1.20	7.07	0.37	0.39
60-65 micron	3232.16	64.14	1.59	1.26	14.60	0.40	0.46
65-70 micron	3619.46	67.87	1.72	1.27	18.08	0.35	0.33
70-75 micron	4173.17	72.88	1.55	1.23	12.92	0.41	0.45
75-80 micron	4907.65	79.05	1.31	1.11	7.99	0.39	0.50
80-85 micron	5415.94	83.04	1.58	1.19	6.20	0.45	0.41
85-90 micron	6329.35	89.77	2.26	1.62	47.50	0.36	0.42
95-100 micron	7298.43	96.40	1.31	1.15	7.70	0.33	0.37

Table 7-14 *Textural and intra-granular deformation parameters, provided by EBSD analysis, for each class of grain size of isothermal experiment OM23 with 9wt%$_{IMA}$ run at 0.5 GPa and 1300°C for 0.5h.*

CLASS	Grain area (micron^2)	Equivalent diameter (micron)	Aspect Ratio	Shape Factor	PARIS Factor (%)	GOS (°)	KAM
5-10 micron	46.60	7.51	1.45	1.19	8.99	0.72	0.19
10-15 micron	136.20	13.09	1.48	1.24	17.29	1.36	0.18
15-20 micron	259.66	18.13	1.61	1.35	25.42	2.33	0.18
20-25 micron	435.71	23.51	1.57	1.39	32.63	2.96	0.17
25-30 micron	624.06	28.16	1.58	1.43	37.05	3.02	0.18
30-35 micron	871.19	33.28	1.61	1.43	38.47	3.60	0.20
35-40 micron	1153.26	38.29	1.48	1.39	36.80	3.03	0.18
40-45 micron	1464.08	43.15	1.50	1.42	40.96	2.84	0.18
45-50 micron	1847.77	48.49	1.56	1.43	43.74	3.61	0.18
50-55 micron	2254.13	53.55	1.49	1.39	40.34	2.93	0.20
55-60 micron	2627.92	57.83	1.49	1.41	39.61	2.72	0.21
60-65 micron	3201.83	63.84	1.88	1.46	43.81	2.92	0.27
65-70 micron	3658.37	68.24	1.32	1.37	41.78	2.46	0.37
75-80 micron	4746.16	77.74	1.64	1.22	18.25	0.97	0.13
80-85 micron	5444.44	83.26	1.59	1.90	103.39	3.34	0.08
100-105 micron	8114.85	101.65	1.74	1.51	47.66	1.43	0.15
105-110 micron	9497.08	109.96	1.45	1.25	26.37	0.76	0.07

Table 7-15 *Textural and intra-granular deformation parameters, provided by EBSD analysis, for each class of grain size of isothermal experiment MG1 with 25wt%$_{IMA}$ run at 0.5 GPa and 1300°C for 24h.*

CLASS	Grain area (micron^2)	Equivalent diameter (micron)	Aspect Ratio	Shape Factor	PARIS Factor (%)	GOS (°)	KAM
10-15 micron	134.66	12.99	1.41	1.11	4.02	0.49	0.69
15-20 micron	266.94	18.38	1.41	1.13	4.13	0.55	0.66
20-25 micron	432.67	23.43	1.41	1.13	4.97	0.56	0.66
25-30 micron	643.36	28.58	1.39	1.14	5.66	0.61	0.62
30-35 micron	876.53	33.37	1.40	1.14	5.91	0.66	0.59
35-40 micron	1149.26	38.22	1.44	1.19	5.50	0.91	0.64
40-45 micron	1486.99	43.49	1.45	1.19	6.78	0.89	0.60
45-50 micron	1858.29	48.62	1.44	1.17	6.93	0.78	0.69
50-55 micron	2258.87	53.61	1.44	1.20	6.33	0.96	0.89
55-60 micron	2668.79	58.27	1.41	1.24	13.15	1.03	0.77
60-65 micron	3139.78	63.21	1.47	1.24	13.00	1.12	1.00
65-70 micron	3666.31	68.31	1.43	1.22	6.18	1.03	0.68
70-75 micron	4233.31	73.40	1.34	1.23	15.25	1.31	0.51
75-80 micron	4784.18	78.04	1.43	1.26	11.41	0.92	0.59
80-85 micron	5560.87	84.13	1.31	1.25	17.32	0.91	1.00
85-90 micron	6086.90	88.03	1.53	1.22	4.56	1.16	0.54
90-95 micron	6811.49	93.12	1.36	1.21	0.60	0.95	0.51

Table 7-16 *Textural and intra-granular deformation parameters, provided by EBSD analysis, for each class of grain size of isothermal experiment MG5 with 50wt%$_{IMA}$ run at 0.5 GPa and 1300°C for 24h.*

CLASS	Grain area (micron^2)	Equivalent diameter (micron)	Aspect Ratio	Shape Factor	PARIS Factor (%)	GOS (°)	KAM
10-15 micron	128.46	12.68	1.72	1.29	12.92	0.44	0.48
15-20 micron	271.21	18.53	1.54	1.30	20.74	0.40	0.54
20-25 micron	432.04	23.41	1.51	1.31	23.55	0.40	0.50
25-30 micron	628.89	28.26	1.60	1.31	23.33	0.42	0.53
30-35 micron	892.95	33.69	1.43	1.24	15.68	0.40	0.48
35-40 micron	1157.40	38.36	1.60	1.38	31.78	0.39	0.48
40-45 micron	1479.52	43.38	1.51	1.36	31.37	0.39	0.49
50-55 micron	2200.76	52.92	1.65	1.40	33.50	0.41	0.47
55-60 micron	2660.61	58.19	1.56	1.31	24.48	0.40	0.48
60-65 micron	3077.19	62.58	1.31	1.28	31.91	0.39	0.49
65-70 micron	3594.10	67.63	1.66	1.59	55.23	0.38	0.47
70-75 micron	4195.33	73.07	1.39	1.25	23.38	0.35	0.71
75-80 micron	4815.20	78.29	1.48	1.37	38.04	0.37	0.50
85-90 micron	5928.28	86.88	1.33	1.34	32.78	0.42	0.40
90-95 micron	6888.94	93.66	1.41	1.53	64.48	0.43	0.46
95-100 micron	7994.71	100.89	1.39	1.23	21.66	0.51	0.22

Table 7-17 *Textural and intra-granular deformation parameters, provided by EBSD analysis, for each class of grain size of step-cooled experiment MG15 with 10wt%$_{IMA}$ run at 0.5 GPa and from 1300 to 1100°C for 72h.*

CLASS	Grain area (micron^2)	Equivalent diameter	Aspect Ratio	Shape Factor	PARIS Factor (%)	GOS (°)	KAM
15-20 micron	266.62	18.39	1.95	1.51	41.93	0.46	0.48
20-25 micron	453.10	23.99	1.47	1.24	17.83	0.58	0.48
25-30 micron	646.71	28.65	1.37	1.19	14.83	0.50	0.44
30-35 micron	889.15	33.61	1.95	1.36	19.38	0.49	0.48
35-40 micron	1214.74	39.31	1.46	1.18	4.69	0.45	0.58
40-45 micron	1488.11	43.51	1.31	1.13	7.91	0.54	0.43
45-50 micron	1853.87	48.54	1.30	1.15	9.93	0.84	0.50
50-55 micron	2285.19	53.92	1.59	1.20	5.18	0.53	0.38
55-60 micron	2541.99	56.89	1.52	1.31	25.43	0.53	0.50
60-65 micron	3066.71	62.48	1.52	1.22	12.63	0.52	0.37
65-70 micron	3742.18	69.02	1.51	1.31	18.82	0.44	0.65
70-75 micron	4262.88	73.67	1.25	1.12	5.68	0.55	0.47
75-80 micron	4687.37	77.25	1.51	1.42	41.11	0.64	0.38
80-85 micron	5328.32	82.36	1.56	1.23	20.20	0.79	0.46
85-90 micron	6132.63	88.35	1.21	1.15	6.79	0.53	0.44
90-95 micron	7050.74	94.75	1.41	1.18	11.78	0.29	0.43
130-135 micron	14037.13	133.69	1.53	1.15	5.27	0.46	0.89

Table 7-18 *Textural and intra-granular deformation parameters, provided by EBSD analysis, for each class of grain size of step-cooled experiment MG4 with 25wt%$_{IMA}$ run at 0.5 GPa and from 1300 to 1100°C for 72h.*

CLASS	Grain area (micron^2)	Equivalent diameter	Aspect Ratio	Shape Factor	PARIS Factor (%)	GOS (°)	KAM
10-15 micron	126.40	12.57	1.58	1.21	8.71	0.46	0.58
15-20 micron	287.51	19.09	1.61	1.23	7.37	0.46	0.51
20-25 micron	433.61	23.46	1.44	1.23	12.82	0.50	0.52
25-30 micron	632.23	28.34	1.51	1.16	6.36	0.49	0.82
30-35 micron	850.86	32.90	1.54	1.26	16.19	0.63	0.56
35-40 micron	1134.53	37.98	1.52	1.30	21.08	0.46	0.71
40-45 micron	1512.95	43.87	1.36	1.21	13.19	0.46	0.67
45-50 micron	1811.48	48.01	1.52	1.27	19.11	0.72	0.70
50-55 micron	2299.77	54.09	1.56	1.35	27.10	0.49	0.56
55-60 micron	2865.74	60.40	1.39	1.14	10.12	0.52	0.48
60-65 micron	3212.11	63.94	1.42	1.29	22.67	0.66	0.61
65-70 micron	3731.01	68.91	1.25	1.16	9.86	0.46	0.58
70-75 micron	4167.80	72.84	1.28	1.48	57.36	0.53	0.60
100-105 micron	8133.94	101.76	1.34	1.27	33.31	0.59	0.59
110-115 micron	10191.20	113.91	1.29	1.21	21.67	0.75	0.42

Table 7-19 *Textural and intra-granular deformation parameters, provided by EBSD analysis, for each class of grain size of step-cooled experiment MG16 with 50wt%$_{IMA}$ run at 0.5 GPa and from 1300 to 1100°C for 72h.*

CLASS	Grain area (micron^2)	Equivalent diameter	Aspect Ratio	Shape Factor	PARIS Factor (%)	GOS (°)	KAM
10-15 micron	127.40	12.63	1.97	1.34	14.91	0.49	0.41
15-20 micron	265.77	18.34	1.85	1.28	11.74	0.53	0.38
20-25 micron	408.76	22.78	1.62	1.38	33.50	0.54	0.37
25-30 micron	670.59	29.20	1.31	1.20	14.45	0.50	0.43
30-35 micron	879.22	33.41	1.66	1.30	18.02	0.58	0.40
35-40 micron	1156.74	38.37	1.37	1.17	8.68	0.56	0.33
40-45 micron	1535.58	44.21	1.80	1.27	11.77	0.45	0.40
50-55 micron	2180.47	52.67	1.45	1.47	48.52	0.49	0.32
60-65 micron	3178.56	63.61	1.52	1.22	14.51	0.45	0.31
70-75 micron	4297.47	73.97	1.21	1.16	18.33	0.57	0.40
80-85 micron	5077.36	80.40	1.87	1.46	34.70	0.47	0.30
85-90 micron	5951.20	87.05	1.24	1.17	12.87	0.42	0.50
100-105 micron	8156.16	101.91	1.56	1.61	75.49	0.71	0.62